

**Porous Silicon Biosensors for Protein Targets:
Modelling and Sensitivity Enhancement**

**Von der Naturwissenschaftlichen Fakultät der
Gottfried Wilhelm Leibniz Universität Hannover
und
dem Senat des Technion – Israel Institute of Technology**

Zur Erlangung des Grades

Doktorin der Naturwissenschaften (Dr. rer. nat.)

und

Doctor of Philosophy (PhD)

genehmigte Dissertation

von

Sofia Arshavsky-Graham, Master (Israel)

2021

Referent: Prof. Dr. rer. nat. Thomas Scheper
Institute for Technical Chemistry
Gottfried Wilhelm Leibniz University Hannover

Referentin: Prof. Ester Segal
Department of Biotechnology and Food Engineering
Technion – Israel Institute of Technology

Korreferentin: Prof. Sharon Weiss
Department of Electrical Engineering and Computer Science
Vanderbilt University

Tag der Promotion: 11.03.2021

Danksagung / Acknowledgements

The Research Thesis was Done Under the Supervision of Prof. Ester Segal in the Department of Biotechnology and Food Engineering (Technion) and Prof. Thomas Scheper at the Institute of Technical Chemistry (Leibniz University Hannover). The Generous Financial Support of the German Research Foundation (grant SCHE 279/32), the Israel Science Foundation (grant No. 704/17), the Technion-Israel Institute of Technology, Leibniz University Hannover, the Russell Berrie Nanotechnology Institute, Miriam and Aaron Gutwirth Fellowship and Daniel Fellowship Administered by the Irwin and Joan Jacobs Graduate School, Cogan Travel Fellowship Administered by Prof. Uri Cogan and TEVA Pharmaceutical Industries are Gratefully Acknowledged.

Kurzfassung

Nanostrukturiertes poröses Silizium (PSi) als optischen Transducer für die Detektion zahlreicher Moleküle wurde in den letzten Jahren intensiv untersucht. Die nanoporöse Struktur wird durch elektrochemisches Ätzen hergestellt, bietet eine hohe interne Oberfläche und ideale Bedingungen zur chemischen Funktionalisierung bei charakteristischen optischen Eigenschaften. Zielmoleküle können mit einem einfachen experimentellen Aufbau markierungsfrei in Echtzeit detektiert werden. Dennoch haben sich PSi-Biosensoren aufgrund ihrer unzureichenden Sensitivität im mikromolaren Bereich für die Detektion von DNA und Proteinen in der klinischen Anwendung nicht durchgesetzt.

Die limitierenden Faktoren PSi-basierter Biosensoren und Methoden werden zu ihrer Optimierung ermittelt. Als Modellsystem werden Fabry-Pérot Dünnschichten untersucht und „reflective interferometric Fourier transform spectroscopy“ Messungen zur markierungsfreien Detektion von unterschiedlichen Zielproteinen erfolgen. Die Selektivität der Biosensoren wird durch die Funktionalisierung mit DNA-Aptameren erreicht. Vorteile dieser synthetischen Fängermoleküle im Vergleich zu traditionell eingesetzten Antikörpern werden untersucht. Im Vergleich zeigen beide Systeme ähnliche Biosensor-Eigenschaften bezüglich Detektionsbereich, Selektivität und Sensitivität, wenn die jeweiligen Fängermoleküle orientiert auf der PSi-Oberfläche immobilisiert werden. Nichtsdestotrotz vereinfachen die Stabilität und die geringen Kosten von DNA-Aptameren im Vergleich zu Antikörpern die Produktion, Haltbarkeit und Wiederverwendbarkeit Aptamer-basierter Biosensoren.

Um die Limitierungen von PSi-Biosensoren zu ermitteln, wurde ein umfangreiches mathematisches Modell, das alle Phänomene der Stofftransport- und Reaktionskinetik berücksichtigen, hergeleitet. Die Lösung erfolgt numerisch und zeigt, dass es erfolgreich Bindungsraten für ausgewählte Zielmoleküle in diesen Biosensoren beschreibt. Das Modell wird verwendet, um den Einfluss von Diffusionsraten zu untersuchen. Darüber hinaus kann damit die Abweichung zwischen experimentellen und theoretischen Affinitäten zwischen Fängermolekül und Zielprotein erklärt und verbessert werden.

Über die Anwendung der Isotachophorese zur „on-chip“ Anreicherung von Proteinen, dem Mischen der Zielmoleküle auf dem Biosensor oder die Integration in mikrofluidische Systeme kann die Sensitivität 1000-fach erhöht werden. PSi-basierte Biosensoren mit aus Polyacrylat bestehenden 3D-gedruckte mikrofluidische Systeme werden beschrieben. So wird die empfindliche poröse Nanostruktur bewahrt, während diese an die raue Polyacrylat-Oberfläche gebunden ist.

Abschließend wird ein PSi-basierter Biosensor für die Detektion relevanter Proteine als Krebs-Biomarker entwickelt und die selektive Detektion in hochkomplexem Pankreassaft präsentiert. Durch die Anwendung der oben beschriebenen Methoden wird die Sensitivität des Biosensors in den nanomolaren Bereich verbessert. Diese Arbeit ebnet den Weg für die klinische Anwendung von PSi-basierten Biosensoren und die Überführung in die patientennahe Diagnostik.

Schlüsselwörter: Optischer Biosensor; Aptamer; Poröses Silizium; Mathematische Modellierung; Mikrofluidik; Isotachophorese; Protein.

Abstract

Abstract

Nanostructured porous silicon (PSi) films have been widely studied for the past two decades as optical transducers for the detection of various molecules, with advantages of simple fabrication, high internal surface, well-established surface chemistry and unique optical properties. Despite these significant advantages, the clinical implementation of label-free PSi-based biosensors has been impaired by their insufficient sensitivity, usually in the micromolar range for protein and DNA targets.

In this work, we investigate the limiting factors of PSi-based optical biosensors and design methods for their improvement. As a model system, we study PSi Fabry-Pérot thin films and utilize reflective interferometric Fourier transform spectroscopy for real-time and label-free detection of different target proteins. The selectivity of the biosensors is achieved by functionalization of the porous layer with DNA aptamers, as capture probes. We investigate the advantages of these emerging synthetic capture probes in comparison to the corresponding gold-standard antibodies. We demonstrate that a similar biosensing performance, in terms of dynamic detection range, sensitivity and selectivity, is achieved when the respective capture probe is carefully immobilized onto the PSi transducer surface, considering orientation and surface density. Nevertheless, the stability and low cost of DNA aptamers in comparison to antibodies facilitate the production, shelf-life storage, and potential reusability of these aptamer-based biosensors.

To decipher the limiting factors of PSi biosensors, we derive a comprehensive mathematical model, which considers all mass transport and reaction kinetics phenomena in these biosensors. We solve the model numerically and demonstrate that the model successfully captures target binding rate in these biosensors, contrary to the conventional model used in the literature. The model is used to elucidate the orders of magnitude deviations between experimental and theoretical affinities between the capture probes and the target proteins observed in these biosensors and to develop rule of thumbs for their optimization.

To enhance the performance of PSi-based biosensors, we design methods for mass transfer acceleration. These include application of isotachopheresis (ITP) method for on-chip protein concentration, target mixing on top of the biosensor or simple microfluidic integration, with up to 1000-fold enhancement in sensitivity. To allow flexible study of different microfluidic designs, we integrate for the first time PSi-based biosensor in 3D-printed polyacrylate microfluidic devices by a simple bonding method and demonstrate an improved performance of the 3D-printed microfluidics, compared to the gold-standard polydimethylsiloxane (PDMS) polymer used for microfluidic fabrication.

Finally, we develop a PSi-based biosensor for detection of a relevant protein cancer biomarker and present a selective target detection in a highly complex fluid of pancreatic juice. By application of the methods described above, we were able to improve the sensitivity of the biosensor to the nanomolar range. This work paves the way towards clinical application of PSi-based biosensors and their translation to point of care settings.

Keywords: optical biosensor; aptamer; porous silicon; mathematical modelling; microfluidics; isotachopheresis; protein.

חיישנים ביולוגיים הינם התקנים אנליטיים המורכבים ממולקולות קולטן ביולוגי, שתפקידה לקשור את מולקולת המטרה, ומתמר, שתפקידו להמיר את הקישור לאות מדיד. חיישנים אלו נחקרים רבות כחלופה לשיטות אנליטיות מסורתיות (כגון: ELISA ו-PCR), אשר אורכות זמן רב, יקרות, דורשות סביבה מעבדתית לביצוען וכוח אדם מיומן. בהיבט של אבחון רפואי, לרוב, חיישנים ביולוגיים משמשים לזיהוי וכימות של מולקולות סמן להתפתחות מחלה בדגימות נוזלי גוף. במרבית המקרים, ריכוזי הסמן בדגימות אלה הינו נמוך מאד ($\leq 10^{-12} M$) ועל כן נדרשת רגישות גבוהה מאד של החיישן כדי להגיע לרלוונטיות קלינית. שתי תכונות חשובות נוספות לפעולת החיישן הינן זיהוי מהיר של מולקולת המטרה וסלקטיביות גבוהה. שלושת אתגרים אלו הינם העיקריים בפיתוח חיישנים ביולוגיים לשימוש קליני. נדבך חשוב נוסף הינו התאמת החיישן לסביבה שאיננה מעבדתית, כך שיוכל לשמש את החולה בביתו או את הרופא ישירות בקליניקה (point-of-care settings) ולצורך כך רצוי כי החיישן יהיה נייד, זול, ידידותי למשתמש ולא פולשני. כלל תכונות אלה צריכות להנחות את תהליך פיתוח החיישן.

סיליקון פורוזיבי נחקר רבות במהלך שני העשורים האחרונים כמתמר אופטי בחיישנים ביולוגיים לזיהוי מגוון רחב של מולקולות מטרה. המבנה הנקבובי הננומטרי מיוצר בקלות יחסית על ידי תהליכי איכול אלקטרוכימי של גביש סיליקון, ומציע מגוון רחב של יתרונות, כגון שטח פנים גדול, כימיית פני שטח מגוונת, ותכונות אופטיות ייחודיות. על ידי ניטור שינויים בתכנית החזרת האור מהסיליקון הפורוזיבי, ניתן לזהות בזמן אמת קישור של מולקולות לפני שטחו, ללא צורך בסימון או עיבוד מקדימים של מולקולת המטרה. למרות יתרונות אלה, חיישנים ביולוגיים המבוססים על סיליקון פורוזיבי לא הגיעו לכדי יישום בקליניקה בעקבות רגישות נמוכה יחסית, בתחום ריכוזים של $10^{-6} M$ בזיהוי חלבונים ודנ"א. מחקרי עבר זקפו זאת למגבלות של מעבר מסה במבנה הננומטרי, ועבודות רבות הציגו שיטות להגברת הרגישות של חיישנים אלה. עם זאת, מרבית השיטות הוסיפו מורכבות למערכת החישה ודרשו סימון של מולקולת המטרה או התבססו על זיהוי שאיננו ישיר של מולקולת המטרה. בעבודה זו אנו חוקרים את הגורמים המגבילים חיישנים ביולוגיים אופטיים המבוססים על סיליקון פורוזיבי ומפתחים שיטות לשיפורם. כמערכת מודל, בחרנו להתמקד במבנה הבסיסי ביותר של שכבה דקה של סיליקון פורוזיבי. על מנת להקנות סלקטיביות למבנה, אנו קושרים בשיטות כימיות מולקולות אפטמר דנ"א בתוך השכבה הפורוזיבית. אלה הן מולקולות חד גדיליות של דנ"א, בעלות קיפול תלת ממדי, המאפשר להן לזהות בצורה ספציפית את מולקולות המטרה שלהן. רצפי האפטמר נבחרים בתהליך של סלקציה מחזורית, שלאחריו, ייצור האפטמר הינו סינתטי לחלוטין. נוסף לכך, גודלם הקטן, מחירם הזול ויציבותם הכימית, העמידו אותם כחלופה מבטיחה לנוגדנים, המשמשים כיום כקולטנים סטנדרטיים בחיישנים. עם זאת, מחקרים אחרונים שהשוו בין אפטמרים ונוגדנים כקולטנים בחיישנים ביולוגיים הציגו תוצאות מגוונות ולא חד משמעיות לגבי יתרונותיהם וחסרונותיהם. על כן, במחקר זה, אנו חוקרים את תפקודם של אפטמרים ונוגדנים כקולטנים בסיליקון פורוזיבי לזיהוי של אותו חלבון מטרה, תוך דגש על צורת הקישור של הנוגדן לפני השטח (עם וללא אוריינטציה). אנו מציגים כי יכולת החישה של החיישנים תהיה דומה, מבחינת טווח הריכוזים, הרגישות והסלקטיביות, כל עוד מבוצעת אופטימיזציה של קישור הקולטן לפני השטח. עם זאת, יציבות מולקולות האפטמר ומחירן הזול מתבטאים ביתרונות בבניית החיישן, אחסונו ושימוש חוזר בו.

כדי לבחון את הגורמים המגבילים את רגישותם של החיישנים המבוססים על סיליקון פורוזיבי, פיתחנו מודל מתמטי אשר מתאר את כל תופעות מעבר המסה וכן את הקינטיקה של הריאקציה בין מולקולות הקולטן ומולקולת המטרה בחיישנים אלה. אנו פותרים את המודל בשיטות נומריות וממחישים כי המודל מתאר בצורה נכונה את קצב קישור מולקולת המטרה אל החיישן, לעומת המודל המתמטי המקובל בספרות. אנו משתמשים במודל שפותח כדי להבין את מידת ההשפעה של קצב הדיפוזיה בחיישנים פורוזיביים אלה ולהבהיר את מקור ההבדלים של מספר סדרי גודל שנצפו בין האפיוניות הניסיונית והתיאורטית בין

Abstract

הקולטן ומולקולת המטרה בחיישנים מסוג זה. בנוסף, בעזרת סימולציות נומריות, אנו ממליצים על מספר כללי אצבע לבניית החיישן, מבחינת תכונות המבנה הננומטרי וצפיפות מולקולת הקולטן על פני השטח של הסיליקון הפורוסיבי. על מנת להגביר את ביצועי החיישן, אנו מפתחים שיטות להגברת קצב מעבר המסה בחיישנים אלה. למשל, יישום של שיטת איזוטאכופוריזה (isotachophoresis) לריכוז החלבון בזמן אמת על גבי החיישן מאפשרת הגברת רגישותו עד פי אלף. כמו כן, מוצגת ההשפעה של ערבוב חלבון המטרה על גבי החיישן ואינטגרציה במערכות מיקרוזרימה. על מנת לאפשר גמישות במחקר של מבנים שונים של מערכות מיקרוזרימה, אנו מציגים לראשונה שילוב של חיישן המבוסס על סיליקון פורוסיבי במיקרו-תעלות פלסטיק שהודפסו במדפסת תלת ממד. פיתחנו שיטה להדבקה בין השניים, המאפשרת את חיבור פני השטח המחוספסים של התעלות המודפסות עם המבנה הננומטרי העדין של הסיליקון הפורוסיבי. אנו מציגים פעילות משופרת של החיישן במיקרו-תעלות המודפסות, לעומת אותו חיישן במיקרו-תעלות העשויות מפולי-די-מתיל-סילוקסאן (PDMS), שהינו הפולימר הנפוץ ביותר כיום לייצור מיקרו-תעלות. לבסוף, אנו מפתחים חיישן המבוסס על סיליקון פורוסיבי לזיהוי של חלבון המהווה סמן להתפתחות מחלת הסרטן. החיישן פועל בצורה סלקטיבית ומזהה את החלבון בדגימה מורכבת מאד של מיצי לבלב. על ידי שילוב של שיטות הגברת רגישות כפי שתוארו לעיל, אנו מצליחים להעלות את סף הזיהוי של החיישן לתחום הננו-מולר. עבודה זו משפרת את הפוטנציאל של שילוב חיישנים מבוססי סיליקון פורוסיבי בקליניקה וכן מקדמת את יישומם בסביבה שאיננה מעבדתית.

מילות מפתח: סיליקון, חיישן אופטי; אפטמר; מידול מתמטי; מיקרוזרימה; סמני סרטן; חלבון.

Table of Contents

Abstract (German)	III
Abstract (English).....	IV
Abstract (Hebrew).....	V
Table of Contents	VII
List of Figures and Tables	VIII
List of Abbreviations.....	XIV

1. Preamble.....	1
2. Literature Survey.....	3
2.1 Lab-on-a-Chip Devices for Medical Diagnostic Applications.....	3
2.2 Porous Silicon-Based Biosensors.....	17
3. Research Aims and Motivation.....	54
4. Experimental.....	55
4.1 Materials.....	55
4.2 Biosensor Construction.....	56
4.3 Microfluidics.....	61
4.4 Protein Targets.....	62
4.5 Biosensing.....	64
5. Results.....	68
5.1 Aptamers vs. Antibodies as Capture Probes in Optical Porous Silicon Biosensors.....	69
5.2 Mass Transfer Limitations of Porous Silicon-Based Biosensors for Protein Detection.....	94
5.3 On Chip Protein Pre-Concentration for Enhancing the Sensitivity of Porous Silicon Biosensors.....	126
5.4 3D-Printed Microfluidics Integrated with Optical Nanostructured Porous Aptasensors for Protein Detection.....	148
5.5 Porous Silicon-Based Aptasensors: Towards Cancer Protein Biomarker Detection.....	171
6. Discussion.....	197
7. Conclusions.....	203
8. References.....	204
9. List of Publications and Conferences	224
10. C.V.....	227

List of Figures

Figure 2.1.1. Schematic illustration of a typical lateral flow assay strip..... 5

Figure 2.1.2. Lateral flow assay-based microfluidic chip, which integrates a self-coalescence module, containing dried inkjet-spotted detection antibodies..... 6

Figure 2.1.3. 3D-origami-based paper device used for detection of a protein A in human synovial fluid..... 7

Figure 2.1.4. Bio-conjugated magnetic nanochains on a microchip as rapid active liquid mixers and capture agents for bio-separation..... 8

Figure 2.1.5. Magnetic particles for signal amplification in lateral flow immunoassay for human chorionic gonadotropin detection..... 9

Figure 2.1.6. Centrifugal microfluidic finger-prick blood biochemical analyser..... 11

Figure 2.1.7. Centrifugal microfluidics device for multiplex foodborne pathogen detection..... 12

Figure 2.1.8. A PoC lateral flow assay system for analysis of lactate dehydrogenase in whole blood..... 13

Figure 2.1.9. A smartphone-based fluorescence detection of Zika, chikungunya and dengue virus’s RNA platform, based on reverse-transcription loop-mediated isothermal amplification assay..... 15

Figure 2.2.1. Schematics and associated optical spectra of common porous silicon structures used for optical biosensing applications..... 22

Figure 2.2.2. A "ring-opening click" reaction of cyclic-silanes with the silanol-terminated pore walls of oxidized PSi..... 24

Figure 2.2.3. Schematic of DNA-induced corrosion process in PSi..... 26

Figure 2.2.4. Performance enhancement of PSi biosensors by capture probe and pore diameter optimization..... 34

Figure 2.2.5. Open-ended PSi membrane biosensing platform outperforms closed-ended films..... 36

Figure 2.2.6. IAW method for reflectivity data processing of PSi reflectivity..... 37

Figure 2.2.7. Signal amplification strategies..... 39

Figure 2.2.8. Signal amplification by target preconcentration..... 40

Figure 2.2.9. Sensitivity enhancement of luminescent-based biosensors..... 43

Figure 2.2.10. Implanted pre-incubated thermally hydrocarbonized PSi rugate filter through the skin of a mouse..... 46

Figure 2.2.11. PSi microarray biosensing platforms, constructed by PSi pre-patterning..... 49

Figure 2.2.12. A PRISM assay for monitoring bacterial response to antimicrobial agents and alkyl-terminated PSi nanoparticles for detection of copper ions..... 51

Figure 5.1.1. (a) Schematic illustration of the coupling steps followed for the immobilization of aptamers and antibodies. (b) ATR-FTIR spectra of PSiO₂ upon the different chemical modification steps throughout aptamer and antibody immobilization on the surface..... 79

Figure 5.1.2. Bioreceptors surface density.....	81
Figure 5.1.3. (a) Relative EOT changes of different P SiO_2 biosensors (random and oriented antibody-conjugated P SiO_2 and aptamer-conjugated P SiO_2) collected after 1 h exposure to varying tyrosinase concentrations. (b) Relative EOT changes vs. time for oriented antibody- or aptamer-immobilized P SiO_2 upon exposure to different concentrations of his-tagged tyrosinase. (c) and (d) Binding rates at 10 min and 60 min of incubation with different tyrosinase concentrations, respectively, for the three types of biosensors.....	83
Figure 5.1.4. The biosensor response, expressed as the relative EOT change, collected after 1 h exposure to different samples: trypsin as a non-target protein, bacterial lysates and lysates spiked with tyrosinase.....	85
Figure 5.1.5. Biosensor regeneration.....	87
Figure S5.1.1. Comparison of the biosensing performance of the immunosensor upon exposure to 56 μM Tyrosinase, for two methods of APTES modification of the P SiO_2 film.....	89
Figure S5.1.2. Real-time relative EOT changes for aptamer, oriented and unoriented antibody-immobilized P SiO_2 upon exposure to 56 μM or 8.25 μM his-tagged tyrosinase.....	91
Figure S5.1.3. Relative EOT changes vs. time for randomly oriented antibody-biofunctionalized P SiO_2 upon exposure to different concentrations of his-tagged Tyrosinase.....	91
Figure S5.1.4. Characteristic relative EOT changes vs. time for the (a) aptasensor and (b) oriented-immunosensor upon exposure to neat bacterial lysate, bacterial lysate spiked with 16.5 μM tyrosinase and 16.5 μM tyrosinase in a buffer.....	92
Figure S5.1.5. Relative EOT changes vs. time upon exposure of the oriented antibody-biofunctionalized P SiO_2 to 56 μM Tyrosinase, followed by washing with PBS and exposure to different regeneration solutions.....	92
Figure S5.1.6. Relative EOT changes vs. time upon exposure of the oriented antibody-biofunctionalized P SiO_2 to 56 μM Tyrosinase in three consecutive biosensing cycles, utilizing a regeneration solution of (I) 1M imidazole, (II) 100 mM HCl pH 2.0 and (III) 10 mM glycine/HCl pH 2.5.....	93
Figure S5.1.7. Comparison of a 30-min and a 5-min exposure time of the immunosensor to a regeneration solution of 10 mM glycine/HCl pH 2.5, presented as the relative signal for each biosensing cycle.....	93
Figure 5.2.1. P Si biosensor setup and characteristic biosensing results for different capture probe-target pairs.....	103
Figure 5.2.2. Schematic illustration of the (a) planar and (b) porous models, describing the mass transfer and reaction kinetic phenomena in the P Si -based biosensors.....	104
Figure 5.2.3. Comparison of experimental binding curves of the investigated aptasensors to numerical simulation results obtained for the porous and planar models, at target concentrations of (a) 50 μM and (b) 10 μM	108

Figure 5.2.4. Simulation of the distribution of the target concentration in z axis at different time points in (a) the bulk solution and (b) the porous layer, obtained by the porous model.....	109
Figure 5.2.5. The effect of biosensor characteristics on the simulated target binding rate.....	112
Figure S5.2.1. Simulated binding rates for the porous and planar models at target concentrations of (a) 1 μM and (b) 0.5 μM	118
Figure S5.2.2. Comparison of experimental binding curves of the investigated aptasensors, at target concentration of 50 μM to numerical simulation results obtained for the porous and planar models, for two different binding affinity interactions with (a) $K_D=1$ nM and (b) $K_D=1$ μM	119
Figure S5.2.3. Change in target concentration in z axis in the bulk solution at different time points, simulated by the planar model.....	120
Figure S5.2.4. Relative EOT changes as a function of time for 10 min-mixed and non-mixed AGR2 biosensing experiments on anti-AGR2 aptasensor.....	120
Figure S5.2.5. Simulated binding rate for the porous model, for different PSi porosity values, at a target concentration of 1 μM	122
Figure S5.2.6. Top view SEM micrographs and reflectivity spectra of PSi with different layer thicknesses.....	124
Figure S5.2.7. (a) Simulated binding rates for the porous model for an optimized aptasensor vs. the original aptasensor for different target concentrations. (b) Comparison of the simulated binding rates for the optimized and original aptasensors as a function of target concentration.....	125
Figure 5.3.1. (a) Schematic illustration of the PSiO_2 biosensor setup and an ITP-based biosensing experiment. (b) Raw fluorescence images of the target protein, focusing under different modes of ITP assay. (c) Averaged relative ΔEOT signal for counter-flow ITP, pass-over ITP and standard configurations for 750 nM target protein.....	134
Figure 5.3.2. (a) Relative ΔEOT changes vs. time of the constructed biosensor during typical ITP-based and standard biosensing experiments with 750 nM target protein. (b) Averaged relative ΔEOT signal for different concentrations of the target protein under standard and ITP conditions.....	135
Figure 5.3.3. (a) Raw fluorescence images of the ITP peak for different concentrations of the labelled target protein. (b) Comparison of the fluorescence intensity values of the labelled protein measured during standard vs. ITP biosensing experiments.....	137
Figure 5.3.4. (a) Relative ΔEOT changes vs. time of the aptamer-based biosensor during a typical ITP experiment with <i>E. coli</i> lysate suspension spiked or non-spiked with the target protein. (b) Averaged relative ΔEOT signal for ITP biosensing experiments of neat target protein, <i>E. coli</i> lysate spiked with the target protein and neat <i>E. coli</i> lysate.....	138
Figure S5.3.1. Characterization of the PSiO_2 nanostructure.....	140
Figure S5.3.2. Relative ΔEOT signal for activation of carboxylated PSi surface with EDC followed by conjugation of amino-terminated 6H7 aptamers.....	141

Figure S5.3.3. Relative Δ EOT changes vs. time of the constructed biosensor during standard biosensing experiment with the target protein.....	142
Figure S5.3.4. Relative Δ EOT changes vs. time of the constructed biosensor during ITP biosensing experiment with target protein at a concentration of 7.5 nM.....	143
Figure S5.3.5. Raw reflectivity spectra and the corresponding FFT peaks of the biosensor before and after exposure to the target protein upon ITP biosensing experiments.....	144
Figure S5.3.6. (a) Relative Δ EOT changes vs. time of the constructed biosensor during standard introduction of LE and TE buffers into the microchannel; (b) Relative Δ EOT changes vs. time of the constructed biosensor during ITP experiment with no protein. (c) Relative Δ EOT changes vs. time of the constructed biosensor during ITP experiment with no protein, without exposure to TE.....	145
Figure S5.3.7. SDS-PAGE analysis of bacteria lysates used for the biosensing experiments.....	146
Figure S5.3.8. Raw fluorescence images of the ITP peak of a target-spiked lysate sample.....	147
Figure 5.4.1. The microfluidic design, the PSi nanostructure, and the bonding method.....	156
Figure 5.4.2. Characterization of the 3D-printed microfluidic-integrated PSi device.....	158
Figure 5.4.3. Biosensing experiments using the 3D-printed microfluidic-integrated PSi aptasensor.....	160
Figure 5.4.4. Averaged relative EOT changes upon exposure of the 3D-printed microfluidic-integrated aptasensor to (a) different concentrations of the target D2 protein; (b) D2 and non-target proteins....	161
Figure 5.4.5 Comparison of the PSi aptasensor performance when integrated in different devices....	163
Figure S5.4.1. A schematic of the optical signal acquisition and analysis.....	165
Figure S5.4.2. Image of the 3D-printed microfluidic experimental setup.....	166
Figure S5.4.3. The integrated 3D-printed microfluidic aptasensor with a dyed solution flowed within the microchannels >1-year post bonding.....	167
Figure S5.4.4. Averaged relative EOT changes for the detection of 1 μ M D2 (target) and D2N (non-target) proteins in the 3D-printed microfluidic integrated aptasensor, where the aptamer molecules are immobilized prior or after the microfluidic integration.....	167
Figure S5.4.5. Real time relative EOT changes upon introduction of D2 (target) or D2N (non-target) protein solutions to the PDMS microfluidic setup, in which the aptamer is immobilized prior to microfluidic integration or within the microchannel.....	168
Figure 5.5.1. PSi aptasensor construction.....	180
Figure 5.5.2. Aptasensor response to AGR2 in solution and in pancreatin.....	182
Figure 5.5.3. Relative EOT changes and calculated slopes upon exposure of aptamer-functionalized PSi to different concentrations of AGR2.....	183
Figure 5.5.4. Time-resolved confocal laser scanning microscopy imaging of AGR2 diffusion within the aptasensor.....	185

List of Figures and Tables

Figure 5.5.5. Strategies for enhancing the sensitivity, by mass transfer acceleration via ITP, target mixing and integration with microchannels.....	188
Figure 5.5.6. Characteristic changes in relative Morlet wavelet phase and net EOT signals as a function of time for the lowest measured AGR2 concentrations in (a) mixing, (b) microchannel and (c) cell setups.....	189
Figure S5.5.1. Schematic illustration of the cationic ITP assay.....	191
Figure S5.5.2. Images of the experimental setups.....	192
Figure S5.5.3. Schematic illustration of the Morlet wavelet phase signal analysis method.....	193
Figure S5.5.4. Characteristic relative EOT changes as a function of time for the (a) aptasensor and (b) neat oxidized PSi upon incubation with 200 $\mu\text{g mL}^{-1}$ Trypsin, BSA or IgG in SB.....	193
Figure S5.5.5. SDS-PAGE characterization of pancreatin at the concentration used for the biosensing experiments.....	194
Figure S5.5.6. Characteristic relative EOT changes as a function of time upon aptasensor incubation with 100 $\mu\text{g mL}^{-1}$ AGR2 in a buffer, pancreatin spiked with 100 $\mu\text{g mL}^{-1}$ AGR2 and neat pancreatin.....	195
Figure S5.5.7. Characteristic relative EOT changes as a function of time upon aptasensor incubation with 100 $\mu\text{g mL}^{-1}$ AGR2 in SB, in a cell setup or in PDMS microchannels.....	195
Figure S5.5.8. Aptasensor selectivity upon Morlet wavelet phase and RIFTS signal processing techniques.....	196

List of Tables

Table 2.2.1. Performance summary of biomolecule detection with different PSi-based optical biosensors from 2016-2018.....	28
Table 4.1. Details of studied aptamers.....	56
Table 4.2. Properties of the studied capture probe and target protein pairs.....	57
Table 4.3. Leading electrolyte and terminating electrolyte buffer compositions used in ITP Assays.....	66
Table 5.1.1. Compositions of regeneration solution for the oriented antibody-based biosensor.....	77
Table S5.1.1 Characterization results of the oxidized PSi nanostructures by spectroscopic liquid infiltration method.....	89
Table S5.1.2. A summary of the applied amount, number of moles cleaved, the immobilized percentage and surface density of the aptamers and oriented and unoriented antibodies within the PSiO ₂	90
Table 5.2.1. Properties of the studied capture probe and target protein pairs and comparison of the theoretical and fitted K_D values.....	98

List of Figures and Tables

Table S5.2.1. Fitting parameters used for the numerical simulations, based on the properties of the different aptasensors.....	116
Table S5.2.2. Quantification of immobilized aptamer concentration and surface density on the P _{SiO} ₂	117
Table S5.2.3. Etching time and characterization results by SLIM.....	123
Table 5.4.1. Analytical results of the 3D-printed microfluidic-integrated aptasensor, compared to a similar aptasensor in a non-microfluidic setup	161
Table S5.4.1. Oxidized P _{Si} nanostructure fabrication and characterization with SLIM.....	166
Table S5.4.2. Overview of the construction of 3D-printed and PDMS-based microfluidic-integrated aptasensors and their biosensing performance.....	170
Table S5.5.1. Leading electrolyte and terminating electrolyte buffer compositions studied for AGR2 focusing on the aptasensor via cationic ITP technique.....	191

List of Abbreviations

3D	-	Three-dimensional
6H7	-	His-tag binding aptamer
AbnA-D2	-	Protein domain 2 of extracellular endo- α -(1->5)-L-arabinanase 1
AbnA-D4	-	Protein domain 4 of extracellular endo- α -(1->5)-L-arabinanase 1
ACN	-	Acetonitrile
AGR2	-	Anterior gradient homolog 2
APTES	-	(3-aminopropyl)triethoxysilane
AP-XPS	-	Angle-resolved X-ray photoelectron spectroscopy
ATR-FTIR	-	Attenuated total reflectance Fourier transform infrared
BAEE	-	N $_{\alpha}$ -benzoyl-L-arginine ethyl ester
BBS	-	Borate buffered saline
BET	-	Brunauer-Emmett-Teller
Bis-Tris	-	Bis(2-hydroxyethyl)amino-tris(hydroxymethyl)methane
BSA	-	Bovine serum albumin
CCD	-	Charge-coupled device
CLSM	-	Confocal laser scanning microscope
CRP	-	C-reactive protein
D2N	-	D2 without his tag
DIEA/EDIPA	-	Ethyl-diisopropylamine
DMSO	-	Dimethyl sulfoxide
DNA	-	Deoxyribonucleic acid
DTT	-	DL-Dithiothreitol
<i>E. coli</i>	-	<i>Escherichia coli</i>
EDC	-	N-(3-Dimethylaminopropyl)-N-ethylcarbodiimide hydrochloride
EDL-ISA	-	Electrical double layer-induced ion surface accumulation
EG	-	Oligo(ethylene glycol)
ELISA	-	Enzyme linked immunosorbent assay
EOF	-	Electroosmotic flow
EOT	-	Effective optical thickness
EtOH	-	Ethanol
FFT	-	Fast Fourier transformation
FITC	-	Fluorescein
FLPC	-	Fast protein liquid chromatography
GA	-	Glutaraldehyde

List of Abbreviations

HEPES	-	4-(2-hydroxyethyl)-1-piperazineethanesulfonic acid
HF	-	Hydrofluoric acid
HRP	-	Horseradish peroxidase
HRSEM	-	High resolution scanning electron microscopy
IAW	-	Interferogram average over wavelength
IgG	-	Immunoglobulin G
IMAC	-	Immobilized metal ion affinity chromatography
IPA	-	Isopropyl alcohol
ITP	-	Isotachopheresis
K_D	-	Dissociation constant
LB	-	Luria-Bertani
LE	-	Leading electrolyte
LED	-	Light-emitting diode
LoC	-	Lab on a chip
LOD	-	Limit of detection
LSPR	-	Localized surface plasmon resonance
MES	-	Morpholinoethanesulfonic acid
MIC	-	Minimal inhibitory concentration
MS	-	Mass spectrometry
NHS	-	N-hydroxysulfosuccinimide
NW	-	Nanowires
PanIN	-	Pancreatic intraepithelial neoplastic
PBS	-	Phosphate buffered saline
PCR	-	Polymerase chain reaction
PDMS	-	Polydimethylsiloxane
PEG	-	Polyethyleneglycol
PL	-	Photoluminescence
PNA	-	Peptide nucleic acid
PoC	-	Point of care
PSi	-	Porous silicon
PSiO ₂	-	Oxidized PSi
QD	-	Quantum dots
RIFTS	-	Reflective interferometric Fourier transform spectroscopy
RNA	-	Ribonucleic acid
SB	-	Selection buffer
SDS	-	Sodium dodecyl sulfate

List of Abbreviations

SELEX	-	Systematic Evolution of Ligands by Exponential Enrichment
SERS	-	Surface-enhanced Raman spectroscopy
SLIM	-	Spectroscopic liquid infiltration method
SNR	-	Signal-to-noise ratio
SOI	-	Silicon-on-insulator
SPDP	-	N-Succinimidyl 3-(2-pyridyldithio)propionate
ssDNA	-	Single stranded DNA
STD	-	Standard
TCPSi	-	Thermal carbonized PSi
TE	-	Terminating electrolyte
Tricine	-	N-[Tris (hydroxymethyl) methyl] glycine
UV	-	Ultraviolet
UV-Vis	-	Ultraviolet–visible

1. Preamble

A biosensor is an analytical device integrating a capture probe molecule with a transduction system, which converts specific analyte binding events into a measurable signal¹. Today, biosensors are widely researched as an attractive alternative for traditional bioanalytical methods such as enzyme linked immunosorbent assay (ELISA) and polymerase chain reaction (PCR), which are laborious, time-consuming, expensive and confined to a laboratory environment^{2,3}. Specifically in medical diagnostics, biosensors should detect target biomarker molecules at typically sub-picomolar concentrations in extracted body fluids to meet clinical criteria⁴. The three benchmarks for a successful clinically-relevant biosensor include high sensitivity, fast response time and selectivity, and they should be carefully considered while designing the biosensor⁵⁻⁸. Furthermore, translation to point-of-care (PoC) settings, in which the biosensor can be utilized at the patient bedside, is of high demand. Thus, the biosensor should be also portable, low-cost, minimally invasive and user friendly^{2,3,9}.

Surface-based biosensors, in which the capture probes are immobilized on the transducing surface, are among the most widespread bioanalytical tools¹⁰⁻¹⁴ and porous silicon (PSi)-based biosensors are an example for such. PSi is an inorganic nanostructured material, fabricated by electrochemical etching processes from a crystalline Si. It presents advantageous features such as high internal surface, simple and low-cost fabrication, well-established surface chemistry, as well as unique and tunable optical properties. Specifically, employing reflective interferometric Fourier transform spectroscopy (RIFTS) as the transduction mechanism enables real-time and label-free target detection¹⁵⁻¹⁸. In this method, a series of Fabry-Pérot interference fringes are produced from incident white light reflections from the top and bottom interfaces of a porous thin film and the fringe pattern depends on the thickness and averaged refractive index of the porous layer.

Label-free PSi-based biosensors have been widely studied for more than two decades; however, and despite their advantages, their clinical application has been impaired by their low sensitivity, usually in the micromolar range for protein and DNA targets¹⁹⁻²⁵. Mass transfer rate has been implied to limit these biosensors and studies have focused on developing assays for enhancing their sensitivity. Nevertheless, many of the suggested methods compromised the simplicity of the biosensor, or its label-free and direct target detection.

For selective target detection, a capture probe should be immobilized within the porous layer. While antibodies are considered the “gold standard”, aptamers have emerged in recent years as a promising alternative. These are single stranded oligonucleotides, which fold into a 3D-structure, enabling specific target binding. Aptamers are initially selected by a process termed Systematic Evolution of Ligands by Exponential Enrichment (SELEX), after which their production is synthetic. This is a great advantage compared to antibodies production, as well as the stability, low cost, and small size of aptamers. Aptamers integration in PSi biosensors has been demonstrated in 2015²⁶ showing promising biosensing

Preamble

results, which evoked a great interest. Since then, the potential of different PSi-based aptasensors has been increasingly studied and successful detection of various molecules was demonstrated^{19, 27-33}. Yet, antibodies are still considered the first choice for a capture probe and studies comparing aptamer and antibody performance in a similar setup have demonstrate variable results in terms of the limitations and strengths of each of the capture probes.

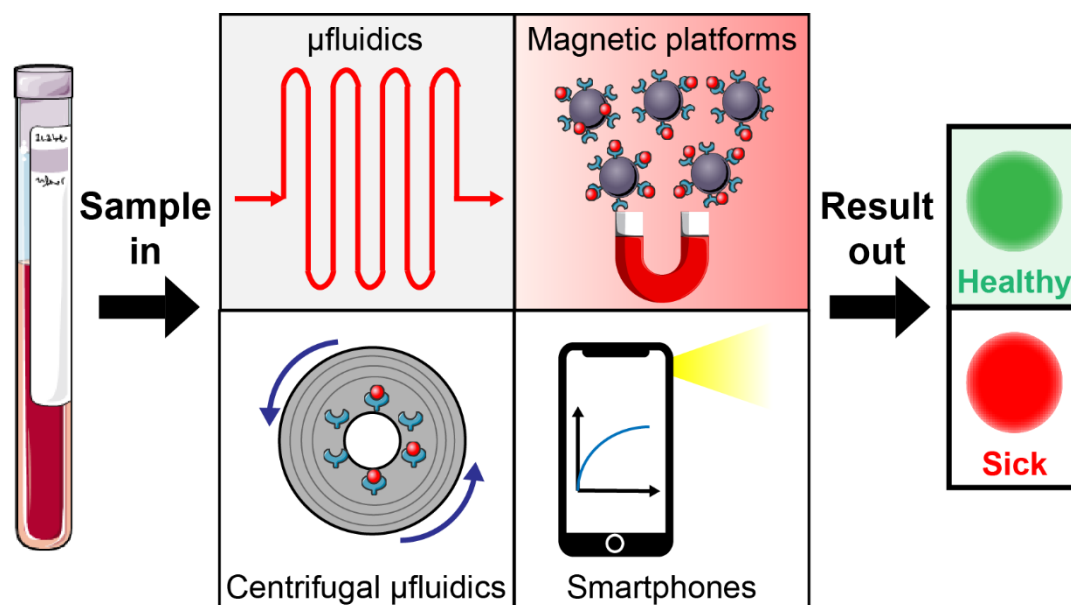
For PoC applications, microfluidic systems and their integration with biosensors are extensively studied^{34, 35}. The miniaturization of such systems reduces sample and reagent volume, shortens assay time, and enables high-throughput detection, portability, and reduced costs^{34, 35}. Importantly, microfluidics improve the mass transfer to the biosensor surface, resulting in a higher sensitivity compared to traditional biosensing setups³⁶⁻³⁸. Nowadays, polydimethylsiloxane (PDMS) is the most common polymer for fabrication of microfluidic devices. Yet, as it requires a master template for each microfluidic design, which is usually fabricated by soft lithography techniques, it challenges the rapid prototyping and translation to commercial scale^{39, 40}. Contrary, 3D printing, which significantly advanced in recent years, facilitates rapid and fully digital prototyping of complex microfluidics in a one step-process, at lower costs and manufacturing time^{40, 41}. To date, PSi-based optical biosensors have been only integrated with PDMS-based microfluidics, fabricated by soft lithography^{23, 30, 42-46}. The main challenge for the integration of PSi in 3D-printed plastic microfluidics is the rough surface of the latter, which needs to be bonded to the delicate nanostructure of the PSi.

In this work, we study PSi Fabry-Pérot thin film as an optical transducer for detection of various target proteins. DNA aptamers are immobilized within the porous layer as capture probes, and their performance is directly compared to antibodies for the detection of the same target protein. To decipher the limiting factors of label-free PSi-based biosensors, we derive a comprehensive mathematical model, which considers all mass transport and reaction kinetics phenomena in these porous biosensors. The model is solved numerically and compared to experimental results of several PSi-based biosensors, as well as to the common model used in the literature. The model is used to decipher the limiting phenomena of these biosensors and derive rule of thumbs for their optimization. We also design techniques for sensitivity enhancement of PSi-based biosensors, all based on mass transport acceleration. These include application of isotachopheresis for on-chip protein preconcentration and target solution mixing on top of the biosensor and microfluidic integration. We also present for the first-time integration of a PSi biosensor in 3D-printed plastic microfluidics via a simple bonding method. Finally, we construct a label-free PSi biosensor for detection of a protein cancer biomarker and demonstrate its successful performance in a highly complex medium of pancreatic juice.

2. Literature Survey

2.1 Lab-on-a-Chip Devices for Medical Diagnostic Applications

The following section is reproduced from the following book chapter: **Sofia Arshavsky-Graham** and Ester Segal. “Lab-on-a-Chip Devices for Point-of-Care Medical Diagnostics”. *In: Advances in Biochemical Engineering/Biotechnology*, Springer, Berlin, Heidelberg (2020).



Respective table of contents image

Abstract

The recent coronavirus (COVID-19) pandemic has underscored the need to move from traditional lab-centralized diagnostics to point-of-care (PoC) settings. Lab-on-a-chip (LoC) platforms facilitate the translation to PoC settings via the miniaturization, portability, integration, and automation of multiple assay functions onto a single chip. For this purpose, paper-based assays and microfluidic platforms are currently being extensively studied, and much focus is being directed towards simplifying their design, while simultaneously improving multiplexing and automation capabilities. Signal amplification strategies are being applied to improve the performance of assays, with respect to both sensitivity and selectivity, while smartphones are being integrated to expand the analytical power of the technology and promote its accessibility. In this chapter, we review the main technologies in the field of LoC platforms for PoC medical diagnostics, and survey recent approaches for improving these assays.

Introduction

Over the years, medical diagnostics has been shifting away from imaging and invasive tissue sampling towards far less invasive tests that detect disease biomarkers in extracted body fluids. Such biomarkers may include small metabolites, nucleic acids, proteins, and cells^{2, 47}. Today, most assays for biomarkers

detection are mainly performed at centralized labs, requiring trained personnel for operation of complex bench-top analyzers, with a correspondingly long time-to-result period. The latter consideration is critical with respect to many medical conditions, for which time is frequently of the essence⁴⁸. In addition, at low resource environments, such analyzers are necessarily limited due to their high costs and the need for skilled operators. As a result, significant efforts are now being directed towards development of point-of-care (PoC) tests which can be operated at the patient sites by non-trained personnel^{47, 49-52}. Such tests should provide accurate, sensitive, and specific results in a rapid manner (with an optimal time-to-result in the range of a few seconds to few hours) at relatively low cost. The ideal vision for such a test would be an independent and self-sustainable operation, that allows a non-trained operator to load a sample of extracted body fluid (e.g., blood, urine, saliva, sweat, etc.) into the instrument and obtain informative results, with minimal user intervention (i.e., sample in-result out). Fully integrated Lab-on-a-chip (LoC) technologies, which incorporate all related analysis steps (including sample loading and preparation) in a single device stand to significantly advance PoC medical diagnostics^{47, 50, 53-58}.

In this chapter, we provide an overview of the primary technologies in the field of PoC medical diagnostics. These include paper-based assays and microfluidics; magnetic-assisted detection; centrifugal microfluidics; and smartphone-based detection. We will highlight the main concepts and directions in each technology, provide several relevant examples from the past three years, discuss the main challenges in the field, and conclude by offering a future-oriented perspective.

From Paper-Based Assays to Microfluidic Chips

Lateral flow assays are widely used for PoC diagnostics. In these assays, a liquid sample containing the target analyte moves (via capillary forces) through various zones of polymeric strips, on which capture probes that can interact with the analyte are immobilized, see Figure 2.1.1^{59, 60}. One of the most common lateral flow assays is the commercial pregnancy test for detecting human chorionic gonadotropin in urine, in which a sandwich-based immunoassay is performed, and detection of the target protein is realized via a color change, which can be observed with the naked eye⁶¹⁻⁶⁴. The main advantages of lateral flow assays are their simplicity, ease of use, extended shelf life and low-cost. However, lateral flow assays require numerous reagents and relatively large volumes of sample, and both multiplexing as well as the control of the flow rate pose challenges⁶¹⁻⁶⁴.

Microfluidic technology has been applied to address these limitations by enabling precise control of the flow by different microchannel geometries^{64, 65}. Capillary-driven microfluidic chips have been used for PoC diagnostics of various analytes^{62, 66-69}. For example, the commercially available Triage system, which is comprised of a portable analyzing instrument and a disposable chip, aims to diagnose a wide variety of health conditions^{70, 71}. Like the lateral flow immunoassay, a biological sample is loaded onto this chip, and the target antigen is first bound to labeled antibodies. The bound conjugates then pass through the detection zone, where they are captured by pre-immobilized antibodies. The cartridge is

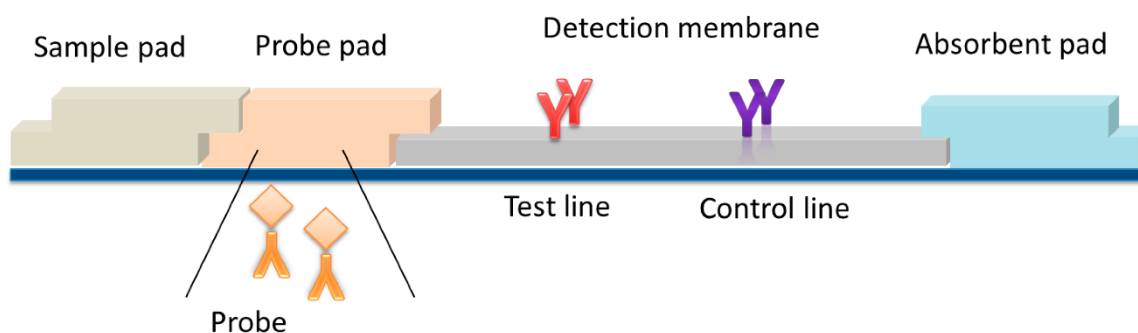


Figure 2.1.1. Schematic illustration of a typical lateral flow assay strip. Few microliters of the sample are loaded to the sample pad, and drawn to the probe pad, via capillary forces. The target is bound by labeled detection probes and transferred to the detection membrane and captured on a line of immobilized capture probes. Reprinted from ref. ⁶³. (Anfossi L. et al. Multiplex Lateral Flow Immunoassay: An Overview of Strategies towards High-throughput Point-of-Need Testing. *Biosensors*. 2018;9(1):2).

fabricated from polymer microfluidic channels, which result in lower batch-to-batch variability when compared to traditional lateral flow immunoassays. The capillary flow is passively controlled by the microstructure and surface characteristics, which increase the incubation time of the target with the detection zone in a controllable manner without the need for active pumps and valves. Thus, for a relatively low cost, a simple and rapid (~15 min) detection platform is realized. Multiplexed biomarker detection from whole blood was achieved by the Lateral Flow Integrated Blood Barcode Chip ⁷². This microfluidic chip, fabricated from a hydrophilic polymer bonded to a glass slide, includes an array of immobilized antibodies that are specific for a variety of protein biomarkers. A few microliters of whole blood with an anticoagulant are loaded onto the chip, and a filter paper is then used to draw the sample and other loaded reagents through the chip via an action of capillary forces. Separation of blood cells from the plasma is achieved by inertial force. A wash buffer is used to reduce background noise by removing an unbound label. Each step in the assay is automatically and sequentially executed, and the whole assay is performed within the span of just 40 minutes. To further automate the system, a self-coalescence module can also be integrated in a microfluidic chip, for the controlled reconstitution and delivery of inkjet-spotted and dried reagents. Well-defined reagent concentration profiles are established based on their initial spotting pattern ⁷³. This was applied in a silicon-based microfluidic chip for detection of a cardiac biomarker (troponin I) in human serum via a sandwich fluorescence immunoassay ⁶¹. Figure 2.1.2A illustrates the platform, where a loading pad receives a sample, which is drawn by capillary forces to a self-coalescence module. The latter contains dried detection antibodies, which are reconstituted by a defined volume of the sample. That mixture then passes to a bead lane with capture antibodies, which selectively bind with the target-detection antibody complexes from the sample. The flow of the samples in the chip is controlled by a capillary pump. The design and image of the silicon microfluidic chip itself is presented in Figure 2.1.2B and 2.1.2C. The assay requires 1 μL of sample, performed within 25 min and a limit of detection of 4 ng mL^{-1} is realized.

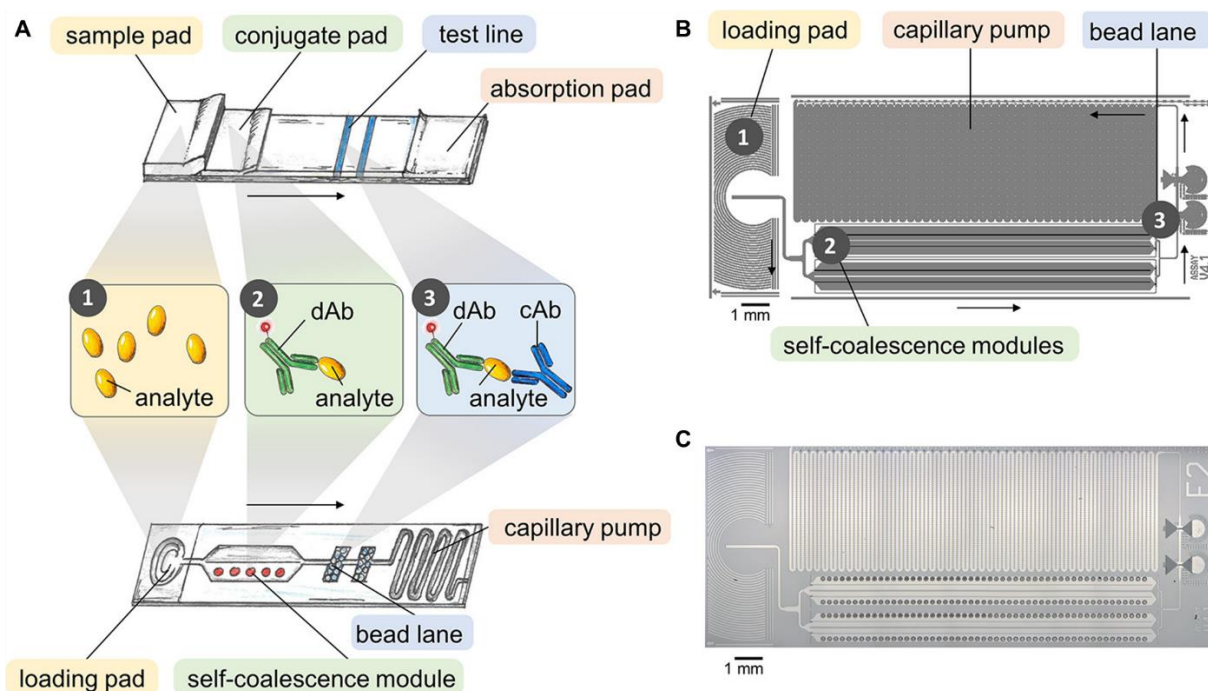


Figure 2.1.2. (A) General concept of a lateral flow assay-based microfluidic chip, which integrates a self-coalescence module, containing dried inkjet-spotted detection antibodies. The flow of the sample is driven by a capillary pump. (B) The design of the corresponding microfluidic chip and (C) optical microscopy image of the fabricated Si microfluidic chip. Reprinted with permission from ref. ⁶¹. (Hemmig E. et al. Transposing Lateral Flow Immunoassays to Capillary-Driven Microfluidics Using Self-Coalescence Modules and Capillary-Assembled Receptor Carriers. *Analytical Chemistry*. 2020;92(1):940-6). Copyright (2020) American Chemical Society.

An additional strategy for achieving reagent storage in paper-based microfluidic assays is seen in the use of a three-dimensional (3D) folding of a paper substrate with an origami-based technique. Different layers and dried reagents can be stacked vertically, and the addition of a buffer solution results in reconstitution via a controlled multi-step process. Parallel tests can be performed using a multilayer fluidic network in a compact device ^{63, 74}. Recently, 3D-origami-based paper device was used for detection of a biomarker for *Staphylococcus aureus* infection within human synovial fluid by an ELISA-based immunoassay ⁷⁵. That platform consisted of a sliding strip and antibody storage functions on a single sheet of paper, as shown in Figure 2.1.3A. The sliding strip acted as a valve to control the serial steps of sample addition, interaction, washing and detection. The sequential flow was carried out by sliding the tab to different positions (see Figure 2.1.3B). Only 3 μL of sample are required, and this procedure can be completed within 7 min. Nevertheless, the manual addition of buffers is still required during this procedure.

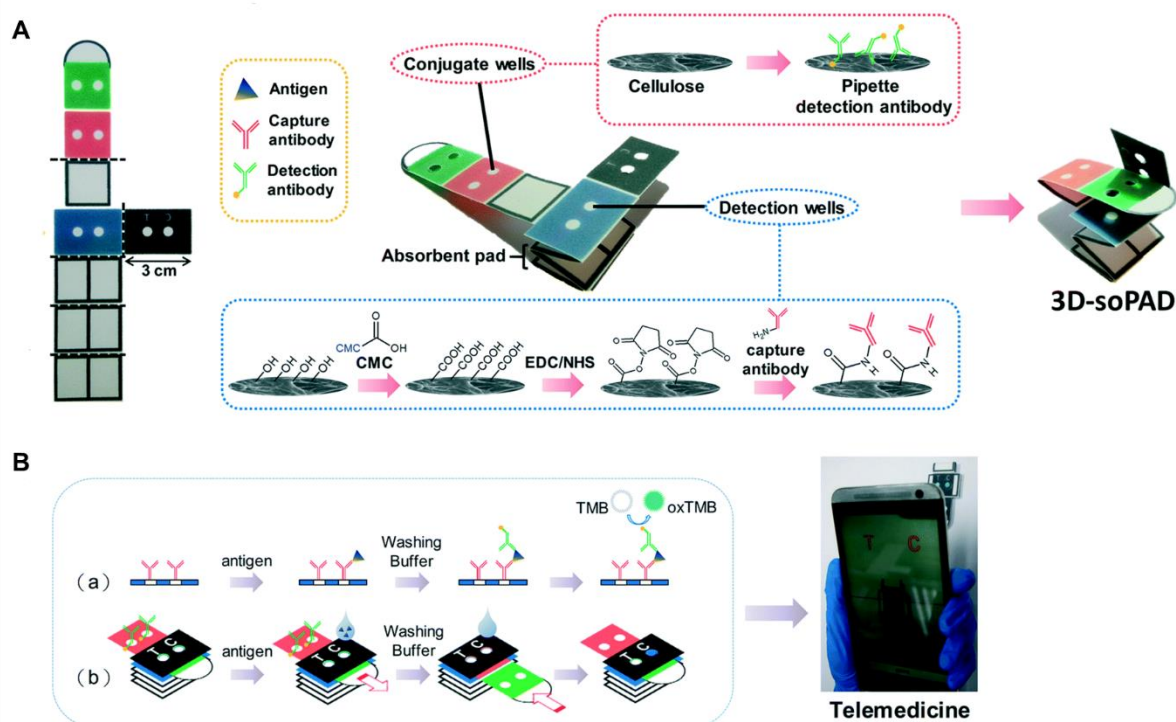


Figure 2.1.3. 3D-origami-based paper device used for detection of a protein A in human synovial fluid: (A) Illustration of the preparation of the platform, by an origami folding. The detection antibodies are impregnated in cellulose, while capture antibodies are covalently immobilized in the detection pad. (B) The testing procedure, where the sliding tab is used to control the flow and the serial step execution of the assay. Reproduced from Ref. ⁷⁵ (Chen C. A et al. Three-dimensional origami paper-based device for portable immunoassay applications. *Lab on a Chip*. 2019;19(4):598-607) with permission from The Royal Society of Chemistry.

Sensitivity enhancement of lateral flow assays has frequently been achieved by incorporating various nanomaterials, such as gold or silver nanoparticles, magnetic nanoparticles, and quantum dots into the system ^{64, 76, 77}. An alternate strategy is the use of external fields (i.e., acoustic, thermal, electric, etc.). Electrophoretic methods, such as ion concentration polarization and isotachopheresis, have also been applied to facilitate separation and concentration within microfluidic devices. In isotachopheresis, ionic species can be focused, based on their electrophoretic mobility, using a discontinuous buffer system. The method enables simultaneous extraction, separation and concentration of the target species ⁷⁸. This method was recently applied for multiplexed detection of two cardiac biomarkers in human serum ⁷⁹. The platform is comprised of a lateral flow paper assembled on a 3D-printed cartridge for buffer reservoirs and electrode connection. The two protein targets are fluorescently labeled and detected by immobilized antibodies on the paper strip. The assay time is 6 min and results in ~1300-fold enrichment of the proteins. Label-free detection with isotachopheresis in a microfluidic assay was demonstrated with porous silicon-based optical biosensors, where the reflectivity changes of the latter upon target binding are monitored in real-time, with no need for target labeling. This was shown for DNA and protein targets with up to 1000-fold enhancement in sensitivity ^{30, 42}. Nevertheless, application of an

external field does require peripheral equipment, which both increases the cost and complicates the setup of the system.

Magnetic-Assisted Platforms

Magnetic nano- and micro-particles are used in LoC devices for fluid manipulation. In many cases, the particles in the fluid are actuated by applying magnetic field to induce the mixing (which is often limited in microfluidic devices due to laminar flow)⁸⁰⁻⁸⁴. Moreover, the particles can be also used as carriers and labels to facilitate both transfer and separation of biomolecules⁸⁰⁻⁸⁴. Magnetic particles are commonly controlled by electro-magnets, coils or permanent magnets, all of which induce an external magnetic field, and often form supramolecular structures in the form of microcolumns due to dipole-dipole interactions^{85, 86}. For example, bio-conjugated magnetic nanochains have been used on a microchip as stir bars to promote liquid mixing, and as capture agents for bio-separation (see Figure 2.1.4)⁸⁷. A simple planar design of a microchip is realized based on flat channels on PDMS-on-glass, and free of built-in components. The magnetic nanochains are biofunctionalized with target specific antibodies and surface-enhanced Raman spectroscopy (SERS)-encoded nanoprobe are used as signaling probes for multiplexed Raman spectroscopic detection. A small amount (~1 μL) of sample fluid is mixed with both components, and the fluid flow and mixing are thereafter controlled via an external spinning magnetic field. Multiplexed detection of three cancer biomarkers in clinical serum and two bacterial species in saliva samples have been demonstrated in just 8 min⁸⁷.

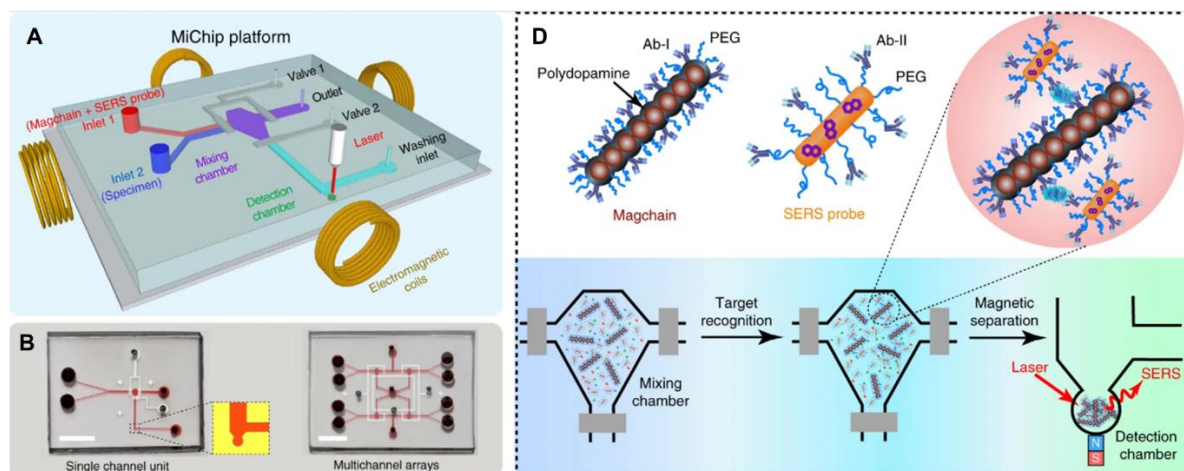


Figure 2.1.4. Bio-conjugated magnetic nanochains on a microchip as rapid active liquid mixers and capture agents for bio-separation: (A) schematic illustration of the assay platform; (B) photographs of the platforms in a single or multi-channel format (scale bar: 0.5 cm) and (C) the detection assay: the sample, antibody-conjugated magnetic nanochains and surface-enhanced Raman spectroscopy (SERS)-encoded probes are mixed in the reaction chamber. Immune complexes are formed and isolated to the detection chambers, which is then subjected to Raman spectroscopic detection. Reprinted from ref.⁸⁷ (Xiong Q. et al. Magnetic nanochain integrated microfluidic biochips. *Nature Communications*. 2018;9(1):1743). Copyright © 2018, Springer Nature.

Magnetic particles have been also used to automate processes in sandwich immunoassays, including the reaction and washing steps⁸⁸. A sample is mixed with gold coated iron oxide nanoparticles that have been functionalized with detection antibodies. The antibody-antigen reaction then forms immunocomplexes, which are electrochemically detected. The reaction and subsequent removal of unbound probes are controlled and accelerated by an external magnetic field. Thus, a simplified platform is obtained, without the need for fluid manipulation components and pre-stored washing buffer. Detection of a prostate specific antigen in 10 μL of human serum is demonstrated with a limit of detection of 0.085 ng mL^{-1} within 5 min⁸⁸. A similar concept was used for developing a PoC multiplexed diagnostic test for differential detection of Ebola, Lassa, and malaria biomarkers in whole blood samples within 30 minutes⁸⁹. Detection antibodies for the target antigens are conjugated to specific SERS nanotags and magnetic nanoparticles, which are stored dried in a test tube, providing a single-use and temperature stable platform that is ideal for field application. A whole blood sample (45 μL) and a lysis buffer are added to rehydrate the dried reagents. After a mixing step, the magnetic microparticles-antigen-SERS nanotag complexes are separated with an external magnet, and an external laser is used for SERS signal monitoring⁸⁹. Magnetic particles have been also used for signal amplification in lateral flow immunoassay strips for human chorionic gonadotropin detection^{90,91}. For example, Pt-decorated magnetic core-shell nanoparticles, functionalized with detection antibodies, have been successfully deployed for this function⁹⁰. These particles have both magnetic and enzyme-like

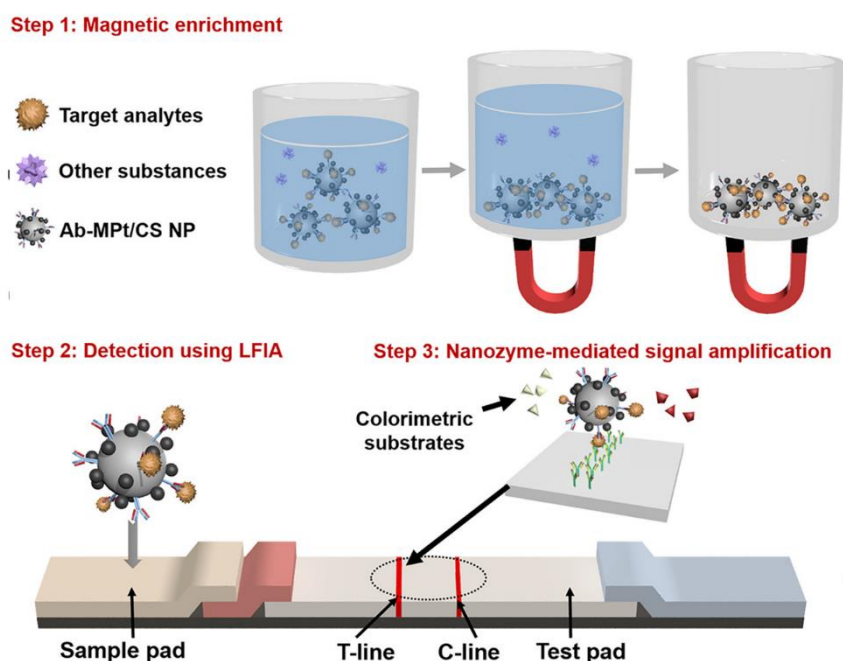


Figure 2.1.5. Magnetic particles for signal amplification in lateral flow immunoassay (LFIA) for human chorionic gonadotropin detection. The particles have both magnetic and enzyme-like properties, enabling target analyte magnetic enrichment and signal amplification. Reprinted with permission from ref.⁹³. (Kim M. S. et al. Pt-Decorated Magnetic Nanozymes for Facile and Sensitive Point-of-Care Bioassay. *ACS Applied Materials & Interfaces*. 2017;9(40):35133-40). Copyright (2020) American Chemical Society.

properties, enabling target analyte magnetic enrichment and signal amplification by a peroxidase-like reaction mediated by the particles (see Figure 2.1.5). The sensitivity is increased by two orders of magnitude when compared to a conventional lateral flow immunoassay⁹⁰.

In terms of nucleic acid analysis, magnetic particles are utilized for extraction, purification, amplification, and detection⁹²⁻⁹⁴. For nucleic acid amplification, isothermal methods are preferable for PoC testing, since they avoid the required thermal cycling in PCR⁹⁵⁻⁹⁷. One such method is so called rolling circle amplification⁹⁸: DNA or RNA target is annealed and ligated to a padlock probe, forming a circular template. The probe is highly sensitive to single base mutations, which result in high specificity⁹⁹. Amplification reaction then proceeds via a phi29 polymerase, which creates a long single stranded DNA concatemer containing repeated copies of the sequence complementary to the padlock probe⁹⁸. Although this is a highly efficient isothermal method, the multiple steps in the assays and the different required reagents make the integration of this method onto a single chip platform a challenging project. Magnetic particles can in turn facilitate the automation of the multi-step assay^{85, 100, 101}. For instance, a magnetic fluidized bed was recently integrated in a simple microfluidic chamber, generating a constant hydrodynamic recirculation in a continuous flow and thereby enabling efficient liquid perfusion and mixing⁸⁵. The magnetic particles are functionalized with an oligonucleotide for the capture of the target DNA. A complete rolling circle amplification assay is performed on chip, with detection carried out in a low-cost polymer-based microarray module by fluorescence microscopy. The platform enables processing of large sample volumes, and a limit of detection of 1 pM is obtained⁸⁵. A similar concept is presented in a multi-chamber polymer-based microfluidic chip, which integrates DNA target capture, transport and an rolling circle amplification assay, using magnetic microbeads¹⁰⁰. The platform requires the manual loading of reagents, after which the assay run automatically in a sequential chamber filling by capillary stop valves and phase guide structures. Opto-magnetic detection of a synthetic DNA target for type-B influenza virus is realized in 45 min, with a limit of detection of 20 pM¹⁰⁰.

Centrifugal Microfluidic Platforms

Multiplexed LoC detection can also be achieved by centrifugal microfluidics, which have been applied for detection of a wide range of analytes and have been thoroughly reviewed in the past¹⁰²⁻¹⁰⁵. The technology is based on a “Lab-on-a-CD” concept, wherein the complete fluidic network and the analysis steps are all embedded onto a single disk. The fluidic processing steps, including separation and reagent mixing, are then automated by implementing different spinning profiles. Integration of multiple assays in a single platform can thereby be achieved. The main advantage of these systems is their simple method of fluid manipulation, which is achieved by a rotary motor without the need for external pumps or high-voltage power supply. The disk can also be synthesized from low cost polymers, which facilitate both mass-production and economical disposal. The Lab-on-a-CD technology has been successfully utilized for PoC diagnostics by several commercial companies. For example, Piccolo Xpress by Abaxis

Inc., USA, ¹⁰⁶ offers a variety of CD-based blood chemistry analyzers with up to 14 tests on a single disc. The platform requires only 0.1 mL of a blood sample, and results are obtained within 12 min. Recently, the centrifugal microfluidic technology was also applied for a low volume blood analysis, using only 12 μL of blood from a finger prick, for automatic monitoring of blood glucose, total cholesterol and triglycerides within ~ 15 min (see Figure 2.1.6A and 2.1.6B). Plasma separation, mixing, reaction, and detection are fully automated with a portable analyzer (Figure 2.1.6C), which shows great potential for blood monitoring at home ¹⁰⁷.

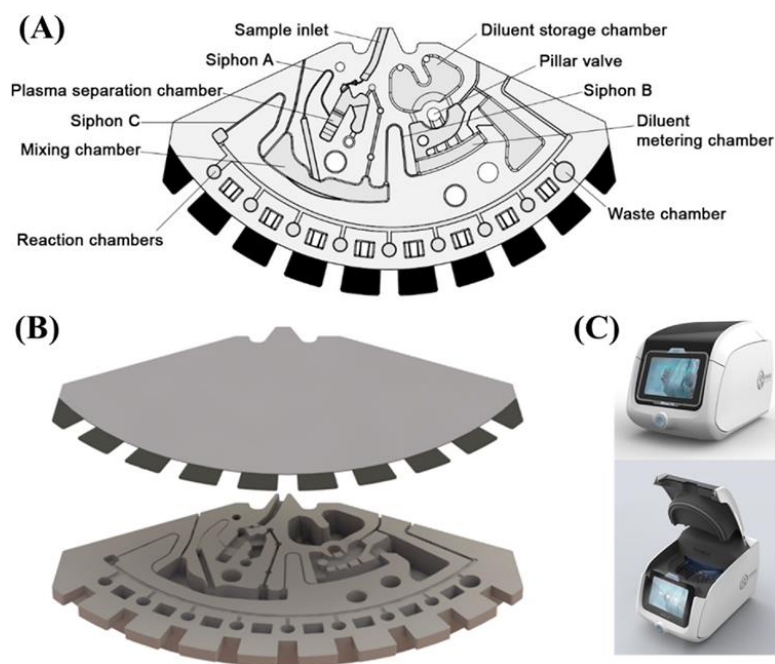


Figure 2.1.6. (A) The design of the centrifugal microfluidic finger-prick blood biochemical analyzer; (B) exploded view of the chip, presenting an upper adhesive tape and bottom polycarbonate layer; (C) the portable biochemical analyzer. Reprinted with permission from ref. ¹⁰⁷. (Zhu Y. et al. Self-served and fully automated biochemical detection of finger-prick blood at home using a portable microfluidic analyzer. *Sensors and Actuators B: Chemical*. 2020;303:127235). Copyright © 2019 Elsevier B.V.

Centrifugal microfluidics is especially advantageous for nucleic acid detection, which requires lengthy and laborious sample pre-processing steps, such as cell lysis, DNA purification, and amplification ¹⁰⁸, ¹⁰⁹. Using this approach, all these steps can be integrated into a single disk and performed automatically and sequentially. For example, a centrifugal microfluidic device was integrated with a 3D-printed solution-loading cartridge for multiplex foodborne pathogen detection, as illustrated in Figure 2.1.7A. The solution loading cartridge pre-stores all required solutions for molecular diagnostics, and connects with the reservoirs on the centrifugal device, minimizing manual processing (Figure 2.1.7B). Sequential loading of the solutions to the device is achieved by controlling the rotational speed, and silica bead-assisted DNA extraction, isothermal DNA amplification, and colorimetric detection by Eriochrome Black T are then carried out. The platform enables detection of four kinds of foodborne pathogens in a real milk sample within 65 min and with a limit of detection of 10^3 cells per mL (see Figure 2.1.7C) ¹¹⁰. Another technology which enables integration of DNA processing is double rotation axes centrifugal

microfluidics, in which the disc can rotate around two rotation shafts, thus avoiding limiting the fluid flow^{111, 112}. This technology has allowed for a completely automated sample-to-result analysis of Hepatitis B virus in whole blood¹¹³. The disc comprises all process chains for the virus DNA detection, including plasma separation from whole blood, lysis, DNA purification and amplification. The double rotation axes centrifugal microfluidics allows for unconstrained and reversible fluid pumping, as well as an efficient spatial utilization of the disc. All reagents are prestored on the disc, and their introduction is controlled by melting ferrowax plugs in the channels with laser irradiation. The only manual step in the assay is the supply of 0.5 mL of a whole blood sample, while the time-to-result is 48 min, with a limit of detection of 10^2 copies per mL¹¹³.

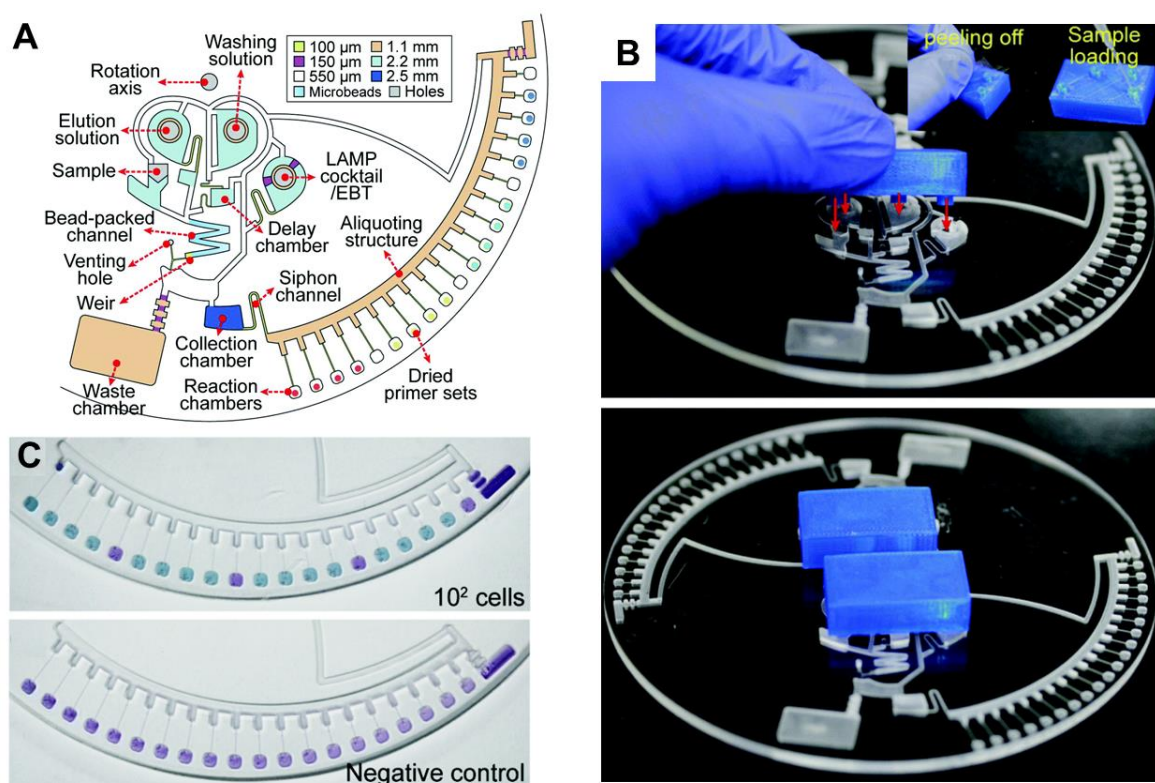


Figure 2.1.7. (A) Design of the centrifugal microfluidics device for multiplex foodborne pathogen detection; (B) A real photograph of the microdevice with the solution loading and reagent storage cartridge; (C) Multiplexed colorimetric detection of four different pathogens in milk sample in comparison to a negative control of pure milk. Reproduced from Ref.¹¹⁰ (Oh S.J. and Seo T.S. Combination of a centrifugal microfluidic device with a solution-loading cartridge for fully automatic molecular diagnostics. *Analyst*. 2019;144(19):5766-74) with permission from The Royal Society of Chemistry.

Smartphone-Based Detection

The high availability of smartphones worldwide, as well as their sophisticated technological features, such as high quality cameras, connectivity and computational power, have increasingly led to their integration into a wide range of analytical sensing systems¹¹⁴⁻¹²¹. Detection via smartphone is commonly based on various forms of optical measurements, including brightfield, colorimetric,

luminescence and/or fluorescence^{114, 115}. The high resolution of the embedded Complementary Metal Oxide Semiconductor image sensor cameras enable high pixel density for optical monitoring, while the high computational power facilitates real time image analysis¹¹⁹. Because smartphone-based PoC platforms have been extensively reviewed in the past few years¹¹⁴⁻¹²², in this section we only briefly survey the main aspects of smartphone-based detection with a few examples from recent years.

Brightfield-based detection is the simplest method, where a sample is illuminated from below with white light and then the transmitted light is measured¹¹⁵. Imaging of living cells or large biomolecules can be achieved in this way^{123, 124}. Colorimetric-based detection is also relatively simple, requiring only illumination and image processing. This has been commonly used in connection with paper-based assays to achieve quantitative results. For example, a custom-built smartphone application was used to quantitate a PoC lateral flow assay for detection of Ebola virus-specific antibodies in clinical human serum samples. This low-cost platform requires only the test strip and a smartphone, and results are obtained within 15 min¹²⁵. Smartphone colorimetric detection of lactate dehydrogenase as a biomarker for cellular damage for early diagnosis of serious illness in neonates was also recently shown, as illustrated in Figure 2.1.8¹²⁶. The PoC platform consists of a plastic cartridge holding disposable filter papers for whole blood filtration, plasma separation, and colorimetric reaction. The cartridge is mounted in a box (Fig. 2.1.8B), which also holds the smartphone at a fixed distance for automatic imaging. A dedicated application is used for analyzing the RGB values of the acquired images and comparable results to standard laboratory analysis are obtained in only 4 min¹²⁶. Colorimetric-based detection using a multichannel smartphone spectrometer as an optical biosensor was recently used to detect protein

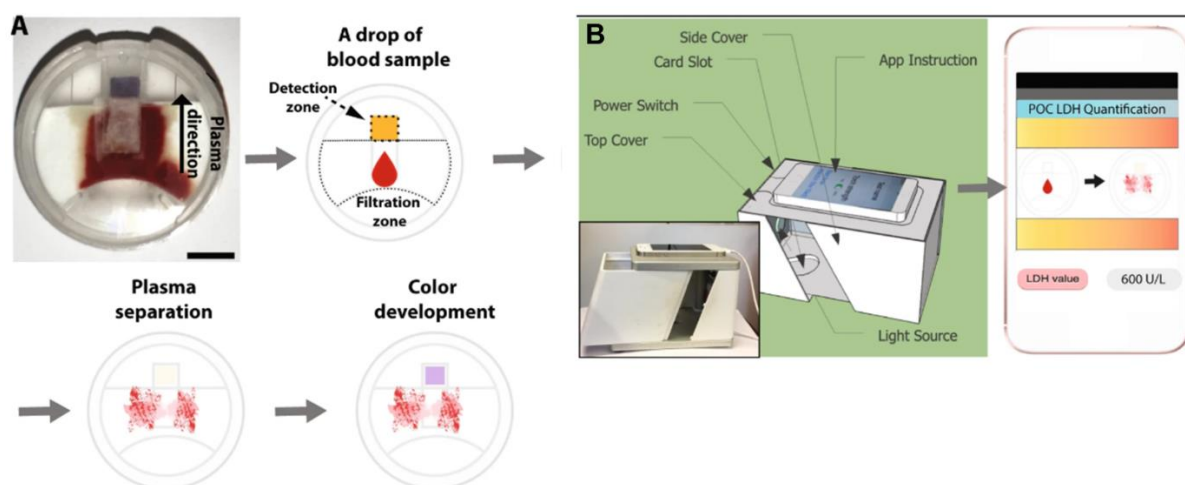


Figure 2.1.8. (A) Schematics of a PoC lateral flow assay system for analysis of lactate dehydrogenase (LDH) in whole blood, consisting of a plastic cartridge holding filter papers. Scale bar: 0.4 cm. (B) The cartridge is placed on a designated slot inside a box; the latter keeps a fix distance between the phone camera and the cartridge for the imaging, while ensuring similar light conditions between different batches. An App is used to guide the user in the assay and analyze the results. Reprinted from ref.¹²⁸. (Halvorsen C.P., et al. A rapid smartphone-based lactate dehydrogenase test for neonatal diagnostics at the point of care. *Scientific Reports*. 2019;9(1):9301). Copyright © 2019, Springer Nature.

content and a cancer biomarker within human serum ¹²⁷. Images captured by the phone camera were converted to transmission and absorbance spectra in the visible light range with high resolution, and the performance of the setup was comparable to benchtop instruments.

To increase the sensitivity of the assay, fluorescence-based detection is also frequently employed. For such systems, an optomechanical modulus containing excitation and/or emission filter and laser diodes for excitation is required ¹¹⁹. For example, a compact multimodal microscope was integrated on a smartphone for targeted DNA sequencing and *in situ* point mutation analysis in tumor samples ¹²⁸. A 3D-printed light-weight optomechanical modulus integrated on the smartphone, and contains two laser diodes for multicolor fluorescence imaging, as well as a white light-emitting diode (LED) for bright-field transmission imaging. DNA sequencing and point mutation analysis are achieved via rolling circle amplification, and the results are comparable to regular benchtop microscopes. Such technology is applicable for genotyping cancer patient biopsies directly in the pathologist office at PoC. Similar concept was shown for multiplexed detection of Zika, chikungunya and dengue viruses (belonging to the Flaviviridae family) directly in human blood, saliva and urine samples (see Figure 2.1.9) ¹²⁹. The platform is comprised of three components: a heating module, a reaction module, and an optical-detection and image analysis module. The latter contains multicolored LED coupled with a multi-pass band filter for fluorescence measurement. The entire platform is fitted with a smartphone, and the camera is utilized for the imaging. A dedicated application is used for fluorescence signal analysis by a novel algorithm, improving the discrimination between positive and negative signals by 5-fold, compared to a naked eye. Target virus RNAs are detected by reverse-transcription loop-mediated isothermal amplification coupled with quenching of unincorporated amplification signal reporters. Recently, microfluidic-based immunoassay based on a smartphone fluorescence detection, was used to conduct troponin I analysis in human serum in clinically relevant concentrations within 12 min ¹³⁰. Although fluorescence-based detection improves the sensitivity of the assay, it also requires the addition of complex and costly optical components to the system. Time-gated photoluminescence-based detection may offer one economical alternative. This concept is demonstrated for human chorionic gonadotropin quantification in a lateral flow assay with a persistent luminescent phosphor reporter ¹³¹. A smartphone's flash is used to excite the nanophosphors, which are then imaged using the smartphone camera. A 10 to 100-fold enhancement in sensitivity is achieved compared to commercial lateral flow assays, without the need for any additional complex optical components.

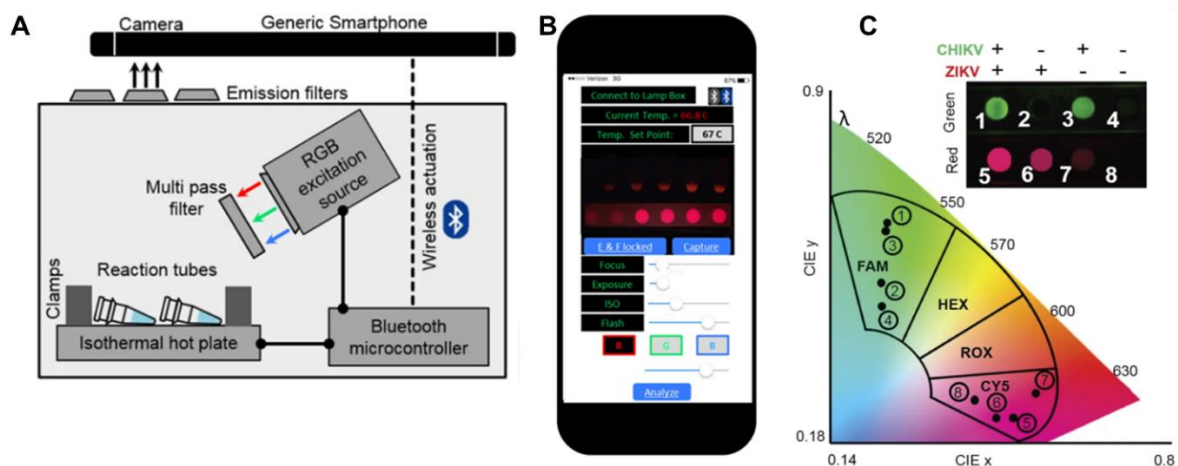


Figure 2.1.9. (A) Schematic illustration of the smartphone-based fluorescence detection of Zika, chikungunya and dengue virus's RNA platform, based on reverse-transcription loop-mediated isothermal amplification assay. The system comprises isothermal heating unit with reaction tubes, LED excitation source and Bluetooth microcontroller. (B) An App is used to wirelessly actuate the isothermal heater and excitation source. The smartphone camera with an emission filter captures the images, analyzed subsequently by the app. (C) Duplex detection of Zika and chikungunya viruses. The images are mapped over predefined fluorophore emission islands to distinguish between different viral target. Adapted with changes from ref. ¹²⁹. (Priye A. et al. A smartphone-based diagnostic platform for rapid detection of Zika, chikungunya, and dengue viruses. *Scientific Reports*. 2017;7(1):44778). Copyright © 2017, Springer Nature.

Conclusions and Outlook

Significant research efforts have already been directed towards the development of simple and low-cost devices for LoC-based medical diagnostics at PoC. Nevertheless, commercialization of such technologies remains limited, and the following aspects must be considered:

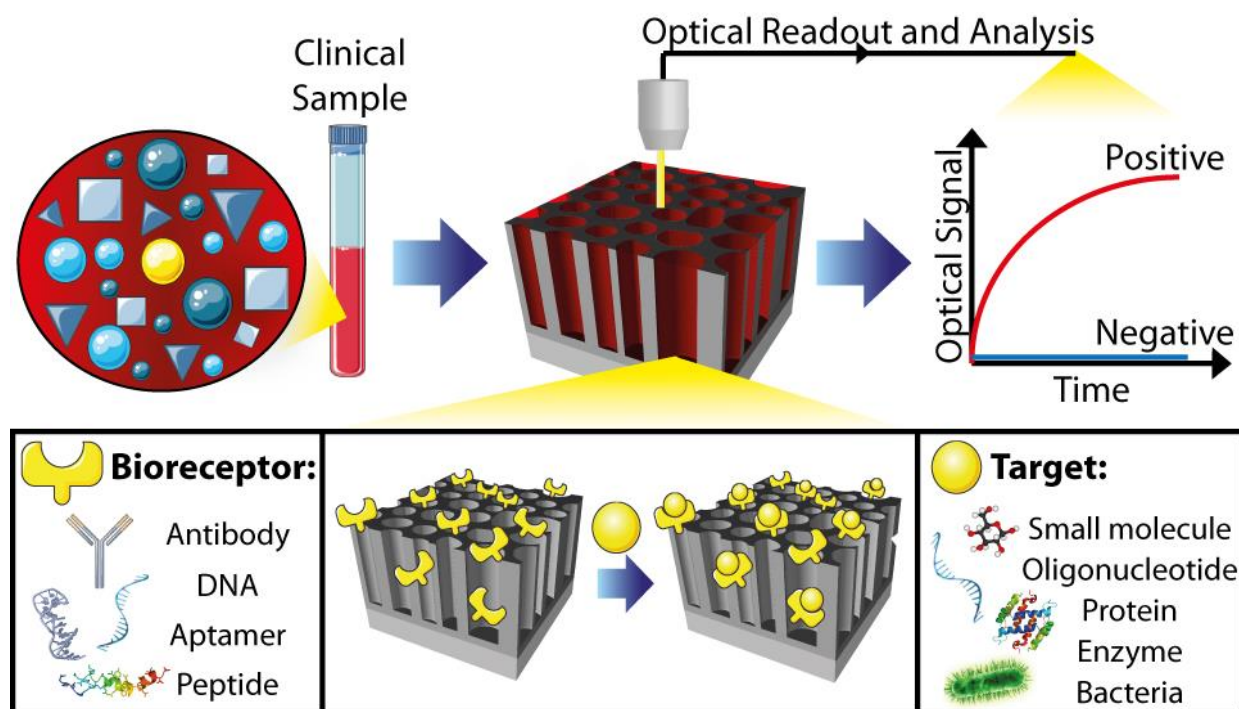
- Real PoC application, in terms of sample in-results out, requires the integration and automation of *all* assay steps. Yet most of the assays still require extensive user intervention, mainly in terms of sample preparation and/or reagent addition. For certain applications, this bottleneck can perhaps be solved by the integration of reagent moduli, where possible, simple reagent storage on the chip.
- The need to improve the sensitivity, selectivity, and stability of the sensing moduli is increasingly leading researches to explore robust recognition elements, such as aptamers, antibody fragments and molecular imprinted polymers. Various nanomaterials are also being incorporated for signal amplification and to improve the total assay performance.
- Scalability is an essential requirement for commercialization, and it continues to pose profound challenges for complex microfluidic structures. As a result, scalability considerations must direct the materials, design, and fabrication methods that are employed for such devices. For example, PDMS, which is commonly used for microfluidic fabrication in the academy, is not suitable for mass production, since it is fabricated mostly via soft lithography techniques. As a result, gold-standard paper-based assays continue to rule the field of PoC diagnostics, by dint of the fact that

they can be mass produced at a very low cost. Advancements in 3D-printed technology will likely begin to close that gap in the near future, at least with respect to plastic-based microfluidics.

- Smartphone technology has expanded the analytical power and increased accessibility of many platforms. But hygiene considerations, including contamination and disposal issues, must be carefully considered if smartphones will be deployed.
- Because multiplexing for the simultaneous detection of several biomarkers is extremely valuable in the context of medical diagnostics, the authors anticipate that research efforts in this direction will continue to increase exponentially.
- Clinical validation of all platforms is required. Many of the published works utilize human biological samples spiked with the analyte; although this is sufficient for a proof-of-concept, real clinical samples from different patients should always be tested to validate the platform's design integrity.
- Finally, the social impact of this emerging technology, as well as corresponding regulatory policies and concerns, should be considered when designing an assay, to facilitate (or at least preserve) the commercialization potential.

2.2 Porous Silicon-Based Biosensors

The following section is reproduced in part from the following manuscript: **Sofia Arshavsky Graham**, Naama Massad-Ivanir, Ester Segal, Sharon Weiss. "Porous Silicon-Based Photonic Biosensors: Status and Emerging Applications". *Analytical Chemistry*, 91(1), 441-467 (2020).



Respective Table of Contents Image

Introduction

Since its first demonstration as a promising material for molecular detection two decades ago, porous silicon (PSi) has become a commercially viable optical biosensor platform attracting sustained research interest. Progress in both fundamental understanding and diverse application areas has occurred. In particular, new approaches for biosensor design, new implementations of PSi as a host matrix for synergistic materials that enable alternate biosensor readout approaches and signal enhancement, new methods to reliably achieve higher detection sensitivity, and new emphases on detection of molecules in complex media, integration with microfluidics for sample handling, and multiplexed detection capabilities have been reported. In all cases, the extremely high internal surface area of PSi, the ease in modifying the surface chemistry of PSi, and the straightforward fabrication of PSi films are key advantages for PSi biosensors. This review focuses on advances in PSi optical biosensors achieved over the past three years.

In general, optical biosensors detect the presence of molecules based on utilization of light to monitor changes in absorption, reflection, transmission, or emission, and they are well-suited to provide a highly scalable solution for molecular detection applications with a need for simple readout, versatility in the

types of molecules to be detected, and relatively rapid results. One of the largest growth areas for the biosensor market, which is anticipated to reach \$27.06 billion by 2022¹³², is in the point-of-care (PoC) diagnostics field^{133, 134} that provides technology solutions that are alternatives to the expensive, time-consuming, bulky, and lab-confined traditional analytical methods of carrying out molecular detection. The primary classes of optical biosensors include surface plasmon resonance biosensors^{135, 136}, evanescent-wave biosensors including fiber optics and planar waveguide technology^{14, 137-139}, interferometric biosensors¹⁴⁰, and localized surface plasmon resonance (LSPR) biosensors including those based on surface enhanced Raman scattering (SERS)^{141, 142}. The primary applications areas for optical biosensors include healthcare, environmental monitoring, and food safety. As discussed in this review, PSi optical biosensors offer the possibility to leverage their high internal surface area to enable high sensitivity detection based on interference, guided waves, or SERS, and their versatility enables utilization across nearly all application areas. Moreover, recent progress in PSi optical biosensors is pushing the technology closer to implementation as a PoC diagnostic tool.

PSi is best described as a nanostructured material comprising air-filled pores of diameter typically smaller than 150 nm in a silicon matrix. PSi is most often fabricated by electrochemical etching techniques from Si substrates, and is widely studied for applications in the fields of optoelectronics¹⁴³, sensors and biosensors^{144, 145}, drug delivery¹⁴⁶, cell culture^{147, 148} and tissue engineering^{148, 149}. PSi was accidentally discovered in 1956 by Arthur and Ingeborg Uhlir during electropolishing experiments, but it was only reported as a technical note without significant attention¹⁵⁰. Only after Canham's discovery in 1990 that PSi exhibits strong and visible photoluminescence (PL) at room temperature¹⁵¹ did the material gain interest and stimulate intensive research in the field of photonics. The next breakthrough occurred in 1997 when Sailor and co-workers demonstrated label-free detection of an oligonucleotide target using a simple PSi Fabry-Pérot interferometer¹⁵. This result stimulated the study of PSi for biosensing applications in a multitude of fields.

PSi presents unique and tunable photonic properties allowing for label-free biosensing, and its fabrication process is relatively simple and cost effective. Its structure and accordingly its optical features can be tuned by the electrochemical etching process parameters to create different nanostructures or nanostructure morphologies. Importantly, PSi has high internal surface (up to $800 \text{ m}^2 \text{ g}^{-1}$), resulting in a large area for hosting biological molecules and interactions. This surface is reactive and can be easily functionalized with chemical and biological molecules by well-established surface chemistries. These features designate PSi as a superior alternative to other planar photonic biosensors for many applications.

Herein, recent progress in PSi-based optical biosensors will be discussed. In the next sections, advancements in structure and chemistry features of PSi will be presented, followed by exploring the sensitivity of different classes of PSi-based optical biosensors and different strategies to improve their sensitivity. Finally, detection in real samples and PoC translation will be evaluated.

New Approaches for Photonic Biosensor Design

Structures and Transducing Mechanisms

While all PSi optical biosensors detect the presence of an analyte based on changes in the optical properties of the PSi film (or species embedded within the porous matrix), the particular optical property measured and the design of the PSi optical structure can be highly varied. Here, we briefly review the main types of PSi structures utilized as optical biosensors and the characteristic transducing mechanisms for each structure. Figure 2.2.1 presents schematics of the most common PSi optical biosensor platforms and their corresponding optical spectra.

The simplest geometry, the single-layer PSi interferometer, has received the most attention over the past two decades. Light reflecting off the top and bottom interfaces of the PSi film interfere, giving rise to characteristic Fabry–Pérot fringes in reflection, as shown in Figure 2.2.1(a). Constructive interference leading to reflection peaks occur when the condition indicated in Eq. 2.2.1 is satisfied.

$$\frac{2nL}{\cos\theta} = m\lambda_0 \quad \text{(Single layer interferometer)} \quad 2.2.1$$

where n is the refractive index of the PSi film, L is the physical thickness of the porous layer, θ is the angle of incident light, m is an integer, and λ_0 is the vacuum wavelength of light.

The PSi formation conditions can be tuned to achieve the desired effective optical thickness (i.e., nL) by adjusting both the porosity, which is directly related to the refractive index through the appropriate effective medium approximation, and the physical thickness of the porous film. The interference fringes become closer together as the PSi effective optical thickness (EOT) increases. When molecules infiltrate the single-layer PSi film, the EOT of the film changes, resulting in a shift in the spectral position of the fringes that is proportional to the magnitude of the refractive index change caused by the molecules. Typically, the fringes shift to higher wavelength when species infiltrate the pores, except for the case of metal nanoparticles which are characterized by refractive index value lower than 1¹⁵². For large changes in the EOT of the film that cause the reflection spectrum to shift by more than the width of a single fringe, it becomes challenging to determine by how much the spectrum has shifted. In these cases, it is common to analyze the Fourier transform of the reflectance spectrum, which yields a single-peaked curve for which the peak position corresponds to twice the EOT of the PSi film. Details regarding this method, referred to as reflective interferometric Fourier transform spectroscopy (RIFTS) can be found in Pacholski et al.¹⁸. We note that double-layer PSi films have also been employed for sensing applications and, for these structures, RIFTS enables independent tracking of refractive index changes in each of the two PSi film layers^{17, 18}. Recently, an alternate data analysis technique based on signal processing was shown to facilitate significant improvements in the achievable detection limit of PSi single layer interferometric biosensors^{19, 20, 25}, as discussed in Section “Sensitivity and Signal Enhancement Methods”.

Multilayer PSi films, including Bragg mirrors, microcavities, and rugate filters, whose optical properties are similarly dictated by thin film interference phenomena, have also been exploited for sensing applications. The reflection spectrum of a PSi Bragg mirror is typically characterized by a relatively broad wavelength range with high reflectance (i.e., stopband), corresponding to a wavelength range over which constructive interference occurs, see Figure 2.2.1(b). The PSi Bragg mirror is designed with alternating layers of high and low refractive index (low and high porosity, respectively), each with an EOT corresponding to one-quarter of the wavelength in the middle of the high reflectance stopband, as specified in Eq. 2.2.2.

$$L_{mirror} = \frac{\lambda_0}{4n} \quad (\text{Bragg mirror}) \quad 2.2.2$$

The width of the stopband is dictated by the refractive index contrast between layers, with higher contrast leading to wider stopbands. The maximum reflectance of the stopband is dictated by the number of layers comprising the Bragg mirror, with more layers leading to higher maximum reflectance values. The entire high reflectance stopband shifts when molecules infiltrate the PSi multilayer stack and increase the effective refractive index of the PSi layers. To determine the magnitude of the stopband shift upon molecular infiltration, the spectral position of one edge of the stopband is typically monitored. However, because it is more straightforward to monitor the spectral position of a sharper feature in the reflectance spectrum upon molecular infiltration, the PSi microcavity and PSi rugate filter are more commonly employed for sensing applications compared to the Bragg mirror. Both the microcavity and rugate filter are characterized by a relatively narrow spectral feature, as shown in Figure 2.2.1(c,d), which shifts when molecules infiltrate the PSi multilayer stack. In the case of the microcavity, the narrow resonance is created by inserting a PSi cavity layer with an EOT corresponding to one-half of the resonance wavelength (or an integer multiple of $\lambda_0/2n$) between two PSi Bragg mirror stacks, as indicated in Eq. 2.2.3.

$$L_{cavity} = \frac{\lambda_0}{2n} \quad (\text{Microcavity}) \quad 2.2.3$$

In the case of the rugate filter, the refractive index profile is continuously tuned according to Eq. 2.2.4 or a similar function where x indicates the direction normal to the PSi multilayer surface, n_0 is the average refractive index of the PSi layers, Δn_0 is the refractive index contrast, and λ_0 is the wavelength of the reflectance peak. The continuously varying refractive index profile, along with appropriate apodization and index matching at the top and bottom of the PSi multilayer stack^{153, 154}, helps to suppress the side lobes that are present in the reflectance spectra of the microcavity and Bragg mirror. The width of the reflectance peak of the rugate filter increases as the refractive index contrast increases, and the peak height increases with the number of periods (i.e., number of repetitions of the sinusoidally varying refractive index profile). To achieve a narrow width and a high contrast reflectance peak for

sensing applications that require accurate tracking of small refractive index changes in the PSi multilayer stack, a rugate filter with a small Δn and many periods should be utilized.

$$n(x) = n_0 + \frac{\Delta n}{2} \sin\left(\frac{4\pi x}{\lambda_0}\right) \quad (\text{Rugate filter}) \quad 2.2.4$$

The aforementioned PSi optical structures all rely on out-of-plane light propagation, which can be convenient for stand-alone measurements using benchtop measurement equipment. However, it has been shown that PSi is also amenable to integration with on-chip silicon photonic optical components and, for these implementations, it is necessary to have in-plane light propagation. Figure 2.2.1(e) shows a planar, two-layer PSi waveguide that supports in-plane light propagation. Light is guided in the top PSi layer by total internal reflection (TIR); the lower PSi layer is essential and has a smaller refractive index than the top layer to ensure that the condition for TIR is met at the bottom interface of the top PSi guiding layer. A grating, as shown in Figure 2.2.1(e), or a prism can be used to couple light into the waveguide from an external light source. The criterion for coupling light into a resonant waveguide mode is given in Eq. 2.2.5 where Λ is the grating pitch, θ is the angle of incidence, m is an integer, n_{eff} is the modal index of the PSi waveguide, n_{inc} is the refractive index of the external medium (e.g., air) and λ_0 is the vacuum wavelength of light. A typical reflectance spectrum is also shown in Figure 2.2.1(e); the resonance angle shifts upon molecular infiltration into the waveguide. Because most of the light is localized within the top guiding PSi layer, molecules need to infiltrate into a significantly thinner region for the waveguide compared to PSi multilayer structures.

$$\Lambda = \frac{m\lambda_0}{n_{eff} - n_{inc} \sin \theta} \quad (\text{Grating-coupled waveguide}) \quad 2.2.5$$

Recently, it has been demonstrated that PSi waveguides can be patterned to form ring resonators¹⁵⁵⁻¹⁵⁷, as shown schematically in Figure 2.2.1(f), and Mach-Zehnder interferometers¹⁵⁸, suggesting that the PSi material system provides the necessary design and fabrication flexibility to achieve most, if not all, of the silicon-based photonic structures typically fabricated on silicon-on-insulator (SOI) wafers. Light can be coupled into these advanced PSi waveguide-based structures from an off-chip light source using a grating coupler or tapered fiber, but a key advantage is that light that is already propagating on a silicon photonic chip can directly couple into these structures. A typical transmission spectrum of a ring resonator is shown in Figure 2.2.1(f) and is characterized by periodic resonance dips. The resonant wavelengths satisfy the constructive interference condition in the ring given by Eq. 2.2.6 where λ_{res} is the resonance wavelength, R is the radius of the ring, n_{eff} is the modal index of the ring resonator, and m is an integer. When molecules infiltrate the PSi ring resonator, a shift of the resonant wavelengths results. Because light is highly localized in the upper guiding layer of the PSi ring resonator, the PSi ring resonator is highly sensitive to molecular infiltration into the guiding layer. For

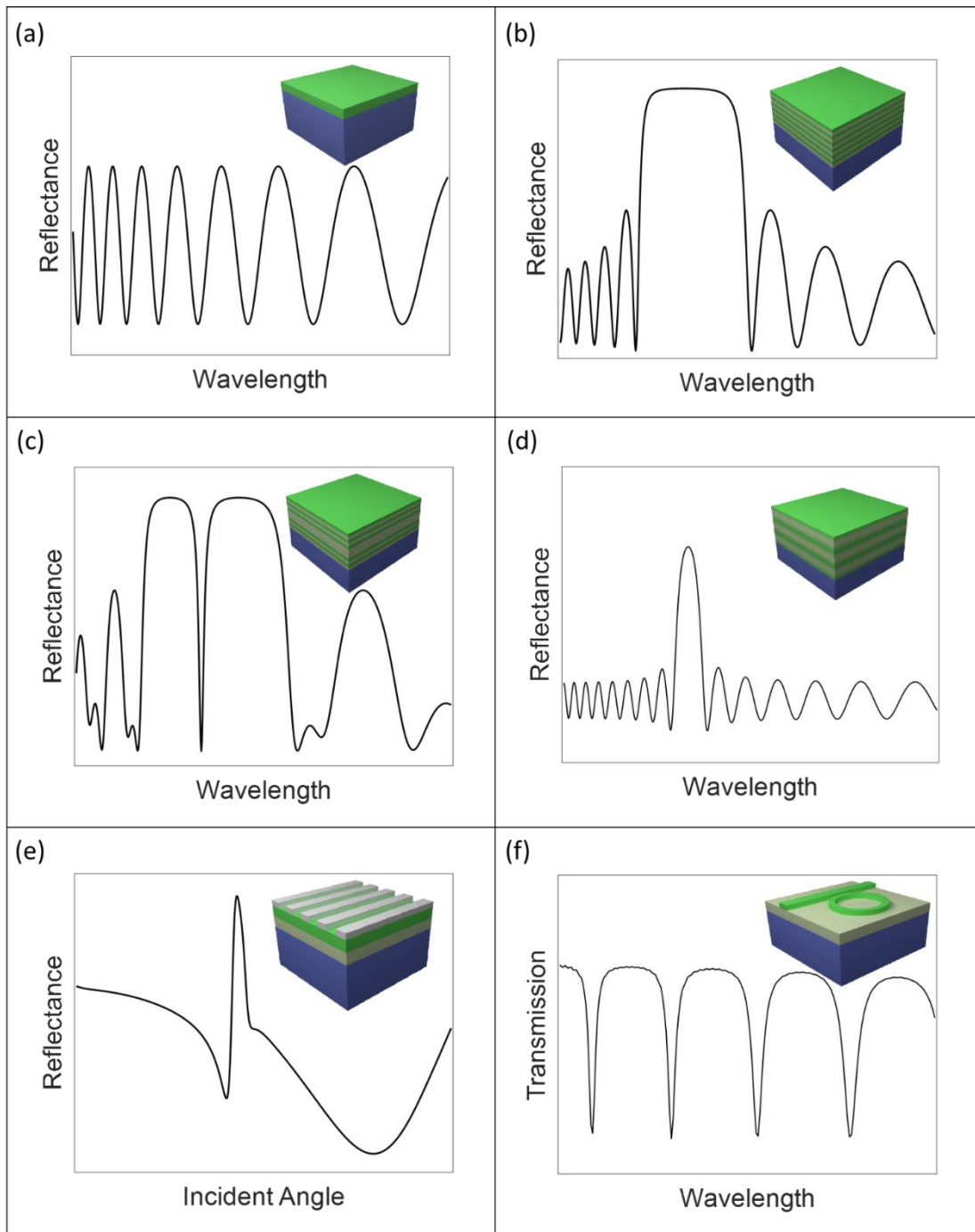


Figure 2.2.1. Schematics and associated optical spectra of common porous silicon structures used for optical biosensing applications: (a) single-layer interferometer, (b) Bragg mirror, (c) microcavity, (d) rugate filter, (e) grating-coupled planar waveguide, and ring resonator.

an equivalent change in the effective refractive index of a PSi guiding layer and a single layer PSi interferometer, there would be a much larger resonance shift for the ring resonator compared to the fringe shift that would be observed in the single layer PSi interferometer.

$$\lambda_{res} = \frac{2\pi R n_{eff}}{m} \quad \text{(Ring resonator)} \quad 2.2.6$$

Surface Chemistry

Surface chemistry design is a crucial stage in the development process of a biosensor. The overall capabilities of the biosensor, including stability, sensitivity, specificity, and reproducibility, are strongly related to the chosen surface chemistry. During the past decade, numerous comprehensive review papers have discussed the importance of surface chemistry in the construction and application of PSi-based biosensors^{144, 147, 159}.

The role of the surface chemistry in PSi biosensor devices is to protect the PSi nanostructure from degradation, prevent non-specific interactions of interfering molecules with the porous surface, and provide specific recognition groups to the target analyte¹⁵⁹. To achieve all these requirements, several stepwise coupling chemistries have been developed over the years. In the following section, we will briefly discuss the main, well-established approaches of PSi surface chemistry and introduce recent advances in the field.

At the end of the anodization process, the freshly-etched PSi nanostructure is composed of hydride terminated pores (Si-H_x , $x = 1, 2$ and 3), which are highly sensitive to aging effects, including the uncontrolled growth of a native oxide and dissolution in corrosive/aqueous environments^{144, 159-161}. These effects may induce zero-point drifts in the reflectivity spectrum of the sensor and thus PSi-based matrices are usually passivated by growing an oxide layer under controlled conditions. This step stabilizes the nanostructure and minimizes the oxidation and/or the dissolution of the porous layer in aqueous environments¹⁶⁰. Different methods can be used to oxidize PSi films, including thermal oxidation, ozone oxidation, high-pressure water vapor annealing, electrochemical oxidation, and oxidation in aqueous solutions¹⁶². Shtenberg et al. has demonstrated that the thermal oxidation step of PSi-based optical nanostructures has a profound effect on its biosensing performance¹⁶³. A greater optical stability and higher sensitivity was achieved when the biosensor surface was oxidized under 800 °C for 1 h, in comparison to thermal oxidation at lower temperatures (600 °C and 400 °C). This work demonstrated that a proper oxidation step can promote efficient immobilization of capture probes, optical signal stability, and higher sensitivity. To further stabilize and activate the biosensor surface with specific receptors/capture probes, several well-established approaches are commonly used, such as silane chemistry (silanization with alkyl silanes)^{164, 165} or hydrosilylation of alkenes and alkynes^{166, 167}. Although hydrosilylation chemistry results in the formation of a very stable monolayer of Si-C bond, the silane chemistry is more common, probably due to its simplicity. The Sailor group has recently reported on a new silanization process, referred to as a “ring-opening click” reaction (outlined in Figure 2.2.2), in which heterocyclic silanes containing Si-N or Si-S bonds in the ring undergo a ring opening reaction with -OH groups at the surface of oxidized PSi (PSiO_2) nanostructures to generate -SH or -NH functional surfaces, grafted via O-Si bonds¹⁶⁸. This room-temperature chemistry approach has been reported to have no by-products and to minimally interfere with protein activity. Another modification approach, which improves the PSi chemical stability and its electrical properties, is

thermal carbonization of PSi. We refer the readers to a recent comprehensive review by Salonen and Mäkilä¹⁶⁹, which discusses the progress made over past decade in thermal carbonized PSi (TCPSi) platforms.

To overcome several drawbacks of silane monolayer deposition on SiO₂, such as unfavorable cross-linking, slow reaction rates and low coupling efficiency, Sailor and co-workers have demonstrated the grafting of organic trihydrosilanes on hydrogen-terminated PSi nanostructures under mild thermal conditions (80°C) without the use of a catalyst¹⁷⁰. The resulting surfaces demonstrated superhydrophobic behavior (with a contact angle of 150°) and were stable in corrosive aqueous solutions and in common organic solvents, such as dimethyl formamide, dimethyl sulfoxide, dichloromethane and tetrahydrofuran. Moreover, the grafted surfaces retained their PL properties and could be further activated with functional groups.

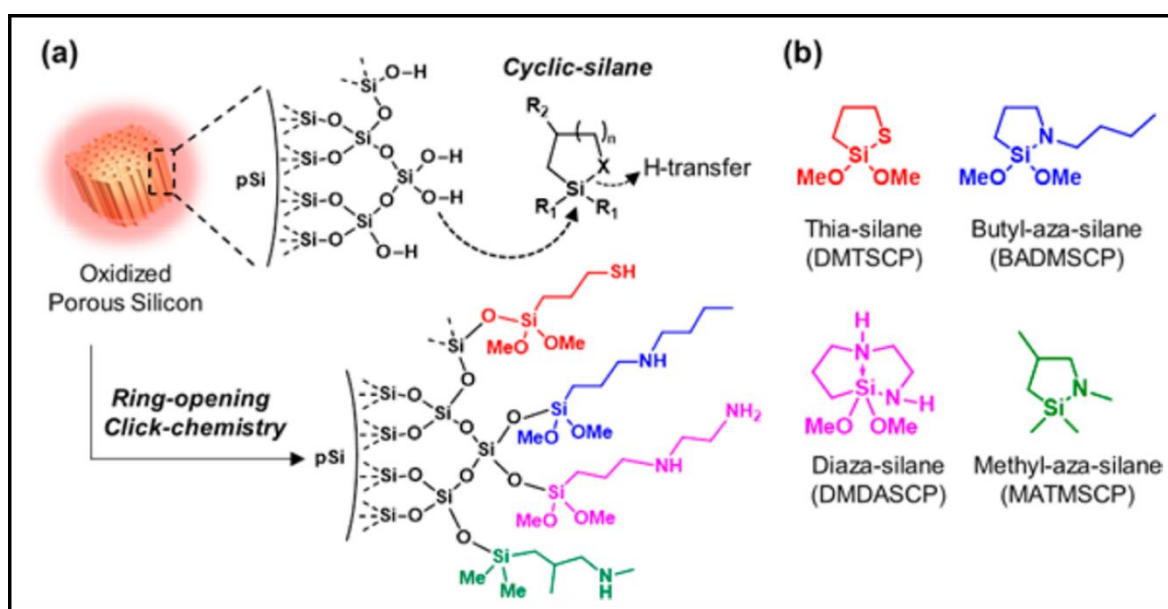


Figure 2.2.2. (a) Schematic illustration of "ring-opening click" reaction of cyclic-silanes with the silanol-terminated pore walls of oxidized PSi. (b) Structures of the reagents, which were used in the study: thia-silane (DMTSCP, 2,2-dimethoxy-1-thia-2-silacyclopentane), butyl-aza-silane (BADMSCP, *N*-*n*-butyl-aza-2,2-dimethoxy-silacyclopentane), diaza-silane (DMDASCP, 2,2-dimethoxy-1,6-diaza-2-silacyclooctane), and methyl-aza-silane (MATMSCP, *N*-methyl-aza-2,2,4-trimethyl-silacyclopentane). $R_1 = \text{OMe}, \text{Me}$. $R_2 = \text{H}, \text{Me}$. Reprinted with permission from ref.¹⁶⁸. (<https://pubs.acs.org/doi/10.1021/jacs.6b08614>).

Following the passivation/stabilization process of the PSi (by one of the methods described above), the subsequent step comprises immobilization of appropriate bioreceptors, such as antibodies^{171, 172}, enzymes^{173, 174}, aptamers^{19, 20, 26}, or DNA^{42, 175, 176}, onto the pore walls. The immobilization can be accomplished *via* standard coupling chemistries such as glutaraldehyde crosslinking chemistry, activation of terminal -COOH groups with ethyl-3-(3-(dimethylamino)propyl)carbodiimide (EDC) and *N*-hydroxysulfosuccinimide sodium salt (NHS), biotin-streptavidin system or *via* click chemistry. The final step in the biofunctionalization process usually involves blocking of residual groups to reduce non-specific adsorption of biomolecules. This step is especially crucial if the biosensor is aimed to

perform in complex biological fluids. The blocking is commonly carried out *via* adsorption or covalent attachment of different blocking agents such as maleimide³³, ethanol amine¹⁷⁷, Tris buffer³⁰, bovine serum albumin protein (BSA)¹⁷⁸, oligo(ethylene glycol) (EG)¹⁵⁹ or polyethyleneglycol (PEG) molecules²⁸. Additional discussion regarding the importance of blocking can be found in the “Real Sample Analysis” Section.

A new approach to improve the immobilization of biological molecules on PSi substrates was recently demonstrated by the Gergely group¹⁷⁹. In this work, the optical properties of PSi microcavities were utilized to study binding affinity, adhesion properties and interactions between peptides and PSi. The main goal of this study was to identify and engineer the shortest peptide sequence with the highest affinity to the silicon surface. This optimal peptide can be subsequently used as an efficient linker for immobilization of biomolecules onto PSi surfaces.

One of the main advantages of PSi biosensors is their high surface area. An interesting approach to exploit the entire porous surface and design sophisticated biosensing platforms (as will be discussed in the “Emerging Applications: Toward Point-of-Care Devices” Section) is to introduce different functionalities to the interior and exterior surfaces of the matrix. Gooding and co-workers have pioneered this route with a method that relies on surface tension and capillarity to either prevent or promote the entrance of solution species into the porous nanostructure¹⁸⁰. Wu and Sailor reported on a simple strategy, termed as “liquid masking”, for differentially modifying the inner pore walls using a hydrophobic organic liquid as a chemical resist mask¹⁸¹. The resulting nanostructure exhibits an inner hydrophilic silicon oxide surface and an outer silicon hydride surface. Other studies have modified this basic approach and were able to fabricate PSi nanostructures bearing carboxyl groups in the internal pore surface and amines on the external surface¹⁸². The selective chemical modification of PSi films can be verified by Fourier transform infrared (FTIR), contact angle measurements and angle-resolved X-ray photoelectron spectroscopy (AR-XPS)¹⁸³. The latter technique allows careful analysis of the distribution of the different functional groups along the entire thickness of the porous layer.

Another important aspect is to achieve sensitive and reproducible monitoring of negatively charged molecules, such as DNA targets, using PSi biosensors. The detection of DNA is very challenging, mostly due to the enhanced corrosion of the PSi scaffold by DNA^{42, 184}, as schematically illustrated in Figure 2.2.3. A recent study by the Weiss group examined the influence of charge density and surface passivation on a DNA-induced corrosion of PSi waveguides in order to improve the biosensor sensitivity, reliability, and reproducibility when exposed to negatively charged DNA molecules¹⁸⁵. This study demonstrated that charge density and surface passivation of PSi have high impact on the biosensor performance. The corrosion process was partially moderated by replacing the DNA probe with neutral-charged-peptide nucleic acids (PNA) or fully reduced by introducing Mg²⁺ ions to shield negative charges on the target DNA backbone during hybridization to the PNA probes.

Over the years, many functionalization procedures for PSi-based materials were developed and applied. Yet, as surface chemistry plays a critical role in the performance of PSi biosensors (e.g., their stability in aqueous media or storage), careful adjustment and optimization of the chemistry for each specific application are required.

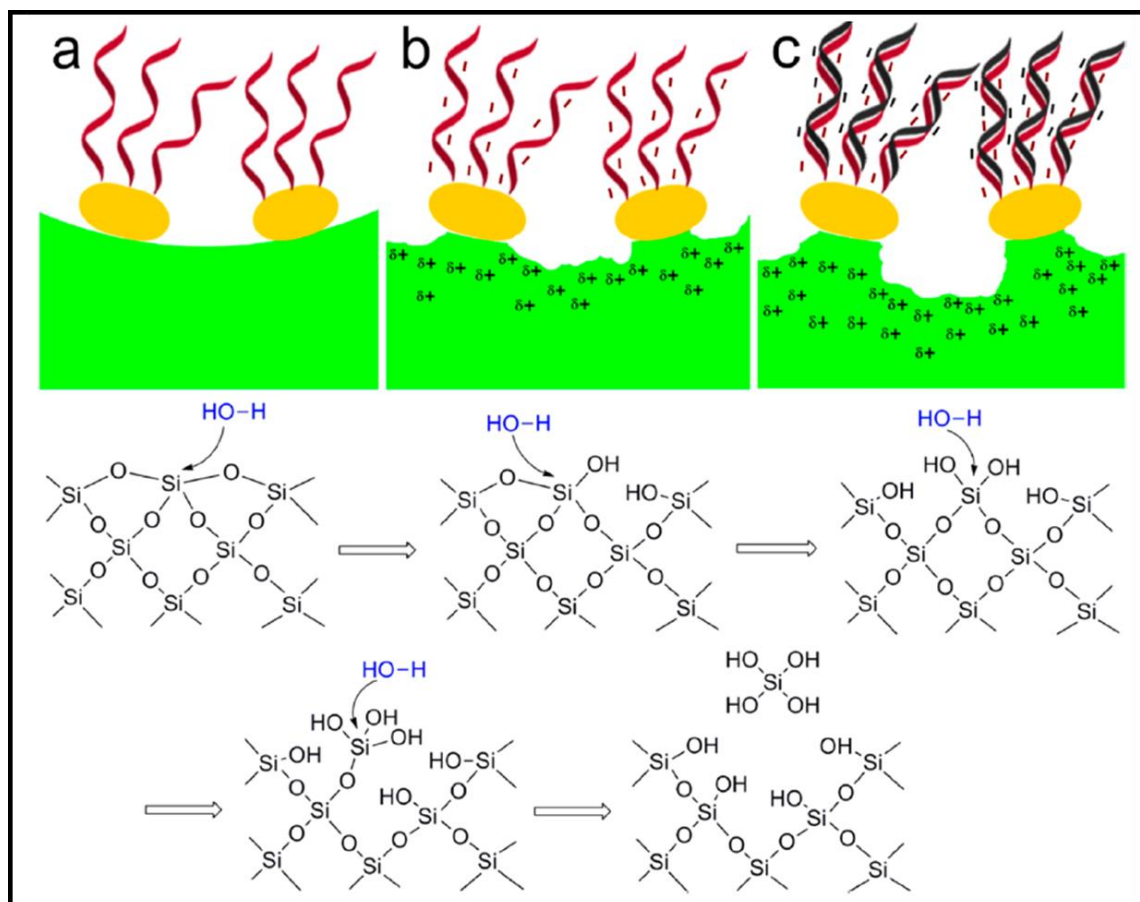


Figure 2.2.3. Schematic of DNA-induced corrosion process in PSi, illustrating surface regions of the waveguide structure. The green region indicates the thermal oxide on pore walls; the yellow represents silane molecules; DNA oligos are represented by the red (probe) and black (target) helix structures attached on the silane molecules. The chemical reactions present a possible mechanism for corrosion of a silicon atom initiated by sequential nucleophilic attacks by water molecules and resulting in the release and dissolution of the atom in the form of $\text{Si}(\text{OH})_4$. Reprinted with permission from ref. ¹⁸⁵ (Zhao, Y.; Lawrie, J. L.; Beavers, K. R.; Laibinis, P. E.; Weiss, S. M. *ACS Applied Materials & Interfaces* 2014, 6, 13510-13519). Copyright (2014) American Chemical Society.

Sensitivity and Signal Enhancement Methods

The clinical relevance of a developed biosensor is examined by its sensitivity and specificity. Biomolecular or cellular targets for biosensor platforms are often present in very low concentrations in highly complex fluids. Kelley has recently reviewed the clinically relevant levels of these targets, which for most protein and oligonucleotide biomarkers lie in the picomolar range ⁴. The large surface area of PSi predestined it as a superior alternative to planar photonic sensors, such as SPR, for many applications and the seminal work by Lin et al. in 1997 strengthened this hypothesis ¹⁵. In terms of sensitivity, PSi-based optical biosensors can be classified into two main groups based on the

transduction mechanism: those that are based on luminescence signal and those that are based on optical monitoring of changes in the average refractive index of the porous nanostructure. The former usually attains higher sensitivity, but also requires target labelling or more sophisticated biosensing platforms. On the contrary, the latter category enables label-free detection with a simple experimental setup, but usually exhibits lower sensitivity. Without applying sophisticated signal amplification techniques or utilizing complex P*Si* structures, label-free P*Si*-based biosensors present a poor sensitivity on the micromolar range^{26, 176, 186, 187}. These experimental results oppose theoretical calculations predicting nanomolar detection range¹⁸⁸ and have been mainly attributed to limited diffusion of the analytes into the porous matrix^{21, 165, 189}, which can be as slow as few molecules per pore per second²³, and non-ideal structures (defects and interface roughness)¹⁹⁰. Thus, significant research effort has been directed towards developing strategies for improving the sensitivity of P*Si*-based optical biosensors. These include tailoring the chemistry and structure features of the porous layer, fabrication of complex multilayered structures, manipulating the experimental platform and data analysis, or applying signal amplification techniques. The following section reviews the current sensitivity limits of different P*Si*-based optical biosensors of various transduction mechanisms, see summary in Table 2.2.1, as well as the progress made over the years of 2016 to 2018 in enhancing their performance (specifically lowering LOD values).

Table 2.2.1. Performance summary of biomolecule detection with different PSi-based optical biosensors from 2016-2018

Target type	Target	PSi Structure	Transducing Mechanism	Capture Probe	Label/Label-Free	Signal Amplification	Detection Range/Tested Concentrations	Assay Time	LOD	Real Sample Analysis	Ref.
Small molecules	EtOH	Microcavity	Reflectivity	-	Label-free	-		-	0.001% 1000 nm RIU ⁻¹ 10 ⁻⁷ RIU	-	¹⁹¹
	NaCl and KCl	Fabry-Pérot thin film	Reflectivity + IAW signal processing	-	Label-free	-	10 ⁻⁵ % to 9% w/w	~1 h	0.001% w/w 10 ⁻⁷ RIU for concentration lower than 0.1% w/w	-	²⁵
	Heavy metals (Lead (II), Arsenic (III) and Cadmium (II) ions)	Thue-Morse	Reflectivity	Oligopeptide	Label-free	-	2 ppb to 100 ppb	-	1.2 ppb for Pb(II)	-	¹⁹²
	Heavy metals (Cadmium (II) ions)	Microcavity	Reflectivity	-	Label-free	Pre-concentration with electrochemical reduction	1 ppb to 1000 ppb	20 min	1.16 ppb 342 nm RIU ⁻¹	Lake water	¹⁹³
	Pyrocatechol (110 g mol ⁻¹)	Fabry-Pérot thin film	Colorimetric	Enzyme	Label-free (indirect detection*)	-	1 μM to 100 μM	~20 min	0.43 μM	-	¹⁹⁴
	Glucose (180 g mol ⁻¹)	Mesoporous Si nanowire array	Photoluminescence	Non immobilized glucose oxidase enzyme	Label-free	-	0.1 mM to 50 mM	~1 h	1.06 μM	-	¹⁹⁵

Table 2.2.1 contd. Performance summary of biomolecule detection with different PSi-based optical biosensors from 2016-2018

Target type	Target	PSi Structure	Transducing Mechanism	Capture Probe	Label/Label-Free	Signal Amplification	Detection Range/Tested Concentrations	Assay Time	LOD	Real Sample Analysis	Ref.
Small molecules	Ochratoxin A (404 g mol ⁻¹)	Fabry-Pérot thin film	Photoluminescence	Antibody	Label-free	-	0.01 ng mL ⁻¹ to 5 ng mL ⁻¹	~30 min	4.4 pg mL ⁻¹	-	196
	Aflatoxin B1 (312 g/mol)	PSi (Fabry-Pérot thin film)-gold nanocomposites	Photoluminescence	Antibody	Label-free	-	0.01 ng mL ⁻¹ to 10 ng mL ⁻¹	-	2.5 pg mL ⁻¹	-	197
	Ochratoxin A	TiO ₂ -deposited PSi Fabry-Pérot thin film	Fluorescence (FRET-based)	Aptamer	Label-free (Indirect detection*)	-	0.1 ng mL ⁻¹ to 10 ng mL ⁻¹	~12 h	15.4 pg mL ⁻¹	Cereal samples (rice, wheat and corn)	198
	Aflatoxin B ₁						0.01 ng mL ⁻¹ to 10 ng mL ⁻¹		1.48 pg mL ⁻¹		
Fumonisin B ₁						0.001 ng mL ⁻¹ to 10 ng mL ⁻¹		0.21 pg mL ⁻¹			
Oligonucleotides	single-stranded DNA, ssDNA (20mer)	Microcavity	Reflectivity	ssDNA	Labeled target	-	0.1 μM to 5.0 μM	~2 h	6.97 nM	-	199
	ssDNA (14mer)	Au/PSi microcavity	Fluorescence	ssDNA	Labeled target	-	10 ⁻⁴ μM to 10 μM	10 h	10 pM	-	200
	ssDNA (18mer)	Double Bragg mirror	Reflectivity	ssDNA	Label-free	-	0.25 μM to 10 μM	~2 h	27.1 nM	-	201

Table 2.2.1 contd. Performance summary of biomolecule detection with different P*Si*-based optical biosensors from 2016-2018

Target type	Target	P <i>Si</i> Structure	Transducing Mechanism	Capture Probe	Label/Label-Free	Signal Amplification	Detection Range/Tested Concentrations	Assay Time	LOD	Real Sample Analysis	Ref.
Oligonucleotides	ssDNA (8mer)	Diffraction grating coupled with 1D photonic crystal	Angle-resolved diffraction	ssDNA	Label-free	-	10 μ M	~2 h	41.7 nM	-	²⁰²
	miRNA-222 (21mer)	P <i>Si</i> membrane-Ag composites	SERS	ssDNA	Labeled target Label-free (indirect detection*)	Secondary labeled probe	2.5 nM to 25 nM 1 nM to 25 nM	1 h 2 h	0.55 nM 1.51 nM	RNA cell extracts	²⁰³
Peptides	Glutathione (307 g mol ⁻¹)	P <i>Si</i> disks-Ag composites	SERS	DTNB Raman reporter (not immobilized)	Label-free (indirect detection*)	-	<568.9 nM	30 min	74.9 nM	Blood serum	²⁰⁴
	Insulin (5.8 kDa)	Fabry-Pérot thin film	Reflectivity	Antibody	Label-free	-	5 μ g mL ⁻¹ to 50 μ g mL ⁻¹	60 min	4.3 μ g mL ⁻¹ for antibody	Human islets	²⁸
				Aptamer	-	12 min		1.9 μ g mL ⁻¹ for aptamer			
Insulin (5.8 kDa)	Rugate filter	Reflectivity	Aptamer	Label-free	-	2.5 μ g mL ⁻¹ to 50 μ g mL ⁻¹	10 min	0.29-0.19 μ g mL ⁻¹ (depending on the buffer)	Human islets	³²	
Proteins	Trypsin (23.3 kDa)	P <i>Si</i> (Fabry-Pérot thin film)-C-dots hybrid	Reflectivity and fluorescence	-	Label-free	-	4.3 μ M to 43 μ M	~20 min	4 μ M	-	²⁰⁵
Small molecules	ATP (507.2 g mol ⁻¹)						0.1 mM to 10 mM		0.1 mM		
Proteins	Protein A (42 kDa)	Fabry-Pérot thin film	Reflectivity	Aptamer	Label-free (indirect detection*)	Secondary antibody	2 μ M to 50 μ M	~2 h	1 μ M	-	²⁹

Table 2.2.1 contd. Performance summary of biomolecule detection with different P*Si*-based optical biosensors from 2016-2018

Target type	Target	P <i>Si</i> Structure	Transducing Mechanism	Capture Probe	Label/Label-Free	Signal Amplification	Detection Range/Tested Concentrations	Assay Time	LOD	Real Sample Analysis	Ref.
Proteins	Streptavidin (52.8 kDa)	Microcavity membrane	Reflectivity	Biotin	Label-free	-	0.5 μ M to 5 μ M	~20 min	-	-	²³
	His-tagged protein (24 kDa)	Fabry-Pérot thin film	Reflectivity	Aptamer	Label-free	ITP	750 nM to 7.5 nM	50 min	7.5 nM	Bacteria lysate	³⁰
	Hydatid disease biomarker	P <i>Si</i> (Fabry-Pérot thin film) on a Silicon-On-Insulator (SOI)	Photoluminescence	-	Label-free	-	2×10^{-8} mg mL ⁻¹ to 2×10^{-3} mg mL ⁻¹	-	0.02 ng mL ⁻¹	-	²⁰⁶
	Cystic hydatid disease antigen (43 kDa)	Microcavity	Angular transmission	Antibody	Label-free	-	0.5×10^{-6} mg mL ⁻¹ to 2.0×10^{-5} mg mL ⁻¹	1 h	0.16 ng mL ⁻¹	-	²⁰⁷
	BSA (66 kDa)	Fabry-Pérot thin film	Reflectivity + IAW signal processing	-	Label-free	-	150 pM to 15 μ M	~1 h	20 pM	-	²⁰
	TNF α (25 kDa)	Fabry-Pérot thin film	Reflectivity + IAW signal processing	Aptamer	Label-free	-	390 nM to 3 nM	~1 h	200 pM	-	¹⁹
	C-reactive protein (25.1 kDa)	Si nanowire array	Photoluminescence	Antibody	Label-free	-	85 pM to 850 nM (could be tailored)	~4 h	1.6 fM	Blood serum	²⁰⁸
	Thrombin (37 kDa)	Fabry-Pérot thin film	Reflectivity	Aptamer	Label-free	-	13 nM to 109 nM	~2 h	1.5 nM	-	²⁷

Table 2.2.1 contd. Performance summary of biomolecule detection with different P*Si*-based optical biosensors from 2016-2018

Target type	Target	P <i>Si</i> Structure	Transducing Mechanism	Capture Probe	Label/Label-Free	Signal Amplification	Detection Range/Tested Concentrations	Assay Time	LOD	Real Sample Analysis	Ref.
Proteins	Prostate specific antigen (30 kDa)	Macroporous thin film	Fluorescence	Antibody	Label-free (indirect detection*)	Secondary labeled antibody	Few tens of pg mL ⁻¹ to 100 ng mL ⁻¹ Few hundred of fg mL ⁻¹ to 100 ng mL ⁻¹	~2 h	100 fg mL ⁻¹	Blood serum	²⁰⁹
	Human kallikrein 2 (28.5 kDa)	Microcavity	Colorimetric	Antigen	Label-free (indirect detection*)	Secondary HRP-labeled antibody	-	-	10 fg mL ⁻¹	Blood serum	²¹⁰
Enzymes	Sortase A (27.1 kDa) and MMPs	Microcavity	Fluorescence (FRET-based)	Peptide substrate	Label-free (indirect detection*)		4.6x10 ⁻¹² M to 4.6x10 ⁻⁸ M	30 min	For reflectivity measurement 4.6*10 ⁻⁸ M For fluorescence measurement 8.0x10 ⁻¹⁴	Human wound fluid and bacterial culture medium	²¹¹
Bacteria	<i>E. coli</i>	Fabry-Pérot thin film	Reflectivity	Antibody	Label-free	-	10 ⁵ cells/ml to 10 ³ cells/ml	~45 min	10 ³ cells/ml	Food industry process water	¹⁷⁷
	<i>E. coli</i>	Fabry-Pérot thin film	Reflectivity	Antibody	Label-free (indirect detection*)	-	10 ⁷ cells/ml to 10 ³ cells/ml	-	10 ³ cells/ml	-	²¹²
	<i>L. acidophilus</i>	Fabry-Pérot thin film	Reflectivity	Aptamer	Label-free	-	10 ⁷ cells/ml to 10 ⁶ cells/ml	~40 min	10 ⁶ cells/ml	-	³³

*Indirect target detection refers to assays in which the target does not directly induce the optical signal measured, e.g., utilization of a secondary probe.

Refractometric-Based PSi Biosensors

Optimization of PSi Nanostructure and Bioreceptor Features

Both the structural features of PSi and the utilized bioreceptors have a profound effect on the biosensor sensitivity. Antibodies are the most commonly used capture probes and thus they are well-studied and established. For antibodies, it was demonstrated that ordered orientation results in improved performance^{155, 172} and a thorough study by Bonanno et al.¹⁶⁴ presented the impact of steric crowding on antibody immobilization. The importance of surface chemistry for antibody conjugation was also emphasized by Martin et al.²¹³. Aptamers are emerging as promising alternatives to antibodies in various biosensing platforms²¹⁴⁻²¹⁶ and have been introduced in recent years as capture probes in PSi biosensors^{26, 217}. One main advantage of aptamer-based PSi biosensors in comparison to conventional PSi-based immunosensors is the ability to easily regenerate the sensor by a short rinsing step for multiple biosensing analyses even in complex biological fluids, as was demonstrated by Urmann et al.²⁶. In a later study, Voelcker and co-workers utilized PSi Fabry-Pérot interferometers to compare antibody and aptamer bioreceptors for the detection of insulin. They established that the aptamer-based biosensor outperforms the antibody-based one, both in terms of the LOD ($1.9 \mu\text{g mL}^{-1}$ [$0.33 \mu\text{M}$] and $4.3 \mu\text{g mL}^{-1}$ [$0.74 \mu\text{M}$], respectively) and the response time (12 min and 60 min, respectively), as shown in Figure 2.2.4A²⁸. It is important to emphasize that the sensitivity and LOD of aptamer-based biosensors are highly dependent on the aptamer immobilization density. Indeed, for aptamer-functionalized PSi, a lower surface coverage has resulted in improved performance, ascribed to minimizing effects of steric hindrance and electrostatic repulsion of the negatively-charged DNA molecules at higher concentrations^{26, 32, 33}. Typical LOD values of PSi Fabry-Pérot aptasensors for detection of proteins are in the micromolar range^{26, 28, 29}. Employing multilayered PSi structures, such as thin rugate filters, was shown to improve the LOD for insulin to $0.19\text{-}0.29 \mu\text{g mL}^{-1}$ ($\sim 33\text{-}50 \text{ nM}$), depending on the analysis buffer³².

Further sensitivity improvement of PSi aptasensors was presented by Barillaro and coworkers¹⁹ by increasing the pore diameter (up to a $3\times$ increase in diameter) of a PSi thin film (see Figure 2.2.4B), without affecting the porosity and the effective refractive index of the layer. This was achieved by etching a parasitic layer at a high current density, followed by its removal and subsequent etching of the PSi sensing layer. Figure 2.2.4B shows a 10-fold improvement in sensitivity of the biosensor with the larger pores, which is attributed to an improved analyte diffusion into the porous layer without decreasing the signal-to-noise ratio, due to the unchanged porosity¹⁹.

Although for direct immobilization of aptamer bioreceptors, a lower immobilization density was proven to enhance the biosensor performance^{26, 32, 33}, *in-situ* DNA and aptamer synthesis for higher probe density has been also found advantageous. Weiss and co-workers⁴³ have synthesized a single-stranded DNA (ssDNA) probe *in-situ*, directly on the surfaces of a photonic sensor. A 5 to 7-fold enhancement in sensitivity was demonstrated, as well as a >3 -fold reduction in response time, compared to a direct

ssDNA immobilization procedure, as shown in Figure 2.2.4C. This behavior was ascribed to a higher surface coverage of the ssDNA probes achieved by *in-situ* synthesis due to the addition of uncharged DNA monomers base-by-base, which in turn reduces the negative effects of steric hindrance and charge repulsion during direct immobilization of long ssDNA molecules. The pore size should be also taken into consideration for *in-situ* oligonucleotide synthesis and DeStefano and co-workers^{27, 218} have demonstrated a higher yield of functionalization for *in situ* synthesis of 17-19-mer DNA sequence on PSiO₂ films with a pore diameter larger than 50 nm, when compared to a film with pores of ~20 nm. The resulting biosensor exhibited a low LOD value of 1.5 nM for thrombin (~37 kDa)²⁷.

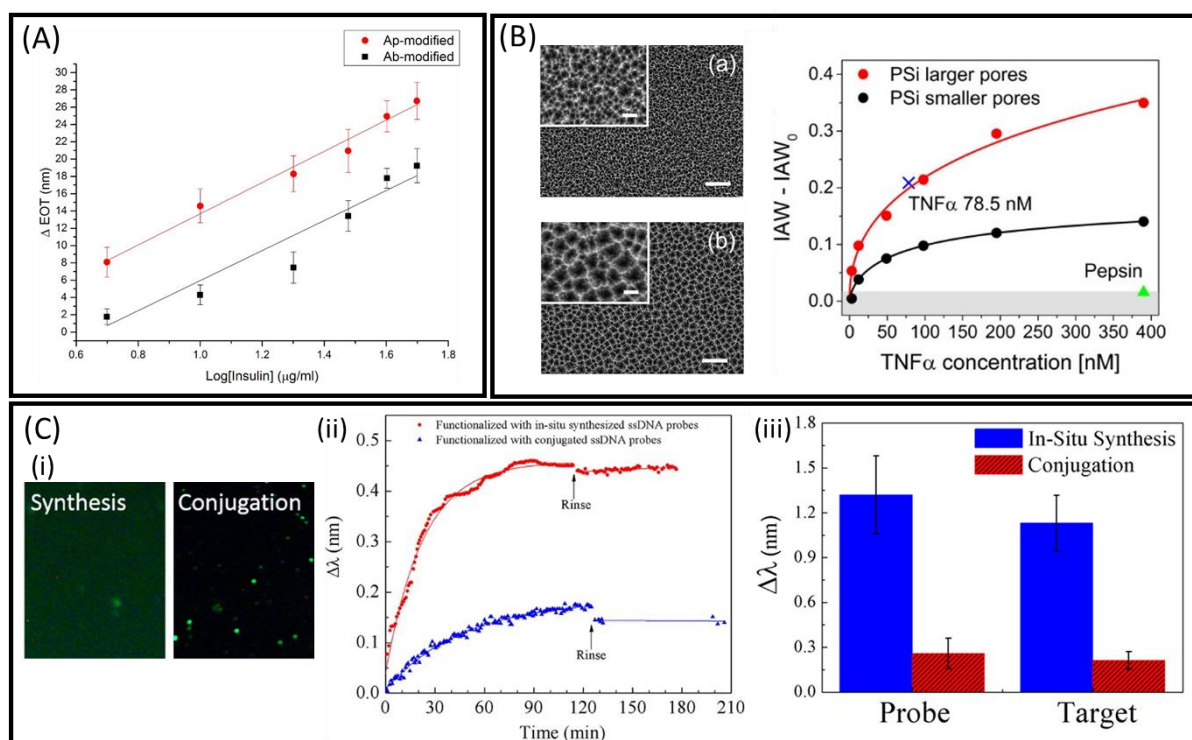


Figure 2.2.4. Performance enhancement of PSi biosensors by capture probe and pore diameter optimization. (A) PSi Biosensor for detection of insulin based on a Fabry-Pérot thin film functionalized with aptamer molecules (red curve) outperforms antibody-functionalized one (black curve). Reprinted with permission from ref.²⁸ (Chhasatia, R.; Sweetman, M. J.; Harding, F. J.; Waibel, M.; Kay, T.; Thomas, H.; Loudovaris, T.; Voelcker, N. H. *Biosensors and Bioelectronics* 2017, 91, 515-522). Copyright (2017) Elsevier. (B) Increasing the pore diameter (up to 3 fold) of a Fabry-Pérot thin film enhanced the detection sensitivity of the biosensor towards the protein TNF- α . Reprinted with permission from ref.¹⁹ (Mariani, S.; Pino, L.; Strambini, L. M.; Tedeschi, L.; Barillaro, G. *ACS Sensors* 2016, 1, 1471-1479). Copyright (2016) American Chemical Society. (C) In-situ synthesis of a ssDNA probe in a ring resonator results in improved performance, compared to direct immobilization of the ssDNA onto the Si surface. (i) Comparison of florescence intensity of a labelled-DNA probe immobilized by the two approaches. (ii) Kinetic binding curve of a ssDNA target to ring resonators, functionalized with a ssDNA probe by in-situ synthesis (red curve) or direct immobilization (blue curve), demonstrating faster response time of the former. (iii) Averaged wavelength shifts for the probe and target binding, upon both functionalization methods. Reprinted with permission for ref.⁴³ (Hu, S.; Zhao, Y.; Qin, K.; Retterer, S. T.; Kravchenko, I. I.; Weiss, S. M. *ACS Photonics* 2014, 1, 590-597). Copyright (2014) American Chemical Society.

Alternative novel capture probes for sensitive detection have been utilized for bacteria and heavy metals targets. Segal and co-workers²¹⁹ immobilized oligomers of acylated lysine (OAK), a synthetic mimetic compound of antimicrobial peptides, on a PSi Fabry-Pérot interferometer for specific detection of *E. coli* fragments. A measured LOD of 10^3 cells mL⁻¹ was demonstrated, similar to monoclonal antibody-based PSiO₂ biosensors^{177, 212, 219}. DeStefano and co-workers functionalized a Thue-Morse PSi structure with Phytochelatin, an oligopeptide targeting heavy metals. However, the latter could not be simply conjugated to solid surfaces due to charge-mediated corrosion upon molecular binding (it presents an isoelectric point of 4.2). Thus, the oligopeptide was derivatized with a six poly-Lysine, resulting in an isoelectric point of 6.9, which could be properly immobilized. Sensitive detection of Lead (II), Arsenic (II) and Cadmium (II) ions was realized with a LOD value for Lead (II) ions of 1.2 ppb¹⁹².

Complex PSi Optical Structures

Improvement in sensitivity by substituting the simple PSi Fabry-Pérot interferometer with sophisticated multilayered-optical structures has already been vastly established¹⁹⁰ and research work in recent years has focused on optimization of these complex structures for improving their sensitivity^{176, 220-226}. Such structures include Bragg mirrors^{227, 228}, rugate filters^{32, 167, 229-231}, microcavities^{43, 164, 191, 213, 232-235}, Thue-Morse structures¹⁹², waveguides^{176, 188}, Vernier effect-based structures²²⁶, Bloch surface wave structures²³⁶, ring resonators^{43, 157}, and diffraction gratings²⁰². Weiss and co-workers extensively studied biosensors based on DNA-PNA (peptide nucleic acid) hybridization with different PSi-based optical structures. A nanomolar LOD was demonstrated with waveguides²³⁷ and ring resonators¹⁵⁷. LOD values in the range of 5.7 nM to 43.9 nM were achieved for biosensors based on DNA hybridization with other PSi structures, such as a polybasic photonic crystal²³⁸, microcavity on a SOI wafer²³⁹, microcavity functionalized with gold nanoparticles²⁴⁰, Bragg mirror on a SOI wafer²²⁸, double-Bragg mirror structure²⁰¹ and diffraction grating coupled with a 1D-photonic crystal²⁰². It should be noted that the fabrication of these multilayered structures is more complex and the accuracy and robustness is limited by the electrochemical etching process parameters^{201, 227, 238}. Moreover, part of these structures require additional fabrication steps, such as photolithography, and more sophisticated optical measurement systems. An example for the latter was proposed by Li et al.²³⁵, where changes in the refractive index of a PSi microcavity during DNA hybridization were detected by the incident angle between a laser and the surface of the PSi, with a LOD value of 87 nM. Another approach for sensitivity enhancement by improving the resolution of the optical readout was presented by Caroselli et al.¹⁹¹. They replaced the spectrometer with an optical interrogator, able to acquire reflectivity spectra every 0.1 s with a resolution of 4 pm. They further reduced the measurement noise by applying a discrete Fourier transform algorithm, resulting in a noise of only 0.2 nm. This high-resolution experimental setup allowed a LOD of 10^{-7} RIU (refractive index unit) with a PSi microcavity sensor¹⁹¹.

One of the main challenges of PSi-based biosensors is overcoming the limited mass-diffusion within the porous nanostructure. By constructing an open-ended PSi microcavity membrane for a flow-through sensing scheme (rather than a conventional flow-over system), as illustrated Figure 2.2.5A, the analyte flux into the biosensor is significantly enhanced²³. A 6-fold improvement in the response time for streptavidin detection by a biotin-functionalized PSi microcavity was achieved, compared to closed-ended films, and 500 nM streptavidin was detected within 20 min (Figure 2.2.5B). In a follow up study, mass transport and reaction kinetics were simulated in open-ended and closed-ended PSi biosensors and the improvement of the performance was again demonstrated for the adsorption of large molecules such as horseradish peroxidase and catalase in an open-ended PSi microcavity membrane, see Figure 2.2.5C²⁴¹.

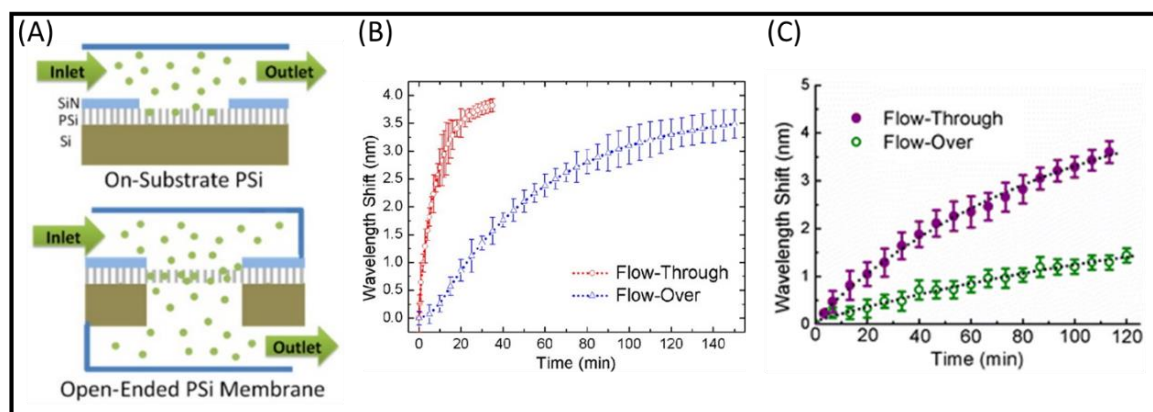


Figure 2.2.5. Open-ended PSi membrane biosensing platform outperforms closed-ended films. (A) Illustration of both biosensing platforms; (B) comparison of biosensing response to streptavidin capturing by a biotinylated-surface, in both flow schemes and (C) comparison of biosensing response to catalase enzyme adsorption, in both flow schemes. Reprinted with permission from ref.²³ and ref.²⁴¹, respectively. (Zhao, Y.; Gaur, G.; Retterer, S. T.; Laibinis, P. E.; Weiss, S. M. *Analytical Chemistry* 2016, 88, 10940-10948); Copyright (2016) American Chemical Society and (Zhao, Y.; Gaur, G.; Mernaugh, R. L.; Laibinis, P. E.; Weiss, S. M. *Nanoscale Research Letters* 2016, 11, 395); (<http://creativecommons.org/licenses/by/4.0/>); copyright © The Author(s). 2016, respectively.

Data Processing

Label-free sensitivity improvement has been demonstrated by Barillaro and co-workers by applying a novel signal processing technique, instead of the common Fourier transform, for the traditional reflectivity measurements of PSi biosensors^{19,20}. This method was termed Interferogram Average over Wavelength (IAW) and is based on subtracting the reflection spectra intensity of a PSi interferometer after and before analyte binding (wavelength by wavelength). This is followed by a simple mathematical manipulation of removal of the mean value and application of an absolute value function to the resulting interferogram. The final IAW signal is obtained by calculating the average value of the processed interferogram over the whole spectral range of interest. This method demonstrated a wide dynamic range of 150 pM to 15 μ M, and a calculated LOD value of 20 pM for BSA adsorption, as depicted in Figure 2.2.6C. The latter represents a four orders of magnitude improvement in the sensitivity in comparison to the traditional Fourier transform manipulation of the reflectance spectra of

PSi by RIFTS (see Figure 2.2.6D)²⁰. Later on, this method was also applied for a specific detection of TNF α biomarker at a concentration down to 3 nM with a calculated LOD of 200 pM¹⁹. Additional sensitivity enhancement, utilizing the IAW method, was demonstrated by exploiting electrical double layer-induced ion surface accumulation (EDL-ISA) on PSiO₂ surface for refractometric applications²⁵. In this fundamental study, it was shown that for solutions with bulk refractive index variation below 10⁻⁴ RIU (i.e. NaCl and KCl (w/w) < 0.1%), the LOD is improved by two orders of magnitude. This is attributed to a surface effect of accumulation of charged cations (Na⁺ and K⁺) on the surface of negatively-charged PSiO₂. For such low concentrations, this surface effect dominates the bulk effect of solution refractive index variation within the porous nanostructure. On the contrary, for higher concentrations, when the bulk refractive index effect dominates the surface effect, the achieved LOD is only $\sim 10^{-5}$ RIU (which is in agreement with the other PSi refractometers). The EDL-ISA method improves the performance of the PSi-based interferometers to that exhibited by more sophisticated photonic and plasmonic sensors²⁵.

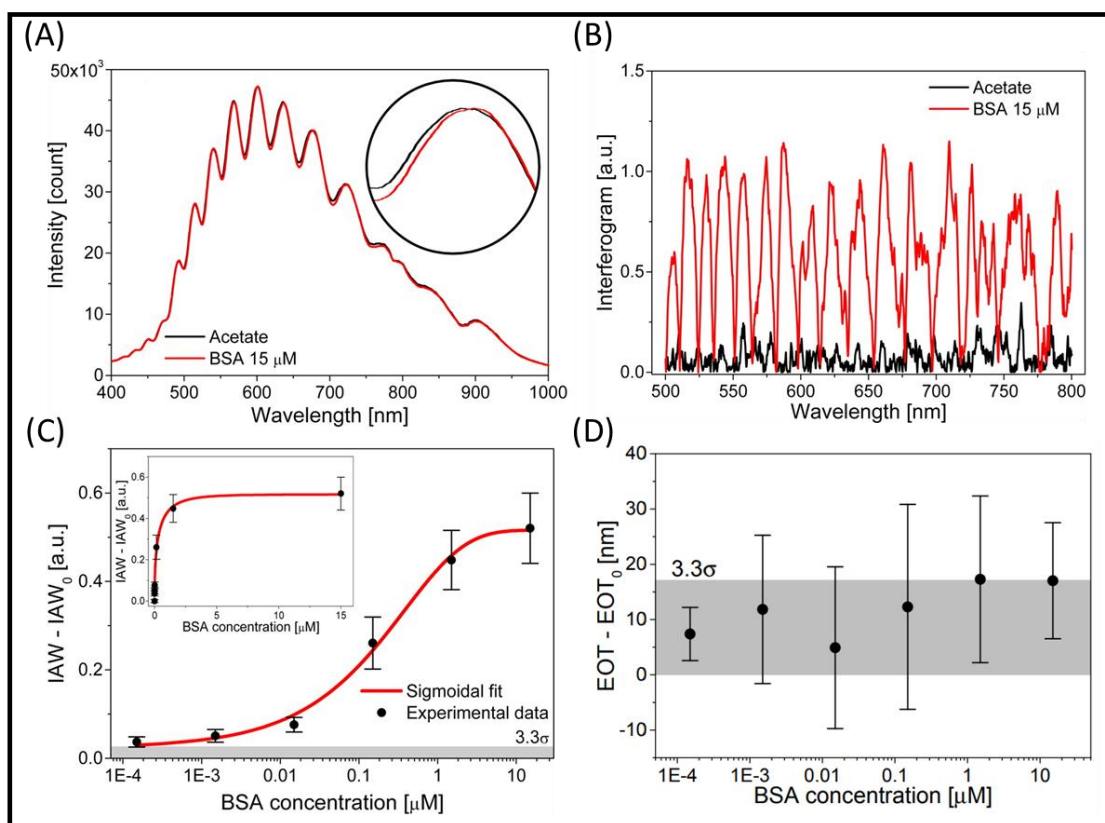


Figure 2.2.6. IAW method for reflectivity data processing of PSi reflectivity. (A) Raw reflectivity spectra of PSi, and (B) interferogram signal calculated by mathematical manipulation of the reflectivity spectra for a baseline buffer (black curve) and upon BSA adsorption (red curve). (C) Calibration curve of IAW signal for different BSA concentrations and (D) corresponding EOT data obtained upon standard FFT analysis, which are below instrumental DL. Reprinted with permission from ref.²⁰ (Mariani, S.; Strambini, L. M.; Barillaro, G. *Analytical Chemistry* 2016, 88, 8502-8509). Copyright (2016) American Chemical Society.

Signal Amplification

One strategy for signal amplification for refractometric-based PSi biosensors is by maximizing the refractive index change upon analyte binding. This is achieved by inducing structural changes to the PSi nanostructure or by filling the entire porous volume with a substrate that will change or degrade upon analyte binding. The basic concept was already reported in 2004 by Steinem et al.¹⁸⁴, where DNA-induced corrosion of a PSi Fabry-Pérot interferometer was used for monitoring hybridization events within the porous layer. The corrosion effect amplified the optical signal upon DNA binding, as the EOT decrease ascribed to the PSi dissolution is significantly higher than the EOT increase observed for DNA infiltration into the pores, and indeed a LOD value of 0.1 nM was reported in comparison to characteristic micromolar values¹⁸⁴. Nevertheless, application of this corrosion-induced biosensing concept is limited due to the poor reproducibility and reliability of the results¹⁸⁵. Detection of PNA-DNA hybridization, which passivates the corrosion effect, results in a 10 nM LOD with a PSi waveguide biosensor²³⁷. Alternatively, Lv et al.¹⁹⁹ have recently presented detection of DNA hybridization by target labelling with quantum dots (QDs) and a LOD value of 6.97 nM was achieved. A similar approach was demonstrated by Gaur et al.²⁴² in an earlier study for the detection of QD-labeled biotin by a streptavidin functionalized-PSi Fabry-Pérot thin film; significant enhancement of three orders of magnitude was realized, as shown in Figure 2.2.7A. Signal amplification for DNA detection was also achieved by induction of a polymerization reaction within the pores²⁴³ (illustrated in Figure 2.2.7B) using PSi functionalized with a capture ssDNA and a target DNA, which is modified with a radical polymerization initiator molecule. After the hybridization reaction, a monomer mixture was introduced, resulting in a polymerization reaction within the pores and signal amplification, ascribed to the significant change in the EOT signal upon polymer formation within the pores. A similar approach was utilized by Gooding and co-workers^{230 231}, who filled the entire porous volume of a PSi photonic crystal with a polymeric substrate for an enzyme target. Figure 2.2.7C schematically illustrates the concept²³⁰, where introduction of the enzyme resulted in the cleavage of the polymer within the pores, inducing a significant change in the reflectivity spectrum and a significant sensitivity enhancement compared to previous work¹⁶⁷ by the same group.

Another method for improving biosensor performance takes advantage of a secondary capture probe, as in a sandwich ELISA assay. Szili et al.²⁴⁴ functionalized PSi with anti-human IgG and, following the binding of the target IgG, a secondary antibody labelled with horseradish peroxidase enzyme was introduced and subsequently its enzymatic substrate. Thus, this *in situ* enzymatic reaction within the porous nanostructure resulted in a signal amplification and LoD of 1.3 nM was achieved²⁴⁴. Urmann et al.²⁹ utilized a similar approach, yet much simpler, for detection of protein A. After binding of protein A to an aptamer-functionalized PSi, an antibody specific to protein A was introduced and amplified the optical signal, leading to a three-fold higher sensitivity (Figure 2.2.7D)²⁹.

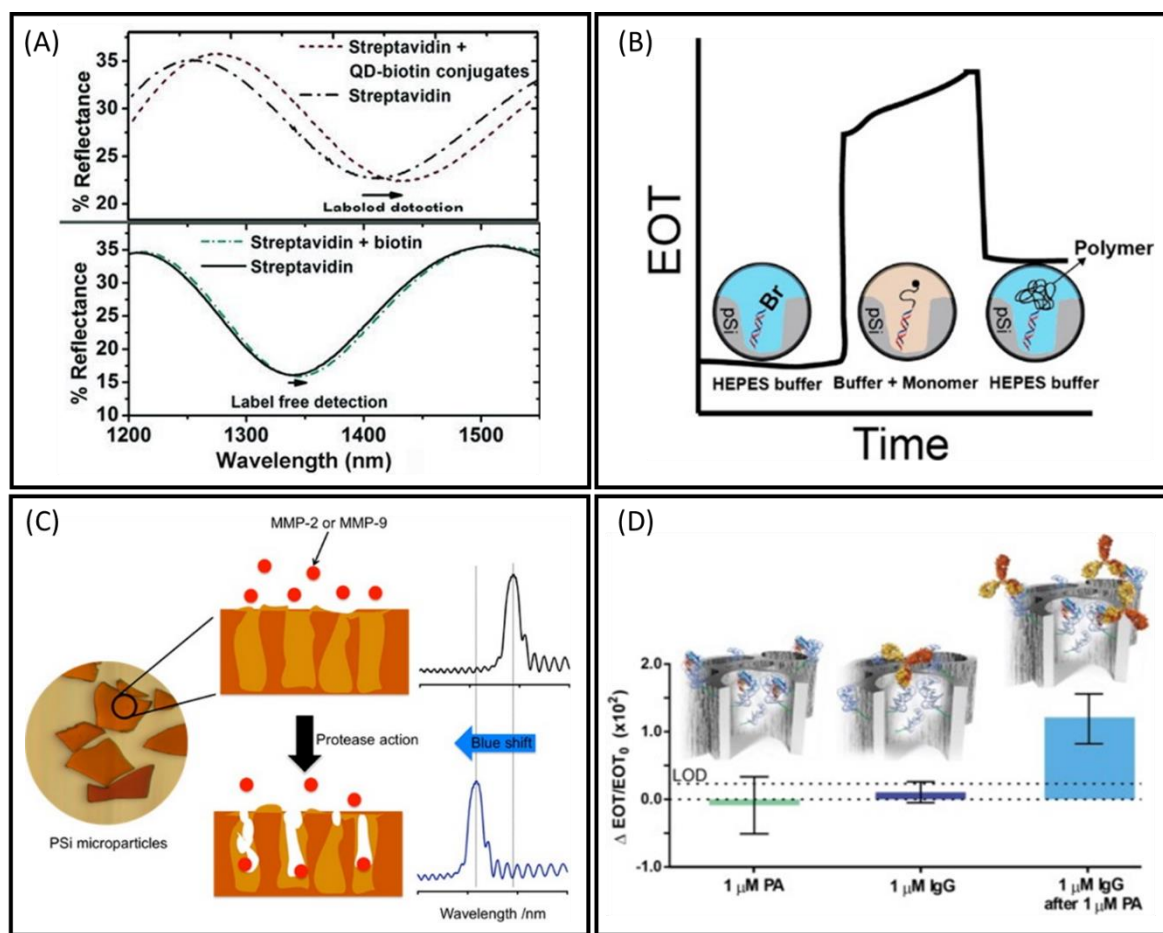


Figure 2.2.7. Signal amplification strategies. (A) Reflection spectra for the detection of a QD-labelled biotin by a streptavidin-functionalized PSi surface (top), compared to a non-labelled biotin (bottom). The former results in a significantly larger spectral shift. Reprinted with permission from ref. ²⁴² (Gaur, G.; Koktysh, D. S.; Weiss, S. M. *Adv. Funct. Mater.* 2013, 23, 3604-3614). Copyright © 2013, John Wiley and Sons. (B) and (C) Illustration of two signal amplification strategies, based on inducing a polymerization reaction within the pores upon target binding or filling the entire porous volume with a substrate for enzymatic cleavage, respectively. Reprinted with permission from ref. ²⁴³ and ref. ²³¹, respectively. (Holthausen, D.; Vasani, R. B.; McInnes, S. J. P.; Ellis, A. V.; Voelcker, N. H. *ACS Macro Letters* 2012, 1, 919-921); Copyright (2012) American Chemical Society and (Gupta, B.; Mai, K.; Lowe, S. B.; Wakefield, D.; Di Girolamo, N.; Gaus, K.; Reece, P. J.; Gooding, J. J. *Analytical Chemistry* 2015, 87, 9946-9953); Copyright (2015) American Chemical Society, respectively. (D) Averaged relative EOT changes upon exposure of an aptamer-functionalized PSi biosensor to protein A (PA), IgG targeting PA or the latter after PA binding. The use of the secondary capture probe results in significant signal enhancement. Reprinted with permission from ref. ²⁹ (Urmann, K.; Reich, P.; Walter, J.-G.; Beckmann, D.; Segal, E.; Scheper, T. *Journal of Biotechnology* 2017, 257, 171-177). Copyright (2017) Elsevier.

The above approaches for sensitivity enhancement pose drawbacks of indirect analyte detection, they require additional experimental steps, as well as the use of reagents. An alternative method for sensitivity enhancement, which allows for direct analyte detection, was recently demonstrated by Segal and co-workers for DNA ⁴² and protein ³⁰ targets. Isotachopheresis (ITP), which is an electrokinetic technique for concentration and separation of charged analytes ²⁴⁵, was applied on a PSiO₂ Fabry-Pérot interferometer for real-time and on-chip pre-concentration of a DNA target, allowing for the delivery

of a highly-concentrated zone of ssDNA molecules to the biosensor surface, with a 10000-fold enhancement in local concentration⁴². While most ITP assays are labelled, in this work DNA hybridization was realized in a label-free format using RIFTS, and a measured LOD value of 1 nM demonstrated. Recently, the group applied this approach for pre-concentration of a his-tagged protein target on a PSiO₂ thin film functionalized with an anti-his tag aptamer, as schematically illustrated in Figure 2.2.8A³⁰. A measured LOD of 7.5 nM was obtained with an up to 1000-fold enhancement in sensitivity compared to a conventional assay (see Figure 2.2.8B)³⁰. A similar strategy for analyte pre-concentration was also applied for heavy metal ions on a PSi microcavity by electrochemical reduction, followed by reflectivity measurements (Figure 2.2.8C and D, respectively)¹⁹³. A LOD value of 1.16 ppb for cadmium (II) was reported while this method also allowed for separation of interfering metal ions by a preliminary electrochemical reduction at specific voltages¹⁹³.

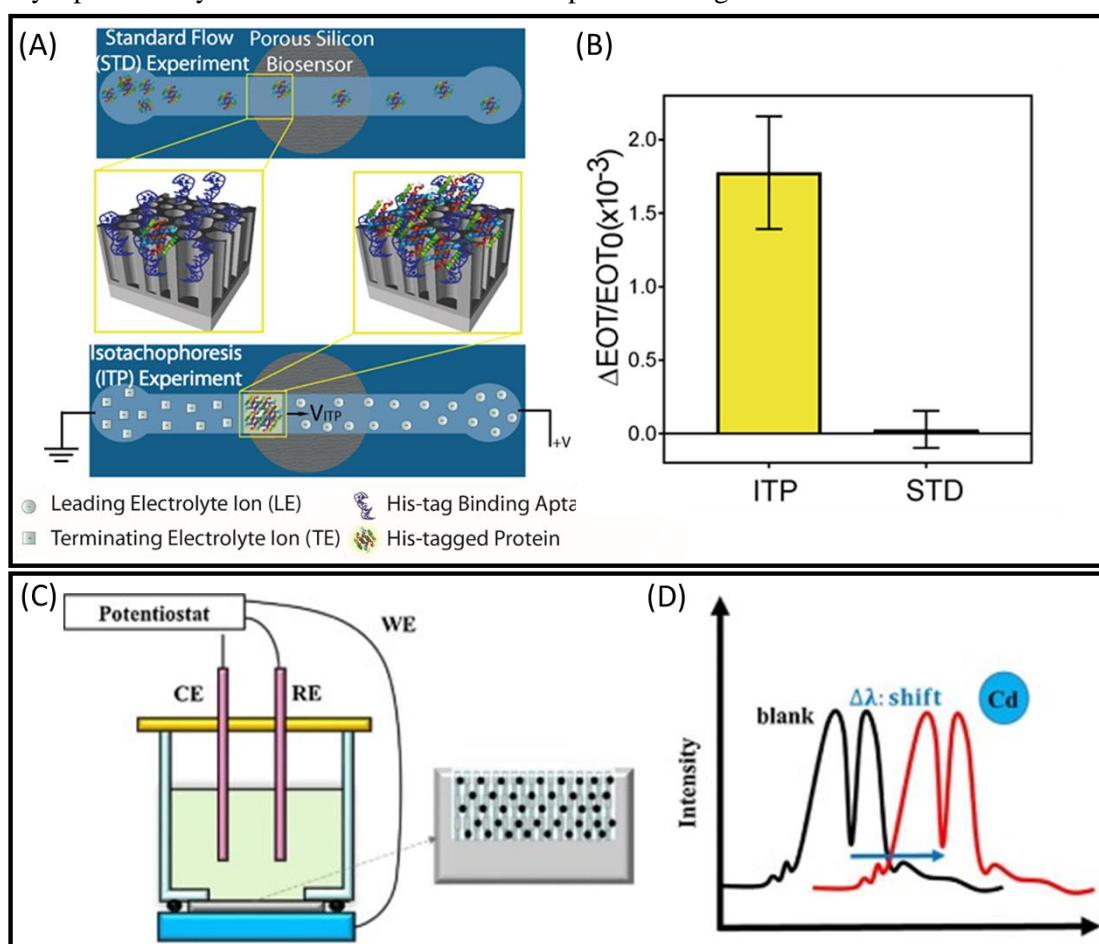


Figure 2.2.8. Signal amplification by target preconcentration. (A) Illustration of ITP method for real time preconcentration of a his-tagged protein target on an aptamer-functionalized PSi biosensor (bottom), in comparison to a standard (STD) biosensing experiment without ITP (top). (B) Averaged relative EOT changes upon 750 nM target binding, with or without ITP application, demonstrating the significant enhancement in the signal. Reprinted with permission from ref.³⁰ (<https://pubs.acs.org/doi/10.1021/acssensors.7b00692>). (C) Schematic of the electrochemical cell for cadmium (II) reduction on a PSi microcavity and the resulting wavelength shift (D). Reprinted with permission from ref.¹⁹³ (Tsai, W.-T.; Nguyen, M.-H.; Lai, J.-R.; Nguyen, H.-B.; Lee, M.-C.; Tseng, F.-G. *Sensors and Actuators B: Chemical* 2018, 265, 75-83). Copyright (2018) Elsevier.

Luminescent-Based Biosensors

Sensitive luminescent-based detection with PSi nanostructures has been demonstrated, utilizing the PL signal of PSi, or embedding other luminescent molecules within the PSi nanostructure. For instance, Iatsunskiy and co-workers demonstrated sensitive toxin detection with gold-coated PSi¹⁹⁷ or macroporous Si films¹⁹⁶. Upon target binding to an antibody-functionalized surface, quenching of the PSi PL signal was observed and LOD values of 2.5 and 4.4 pg mL⁻¹ were realized for Aflatoxin B1 and Ochratoxin A, respectively^{196,197}. A similar biosensing mechanism was demonstrated with a film of Si nanowires (NWs) functionalized with antibodies targeting the cardiovascular disorder biomarker, C-reactive protein (CRP), as schematically depicted in Figure 2.2.9A. Upon CRP binding, quenching of the PL signal was observed, resulting in a highly sensitive detection of CRP with a LOD value of 1.6 fM, which could be also detected in blood serum samples (Figure 2.2.9B)²⁰⁸. An array of mesoporous Si NWs was also utilized for detection of glucose in the presence of glucose oxidase, based on enhancement of the PL signal. The enhancement was observed for higher target concentrations and a LOD of 1.06 μM was attained¹⁹⁵. Although measurement of PL can result in sensitive detection, it should be noted that the PL of PSi nanostructures tends to be unstable and sensitive to the chemical environment.

An alternative concept utilizes PSi as a host matrix for fluorescent probes, where its role is to enhance the fluorescence intensity of the embedded fluorophores. Zhang et al. utilized Rhodamine B as a fluorescence label in a PSi Fabry-Pérot film and further stabilized and enhanced the signal by using deposited AgNPs. Fluorescence-based detection of an antifreeze protein target (12.7 kDa) was achieved with an antibody capture probe, and the sensitivity was further enhanced by tailoring the surface chemistry with a LOD value of 16.5 ng mL⁻¹ (1.3 nM)²⁴⁶. A similar concept was presented by Voelcker and co-workers, utilizing resazurin as a label in a microcavity structure for detection of *L*-Lactate dehydrogenase (LDH)²⁴⁷. In the presence of *L*-lactate (the enzyme substrate) and the coenzyme NAD⁺, resazurin was reduced to resorufin, resulting in an increased fluorescence emission and a LOD of 0.08 U mL⁻¹²⁴⁷. Microcavities can efficiently enhance the fluorescence of fluorophores by tailoring the wavelength of the microcavity resonance dip to align with the emission wavelength of the fluorophore²⁴⁸. Indeed, in this case a 10-fold signal enhancement of the microcavity was demonstrated in comparison to a simple PSi thin film²⁴⁷. The same group also designed FRET-based biosensors for detection of matrix metalloproteinases (MMP)^{211, 249} and a bacterial wound infection biomarker, the enzyme Sortase A (SrtA)²⁴⁹. The biosensors comprised a PSi microcavity functionalized with a fluorogenic peptide, which served as a substrate for enzymatic cleavage, and the peptide substrate was modified with a fluorescent dye and a quencher. Upon introduction of the target enzyme, the substrate peptide is cleaved, and the quencher is removed, resulting in fluorescence enhancement, as depicted in Figure 2.2.9C. The PSi microcavity structure served as a fluorescence enhancer, resulting in 13-fold emission enhancement and emission peak narrowing (Figure 2.2.9D). Based on reflectivity

measurements, the LOD for SrtA was 4.6×10^{-8} M, while fluorescence detection enabled a LOD of 8.0×10^{-14} M with an assay time of 30 min²¹¹. In an earlier study, an outstanding LOD value of 7.5×10^{-19} M was obtained for MMP-1 with an assay time of 5 min²⁴⁹. A similar concept was presented by Liu et al.¹⁹⁸, with a 14-times higher fluorescence signal enhancement by deposition of TiO₂ monolayer onto a PSiO₂ thin film compared to neat PSiO₂ (see Figure 2.2.9F). These PSiO₂-TiO₂ films were used for sensitive detection of various mycotoxins (Ochratoxin A, Aflatoxin B₁ and Fumonisin B₁) by FRET, where the PSi-TiO₂ film was functionalized with a fluorescently-labelled aptamer capture probe bound to a quencher-labelled anti-aptamer sequence. Thus, upon mycotoxin binding, the anti-aptamer-quencher was released, resulting in a fluorescence signal, as illustrated in Figure 2.2.9E, and the achieved LOD values are detailed in Table 2.2.1¹⁹⁸. Wang et al.²⁰⁰ presented a similar strategy by depositing gold NPs on a PSi microcavity for fluorescence signal enhancement; DNA hybridization was detected with fluorescently-labelled DNA target with a LOD value of 10 pM.

QDs and more recently carbon dots (C-Dots) have been utilized as a target label to enhance the sensitivity in reflectivity-based biosensors, but their infiltration into the porous layer was also proven to result in enhanced fluorescence signal²⁴². Yet, these embedded QDs (or C-dots) also can be exploited for label-free biosensing as was recently described by Massad-Ivanir et al.²⁰⁵. The PSi/C-dots hybrid (Figure 2.2.9G) was used for dual mode detection of ATP using both the reflectivity of the PSi and the fluorescence signal of embedded C-dots (see Figure 2.2.9H); the LOD achieved via fluorescence measurements was orders of magnitude lower.

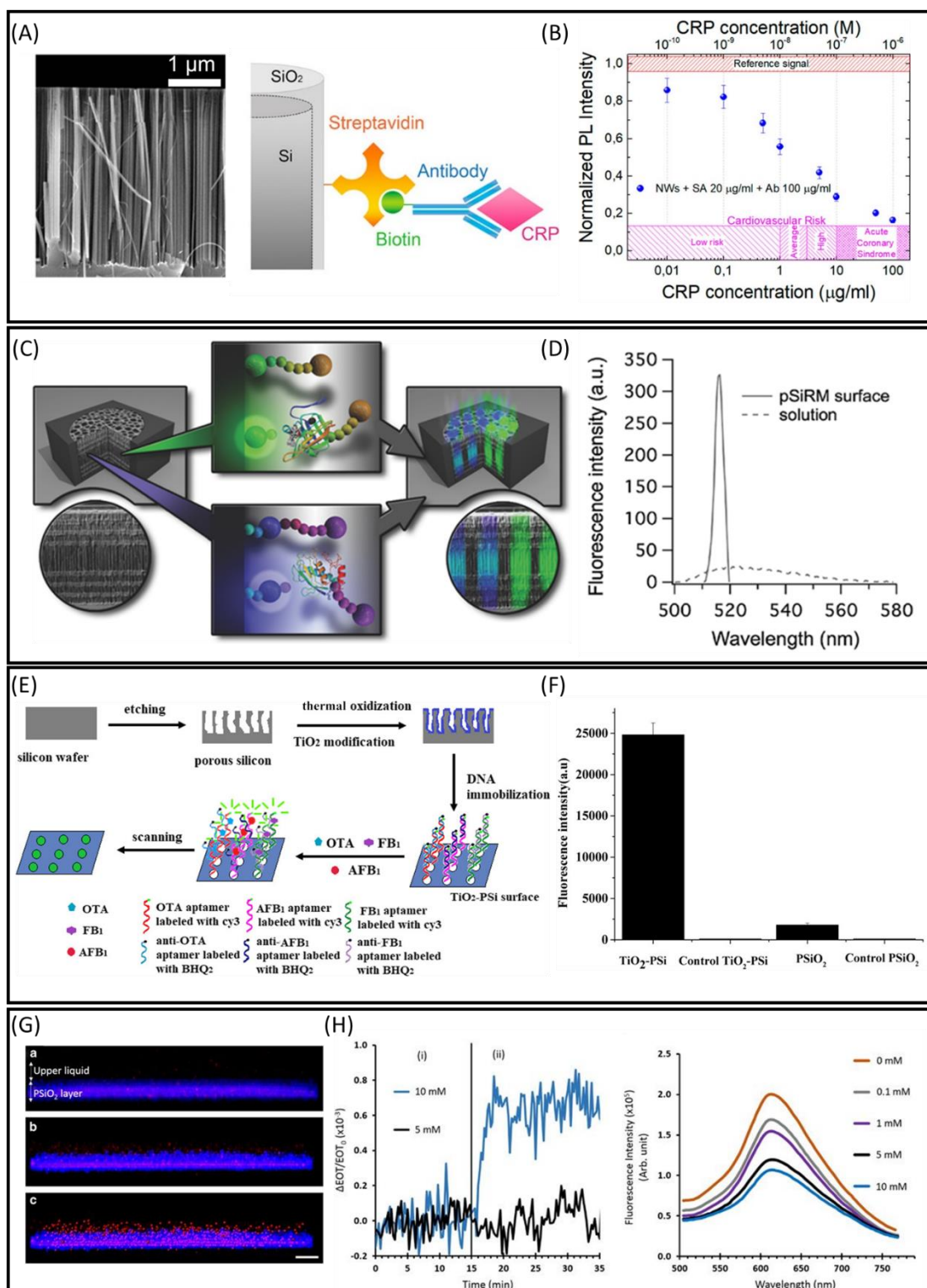


Figure 2.2.9. Sensitivity enhancement of luminescent-based biosensors. (A) SEM micrograph and schematic illustration of a Si NWs array functionalized with an antibody targeting CRP and (B) PL intensity for different CRP concentrations spiked in blood serum, demonstrating the matching of the dynamic range to the critical range for cardiovascular risk in blood. Reprinted with permission from ref. ²⁰⁸ (Irrera, A.; Leonardi, A. A.; Di Franco, C.; Lo Faro, M. J.; Palazzo, G.; D'Andrea, C.; Manoli, K.; Franzò, G.; Musumeci, P.; Fazio, B.; Torsi, L.; Priolo, F. *ACS Photonics* 2018, 5, 471-479). Copyright (2018) American Chemical Society. (C) Illustration of the FRET-based biosensor for detection of SrtA and MMP. A PSi microcavity (left) is functionalized with FRET peptide substrates for the enzymes in an array form (middle), which upon cleavage results in fluorescence enhancement (right) and (D) fluorescence emission of the SrtA fluorogenic peptide in solution (dashed line) and

*immobilized on the PSi microcavity (full line) after incubation with SrtA, demonstrating the significant fluorescence enhancement feature of the PSi microcavity structure. Reprinted with permission from ref. ²¹¹ (Krismastuti, F. S. H.; Cavallaro, A.; Prieto-Simon, B.; Voelcker, N. H. *Advanced Science* 2016, 3, 1500383). (<http://creativecommons.org/licenses/by/4.0/>); Copyright © 2016 The Authors. (E) Schematic of the FRET-based multiplex mycotoxin detection with a PSi-TiO₂ structure. (F) Comparison of fluorescence intensity of a labelled-aptamer immobilized on a PSiO₂-TiO₂ and neat PSiO₂, demonstrating the significant fluorescence enhancement due to TiO₂ deposition. Controls are the background fluorescence intensity. Reprinted with permission from ref. ¹⁹⁸ (Liu, R.; Li, W.; Cai, T.; Deng, Y.; Ding, Z.; Liu, Y.; Zhu, X.; Wang, X.; Liu, J.; Liang, B.; Zheng, T.; Li, J. *ACS Applied Materials & Interfaces* 2018, 10, 14447-14453). Copyright (2018) American Chemical Society. (G) Confocal laser scanning microscopy projection images of a neat PSiO₂ (a), C-dots/PSiO₂ hybrid (b) and the hybrid in which the fluorescence signal of the C-dots is falsely coloured red to aid observation (c). (H) Fluorescence based-detection of ATP with the embedded C-dots in the PSiO₂ layer (left) results in more than 50-times lower LOD compared to reflectance-based detection (right). Reprinted with permission from ref. ²⁰⁵ (Massad-Ivanir, N.; Bhunia, S. K.; Raz, N.; Segal, E.; Jelinek, R. *Npg Asia Materials* 2018, 10, e463). (<http://creativecommons.org/licenses/by/4.0/>).*

Other Optical Transduction Mechanisms

PSi has also been utilized as a solid support, exploiting the advantage of its enhanced surface area for colorimetric analyte detection. These biosensors involve enzymatic reaction to produce a color product that can be measured with ultraviolet–visible (UV-Vis) spectroscopy. The analyte detection is indirect and requires the addition of other reagents. Lasmi et al. ¹⁹⁴ immobilized Tyrosinase on a PSi thin film and the small molecule pyrocatechol (110 g mol^{-1}) was detected indirectly by UV-Vis absorbance measurements of the enzymatic reaction product. A LOD value of $0.43 \text{ }\mu\text{M}$ was achieved, but required also the addition of a chemical enzymatic product stabilizer ¹⁹⁴. Ramakrishan et al. ²¹⁰ constructed a PSi microcavity functionalized with a peptide antigen for colorimetric detection of a target antibody. The assay was performed similarly to ELISA utilizing a secondary horseradish peroxidase (HRP)-labelled antibody; a LOD of 10 fg mL^{-1} was attained with a 1000-fold enhancement compared to similar flat Si surface-based biosensors, demonstrating the advantage of the large surface area and the light enhancing properties of PSi ²¹⁰.

Additionally, *in situ* synthesis of metal NPs within the porous nanostructures results in Raman enhancement, enabling sensitive SERS-based detection ^{203, 204, 250, 251}, of multiple targets such as microRNA ^{203, 250} and Glutathione ²⁰⁴ (LOD values are specified in Table 2.2.1).

Real Sample Analysis

Proving relevant sensitivity in a clean buffer is not sufficient for clinical application since in most cases targets are outnumbered by a million fold of non-target species in real clinical samples ⁴. The required specificity and the ability of the biosensor to remain active in a complex biological fluids is the ultimate challenge in a biosensor construction. Signal stability, cross-reactivity and background noise are only part of the encountered issues. Although most of the works demonstrate biosensor specificity by the ability to discriminate between a target and a non-target in a clean buffer, application of the biosensors in real clinical specimens is limited. Bonanno and De Louise ¹⁷⁸ were the first to demonstrate a label-free PSiO₂-based biosensor for detection of IgG in whole blood and serum samples. The pore

dimensions of the P_{Si}O₂ were tailored to size-exclude cells and large proteins from infiltrating into the porous nanostructure while enabling the entrance of the IgG target. The biosensor's stability was enhanced with a buffer containing trehalose and non-specific binding was minimized by blocking with BSA. Whole blood and serum samples were directly analyzed by the biosensor and successful detection of IgG in a clinically relevant range was demonstrated, with a comparable performance to an ELISA assay¹⁷⁸. In a later study, the same group demonstrated indirect detection of opiates in undiluted urine samples by using a Bragg-mirror-based biosensor in a competitive assay with an antibody probe. Optimization of the chemistry, BSA blocking and the volume of the urine specimen applied to the sensor enabled tunable specificity and a relevant detection range^{252, 253}. Additional real samples that were analyzed with P_{Si}-based optical biosensors include different water samples^{177, 193, 254}, cereal samples¹⁹⁸, cell cultures^{230, 231}, bacteria lysates^{26, 30, 186}, RNA cell extracts²⁰³, and blood serum^{204, 208-210}. Substantial advancements in real sample analysis has been also achieved by the group of Voelcker, designing P_{Si}-based biosensors for enzyme^{211, 249} and glucose²⁵⁵ detection in wound fluids, unmodified²¹¹ or diluted by ten-fold^{249, 255}, as well as more recently insulin detection in human islets of Langerhans^{28, 32}. The group also studied the ability of a P_{Si}-based biosensor to perform *in vivo* using a thermally-hydrocarbonized rugate filter which was implanted subcutaneously in a mouse model, as shown in Figure 2.2.10 (top panel)²⁵⁶. The optical signal could be clearly read through the skin of living mice one week after implantation, proving its optical functionality, as shown in Figure 2.2.10 (bottom panel). The work emphasized the importance of surface stabilization for minimizing structure dissolution in physiological media and thermal-hydrocarbonized P_{Si} was found to outperform thermally-oxidized P_{Si}. Moreover, mitigation of cytotoxicity was achieved by pre-incubating the structures in cell medium for ten days prior to implantation²⁵⁶.

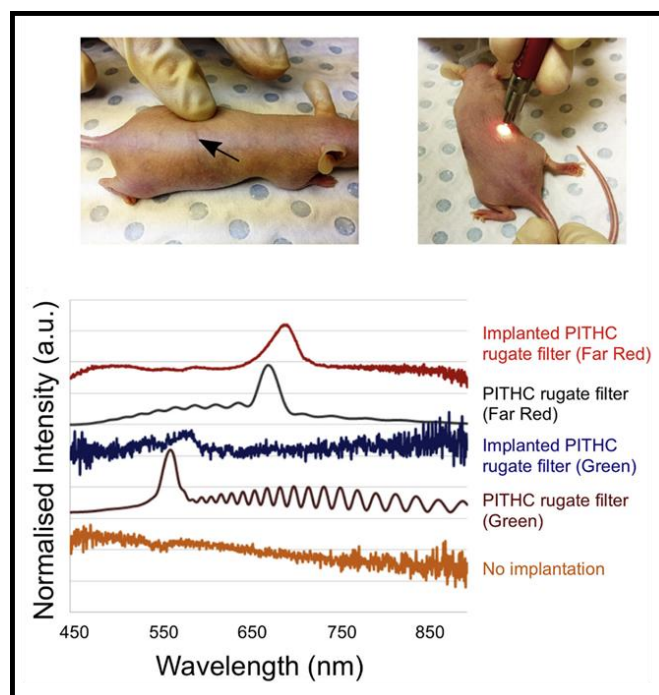


Figure 2.2.10. Top: Images showing the reading of the implanted pre-incubated thermally hydrocarbonized (PITHC) PSi rugate filter through the skin of a mouse. Bottom: photonic peaks of “Green” and “Far Red” PITHC PSi rugate filter being read through the skin, along with the optical reflectance of these rugate filters immersed in water and the reflectance of a blank skin section. Reprinted with permission from ref. ²⁵⁶ (Tong, W. Y.; Sweetman, M. J.; Marzouk, E. R.; Fraser, C.; Kuchel, T.; Voelcker, N. H. *Biomaterials* 2016, 74, 217-230). Copyright (2016) Elsevier.

Two additional important features that should be considered for real sample analysis are the capture probe, which determines the specificity, and surface blocking for minimizing non-specific binding. Aptamers have been suggested as good candidate for analyte detection in complex media due to their stability and high affinity. Indeed, recent PSi-based optical aptasensors have been able to perform in complex media of bacteria lysates ^{26,30}, cereal samples ¹⁹⁸ and human islets of Langerhans ^{28,32}. It should be also emphasized that the biosensing performance could be further improved by custom selection of the aptamer directly in the complex fluids, which would further improve the stability and functionality in these environments ²⁵⁷.

As mentioned in “Surface Chemistry” Section, blocking of the unreacted surface sites following bioreceptor immobilization is a key step to prevent nonspecific binding. Carbodiimide or glutaraldehyde bioreceptor coupling are the most common conjugation approaches and in these cases, blocking is performed with amine-containing molecules to block residual surface active sites. These include small molecules, such as Tris ^{26,30}, ethanolamine ^{177,211} and glycine methyl ester ¹⁸⁶, or proteins such as BSA. The latter is a common blocking agent for biosensors in real samples ^{178,203,210,252,253}. An additional approach for blocking is by PEG passivation that was found to prevent nonspecific binding ²⁵⁸⁻²⁶⁰. For example, bis PEG-amine (with a molecular weight of 3000) was used to block residual active NHS sites and passivate the surface, successfully preventing non-specific binding in undiluted human islet fluid ^{28,32}.

Additional strategies to improve specificity include sample pre-treatment or application of sample separation techniques. Real sample pre-treatment steps, such as filtration^{186, 198} or dilution with a buffer^{249, 255} minimize the background noise, but also add significant complexity to the experimental assay. Moreover, sample dilution also dilutes the target analyte and thus raises the sensitivity challenge. Pre-separating the target from interfering species within the complex fluid has been shown to improve specificity. For example, the ITP method separates ionic species based on their effective electrophoretic mobility and its application on a PSi biosensor resulted in a real time formation of a neat target zone that could be detected separately from other interfering species in the sample^{30, 42}. In a similar strategy, an electrochemical reduction was used to pre-remove interfering metal ions from a tested sample for detection of a specific metal ion¹⁹³.

Emerging Applications: Towards Point-of-Care Devices

In recent years, PoC adaptation of constructed biosensors is gaining significant interest. This includes means such as microfluidic integration, smartphone connection and multiplexing to obtain biosensors that could perform outside traditional laboratory settings. For PSi-based optical biosensors, advancements in the former two aspects is yet limited, while the latter was more extensively studied over the past years. This section will highlight the recent advances in each aspect and finally discuss some intriguing applications.

Microfluidic Integration and Smartphone Connection

Introducing microfluidics to biosensors has gained much interest in the past decade, as it serves as an integrating force for PoC devices. It enables portability, assay automation, lower consumption of reagents and shorter assay time^{34, 261}. PSi-based optical biosensors have been integrated with microfluidic devices, mainly fabricated from PDMS^{23, 30, 42-45, 241, 262}. PDMS flow cells are usually constructed by replica molding from a master template, created by soft lithography, and sealed with PSi by plasma activation. The advantages of microfluidic integration have been proven by DeStefano and co-workers^{44, 46, 263}. During biofunctionalization of a microfluidic-integrated biosensor, a reduction in sample volume from 30 μl to less than 5 μl was achieved. The optical signal observed was higher and the process time was shortened from an overnight treatment to 3 h, when compared to a non-integrated biosensor. The former was attributed to a higher ratio of surface active sites to applied probe concentration, while the latter to a shortened diffusion time in the nanoliter volume of the microchannel, compared to a microliter volume scale^{44, 46}. Microfluidic integration also allows the implementation of electrokinetic techniques, such as ITP^{30, 42}, as described in Section “Signal Amplification”.

Utilizing smartphones for detection in a biosensing platform has the potential to significantly reduce the cost and complexity of the assay and allow portability, replacing laboratory instruments such as spectrometers and microscopes^{264, 265}. Smartphones have been already integrated with various optical detection schemes, including a label-free photonic crystal biosensor²⁶⁶. The feasibility of employing smartphones for readout analysis of PSi-based optical biosensors was also recently demonstrated by

correlating the reflectivity changes upon molecular binding to changes in the light intensity of a digital image²⁶⁷⁻²⁶⁹. Cao et al.²⁷⁰ presented glucose and protein detection by this correlation, with a LOD of 7×10^{-4} RIU. Additionally, a colorimetric-based assay on a PSi microcavity biosensor, similar to a sandwich ELISA, was also monitored with a smartphone camera followed by image RGB intensity analysis²¹⁰.

Multiplexing

Microarray technology is the most accepted way to achieve miniaturization, high-throughput analysis, and multi-target detection. PSi has been well-studied in the past two decades as a substrate for microarray construction. An array of sensing spots can be achieved by three main fabrication routes: pre-patterning of PSi regions on a crystalline Si, chemical patterning of PSi at specific positions, or by capture probe spotting via printing techniques. Pre-patterning of PSi on top of a Si wafer is most commonly achieved by photolithographic techniques such as the deposition of a masking layer followed by an etching process²⁷¹⁻²⁷⁷. For example, an array of PSi Bragg mirrors was fabricated by Rea et al.²⁷⁸ utilizing a Si nitride mask with the desired array pattern. The process required pre-deposition of Si nitride on the Si substrate followed by patterning using photolithography and reactive ion etching, as illustrated in Figure 2.2.11A. The resulting array was employed for simultaneous reflectivity measurements of complementary DNA hybridization to immobilized probes in parallel to a control of non-complementary ssDNA, see Figure 2.2.11B²⁷⁸. Novara et al.^{203, 279} presented a simpler method for patterning utilizing patterned PDMS as a masking layer during the etching process. Partially cured PDMS was also used to detach the freshly etched PSi, creating PSi membranes on a PDMS substrate, which were further sealed with PDMS resulting in microfluidic chambers^{203, 279}; simultaneous label-free multianalyte detection of four model oligonucleotides was successfully demonstrated, as shown in Figure 2.2.11C and 2.2.11D²⁷⁹. Other methodologies for PSi pre-patterning include ion beam metal deposition followed by metal-assisted etching²⁸⁰, dry-removal soft lithography with a PDMS stamp²⁸¹, and direct UV laser writing²⁸².

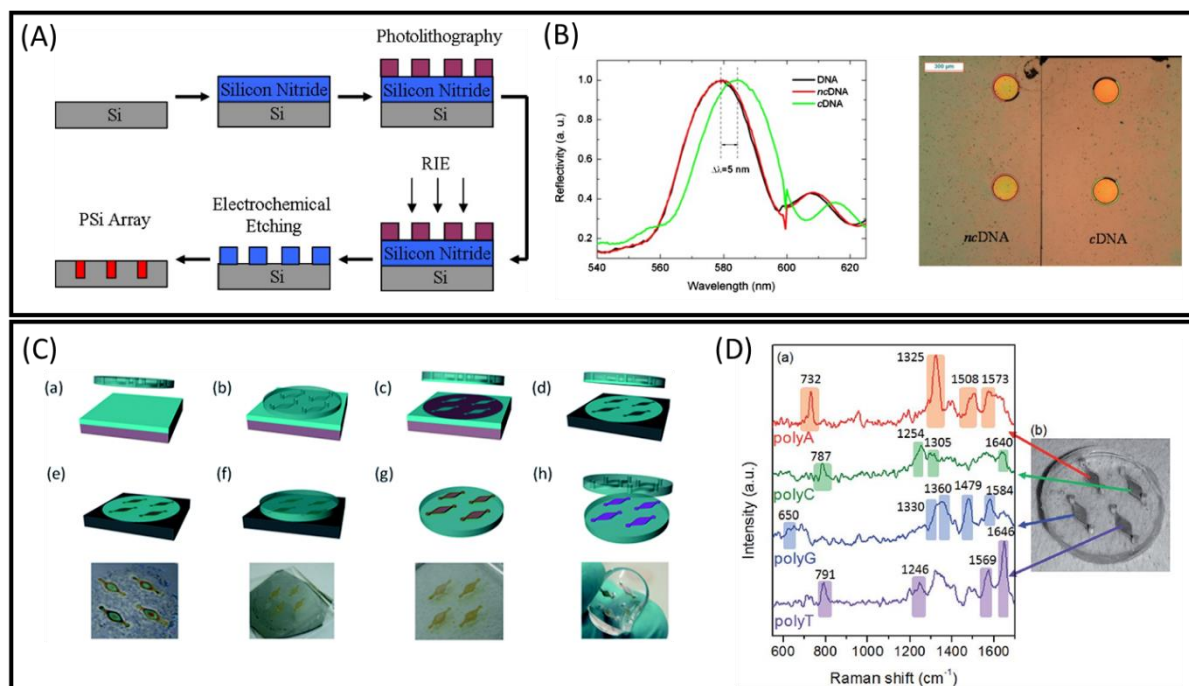


Figure 2.2.11. PSi microarray biosensing platforms, constructed by PSi pre-patterning. (A) Microarray construction by pre-patterning Si wafer via a photolithographic process. (B) Reflective-based detection of a complementary DNA hybridization, in parallel to a non-complementary control. Reprinted with permission from ref. ²⁷⁸ (Rea, I.; Lamberti, A.; Rendina, I.; Coppola, G.; Giofrè, M.; Iodice, M.; Casalino, M.; Tommasi, E. D.; Stefano, L. D. *Journal of Applied Physics* 2010, 107, 014513). Rights managed by AIP Publishing. (C) PSi patterning by PDMS masking. (a) PDMS precursor mixture is spread on a smooth surface and covered with a patterned PDMS cover (b); the latter is then removed (c) resulting in a stamp of the cover pattern on the silicon dice (d); (e) patterned PSi after HF anodization; (f) partially cross-linked PDMS is used (f) to transfer the PSi membranes to the PDMS substrate (g); (h) The PSi membranes are coated with silver nanoparticles and sealed with a PDMS, resulting in an optofluidic chip. (D) Multianalyte SERS-based detection. (a) SERS spectra of Polyadenine (polyA), polycytosine (polyC), polyguanine (polyG) and polythymine (polyT) in four different chambers. The oligonucleotides solutions are introduced into the four chambers. The SERS signal was recorded under 20X objective of the Raman microscope. The spectra were recorded at 514.5 nm after drying. (D) A picture of the four-chamber optofluidic chip. Reprinted with permission from ref. ²⁷⁹ (Novara, C.; Lamberti, A.; Chiadò, A.; Virga, A.; Rivolo, P.; Geobaldo, F.; Giorgis, F. *RSC Advances* 2016, 6, 21865-21870). Copyright © The Royal Society of Chemistry 2016.

The second level of microarray construction is at the chemical functionalization process. Gooding and co-workers ^{283, 284} have chemically patterned thermally hydrosilylated PSi rugate filters by microfabrication and surface chemistry. A desired array pattern was created by titanium deposition, followed by photolithography and wet etching. Two different click reactions were then carried out, before and after removal of the titanium layer, creating an array of different chemical functionalities inside and outside the array spots ²⁸⁴. In a follow up work, the use of the metal protection was eliminated and only a photoresist was utilized for the array patterning by photolithography. High throughput reflectivity measurements were successfully carried out in an array format, demonstrating enzymatic cleavage of gelatin substrate within the array spots, by subtilisin enzyme ²⁸³.

Another strategy for chemical microarray construction is contact pin-printing. Bright and co-workers have thoroughly investigated this approach for creating an array of chemical functionalities on PSi

surfaces, by printing organosilanes or hydrosilylating agents²⁸⁵⁻²⁸⁸. Printing was also utilized for dispensing capture probes at specific array positions and early work by Laurell and co-workers^{289, 290} has successfully demonstrated high-throughput fluorescence detection of labelled antibody or labelled-prostate specific antigens using a macroporous Si substrate. In recent years simultaneous fluorescent multi-target detection was realized by dispensing different probes for multiple targets on PSi substrates^{198, 209, 211}. Microarrays could be also fabricated during the chemical modification of a PSi surface, by masking via a photolithographic process. This approach was presented by Wang et al.²⁹¹, who created a DNA microarray on a polymer-modified PSi surface, masked with a photoresist in a desired pattern, demonstrating simultaneous two color fluorescent detection when two different probes were printed at specific spot positions. It should be noted that fluorescence detection dominates in microarray-integrated PSi sensors, while reflection-based detection is still in its infancy. This is attributed to the availability of well-established automated fluorescence imaging systems, while reflection-based detection was achieved by utilization of an XY automated stage for real-time reflectivity measurements from precise array positions²⁸³. Additionally, in recent years, work has been done for developing digital imaging of PSi arrays and correlating the reflectivity changes to the brightness variation of the digital image. This enables faster, simpler and high-throughput data acquisition²⁶⁷⁻²⁶⁹.

Besides microarray technology, multi-target detection can be also attained by alternative strategies. For example, Sailor and co-workers encoded a spectral barcode into PSi microparticles via a programmable electrochemical etching process, and utilized them for multiplex DNA detection²⁹². Krismastuti et al.²⁹³ have integrated their previously constructed FRET-based biosensor for MMPs detection²⁴⁹ with magnetic immunoparticles (nanoparticles functionalized with antibodies targeting different MMPs). MMPs captured by the immunoparticles were then introduced into a PSi microcavity, functionalized with a peptide substrate for enzymatic cleavage. The latter resulted in fluorescence signal based on a FRET mechanism, allowing to successfully distinguish between two different MMP targets in a buffer and a chronic wound fluid²⁹³.

Emerging Applications

Throughout this review, various applications have been described, which are also summarized in Table 2.2.1. These include medical diagnostics and disease monitoring using biosensors targeting pathological condition biomarkers^{27, 208, 247}, such as protein biomarkers for cancer²⁰⁹, hydatid disease²³³, inflammation and sepsis¹⁹ and wound infection and healing^{211, 249, 293}, as well as detection of medically-relevant antibodies²¹⁰. Numerous platforms for oligonucleotide detection have been designed, as summarized in Table 2.2.1, including miRNA detection^{203, 250}. Additionally, detection of clinically-relevant small molecules, such as insulin and glucose, was also realized^{28, 32, 195, 255}. A promising medical application of immense potential is the evaluation of antibiotic susceptibility. Extensive antibiotic use has led to an antimicrobial resistance crisis in the world²⁹⁴. Leonard et al. designed a Si micropillar structure for determination of the correct type and concentration of an antimicrobial agent effective

against infection. The microstructures were used to colonize *E. coli* as model bacteria and enable optical monitoring of the bacterial response to different concentrations of antibiotics using reflectance spectroscopy (named the PRISM method). The minimal inhibitory concentrations (MIC) could be determined in a label-free and rapid manner (3 h *versus* 8 h) compared to standard methods utilized in the clinic (Figure 2.2.12A and B) ²⁹⁵.

Si-based optical biosensors for applications relevant for the food industry include the detection of infectious microorganisms and various toxins ^{196, 197, 212, 219, 296}. The platforms were even applied in food industry process water ¹⁷⁷ and cereal samples ¹⁹⁸. Nevertheless, it should be noted that detection of

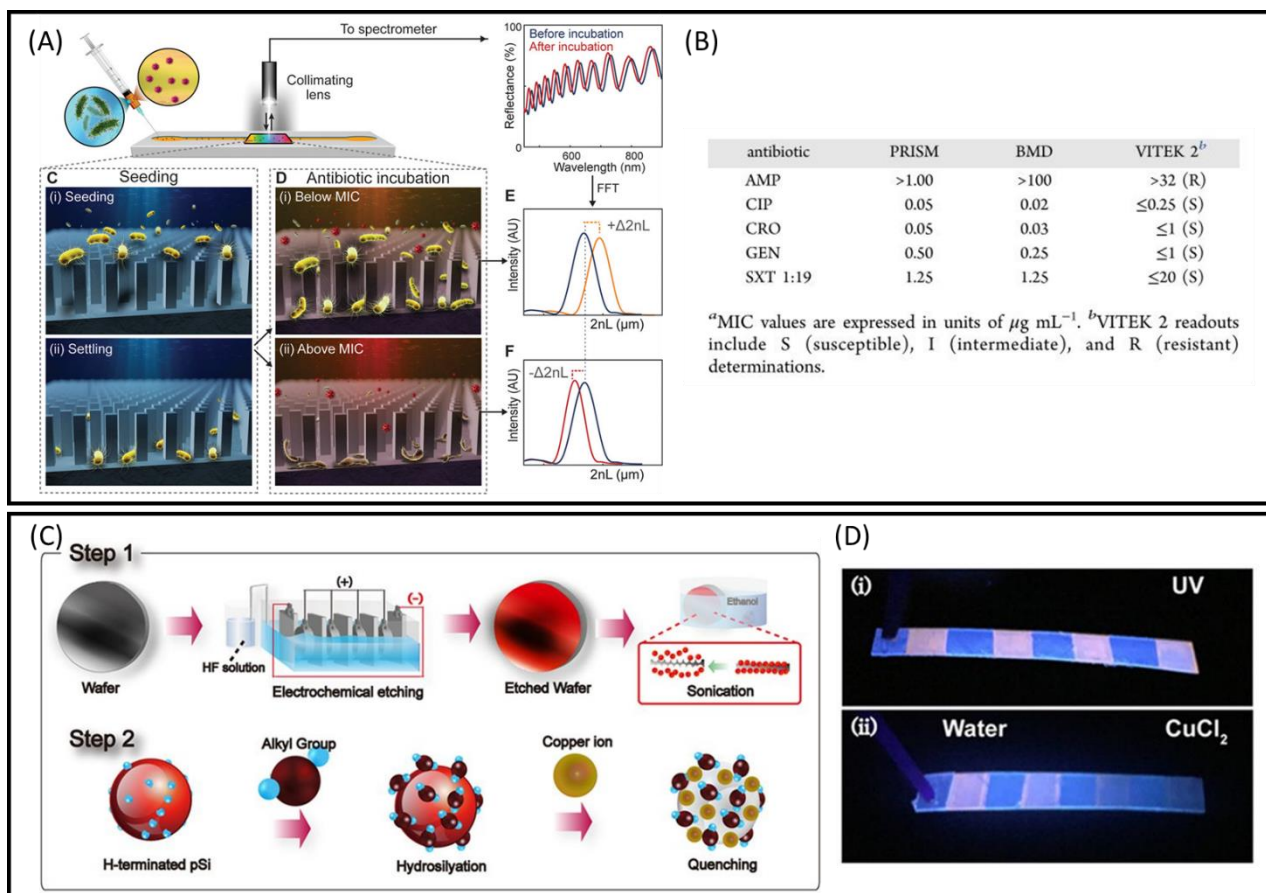


Figure 2.2.12. (A) Schematic illustration of PRISM assay for monitoring bacterial response to antimicrobial agents. Bacterial suspension or antibiotics in growth medium are injected into a microfluidic-integrated Si micropillar structure. At the first stage, bacteria are seeded on the Si microstructures (seeding), followed by antibiotic introduction and incubation. This leads to either increased bacterial proliferation at ineffective sub-inhibitory concentrations and an increased 2nL value or to growth hindrance and cell death above MIC and a decreased 2nL value. (B) MIC determination for *E. coli* K12 by PRISM and standard clinical methods (broth microdilution testing (BMR) and VITEK 2). Reprinted with permission from ref. ²⁹⁵ (Leonard, H.; Halachmi, S.; Ben-Dov, N.; Nativ, O.; Segal, E. *ACS Nano* 2017, 11, 6167-6177). Copyright (2017) American Chemical Society. (C) Schematic presenting the alkyl-terminated PSi nanoparticles for detection of copper ions. (D) The constructed portable detection stick. Top: presenting the orange-red fluorescence signal under UV excitation; bottom: fluorescence signal quenching in response to 10 mM CuCl₂ solution, dropped onto the two films on the right. Reprinted with permission from ref. ²⁵⁴ (Hwang, J.; Hwang, M. P.; Choi, M.; Seo, Y.; Jo, Y.; Son, J.; Hong, J.; Choi, J. *Scientific Reports* 2016, 6, 35565). (<http://creativecommons.org/licenses/by/4.0/>).

microorganisms is still limited to model bacteria, mainly *E. coli*. In terms of environmental monitoring, biosensors have been designed for detection of heavy metals^{192, 193, 297}. An example for PoC adaptation can be found in the work of Hwang et al. They integrated alkyl-terminated PSi nanoparticles for detection of copper ions based on PL quenching into two different detection kits: a 96-well paper kit and a portable detection stick (Figure 2.2.12C and D). Monitoring of copper ions in tap water was reported²⁵⁴. Other applications worth mentioning are the use of PSi membranes for optical monitoring of DNA translocation events for DNA sequencing applications, demonstrated by Yamazaki et al.²⁹⁸⁻³⁰¹, and the construction of lipid bilayer membranes on PSi substrates for monitoring membrane-associated processes or targets^{262, 302}.

Conclusions and Outlook

Following the research work of more than two decades, the basic technology of PSi-based optical biosensors is already established, including the structure, chemistry, and application in various fields. Thus, the work in the field has shifted in recent years towards improvement and extension of capabilities: sophisticated structures have and are continuing to be developed, the chemistry continues to be improved for higher stability and multiple functionalities and new capture probes are being integrated and studied. The challenge of acquiring clinically relevant sensitivity is gaining more attention and more research is dedicated to sensitivity enhancement and strategies for signal amplification. Moreover, the need for PoC devices has driven progress in this direction, as well.

Although PSi presents beneficial features compared to other planar photonic sensors, the sensitivity is not sufficient for all applications. Achieving a clinically relevant detection is possible using luminescent-based transduction approaches with PSi biosensors. However, these biosensors often require target, probe or structure labelling, utilization of a secondary labelled probe or addition of external components, resulting in complex biosensing platforms. For refractometric-based transduction with PSi biosensors, a label-free and direct target detection is feasible, which is highly desired for both benchtop and PoC devices. Nevertheless, the sensitivity of label-free PSi biosensors compared to luminescent-based biosensors is limited. Therefore, in recent years, the main focus has been to develop strategies to enhance the sensitivity and detection limit of these platforms using approaches ranging from tuning of the intrinsic structure, chemistry and capture probe features to modification of the experimental setup and data analysis procedures. Additionally, several efficient strategies for signal amplification have been demonstrated over the past three years. Yet, a robust and generic method for sensitivity enhancement that enables PSi optical biosensors to achieve the necessary detection limit for all desired application areas is still missing and studies in this path are expected to carry on.

An additional and necessary challenge to tackle is target detection within real samples. Although progress in the direction of in-vivo monitoring with a PSi platform has been recently demonstrated, examples of monitoring in complex biological fluids with PSi-based optical biosensors are still quite limited. Minimizing cross reactivity and non-specific binding and improving biosensor and signal

stability in complex fluids should continue to be studied in the future. Aptamers are promising capture probes for these purposes and are gaining significant popularity since their first integration in PSi biosensors in 2015. This trend is anticipated to continue, as aptamer technology is also advancing, and more aptamers are being selected for various targets.

Lastly, there is strong demand for PoC adaptation of biosensors in recent years and several steps in that direction have commenced for PSi optical biosensors. Methods for constructing microarrayed PSi biosensors is well-studied, which paves the way for miniaturization, multi-target detection and high-throughput analysis. Additionally, basic microfluidic and smartphone integration of PSi biosensors has been demonstrated. All these means illustrate the potential of developing PoC PSi-based optical biosensors, and in the future this topic is anticipated to sustain high attention.

3. Research Aims and Motivation

3.1 Research Aims

The main aim of this research is to characterize PSi-based optical biosensors for protein targets and their limiting factors and to rationally design methods for the enhancement of their performance, such as sensitivity and response time. As a model platform, PSi Fabry P erot thin films are functionalized with aptamers for specific capture of target proteins. We aim to investigate theoretically and experimentally mass-transfer phenomena and reaction kinetics in these biosensors and develop rule of thumbs for their optimization.

The specific aims of this research include:

- a. *Fabrication of PSi Fabry P erot thin films and conjugation with aptamers specific for target proteins.* Aptamer immobilization and functionality will be characterized, and their performance as capture probes on a PSi-based biosensor will be compared to conventional antibody capture probes.
- b. *Theoretical modelling of the governing phenomena of target capture by PSi-based biosensors.* Numerical simulations will be performed to investigate the effect of biosensor characteristics on the target capture rate.
- c. *Design and study of methods for performance enhancement of PSi-based biosensors.* These include mass transfer acceleration such as application of isotachopheresis technique for real-time on-chip protein preconcentration and microfluidic integration. 3D printing will be studied as a fabrication method of the latter.
- d. *Application for cancer biomarker detection.* The biosensor will be investigated in complex body fluids.

3.2 Motivation

PSi-based optical biosensors have been widely studied over the past two decades for various target molecules. Nevertheless, the promising advantages of the PSi nanostructure, which include its high surface area, low cost fabrication and unique optical properties, have not been translated to clinically-applicable platforms. Irrelevant sensitivity and response time have been often encountered and orders of magnitude differences between theoretical and experimental performance. This research aims to elucidate the limiting factors of PSi-based biosensors and develop a useful model, which could lead the rational design of these biosensors. Furthermore, development of simple methods for sensitivity enhancement of PSi-based biosensors, as well as their microfluidic integration, can raise their potential for clinical application at the point-of-care, while exploiting the advantages of the PSi nanostructure.

4. Experimental

4.1 Materials

Reagents and Buffers. Highly doped p-type Si wafers (boron doped, 0.90-1.0 m Ω -cm resistivity, <100>-oriented) were purchased from Sil'tronix Silicon Technologies. Ethanol absolute, toluene and isopropyl alcohol were supplied by Bio-Lab Ltd. Dimethyl sulfoxide (DMSO) was purchased from Carlo Erba Reagents. Alexa Fluor® 488 Succinimidyl Ester was purchased from ThermoFisher Scientific. Sylgard® 184 Silicon Elastomer kit (Polydimethylsiloxane, PDMS) was purchased from Dow Corning. Aqueous HF (48%), (3-aminopropyl)triethoxysilane (APTES), ethyldiisopropylamine (DIEA), glutaraldehyde 25% solution (GA), ethanolamine, *N*-(3-Dimethylaminopropyl)-*N*-ethylcarbodiimide hydrochloride (EDC), acetonitrile (ACN) succinic acid, succinic anhydride, sodium cyanoborohydride, sodium dodecyl sulfate (SDS), *N*-Succinimidyl 3-(2-pyridyldithio)propionate (SPDP), DL-Dithiothreitol (DTT), Bis(2-hydroxyethyl)amino-tris(hydroxymethyl)methane (Bis-Tris), *N*-[Tris(hydroxymethyl) methyl] glycine (Tricine), morpholinoethanesulfonic acid (MES), MES sodium salt, Tris base, *N* _{α} -benzoyl-L-arginine ethyl ester (BAEE) and buffer salts were supplied by Merck. Buffers were prepared with deionized water (18.2 M Ω cm, ddH₂O) and filtered prior to use. Buffers included 10 mM phosphate buffered saline (PBS) composed of 137 mM NaCl, 2.7 mM KCl, 10 mM Na₂HPO₄ and 2 mM KH₂PO₄ (pH 7.5), 0.5 M MES buffer prepared from 0.27 M MES and 0.23 M MES sodium salt (pH 6.1) and Tris buffer composed of 50 mM Tris base (pH 7.4).

Aptamers and Selection Buffers. Anti-his-tag aptamer 6H7 (5'- GCT ATG GGT GGT CTG GTT GGG ATT GGC CCC GGG AGC TGG C - 3') sequence was taken from U.S. patent 7329742³⁰³ and purchased with a 5'-amino modification or 5' thiol modification and 3' 6-FAM modification from Integrated DNA Technologies. Anti-his tag selection buffer (SB) was composed of 50 mM K₂HPO₄ and 150 mM NaCl (pH 7.4) and anti-his tag elution buffer was composed of 50 mM K₂HPO₄, 150 mM NaCl, and 1 M Imidazole (pH 7.4). Anti-AGR2 aptamer sequence (5'-TCT-CGG-ACG-CGT-GTG-GTC-GGG-TGG-GAG-TTG-TGG-GGG-GGG-GTG-GGA-GGG-TT-3') was obtained from Wu et al³⁰⁴ and was purchased with a 5'-amino modification or 5' thiol modification and 3' 6-FAM modification, or 5'-amino modification and 3'-Cy5 fluorescent dye modification from Integrated DNA Technologies. Anti-AGR2 aptamer SB was composed of 137 mM NaCl, 20 mM KCl, 10 mM Na₂HPO₄ and 2 mM KH₂PO₄ (pH 7.4). Anti-protein A aptamer, selected by Stoltenburg et al³⁰⁵, was used in truncated form PA#2/8[S1-58]: 5'- ATA CCA GCT TAT TCA ATT AGC AAC ATG AGG GGG ATA GAG GGG GTG GGT TCT CTC GGC T-3', and purchased with a 3'-amino-C6 modification. Its SB was composed of 20 mM Tris base, 100 mM NaCl, 5 mM KCl, 10 mM MgCl₂, and 1 mM CaCl₂. Table 4.1 summarizes the details of the utilized aptamers.

Table 4.1. Details of studied aptamers.

Aptamer	Sequence	Modification	Selection Buffer
Anti-his tag	5'- GCT ATG GGT GGT CTG GTT GGG ATT GGC CCC GGG AGC TGG C - 3'	5'-amino 5' thiol and 3' 6-FAM	50 mM K ₂ HPO ₄ and 150 mM NaCl (pH 7.4)
		5'-amino	
Anti-AGR2	5'-TCT-CGG-ACG-CGT-GTG- GTC-GGG-TGG-GAG-TTG- TGG-GGG-GGG-GTG-GGA- GGG-TT-3'	5' thiol and 3' 6-FAM 5'-amino and 3'-Cy5 fluorescent dye	137 mM NaCl, 20 mM KCl, 10 mM Na ₂ HPO ₄ and 2 mM KH ₂ PO ₄ (pH 7.4)
Anti-protein A	5'- ATA CCA GCT TAT TCA ATT AGC AAC ATG AGG GGG ATA GAG GGG GTG GGT TCT CTC GGC T-3'	3'-amino-C6	20 mM Tris base, 100 mM NaCl, 5 mM KCl, 10 mM MgCl ₂ , and 1 mM CaCl ₂

Proteins. Mouse anti-his monoclonal antibody (catalogue number MCA1396) was obtained from Enco. Streptavidin, biotinylated protein A and recombinant protein A from human serum were purchased from Merck. His-tagged protein domain 4 (AbnA-D4) and domain 2 (AbnA-D2) of extracellular endo-alpha-(1->5)-L-arabinanase 1 (from *Geobacillus stearothermophilus* T-6, expressed in *Escherichia coli*) were generously supplied by Prof. Yuval Shoham, Technion. 6xhis tyrosinase from *Bacillus megatherium* (recombinant, expressed in *Escherichia coli*) was generously supplied by Prof. Ayelet Fishman, Technion. AGR2 protein was purchased from MyBioSource Inc. Trypsin from porcine pancreas, Bovine Serum Albumin (BSA), and pancreatin from porcine pancreas (4x USP) were purchased from Merck. Rabbit Immunoglobulin G (IgG) was purchased from Jackson ImmunoResearch Labs Inc. *E. coli* K12 was generously supplied by Prof. Sima Yaron, Technion. *E. coli* was cultured in Luria broth (LB) medium (10 g L⁻¹ casein peptone, 10 g L⁻¹ NaCl, 5 g L⁻¹ yeast extract, all purchased from Merck).

4.2 Biosensor Construction

The studied biosensors include several PSi-based aptasensors and a representative immunosensor, as detailed in Table 4.2. All biosensors employ a similar PSi nanostructure as the optical transducer and capture probe molecules (aptamer or antibody) are immobilized onto the surface.

Table 4.2. Properties of the studied capture probe and target protein pairs.

Aptamer/Antibody	Target	Molecular Weight (kDa)	Literature K_D
Anti-his tag aptamer	AbnA-D2	60	
Anti-his tag aptamer	AbnA-D4	24	$\sim 4.6 \mu\text{M}^{306}$
Anti-his tag aptamer	Tyrosinase	35	
Anti-his tag antibody	Tyrosinase	35	$\sim 10 \text{ nM}^{307}$
Anti-AGR2 aptamer	AGR2	22	$\sim 13 \text{ nM}^{304}$
Anti-protein A aptamer	Protein A	45	$\sim 0.522 \mu\text{M}^{305}$

4.2.1 PSi Fabrication

PSi Fabry-Pérot thin films are fabricated from a highly doped p-type crystalline Si wafers, using a two-step anodic electrochemical etching process¹⁶. This process is required to remove a sacrificial layer formed at the initial etching process, in which the pores are partly blocked. A Si wafer with exposed area of 1.33 cm^2 is contacted on its back side with a strip of aluminum foil and mounted in a Teflon etching cell and a Platinum wire is used as the counter electrode. **Caution:** HF is a highly corrosive liquid thus should be handled with extreme care! First, a sacrificial layer is etched at a constant current density of 300 mA cm^{-2} or 375 mA cm^{-2} for 30 s in a 3:1 (v/v) solution of aqueous HF (48%) and ethanol, respectively. The resulting sacrificial porous layer is removed by exposure to 0.1 M NaOH for 2 min, followed by a 1 min exposure to a solution of 1:3:1 (v/v) HF, ethanol and ddH₂O, respectively. Next, a second etching is conducted, at the same etching conditions as above. After each step, the silicon surface is thoroughly rinsed with ethanol and dried under nitrogen stream. The freshly etched PSi is thermally oxidized in a tube furnace (Thermo Scientific, Lindberg/Blue M™ 1200 °C Split-Hinge) at 800 °C for 1 h in ambient air, resulting in an oxidized PSi scaffold¹⁵⁹.

For ITP experiments, prior to the etching process, the Si wafers are cleaned in an ultrasonic bath (Elmasonic S 10, Elma Schmidbauer GmbH) in isopropyl alcohol for 15 min, rinsed with ethanol and dried under nitrogen stream. The freshly etched PSi is then thermally oxidized in a tube furnace (thermolyne) at 1000 °C for 46 h under constant oxygen flow of 0.5 L min^{-1} . These harsh oxidation conditions are employed to ensure an insulating oxide layer, capable to withstand high voltage values³⁰.

4.2.2 PSi Nanostructure Characterization

Scanning electron microscopy (SEM). The oxidized PSi nanostructure, pore diameter and film thickness are characterized by high-resolution scanning electron microscopy (Carl Zeiss Ultra Plus), at an accelerating voltage of 1 keV.

Spectroscopic liquid infiltration method (SLIM). SLIM is a non-destructive method used to determine the thickness and porosity of the porous layer. The interferometric reflectance spectrum of the porous film is measured in air and while immersed in ethanol and acetone, having refractive indices of 1.359 and 1.357, respectively. The refractive index of the SiO₂ portion is assumed to be 1.455. The optical parameters from the reflectance spectra are then fitted to a Bruggeman effective medium approximation, yielding the thickness and the porosity of the porous layer.

4.2.3 Surface Chemistry

4.2.3.1 Capture Probes Immobilization

Aptamer Immobilization. Amino-terminated aptamers are conjugated to the oxidized PSi films by carbodiimide coupling chemistry. In general, this includes amino-silanization with APTES, followed by surface carboxylation and activation with EDC; the latter replaced by the amine-terminated aptamer. Two slightly different protocols were used for the different aptamers, differing in the solvents and materials in the amino-silanization and carboxylation processes. For the anti-AGR2 aptamer immobilization, the oxidized PSi film is amino-silanized by incubation in 1% v/v APTES and 1% v/v DIEA in ddH₂O solution for 1 h, followed by washing with ddH₂O and ethanol and drying under a nitrogen stream. Subsequently, the amino-activated PSi samples are annealed at 100 °C for 15 min. Next, carboxylation is achieved by incubation in a solution of succinic anhydride (10 mg mL⁻¹) and 2% v/v DIEA in ACN for 3 h, followed by extensive rinsing with ACN and ddH₂O and drying under a nitrogen stream.

The anti-his-tag aptamer, 6H7, and the anti-protein A aptamer are immobilized by the method described by Urmann et al.^{26, 29}. The oxidized PSi films are reacted with a solution of 42 mM APTES in toluene for 1 h, followed by a thorough rinsing with toluene, ethanol and acetone and drying under a nitrogen stream. A similar annealing step is then performed, as described above. The APTES-modified surface is then incubated in a solution of 100 mg of succinic acid in 4.7 mL of DMSO and 300 μL of 0.1 M NaHCO₃ (pH 9.4) for 30 min, followed by washing with DMSO and ddH₂O and dried under a stream of nitrogen.

Subsequently, for both systems, the carboxylated samples are reacted with EDC (10 mg mL⁻¹) in the corresponding selection buffer (SB) for 1 h, followed by introduction of 50 μM anti-AGR2 aptamer or 75 μM anti-his tag or anti-protein A aptamers in SB, and incubation for 1 h. The samples are then washed with Tris buffer (50 mM, pH 7.4) to deactivate remaining reactive EDC groups on the surface. Finally, the aptamer-functionalized PSi is exposed to boiling ddH₂O for 2 min, and gently dried under a nitrogen stream, to unfold any secondary structures of the aptamer prior to further use.

Experimental

For experiments in microchannels, the carboxylated PSi is integrated in the microfluidic device and the remaining functionalization steps are carried out inside the microchannels. The microchannels are first washed with EtOH (50 %v/v) in ddH₂O for 5 min to remove any air bubbles inside the channels, followed by subsequent washing with SB buffer at 100 $\mu\text{L min}^{-1}$ for 10 min. Next, EDC in SB buffer (10 mg mL⁻¹) is introduced at 30 $\mu\text{L min}^{-1}$ for 30 min, followed by introduction of aptamer (75 μM , 250 μL) at 30 $\mu\text{L min}^{-1}$. The aptamer is then allowed to react with the surface for 1 h without flow. Subsequently, the microchannel is washed with Tris buffer at 30 $\mu\text{L min}^{-1}$ for 15 min to deactivate any remaining reactive EDC groups on the surface.

Antibodies Immobilization. Two antibody immobilization techniques are studied, either direct immobilization via covalent binding, leading to a random antibody orientation, or conjugation via the biotin-streptavidin linkage to result in an oriented antibody configuration^{177, 308}. For random antibody immobilization, the PSiO₂ surface is incubated with a solution of 1% APTES and 1% EDIPA in water for 30 min. After removing the solution, the sample is rinsed with water and ethanol, and then dried under a nitrogen stream. Subsequently, the film is incubated in a 2% aqueous GA solution for 30 min, washed with water and dried under a stream of nitrogen. In the next step, the antibody solution (50 μL ; 100 $\mu\text{g mL}^{-1}$ in PBS) is introduced and incubated for 1 h at room temperature and then stored overnight at 8 °C. Next, unbound antibodies are removed by thorough washing with PBS and residual reactive groups are capped by incubation of the porous film with 0.1 M aqueous solution of ethanolamine for 30 min.

For oriented antibody immobilization, silanization and modification with GA are performed as described above, followed by incubation with 50 mM sodium cyanoborohydride in HEPES for 30 min to stabilize the Schiff base formed during reaction of the aldehyde groups with the amine groups²⁴². After washing with HEPES, the PSiO₂ film is placed in a humidity chamber and a freshly-prepared streptavidin solution (100 μL ; 100 $\mu\text{g mL}^{-1}$ in PBS) is introduced onto the surface and incubated for 1 h. A thorough rinsing with PBS is performed before a repetition of the reduction in sodium cyanoborohydride for the stabilization of the Schiff base, formed during streptavidin fixation. Next, the streptavidin-modified surface is blocked with ethanolamine, followed by incubation with biotinylated protein A (100 μL ; 100 $\mu\text{g mL}^{-1}$ in PBS) for 1 h in a humidity chamber. Finally, the sample is rinsed with PBS and incubated with the antibody (50 μL ; 100 $\mu\text{g mL}^{-1}$ in PBS; humidity chamber) for 1 h at room temperature and then overnight at 8 °C. On the next day, the film is rinsed and stored in PBS buffer (at 8 °C) for up to one day prior to biosensing experiments.

4.2.3.2 Surface Chemistry Characterization

Infrared Spectroscopy. Chemical modification steps are verified using attenuated total reflectance Fourier transform infrared (ATR-FTIR) spectroscopy. Spectra are recorded using a Thermo Fisher 6700 FTIR instrument equipped with a Smart iTR diamond ATR device (USA). Background and all sample

Experimental

spectra are measured in dry air, utilizing an IR source and a DTGS KBr detector. Number of scans is set to 256, at a resolution of 4. The samples are dried under a nitrogen stream before each measurement.

Chemistry characterization with confocal laser scanning microscopy: Cy5-labelled aptamer is immobilized onto the PSi, followed by scanning with a confocal laser scanning microscope (LSM 700, Carl Zeiss, Inc.), linked to a Zeiss inverted microscope equipped with a Zeiss X63 oil immersion objective. PSi photoluminescence and Cy5-labelled aptamers are excited with laser lines of 405 nm and 639 nm, respectively. For three-dimensional image projection of the porous structure, z-scans in 0.4 μm increments over a depth of $\sim 12 \mu\text{m}$ are taken and projected with a standard Carl Zeiss software (ZEN 2009). Further image analysis is performed by Imaris Bitplane scientific software.

4.2.3.3 Surface Density Determination

Aptamers. Quantification of the immobilized aptamer concentration is carried out by the method described by Hu et al ⁴³, for the anti-AGR2 and anti-his tag aptasensors. We used aptamers with a thiol and FAM6 modification which are diluted in TE buffer (10 mM Tris and 1 mM EDTA, pH 8.0), supplemented with 30 mM DTT. Prior to use, the aptamer is cleaned in NAP-5 column (GE healthcare), in HEPES buffer (0.05M HEPES, pH 7.5) to remove the DTT reducing agent. After amino-silanization of the oxidized PSi films, the samples are reacted with SPDP (6.5 mM in ethanol) for 30 min, followed by washings with IPA and ddH₂O, three times. 50 μM anti-AGR2 or 75 μM 6H7 aptamers in HEPES buffer are then introduced to the samples and incubated for 1 h, followed by extensive washing with HEPES, to remove physisorbed aptamer molecules. As a control, oxidized PSi is similarly functionalized with SPDP, but without aptamer. The surface is washed until no fluorescence signal is detected in the collected washing solution, compared to the control.

For the anti-AGR2 aptamer, the aptamer-functionalized PSi is incubated with DTT solution (250 μL ; 25 mM in HEPES, pH 7.5) for 30 min, resulting in immediate aptamer cleavage from the surface, by disulfide bond reduction. The cleaved aptamer solution is collected and the absorbance is measured at 495 nm using a plate reader (Thermo Scientific Varioskan), as described by Hu et al ⁴³. For the anti-his tag aptamer, the aptamer cleavage from the surface is slower, attributed to the different amino-silanization procedure. Thus, the aptamer functionalized surface is incubated with reducing solution for 24 h, followed by solution collection and replacement with a new reducing solution. This process is repeated until no fluorescence signal is observed in the collected solution (compared to the control). The fluorescence of the collected solutions is analyzed by a plate reader at excitation and emission wavelength values of 490 nm and 525 nm, respectively, enabling more sensitive determination of the slower cleavage process. The measured absorbance or fluorescence values are correlated to the respective aptamer concentrations using a calibration curve, which is constructed using known concentrations of FAM6-labeled aptamer (in 25 mM DTT in HEPES buffer).

Antibodies. a FITC-labelled IgG is immobilized in a random or oriented-configurations within the PSiO₂ film, as described above. As a control, PSiO₂ films are chemically activated by the full chemistry

Experimental

procedure, but without antibody application. After immobilization, the samples are extensively washed with PBS and sodium acetate buffer (0.1 M, pH 4.5) to remove any unbound IgG molecules from the surface. The latter is confirmed by monitoring the fluorescence signal (excitation and emission wavelength values of 490 nm and 525 nm, respectively using a Thermo Scientific Varioskan Flash) of the washing solutions until no signal is measured, in comparison to the controls. Then, 250 μL of pepsin solution (100 $\mu\text{g mL}^{-1}$ pepsin in sodium acetate buffer) is introduced onto the immunosensor and incubated for 24 h at 37 °C for proteolytic digestion. After 24 h, the solution is collected and replaced by a fresh pepsin solution for additional cleavage. The concentration of the IgG in the collected solution is determined by fluorescence measurements at excitation and emission wavelength values of 490 nm and 525 nm, respectively (Thermo Scientific Varioskan Flash). The measured fluorescence values are correlated to the respective IgG concentrations using a calibration curve, which is constructed using known concentrations of FITC-labelled IgG. For the calibration curve preparation, FITC-labelled-IgG is diluted in sodium acetate buffer, containing also biotinylated protein A and streptavidin, in the relevant concentrations applied for the immobilization chemistry procedure. Then, pepsin is added to a final concentration of 100 $\mu\text{g mL}^{-1}$, and the calibration curve samples are incubated for 24 h at 37 °C, followed by fluorescence analysis.

4.3 Microfluidics

4.3.1 3D-Printed Microfluidics

Design and Fabrication. The microfluidic device is designed in SolidWorks software (Dassault Systèmes) and printed using 3D Systems Projet MJP 2500 Plus multijet printer. Polyacrylate-based photopolymer material (VisiJet M2R-CL, 3D Systems) and hydroxylated wax (VisiJet M2 Sup, 3D Systems) are used as the printing and support materials, respectively. After printing, the devices are subjected to several post processing steps, as previously described^{40, 309}. Briefly, after the devices are cooled down, they are placed in a heat steam bath (EasyClean unit, 3D Systems) at 65 °C for 30 min and are subsequently immersed in hot biological oil bath (EasyClean unit, 3D Systems) at 65 °C for 30 min, to remove the support material. Next, hot oil is introduced into the channels using a syringe to remove any residues of support material. Finally, the devices are sonicated at 60 °C for 30 min in deionized water with detergent (Fairy Ultra Plus, Procter and Gamble) in an ultrasonic bath (Bandelin electronic), followed by wash with 70% EtOH.

Integration. Prior to bonding the 3D-printed device to the PSi film, the devices are first gently polished with a standard grid paper (1000 grit), washed with water and soap, and flattened at 60 °C by applying a pressure of ~ 38 kPa for 1 h. Next, UV curable adhesive (Norland Optical Adhesive 72, Norland Products Inc.) (50 μL) is spread on a transfer wafer with a K hand coater no. 2 (Printcoat Instruments) and the printed device is placed on top of the adhesive layer two times for the glue transfer. Finally, the device is carefully placed on top of carboxylated PSi films, followed by UV curing at 365 nm (1.5 mW cm^{-2}) for 30 min (VL-6.LC UV lamp 365/254 nm 6 W, Vilber Lourmat).

Experimental

Characterization. The 3D-printed microfluidic devices, integrated with the PSi, are characterized by several methods. A standard food color solution is introduced into the microchannels to visualize possible leakage. The integrated devices are imaged with an upright optical microscope Olympus BX51 (Olympus). Cross-sections of the integrated devices are characterized by Carl Zeiss Ultra Plus HRSEM, at an accelerating voltage of 1 keV. The cross sectioned samples are prepared by embedding the devices in epoxy (EpoFix resin, Struers), which is refilled several times under vacuum (1 torr) to remove any air, followed by curing at room temperature for 48 h. The cured epoxy block is sectioned using a IsoMet™ low speed saw (Buehler) and polished in EcoMet™ 3 variable speed grinder-polisher (Buehler) with sandpaper with increasing grit, as well as an Alumina Suspension (50 nm Neutral). Finally, the cross-sectioned samples are sputtered with carbon.

4.3.2 PDMS Microfluidics

PDMS microchannels are fabricated based on an SU8 template or a 3D-printed polyacrylate template. The former is constructed by standard lithography at Stanford Microfluidic Foundry (Stanford University, Stanford, CA, <http://www.stanford.edu/group/foundry/>)³¹⁰. Using the template, the microfluidic channels are fabricated in-house from PDMS at 10:1 ratio of polymer and cross-linker, respectively, followed by curing at 100 °C for 3 h. The PDMS microchannels are attached to the SiO₂ chip (containing both planar and porous SiO₂ regions), by treating the inner surface of the PDMS with corona for 40 s, using a laboratory corona treater (BD-20V Electro-Technic Products), followed by baking at 90 °C for 4 h or at 100 °C for 3 h^{30,42}.

4.4 Protein Targets

60 kDa and 24 kDa his-tagged proteins from the Arabinanase family, named abnA-D2 and AbnA-D4, respectively, and a 35 kDa his-tagged tyrosinase from *B. megatherium* are used as targets for the anti-his tag 6H7 aptamer-functionalized PSi²⁶. The his-tagged tyrosinase is also detected by an anti-his tag antibody-functionalized PSi. The 45 kDa recombinant protein A from *S. aureus* is used as a target for the anti-protein A aptamer²⁹ and the 22 kDa AGR2 protein is detected by the anti-AGR2 aptamer functionalized PSi. The proteins are summarized in Table 4.2.

Protein Production and Purification. AbnA-D2 and AbnA-D4 his-tagged proteins are produced and purified using the following method. *E. coli* BL21 cells, transformed with the target protein gene, are grown overnight at 37 °C on LB plates with appropriate antibiotic. The cells are transferred to a Terrific Broth (TB) medium for overnight growth in a shaker (230 rpm) at 37 °C. The cells are then cooled on ice for 15 min, harvested by centrifugation, and re-suspended in binding buffer (20 mM imidazole, 0.5 M NaCl, and 20 mM phosphate buffer, pH 7.4). Subsequently, the cells are disrupted by two passages through an Avestin Emulsiflex C3 Homogenizer, 1500 psi (Avestin, Ottawa, Canada) at room temperature, and centrifuged at 7000 rpm for 30 min. The supernatant is then heated at ~50 °C for 30 min and centrifuged again.

Experimental

The his-tagged proteins are purified by fast protein liquid chromatography (FPLC) using the ÄKTA Avant-25 chromatography system (GE Healthcare Life Sciences) equipped with HisTrap column (1- or 5-ml column volume, GE Healthcare Life Sciences). The protein is eluted with a 10 CV gradient of elution buffer that contained 0.5 M imidazole, 0.5 M NaCl, and 20 mM phosphate buffer (pH 7.4). A similar protein without a his-tag (AbnA-D2, without his tag, named D2N) is purified via gel filtration using a Superdex 200 26/60 column, ÄKTA Avant (GE Healthcare Life Sciences), running at 2.5 ml/min with 50 mM Tris-HCl buffer pH 7.0, 100 mM NaCl and 0.02% sodium azide. Injected samples volumes are ~14 ml (~5% column volume).

Pancreatin. For experiments with simulated pancreatic juice, pancreatin is utilized. It is diluted according to its trypsin activity to provide 100 *p*-toluene-sulfonyl-L-arginine methyl ester units per mL³¹¹. The trypsin activity of 0.45 µm filtered pancreatin in SB is determined by a standard BAEE assay³¹² and diluted accordingly. The total protein amount within this sample is determined with NanoDrop instrument (NanoDrop 2000 spectrophotometer, Thermo Scientific)

Bacteria Lysates Preparation. *E. coli* K12 is cultivated in LB medium overnight under continuous shaking at 37 °C. The culture is spun down in a standard lab centrifuge (2-16P, Sigma Laboratory Centrifuges, Sigma-Aldrich) at 4500 rpm for 10 min, and the supernatant is replaced with the desired buffer. This step is repeated twice. Subsequently, the culture is ultrasonicated on ice in a Vibra cell VCX 750 instrument (Sonics & Materials Inc.) for 2 min, with 30 s pulses and 30 s pauses in between. The temperature and the amplitude are set to 4 °C and 40%, respectively. Cell debris are removed by ultracentrifugation at 4 °C for 30 min at 12000 g (1-15K, Sigma Laboratory Centrifuges, Sigma-Aldrich), and the supernatant is analyzed for protein content in NanoDrop instrument (NanoDrop 2000 spectrophotometer, Thermo Scientific), assuming 1 ABS=1 mg mL⁻¹.

Protein Labelling. The AbnA-D4 protein and bacteria lysates are fluorescently labelled with Alexa Fluor® 488 succinimidyl ester. The protein or lysate samples are mixed with the dye at a ratio of 1:5 (molar ratio for the protein and weight ratio for the lysate) in NaHCO₃ buffer for 1 hr. Then the labelled proteins are separated from the free dye by PD SpinTrap G-25 (GE Healthcare Life Sciences) and eluted with PBS buffer. All concentrations are determined with NanoDrop instrument (NanoDrop 2000 spectrophotometer, Thermo Scientific). After addition of 10% glycerol, the labelled samples are aliquoted and stored at -20 °C until further use.

AGR2 protein is fluorescently-labeled with Atto-647N succinimidyl ester. The protein buffer is replaced with 5 mM PBS using PD SpinTrap G-25. The protein is mixed with the dye at a ratio of 1:2 in 5 mM PBS and the labelled proteins are separated from the free dye as described above.

SDS-PAGE. Proteins and complex samples, such as bacteria lysates, are analyzed with a standard SDS-PAGE. The analysis is performed on a discontinuous buffer system³¹³, using 15% separating gel and 4% stacking gel. 30 µL of samples are mixed with 10 µL sample buffer (4x) and heated for 10 min at 95 °C. The gel is stained with 0.25% Coomassie brilliant blue (R-250) in 50% ethanol and 10% acetic acid and destained in 20:10:70 (v/v/v) methanol:acetic acid:water.

Time-Resolved Mass Transfer Visualization. Infiltration of a fluorescently-labelled AGR2 protein into the aptasensor is monitored in real time by confocal laser scanning microscopy. The scanning is conducted with a LSM 510 confocal laser-scanning microscope (Carl Zeiss, Inc.), linked to a Zeiss upright microscope equipped with a Zeiss X63 oil immersion objective. PSi photoluminescence and Atto-647N-labelled AGR2 are excited with laser lines of 458 nm and 633 nm, respectively. For three-dimensional image projection of the porous structure, z-scans in 0.73 μm increments over a depth of $\sim 15 \mu\text{m}$ are taken, every 30 s, and projected with a standard Carl Zeiss software (ZEN 2010). Initially, the photoluminescence and AGR2 fluorescence signals are scanned within the aptasensor with 10 μL of SB buffer for 10 min. Then, a 1 μM solution of Atto-647N-labelled AGR2 in SB (40 μL) is introduced and the photoluminescence and AGR2 fluorescence are measured continuously for additional 50 min. A relatively low AGR2 concentration is used for the measurements to obtain a time-resolved visualization of the protein infiltration before signal saturation is reached. Image analysis is performed by Imaris Bitplane scientific software.

4.5 Biosensing

4.5.1 Optical Setup

General. Reflective interferometric Fourier transform spectroscopy (RIFTS) method is utilized for real-time monitoring of changes occurring within the porous nanostructure by detection of variations in the average refractive index of the porous layer^{17, 18, 26}. The aptamer or antibody functionalized PSi sample is mounted in a custom-made Plexiglas cell, which is fixed during the experiments to ensure that the reflectivity is measured at the same spot throughout the experiment. Interferometric reflectance spectra are collected with a charge-coupled device (CCD) spectrometer (Ocean Optics, USB 4000) fitted with an objective lens coupled to a bifurcated fiber-optic cable. A tungsten light source is focused onto the center of the sample with a spot size of approximately 1 mm^2 . Illumination and reflectivity detection are performed perpendicular to the surface. Reflectivity spectra are collected in real time in a wavelength range of 450-900 nm and analyzed by applying fast Fourier transformation (FFT), as previously described by Massad-Ivanir et al.¹⁷². The latter results in a single peak, which position along the x-axis equals the effective optical thickness (EOT) of the porous layer and is the product of average refractive index and the thickness of the porous layer.

ITP Assay. For ITP-based experiments, the reflectance spectra and fluorescence signal are monitored concurrently. Thus, a customized Zeiss upright microscope equipped with an Ocean Optics charge-coupled device (CCD) USB 4000 spectrometer, is utilized. A two-port adapter is used to selectively transmit the light either to the microscope camera (Axio Cam MRc, Zeiss) or to the collimator, coupled to a fiber optic. An additional two-port adapter was used to switch between light from a halogen source (halogen100 illuminator, Zeiss) and X-Cite® 120Q excitation light source (Excelitas Technologies). The PSiO₂-microfluidic device is fixed to the microscope stage, under the objective. For the reflectance spectra measurements, the PSiO₂ region of the microchannel is illuminated with light from a halogen

Experimental

source, focused through an A-Plan objective (10x magnification, 0.25 NA, Zeiss). The size of the illumination spot is controlled by the microscope iris and adjusted to the microchannel width of 350 μm . For the fluorescence imaging, the illumination is switched to a light coming from X-Cite® 120Q excitation light source. The imaging is conducted with the camera, at a constant exposure time of 100 ms, concurrently to the reflectance measurements.

Microfluidics. The microfluidic-integrated P*Si* is fixed on a motorized linear translation stage (Thorlabs, Inc.), allowing to monitor different spots along a single microchannel in each experiment. A syringe pump (Fusion 200, Chemyx) is used to control the flow rate. The 3D-printed microfluidic device is connected to tubes through a Dolomite 4-way microfluidic connector and a 4 mm top interface (The Dolomite Center Ltd.). Female-to-male Luer Assy and flangeless fittings (IDEX Health and Science LLC) are used to connect the tubes to a syringe. The spectral acquisition and the stage movement are controlled with a LabView software (National Instruments). The spectra were acquired at an integration time of 30 ms and with a scan average of 160.

4.5.2 Experimental Procedure

General. For the anti-his tag biosensor, the surface is first washed with elution buffer for 30 min to unfold the aptamer. Then and for all biosensing systems, the P*Si* biosensor is incubated with the baseline buffer, corresponding selection buffer for the aptasensors, PBS for the immunosensor or 2:1 LE:TE (leading electrolyte: terminating electrolyte) for ITP-based control experiments, for at least 30 min and until a stable baseline is acquired. Next, the target protein, diluted in the baseline buffer, is introduced with a pipette (50 to 100 μL), and allowed to incubate for 1 h or until a steady state signal. Subsequently, the biosensor is extensively washed with the baseline buffer (10 mL). For the anti-his tag aptasensor, the surface can be regenerated by incubation with elution buffer for 30 min, followed by wash in SB for 30 min. Throughout the experiment, the reflectivity spectra are recorded every 15 s, while during buffer exchange and rinsing steps, reflectivity measurements are shortly paused. In some experiments, mixing is applied by manual pipetting of the protein solution over the aptasensor, followed by an incubation without mixing.

ITP Assay. For the ITP-based biosensing experiment, a similar protocol as reported by Vilensky *et al.*⁴² is utilized. The buffer composition depends on the protein target and is detailed in Table 4.3. The microchannel's east reservoir and the microchannel itself are filled with LE buffer using a vacuum pump and an EOT baseline is obtained. The measuring site is maintained constant throughout the whole experiment. Then, the microchannel's west reservoir is rinsed with deionized water several times and filled with the protein sample, diluted in TE. To initiate ITP, a constant voltage of 350 V is applied across the channel, using a high-voltage power supply (model PS375, Stanford Research Systems, Inc.). The location of the ITP peak is visualized by the fluorescence microscope camera and its location is controlled by applying a pressure driven counter-flow, produced by an external water column connected to the east reservoir. For the counter-flow ITP mode, once the ITP focusing zone arrived to the P*SiO*₂

Experimental

measuring site, it is kept stationary by applying a positive pressure to counter electromigration with the water column, for as long as the ITP plug is stable or for a maximum voltage time of 30 min. During this time, the reflectance spectra are recorded and analyzed in real-time, concurrently to monitoring the position of the ITP plug with the microscope camera. The reflectivity acquisition is not performed in fixed time intervals, but upon stabilization of the ITP plug on top of the biosensor. Next, the voltage is turned off and the ITP plug was pushed back to the west reservoir by negative pressure. The channel is then rinsed thoroughly with LE buffer using a vacuum pump, to remove any unbound proteins. For all the baseline and rinsing steps, the reflectance spectra are recorded every 15 s.

Table 4.3. Leading electrolyte (LE) and terminating electrolyte (TE) buffer compositions used in ITP Assays.

ITP	Aptasensor	LE	TE
Anionic	Anti-AGR2	200/150/100mM	20/10 mM BisTris/Tricine
	Anti-his tag	BisTris/NaCl/HCl	
Cationic	Anti-AGR2	200/100 mM HEPES/KOH	20/10 mM HEPES/Pyridine
Cationic	Anti-AGR2	200/100 mM HEPES/KOH	20/10 mM HEPES/BisTris
Cationic	Anti-AGR2	200/100 mM MOPS/KOH	20/10 mM HEPES/BisTris
Cationic	Anti-AGR2	200/100 mM MES/KOH	20/10 mM HEPES/BisTris
Cationic	Anti-AGR2	200/100/80 mM HEPES/KOH/HCl (pH 6.4)	20/10/7 mM HEPES/BisTris/HCl (pH 5.9)
Cationic	Anti-AGR2	200/100 mM HEPES/KOH (pH 7.4)	20/10/7 mM HEPES/BisTris/HCl (pH 5.9)

For the pass-over ITP mode, the reflectance spectra are recorded continuously, every 1 s, and analyzed in real-time. As the ITP plug electromigrates above the measuring site, the voltage is turned off and the channel was washed with LE buffer.

For the control experiments of ITP without protein, the experiment is conducted as for the pass-over ITP mode. To prevent arrival of TE buffer to the measuring site, a total voltage time of 15-20 min is measured, before the voltage is turned off and the channel is rinsed with LE buffer.

4.5.3 Data Analysis

Reflectivity data are presented as relative Δ EOT, defined as

Experimental

$$\frac{\Delta EOT_t}{EOT_0} = \frac{EOT_t - EOT_0}{EOT_0}$$

where EOT_0 is the averaged EOT signal obtained during baseline establishment.

The signal-to-noise ratio (SNR) values are calculated as the ratio of the relative EOT signal to the standard deviation of the baseline in SB prior to protein introduction. Limit of detection (LOD) is calculated as the protein concentration for which the optical signal equals $3 \cdot \sigma$, where, σ is the standard deviation between relative EOT values, measured during baseline establishment. Non-linear regression of obtained data is performed with GraphPad Prism software utilizing the model for specific binding with a hill slope, according to:

$$Y = \frac{B_{\max} \cdot X^h}{(K_D^h \cdot X^h)}$$

B_{\max} is the interpolated concentration at which the maximum biosensor response is reached and K_D is the apparent dissociation constant, which is the target concentration needed to reach the half-maximum biosensing signal. h is the Hill coefficient, which gives information about the apparent stoichiometry of the binding interaction^{314, 315}.

All data is presented as the mean of $n \geq 3$ with standard deviation of the mean. For statistical evaluation, unpaired t-test is performed with two-tailed distribution and unequal variance. P values below 0.05 are considered for significant difference between two groups.

4.5.4 Numerical Simulations

Numerical simulations of governing equations are performed using finite differences. Initially, the spatial derivatives are discretised using a second-order central difference approximation with uniform grid spacing, leading to a series of coupled ordinary differential equations. Then the resulting set of ordinary differential equations are integrated forward in time using Matlab's routine ode15s (Matlab R2018sb, MathWorks, Inc.).

5. Results

This section concludes five papers of which four were already published in peer-reviewed journals and the fifth was submitted to *ACS Measurement Science Au*:

5.1 **S. Arshavsky-Graham***, K. Urmann *, R. Salama, N. Massad-Ivanir, J.G. Walter, T. Scheper, and E. Segal, “Aptamers vs. Antibodies as Capture Probes in Optical Porous Silicon Biosensors.” *Analyst* 145, 4991-5003 (2020) (*Equal contribution).

5.2 **S. Arshavsky-Graham**, E. Boyko, R. Salama, and E. Segal. “Mass Transfer Limitations of Porous Silicon-Based Biosensors for Protein Detection.” *ACS Sensors* 5 (10), 3058-3069 (2020).

5.3 **S. Arshavsky-Graham**, N. Massad-Ivanir, F. Paratore, T. Scheper, M. Bercovici, and E. Segal. “On Chip Protein Pre-Concentration for Enhancing the Sensitivity of Porous Silicon Biosensors.” *ACS Sensors* 2 (12), 1767-1773 (2017).

5.4 **S. Arshavsky-Graham**, A. Enders, S. Ackerman, J. Bahnemann and E. Segal. “3D-Printed Microfluidics Integrated with Optical Nanostructured Porous Aptasensors for Protein Detection.” *Microchimica Acta* 188, 67 (2021).

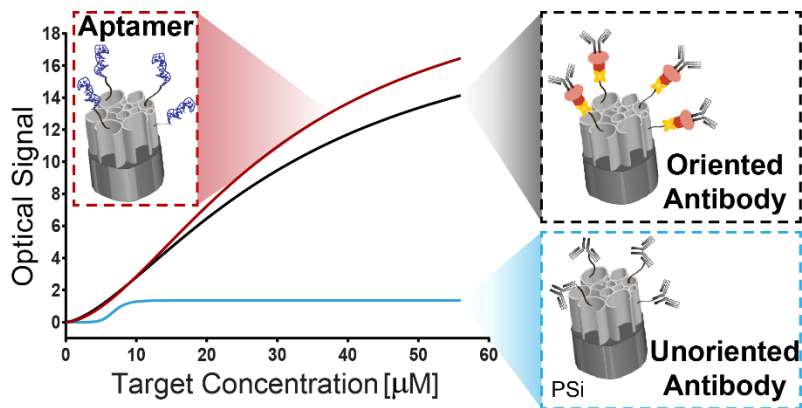
5.5 **S. Arshavsky-Graham**, N. Massad-Ivanir, T. Scheper, and E. Segal. “Porous Silicon-Based Aptasensors: Towards Cancer Protein Biomarker Detection.” Submitted to *ACS Measurement Science Au*.

1.1 Aptamers vs. Antibodies as Capture Probes in Optical Porous Silicon Biosensors

Sofia Arshavsky-Graham*, Katharina Urmann*, Rachel Salama, Naama Massad-Ivanir,
Johanna G. Walter, Thomas Scheper, and Ester Segal

*Equal Contribution

Analyst 145, 4991-5003 (2020)



Respective Table of Contents Image

Abstract

Over the past decade aptamers have emerged as a promising class of bioreceptors for biosensing applications with significant advantages over conventional antibodies. However, experimental studies comparing aptasensors and immunosensors, under equivalent conditions, are limited and the results are inconclusive, in terms of benefits and limitations of each bioreceptor type. In the present work, the performance of aptamer and antibody bioreceptors for the detection of a his-tagged protein, used as a model target, is compared. The bioreceptors are immobilized onto a nanostructured porous silicon (PSi) thin film, used as the optical transducer, and the target protein is detected in a real-time and label-free format by reflective interferometric Fourier transform spectroscopy. For the antibodies, random-oriented immobilization onto the PSi nanostructure results in a poor biosensing performance. Contrary, Fc-oriented immobilization of the antibodies shows a similar biosensing performance to that exhibited by the aptamer-based biosensor, in terms of binding rate, dynamic detection range, limit of detection and selectivity. The aptasensor outperforms in terms of its reusability and storability, while the immunosensor could not be regenerated for subsequent experiments.

Introduction

Over the past 20 years, numerous publications and review articles have elaborated on the advantageous properties of aptamers as capture probes for biosensing^{28, 214, 316-320}. Aptamers have been termed “chemical antibodies” and predicted to replace antibodies in the near future^{318, 319, 321}. The possibility of selecting high affinity aptamers via SELEX (Systematic Evolution of Ligands by Exponential Enrichment) for a wide range of targets (including small molecules, proteins and whole cells), their small size, their high stability and outstanding performance in complex media have provoked the extensive research effort in their integration into various biosensing schemes^{215, 318, 322, 323}. However, antibodies, which have been used as capture probes for biosensor design for over 70 years, are still considered as the “gold standard”^{324, 325}.

While some studies present results of different bioassays using antibodies or aptamers as capture probes towards the same target analyte³²⁶⁻³²⁸, only few papers have experimentally compared between aptasensors and immunosensors under equivalent conditions^{28, 317, 320, 329}, and there is a lack of consensus in the field. Similar biosensing performance, in terms of selectivity and sensitivity, was demonstrated for quartz crystal-based biosensors for IgE detection³²⁰ and nanogap impedance-based biosensor for thrombin detection³²⁹. However, the former also showed an extended linear detection range, reusability and greater stability for the aptasensor, in comparison to the immunosensor. In contrast, an aptasensor for detection of a prostate specific antigen showed a comparable limit of detection (LOD), selectivity, and reusability, to an immunosensor³¹⁷. Both biosensors were based on nano-modified screen-printed electrodes, in three electrochemical detection techniques³¹⁷. Recent reviews have also highlighted that antibody- and aptamer-based biosensors are comparable in their performance (i.e., sensitivity and selectivity), but emphasize that their immobilization onto the

Results

transducer and the detection mode have a more significant impact on the resulting sensitivity and selectivity^{316, 328}. On the other hand, a superior biosensing performance of an aptamer over an antibody was observed in a porous silicon (PSi)-based optical biosensor for detection of insulin²⁸. The aptamer outperformed the antibody in response time and LOD. However, it should be noted that in this study the antibody was covalently immobilized to the surface, resulting in a random orientation that limits its performance. This variability in the studies emphasizes the need for additional research in the field, specifically studying the behavior of these capture probes on similar transducers under comparable conditions and characterizing the limitation and strength of each bioreceptor.

The present study aims to compare between aptamer and antibody capture probes, which are immobilized on the same nanostructured PSi-based transducer, for the detection of a specific target analyte and to investigate the performance and benefits of each receptor. PSi-based optical biosensors in which antibodies have been employed as capture probes were extensively studied over the past 20 years^{164, 165, 330-332}. Many of these biosensors employ reflective interferometric Fourier transform spectroscopy (RIFTS) for real-time and label-free monitoring of changes in the refractive index or reflection intensity for various relevant targets, such as DNA⁴², protein^{19, 24, 28} and bacteria^{33, 177}. The first application of aptamers as bioreceptors in PSi-based optical biosensors has been demonstrated in 2015²⁶, showing promising biosensing results, which evoked a great interest. Since then, the potential of different PSi-based aptasensors has been increasingly studied and successful detection of various molecules was demonstrated^{19, 27-33}.

In our previous work^{26, 29, 30, 33}, we have successfully constructed and characterized several PSi aptasensors for various targets. In the present work, we focus on the direct comparison of the performance of PSi-based aptasensor and immunosensor for detection of the same target protein. To the best of our knowledge, this is the first comparison of aptamers to random- or oriented-immobilized antibodies as capture probes. An oxidized PSi (PSiO₂) nanostructure (Fabry-Pérot thin film), used as the optical transducer, was functionalized with a well-characterized his-tag binding aptamer (6H7)^{30, 303, 306, 333, 334} or an anti his-tag antibody for the detection of a model his-tagged protein, 6x-his tyrosinase from *Bacillus megatherium* (35.3 kDa). Successful conjugation of the capture probes onto the nanostructured PSiO₂ was confirmed by attenuated total reflectance Fourier transform infrared (ATR-FTIR) spectroscopy, and surface density was quantified by cleavage of the bioreceptors from the surface and subsequent fluorescence analysis. The binding of protein target molecules to the immobilized bioreceptors was monitored in real time by RIFTS and the biosensing performance, in terms of binding rate, dynamic range and sensitivity, was compared for the aptamer and the antibody-conjugated biosensors. The latter was further studied in a random or Fc-oriented conjugation to the PSiO₂ surface. Focus was laid especially on comparing the selectivity and the performance of both bioreceptors in the detection of the target protein within complex biological samples, utilizing bacteria lysates as a model, as well as the recyclability of the biosensors.

Experimental

Materials

Si wafers (p-type, boron doped, 0.00095 $\Omega \cdot \text{cm}$ resistivity, <100>-oriented) were purchased from Siltronic Corp (France). Aqueous hydrofluoric acid (HF) (48%) and ethanol absolute were purchased from Merck (Germany). Dimethyl sulfoxide (DMSO) and Toluene were purchased from Carlo Erba Reagents and Bio-Lab Ltd, respectively. (3-aminopropyl)triethoxysilane (APTES), ethyldiisopropylamine (EDIPA), glutaraldehyde 25% solution (GA), ethanolamine, N-(3-Dimethylaminopropyl)-N-ethylcarbodiimide hydrochloride (EDC), succinic acid, sodium cyanoborohydride, sodium dodecyl sulfate (SDS), N-Succinimidyl 3-(2-pyridyldithio)propionate (SPDP), DL-Dithiothreitol (DTT), isopropyl alcohol (IPA) and buffer salts were supplied by MERCK (Israel). Buffers were prepared with deionized water (18.2 M Ω cm) and filtered prior to use. Anti-his-tag aptamer 6H7 (5'- GCT ATG GGT GGT CTG GTT GGG ATT GGC CCC GGG AGC TGG C - 3') sequence was taken from U.S. patent 7329742³⁰³. 6H7 was selected in 50 mM K₂HPO₄, 150 mM NaCl, 0.05% Tween 20 (this buffer is subsequently abbreviated as SB-T). To prevent possible blocking of the amino-modified surfaces, Tween 20 was omitted during immobilization and washing steps, as well as renaturation of the aptamer (and this composition is termed as the selection buffer, SB). Additional buffers were phosphate buffered saline (PBS, 1 mM phosphate buffer, 154 mM NaCl, pH 7.4) and 4-(2-hydroxyethyl)-1-piperazineethanesulfonic acid (HEPES), which were prepared according to standard recipes. Aptamers were purchased with a 5'-amino modification or a 5' thiol modification and 3' 6-FAM modification from Integrated DNA Technologies (USA). Mouse anti-his monoclonal antibody (catalogue number MCA1396) was obtained from Enco (Israel). This antibody was validated by the manufacturer for ELISA, immunoprecipitation and western blotting applications. Mouse anti-his monoclonal antibodies are commonly used for these applications, as well as for biological detection and purification assays³³⁵⁻³⁴⁰. Streptavidin and biotinylated protein A were purchased from Sigma-Aldrich Chemicals. Proteins for biosensing experiments included trypsin from porcine pancreas (Sigma-Aldrich Chemicals) and 6xhis tyrosinase from *Bacillus megatherium* (recombinant, expressed in *Escherichia coli*), generously supplied by Prof. Ayelet Fishman, Technion. As an additional negative control and for simulation of complex media, *Escherichia coli* (*E. coli*) lysates were used. For this purpose, *E. coli* strain JL-102 was cultured in Luria broth (LB) medium (10 g L⁻¹ casein peptone, 10 g L⁻¹ NaCl, 5 g L⁻¹ yeast extract, all purchased from Sigma-Aldrich Chemicals).

Preparation of Bacteria Suspensions and Bacteria Lysates

A flask with 20 mL sterile LB medium was inoculated with 100 μL of a frozen culture of *E. coli* JL-102 (free of plasmids) and cultured overnight under shaking at 37°C. The resulting culture was used for biosensing experiments to mimic a biologically relevant complex fluid.

A volume of 2 mL of the bacteria culture was spun down in a standard lab centrifuge and the supernatant was replaced by 1 mL PBS selection buffer. Following the re-suspension, the culture was ultrasonicated

Results

at 4°C (Labsonic M, Sartorius Stedim Biotech, Germany). The resulting suspension was centrifuged again to remove cell debris and the supernatant was transferred to a fresh tube and further used as the bacteria lysate.

Preparation of Oxidized PSi (PSiO₂)

Silicon was anodized at a constant current density of 375 mA cm⁻² for 30 s in a 3:1 (v/v) solution of aqueous HF (48%) and ethanol. The anodization setup is similar to previous work²⁶. Briefly, a Si wafer with exposed area of 1.33 cm² was contacted on its back side with a strip of aluminium foil and mounted in a Teflon etching cell and a Platinum wire was used as the counter electrode. The freshly-etched PSi film was rinsed with ethanol several times and subsequently dried under nitrogen gas flow. The resulting PSi sample was then thermally oxidized at 800°C for 1 h in ambient air in a tube furnace (Thermo Scientific, Lindberg/Blue M™ 1200°C Split-Hinge, USA).

Characterization of PSiO₂ Films

Specific properties (i.e. thickness and porosity) of the fabricated PSiO₂ layers were characterized by several techniques: HRSEM (high resolution scanning electron microscopy), and SLIM (spectroscopic liquid infiltration method) methods, as previously described³³⁰.

Immobilization of Aptamers onto PSiO₂

The anti-his-tag aptamer (6H7) was conjugated onto the surface of the PSiO₂ film by EDC-mediated covalent attachment²⁶. PSiO₂ sample was first incubated with a 2% (v/v) APTES solution in toluene for 1 h. After thorough rinsing with toluene, ethanol, and acetone and drying under a nitrogen stream, the amine-modified surface was immersed in a freshly prepared solution of 100 mg of succinic acid in 4.7 mL of DMSO and 300 µL of 0.1 M NaHCO₃ (pH 9.4) for 30 min. After rinsing with DMSO and purified water and drying under a nitrogen stream, EDC solution at a concentration of 52 mM (in SB) was introduced and allowed to react for 1 h. Successively, the activated PSiO₂ surface was incubated with the aptamer solution (75 µM, 50 µL in SB) for 1 h, followed by thorough washing with 50 mM Tris buffer (pH 7.4) for 20 min, to block remaining active sites. Finally, the biosensor was exposed to boiling deionized water for 2 min and gently dried under a nitrogen stream to unfold any aptamer secondary structures. The resulting aptasensors were stored dried in a desiccator for up to 4 days post immobilization. Prior to biosensing experiments, the aptasensors were incubated in a solution of 1 M imidazole in SB (pH 7.4), followed by incubation in SB for 30 min, in order to allow the immobilized aptamer to properly fold.

Immobilization of Antibodies onto PSiO₂

The anti-his antibody was either directly immobilized via covalent binding, leading to a random antibody orientation, or conjugated via the biotin-streptavidin linkage to result in an oriented antibody configuration^{177, 308}.

Results

For random antibody immobilization, the PSiO_2 surface was incubated with a solution of 1% APTES and 1% EDIPA in water for 30 min. After removing the solution, the sample was rinsed with water and ethanol, then dried under a nitrogen stream. Subsequently, the film was incubated in a 2% aqueous GA solution for 30 min, washed with water and dried under a stream of nitrogen. In the next step, 50 μL of the antibody solution ($100 \mu\text{g mL}^{-1}$ in PBS) were introduced and incubated for 1 h at room temperature and then stored overnight at 8°C . Next, unbound antibodies were removed by washing with PBS and residual reactive groups were capped by incubation of the porous film with 0.1 M aqueous solution of ethanolamine for 30 min.

For oriented antibody immobilization, silanization and modification with GA were performed as described above, followed by incubation with 50 mM sodium cyanoborohydride in HEPES for 30 min, in order to stabilize the Schiff base formed during reaction of the aldehyde groups with the amine groups²⁴². After washing with HEPES, the PSiO_2 film was placed in a humidity chamber and 100 μL of a freshly-prepared streptavidin solution ($100 \mu\text{g mL}^{-1}$ in PBS) were introduced onto the surface and incubated for 1 h. A thorough rinsing with PBS was performed before a repetition of the reduction in sodium cyanoborohydride for the stabilization of the Schiff base, formed during streptavidin fixation. Next, the streptavidin-modified surface was blocked with ethanolamine, followed by incubation with biotinylated protein A (100 μL ; $100 \mu\text{g mL}^{-1}$ in PBS) for 1 h in a humidity chamber. Finally, the sample was rinsed with PBS and incubated with the antibody (50 μL ; $100 \mu\text{g mL}^{-1}$ in PBS; humidity chamber) for 1 h at room temperature and then overnight at 8°C . On the next day, the film was rinsed and stored in PBS buffer (at 8°C) for up to one day prior to biosensing experiments.

Infrared Spectroscopy

Chemical modification steps were verified using attenuated total reflectance Fourier transform infrared (ATR-FTIR) spectroscopy. Spectra were recorded using a Thermo Fisher 6700 FTIR instrument equipped with a Smart iTR diamond ATR device (USA). Background and all sample spectra were measured in dry air, utilizing an IR source and a DTGS KBr detector. Number of scans was set to 256, at a resolution of 4. The samples were dried under a nitrogen stream before each measurement.

Bioreceptors Surface Density

For the antibody quantification, a FITC-labelled IgG was immobilized in a random or oriented-configurations within the PSiO_2 film, as described above. As a control, PSiO_2 films were chemically activated by the full chemistry procedure, but without antibody application. After immobilization, the samples were extensively washed with PBS and sodium acetate buffer (0.1 M, pH 4.5) to remove any unbound IgG molecules from the surface. The latter was confirmed by monitoring the fluorescence signal (excitation and emission wavelength values of 490 nm and 525 nm, respectively, using a Thermo Scientific Varioskan Flash) of the washing solutions until no signal was measured, in comparison to the controls. Then, 250 μL of pepsin solution ($100 \mu\text{g mL}^{-1}$ pepsin in sodium acetate buffer) was introduced

Results

onto the immunosensor and incubated for 24 h at 37 °C for proteolytic digestion. After 24 h, the solution was collected and replaced by a fresh pepsin solution for additional cleavage. The concentration of the IgG in the collected solution was determined by fluorescence measurements at excitation and emission wavelength values of 490 nm and 525 nm, respectively (Thermo Scientific Varioskan Flash). The measured fluorescence values were correlated to the respective IgG concentrations using a calibration curve, which was constructed using known concentrations of FITC-labelled IgG. For the calibration curve preparation, FITC-labelled-IgG was diluted in sodium acetate buffer, containing also biotinylated protein A and streptavidin, in the relevant concentrations applied for the immobilization chemistry procedure. Then, pepsin was added to a final concentration of 100 $\mu\text{g mL}^{-1}$, and the calibration curve samples were incubated for 24 h at 37 °C, followed by fluorescence analysis.

For the aptamer, we adapted the method described by Hu et al.⁴³. Following silanization with APTES (as described above), the amine-terminated surfaces were reacted with 6.5 mM N-Succinimidyl 3-(2-pyridyldithio)propionate (SPDP) in ethanol for 30 min and washed thoroughly with IPA and ddH₂O. Subsequently, 75 μM thiol modified and FAM6-labeled aptamer in HEPES buffer (0.05M HEPES, pH 7.5) was introduced and incubated for 1 h. The functionalized PSiO₂ was extensively rinsed with HEPES, to remove physisorbed aptamer molecules, until no fluorescence signal was observed for the collected washing solution (compared to a control, i.e., PSiO₂ which was similarly functionalized with SPDP, but without aptamer). It should be noted that the aptamer stock was diluted in TE buffer (10 mM Tris and 1 mM EDTA, pH 8.0) with 30 mM DTT and prior to its use, the aptamer was cleaned in NAP-5 column (GE healthcare) to remove the DTT reducing agent and replace the buffer with HEPES. The resulting aptamer-functionalized PSiO₂ was incubated with DTT solution (250 μL of 25 mM DTT in HEPES buffer, pH 7.5) for 24 h. The solution was collected and replaced by a new reducing solution and the fluorescence signal of the collected solution was measured using a plate reader at excitation and emission wavelength values of 490 nm and 525 nm, respectively. The cleavage process was repeated until no fluorescence signal was observed for the collected solution (compared to the control). The measured fluorescence values were correlated to the respective aptamer concentrations using a calibration curve, which was constructed using known concentrations of FAM6-labeled aptamer. For the calibration curve preparation, FAM6-labeled aptamer was dissolved in 25 mM DTT in HEPES buffer and the fluorescence of these solutions was measured.

The respective bioreceptor surface density values were calculated by dividing the number of bioreceptor moles by the porous surface area. The latter was measured in a previous study³⁴¹ by nitrogen adsorption isotherms and application of BET (Brunauer-Emmett-Teller) model for a similar PSiO₂ nanostructure, see Supporting Information.

Measurement of Interferometric Reflectance Spectra

Interferometric reflectance spectra of the samples were collected as was previously described²⁶. Briefly, interferometric reflectance spectra of the PSiO₂ films were collected using an Ocean Optics charge-

Results

coupled device (CCD) USB 4000 spectrometer coupled with a microscope objective lens by a bifurcated fiber-optic cable (USA). A tungsten light source was focused onto the surface of the sample with a spot size of approximately 1–2 mm². The reflectivity spectrum of the PSiO₂ film is comprised of a series of Fabry–Pérot interference fringes, where the maxima of these fringes are governed by the following equation:

$$m \cdot \lambda = 2 \cdot n \cdot L \quad 5.1.1$$

where, m is an integer, λ is the light wavelength, n is the average refractive index of the porous film and L refers to its thickness. The term $2nL$ represents the effective optical thickness (EOT), where a change in the latter indicates a change in the refractive index.

Reflectivity data were recorded every 30 s in a wavelength range of 400–1000 nm and spectral acquisition time 100 ms. The spectra were analyzed by applying fast Fourier transformation (FFT), which leads to a single peak for each spectrum, whose position (corresponds to the value of $2nL$, i.e., the EOT) was monitored. In this work, data are presented as relative ΔEOT , defined as:

$$\frac{\Delta EOT}{EOT_0} = \left(\frac{EOT_{readout} - EOT_{at\ baseline}}{EOT_{at\ baseline}} \right) \quad 5.1.2$$

The term EOT_0 refers to the averaged EOT obtained during baseline measurement at the beginning of each optical experiment.

Protein Biosensing

Biosensing experiments were carried out in a cell configuration. The biofunctionalized PSiO₂ samples were mounted into a custom-made Plexiglas cell. An O-ring inside the cell seals off the exposed area and an in- and outlet allow introducing solutions for subsequent reaction steps. At first, spectra were recorded until a stable baseline was achieved in either PBS or SB, depending on the respective capture probe. Functionalized PSiO₂ films were then incubated with 100 μ L of the protein solution for 1 h (without flow). Tyrosinase was diluted in PBS or SB for the antibody or aptamer functionalized PSiO₂, respectively. The complex samples, including trypsin, lysate and spiked lysate, were prepared in SB-T for the aptamer-based biosensor to reduce nonspecific binding, according to previous studies²⁶. After removal of the protein solution, the sample was rinsed and incubated for 30 min with PBS/SB. Each aptamer-based biosensor was utilized for multiple biosensing experiments, through surface regeneration, as previously described²⁶. The protein was eluted with 1 M imidazole in SB (pH 7.4) for 30 min, followed by the regeneration of aptamers in SB for 30 min. Antibody-conjugated biosensors were used only once.

Regeneration of the oriented antibody biofunctionalized PSiO₂ was studied by exposure of the surface to different solutions for 30 min, as summarized in Table 5.1.1.

Table 5.1.1. Compositions of regeneration solution for the oriented antibody-based biosensor.

Solution Composition
1M imidazole in SB (pH 7.4)
10 mM glycine/HCl pH 2.5 ³⁴²
100 mM glycine/HCl pH 2.5 ³⁴³
100 mM HCl pH 2.0 ^{344, 345}
200 mM glycine/HCl pH 2.3 + 1% DMSO ³⁴⁶
1% SDS in ddH ₂ O ³⁴⁷

Statistical Analysis and Data Regression

For statistical analysis, unpaired t-tests were performed, with two tail distribution and unequal variance. Resulting two-tailed P values below 0.05 were required to consider the compared groups as significantly different from each other.

Non-linear regression of obtained data was performed with GraphPad Prism software utilizing the model for specific binding with hill slope. The following equation was used for modelling:

$$Y = \frac{B_{max} \cdot X^h}{(K_d^h + X^h)} \quad 5.1.3$$

Herein, B_{max} is the interpolated concentration at which the maximum biosensor response is reached. K_D (also known as the apparent dissociation constant) is the target concentration needed to reach the half-maximum biosensing signal. The parameter h is the Hill coefficient, which gives information about the stoichiometry of the occurring binding ^{314, 315}.

Results and Discussion

Immobilization of Bioreceptor Molecules onto PSiO₂

The porous nanostructures were fabricated by anodization and subsequent thermal oxidation to yield PSiO₂ films with a thickness of 5500 nm and characteristic interconnected cylindrical pores with a typical diameter between 35 and 65 nm (see Table S5.1.1, Supporting Information, for a summary of the PSi nanostructure characteristics). Figure 5.1.1a (upper panel) schematically illustrates the immobilization of the amino-modified 6H7 aptamer onto the PSiO₂ film. The latter was first amino-silanized using APTES dissolved in toluene (2%) and subsequent carbodiimide coupling was employed to conjugate the amine-terminated 6H7 aptamers, as we previously reported ^{26, 30}. Successful aptamer conjugation was confirmed by ATR-FTIR spectroscopy. The spectra following each of the modification steps are presented in Figure 5.1.1b (upper panel). After the amino-silanization, a small peak at 1639 cm⁻¹ is observed, attributed to the bending of the primary amines ^{302, 348}. Following the carboxylation of the surface with succinic acid, the spectrum depicts two strong peaks at 1556 and 1632 cm⁻¹ attributed

Results

to amide II and amide I bonds, respectively, and a peak at 1400 cm^{-1} is assigned to the carboxylic acid groups^{302, 348}. After EDC introduction, the carboxylic acid peak is observed to diminish, suggesting successful activation. Following aptamer conjugation, multiple characteristic DNA bands appear between $1780\text{-}1530\text{ cm}^{-1}$ and $1550\text{-}1250\text{ cm}^{-1}$, attributed to the carbonyl groups and vibrations of saccharides³⁴⁹, similarly to our previous report²⁶.

For the antibody immobilization, two different strategies were used (as schematically illustrated in Figure 5.1.1a, middle and bottom panels): (1) straightforward conjugation in random orientation via an amine-group within the antibody to an aldehyde-modified surface (this immobilization route will be referred as ‘random conjugation’), and (2) oriented conjugation of the antibody Fc-region to a protein A-modified surface. For both immobilization routes, the PSiO_2 was first silanized using an aqueous APTES solution (1%). It should be noted that this step was slightly modified in comparison to the aptamer immobilization route to allow an optimal immunosensor performance (see Figure S5.1.1, Supporting Information). Next, the amine-activated PSiO_2 was reacted with glutaraldehyde. For the random immobilization route, the aldehyde-activated PSiO_2 surface was immediately incubated with the antibody solution. Thus, the antibody is conjugated through its primary amines to available aldehyde groups on the PSiO_2 surface. Following a thorough rinsing, residual amines were blocked by incubation with ethanolamine. For the oriented antibody conjugation, protein A layer was formed on a glutaraldehyde-reacted PSiO_2 surface through streptavidin-biotin linkage, followed by antibody conjugation to the protein A through the Fc-region, as shown in Figure 5.1.1a (bottom panel). For both conjugation routes, the conditions were optimized in previous studies^{164, 177} to minimize steric hindrance and crowding effects.

Figure 5.1.1b, middle and bottom panels, present the ATR-FTIR spectra of the corresponding chemical modification steps for the random and oriented conjugation routes, respectively. For both, following amino-silanization, a peak at 1637 cm^{-1} appears, attributed to the bending of primary amines. Upon glutaraldehyde functionalization, peaks are observed at $1720, 1637, 1560, 1445$ and 1401 cm^{-1} , which are ascribed to the (C=O) stretching vibrations, the imine bond, and (C-H) and (C-C) bond vibrations, respectively³⁴⁹. For the random conjugation route, antibody immobilization results in peaks at 1643 and 1555 cm^{-1} , which are attributed to the bending of amide I and amide II, respectively³⁴⁸. For the oriented conjugation route, similar peaks are observed for streptavidin, protein A and antibody immobilization, with greater absorbance respective to the preceding step, suggesting successful modification of the PSiO_2 film.

It should be emphasized that while chemical route for the construction of the immunosensor is well established, it involves multiple steps and thus the immobilization procedure is >3 times longer (~ 4 times for the oriented antibody) in comparison to that of the aptasensor. Moreover, there are significant differences in the cost of the biosensors, which results from both the price of the bioreceptors and the reagents used for their immobilization. Thus, the immunosensors cost is >5 times higher than that of the aptasensors.

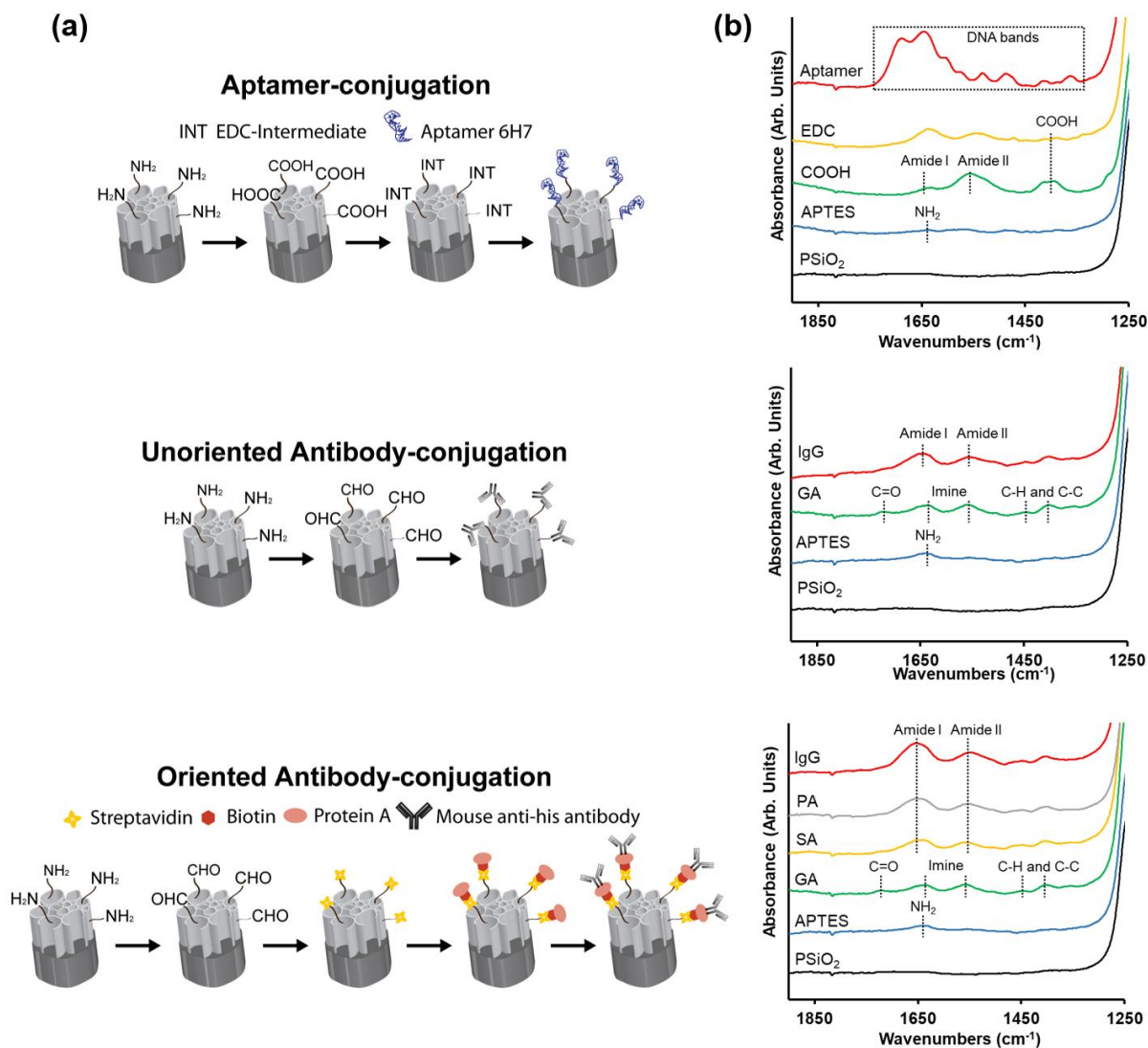


Figure 5.1.1. (a) Schematic illustration of the coupling steps followed for the immobilization of aptamers (upper panel) and antibodies (via random and oriented conjugation, middle and bottom panels, respectively) to PSiO_2 . (b) ATR-FTIR spectra of PSiO_2 upon the different chemical modification steps throughout aptamer and antibody immobilization on the surface.

Bioreceptors Surface Density

Surface density has a major impact on the performance of biosensors. It determines the bioreceptor orientation, the uniformity of the sensing layer and the steric crowding within the sensing layer^{350, 351}. It also influences the target capture kinetics and the overall sensitivity of the biosensor^{21, 352}. Thus, the bioreceptor surface coverage for the aptasensor and the immunosensor was determined by quantifying the amount of immobilized aptamer and antibody, respectively, onto the PSiO_2 surface. In both cases, the immobilized bioreceptors were cleaved from the respective biosensor and their concentration in the solution was measured, as illustrated in Figure 5.1.2. For the immunosensor, a fluorescently labelled antibody (in which the fluorophore is conjugated to the amine groups) was immobilized in a random or oriented configuration; after which, the functionalized surface was subjected to proteolytic digestion (using pepsin), as depicted in Figure 5.1.2a. The pepsin cleaves the IgG into $(\text{F}(\text{ab}')_2)$ molecules, and

Results

the Fc fragment (as well as other proteins) into lower molecular weight fragments³⁵³. Thus, following digestion, these cleaved fragments are released to the solution and quantified (by fluorescence measurements). For the immobilized aptamer, a fluorescently-labelled and thiol-modified aptamer was conjugated to the surface using SPDP linker, as illustrated in Figure 5.1.2b. This allows to cleave the immobilized fluorescent aptamer by disulfide bond reduction and subsequent quantification of the solution fluorescence, as described by Hu et al⁴³.

Figure 5.1.2c presents the accumulated moles of antibody and aptamer cleaved from the surface vs. time. For the aptamer, the cleavage is fast and the accumulated amount of the “released” aptamer stabilizes within 24 h. For the antibody, the cleavage is much slower, as the relatively large pepsin molecules are required to infiltrate into the porous layer to catalyze the digestion, followed by out diffusion of the resulting protein fragments to the solution. For the aptamer, a total amount of 1.89 ± 0.02 nmol was released, which is approximately half of the aptamer amount used for the conjugation. For the oriented and unoriented antibody, the total amount was 0.045 ± 0.002 and 0.0430 ± 0.0006 nmol, respectively, which is two orders of magnitude lower than that of the aptamer. As the specific surface area for both biosensors are similar, the significant difference in the amount of the immobilized bioreceptors correlate to the respective calculated surface density (see Table S5.1.2, Supporting Information). Thus, the results demonstrate the significantly higher surface density of the aptamer molecules immobilized within the porous nanostructure film, compared to the antibodies. This is mainly ascribed to the profound differences in the size of the two bioreceptors; where the aptamer is approximately >10-fold smaller than the antibody^{318, 320, 354}, which enables higher immobilization density and surface coverage. Thus, for the aptasensor, a greater number of binding sites are available for the target within the same nanostructure, compared to the immunosensor^{320, 355}. This in turn is highly advantageous for enhancing the sensitivity of the biosensor²¹. It should be emphasized that although a different immobilization chemistry was utilized for quantifying the aptamer surface density (and as such the total number of immobilized aptamer molecules is not accurate), its effect on the obtained value may be neglected due to the profound difference of 2-orders of magnitude in surface densities between the aptasensor and immunosensor. In addition, for the immunosensor constructed via random conjugation, our quantification method underestimates the total number of immobilized antibody molecules (see Table S5.1.1, Supporting Information). As in this case the antibodies are covalently bound to the porous surface, a fragment of the antibody is expected to remain attached to the surface after pepsin digestion, resulting in an incomplete cleavage. This is in contrast to the oriented immobilization, where the antibodies are conjugated to the protein A layer, which is digested by the pepsin, leading to a complete release of the immobilized antibodies.

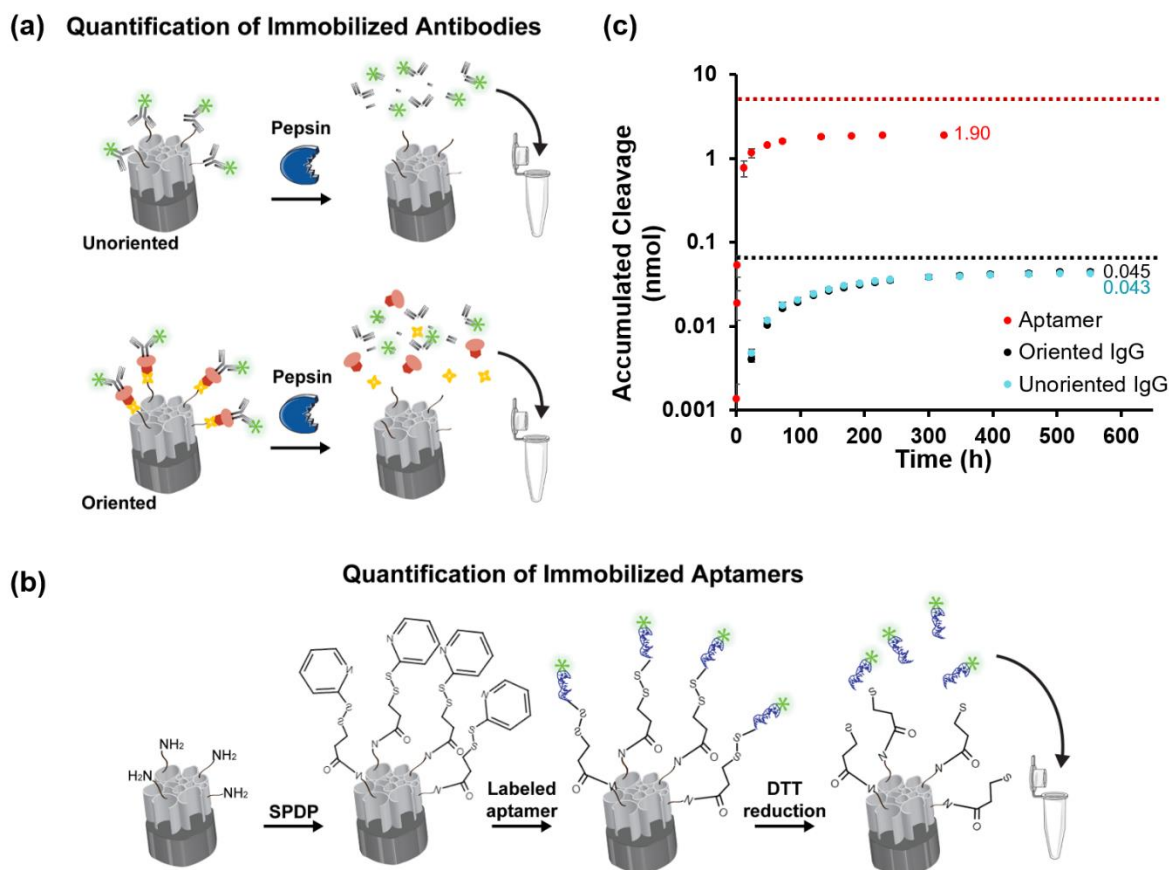


Figure 5.1.2. Bioreceptors surface density. Schematic illustration of the quantification method used for (a) the immunosensors and (b) the aptasensors. (c) The accumulated number of moles of aptamer and antibody molecules (oriented and unoriented) cleaved from the PSiO₂ surface vs. time ($n = 3$). The dashed lines represent the applied amount of the respective bioreceptor during immobilization.

Biosensing Experiments

For the biosensing experiments, the antibody-conjugated and the aptamer-conjugated PSiO₂ films were exposed to different protein solutions (5 μ M to 56 μ M) and Figure S5.1.2 (Supporting Information) presents characteristic results in terms of the relative EOT changes vs. time. Initially, PBS or SB (for antibody- and aptamer-conjugated PSiO₂, respectively) were introduced to establish a stable EOT baseline. Next, different analyte solutions were introduced onto the studied biosensor and allowed to react with the respective functionalized surface for 1 h (without flow). Subsequently, the biosensors were extensively rinsed with buffer (PBS or SB) to remove unbound molecules until a stable baseline is reached.

Figure 5.1.3a presents the averaged EOT values (attained after 1 h incubation with the target and subsequent washing with the buffer) for increasing protein concentrations and the corresponding curve fit utilizing a model for specific binding with a Hill slope (see Equation 5.1.3). Oriented antibody and aptamer-based biosensors result in a target binding behavior that can be modelled according to Equation 5.1.3, with a good fit ($R^2=0.9490$ and $R^2=0.9731$, respectively). For the unoriented immunosensor, no statistically significant differences were observed between the EOT signals measured for the different

Results

protein concentrations. Thus, owing to the poor performance of this biosensor, which is discussed in detail at the end of this section, we focus our discussion on the comparison between the aptasensor and oriented immunosensor. The dynamic range of these biosensors is from 8.25 μM to 56 μM , and the lowest measured target concentration is 5 μM , with an average relative ΔEOT signal of 1.9 ± 0.8 and 1.5 ± 0.3 for the oriented-immunosensor and aptasensor, respectively. These signals can be reliably distinguished from the baseline, with a baseline noise equivalent to three standard deviations of 0.4 and 0.3 for the immunosensor and aptasensor, respectively. The observed micromolar detection limit agrees with the common limit of detection (LoD) values of label-free P*Si*-based optical biosensors²². We ascribe this high value mainly to mass transfer phenomena, specifically to the diffusion rate to and within the P*SiO*₂ nanostructure, which has a profound effect at lower target concentrations^{21, 23, 36, 165, 189}. This in fact does not allow a proper comparison between both bioreceptors in the lower detection range, as both biosensors are limited by the P*SiO*₂ transducer, regardless of the bioreceptor type. Thus, we cannot draw a conclusion on which of the bioreceptor results in improved biosensor sensitivity. Overall, both biosensors perform in a similar manner, in terms of their dynamic range and sensitivity. This is also apparent in the binding rates for the aptamer and oriented antibody-based biosensors. Figure 5.1.3b depicts real time changes in the relative EOT signal (with respect to the baseline) for the oriented-antibody and aptamer-based biosensors upon incubation with increasing concentrations of tyrosinase. Both biosensors exhibit a similar target binding trend and a concentration-dependent behavior. The calculated binding rates are presented in Figures 5.1.3c and 5.1.3d, as the initial (0 to 10 min) and total (0 to 60 min) values for different concentrations of tyrosinase, respectively. An insignificant difference is observed between both types of biosensors, regardless of the analyzed duration, i.e. the initial or the total binding rate. The only apparent difference is observed at a longer binding time of 60 min, where the immunosensor reaches almost equilibration, while the signal for the aptasensor is far from surface saturation and keeps increasing (see Figure 5.1.3b). This behavior is ascribed to the greater number of available binding sites for the target protein in the aptamer-based biosensor, in comparison to the antibody-based one (see Figure 5.1.2c). This also results in greater signal values for target concentrations $\geq 16.5 \mu\text{M}$, as observed in Figure 5.1.3a. The greater number of available protein binding sites for the aptamer-based biosensor, maximizes target capture onto the P*SiO*₂ surface and consequently resulting in a higher signal⁴³.

Results

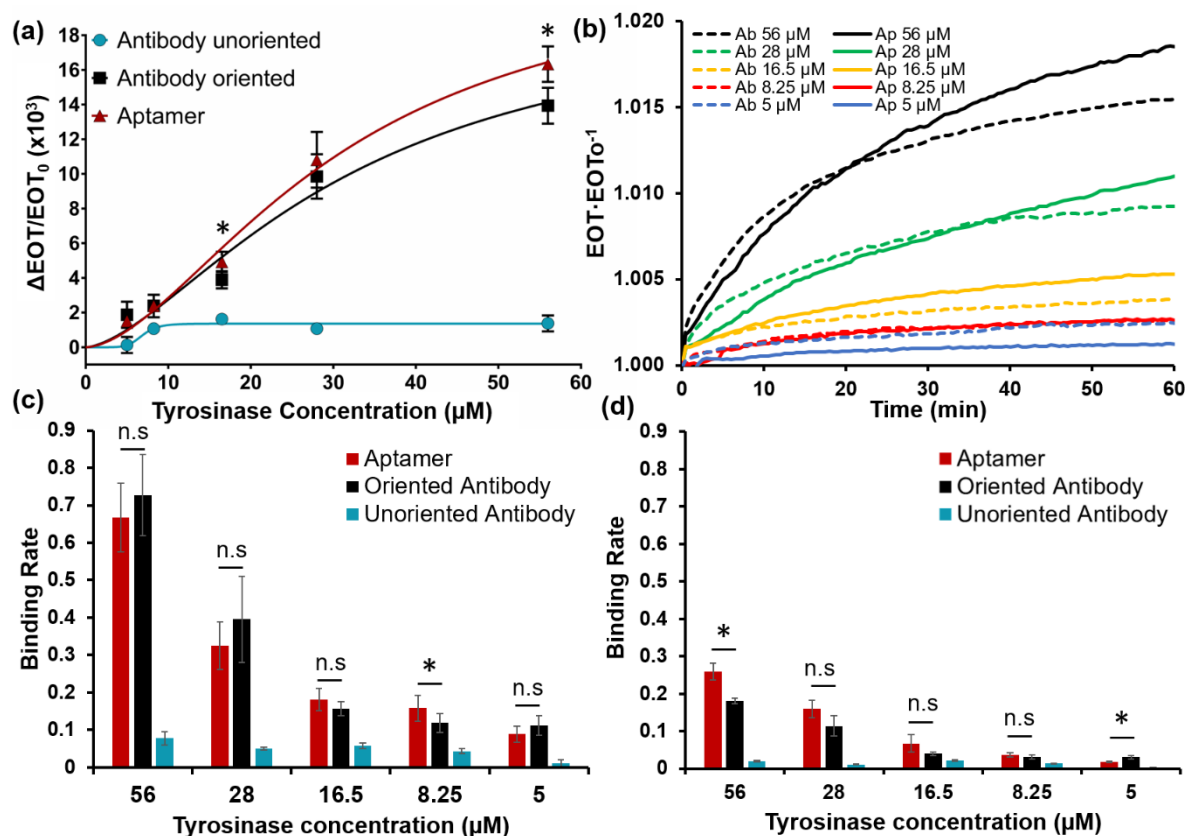


Figure 5.1.3. (a) Relative EOT changes of different PSiO₂ biosensors (random and oriented antibody-conjugated PSiO₂ and aptamer-conjugated PSiO₂) collected after 1 h exposure to varying tyrosinase concentrations. The lines show the curves fitted for specific binding with Hill slope. (b) Relative EOT changes vs. time for oriented antibody (Ab)- or aptamer (Ap)-immobilized PSiO₂ upon exposure to different concentrations of his-tagged tyrosinase (data represents an average of $n \geq 3$). (c) and (d) Binding rates [$(EOT \cdot EOT_0^{-1} \cdot \text{min}^{-1}) \cdot 10^3$] at 10 min and 60 min of incubation with different tyrosinase concentrations, respectively, for the three types of biosensors. (n.s) or (*) Indicate non-significant or statistically significant difference, respectively, between the total binding or the binding rate of the oriented antibody and aptamer-based biosensors (t test, $n \geq 3$, $p < 0.05$).

The performance of the randomly conjugated antibody-immunosensor was generally poor. A significantly lower EOT signals were observed (see Figure 5.1.3a), as well as 10-fold lower binding rates, compared to the oriented antibody and aptamer-based biosensors (see Figure 5.1.3c and 5.1.3d). Also, a poor dependence of the binding rate in the protein concentration is found (see Figure S5.1.3, Supporting Information). Antibody conjugation via its primary amines is typically highly random, owing to the large number of amine groups in the antibody structure³⁵⁶⁻³⁶⁰. Thus, the functionality of these antibodies varies dramatically, and the resulting performance of the biosensors is limited. Since the total amount of antibodies immobilized within the porous layer for the random conjugation is similar or higher than for the oriented conjugation route, these results indicate that for the random conjugation less than ~10% of the immobilized antibodies are active, compared to the oriented immobilization. Our results suggest that immobilization of antibodies via a random amine-functionality is not preferable for fabrication of robust and specific PSiO₂ biosensors and this is in agreement with other biosensing

Results

systems³⁶¹⁻³⁶⁴. The similar binding rate, dynamic detection range and sensitivity of the oriented antibody and aptamer-based biosensors indicate that by optimization of the bioreceptor immobilization, e.g., oriented vs. random antibody conjugation, a similar performance can be achieved utilizing the same transducer. Immobilization of the antibodies in an oriented configuration increases the active portion of the antibodies³⁶⁰⁻³⁶², resulting in a similar biosensing performance to that of the aptasensor, in which the aptamers are immobilized in a naturally orientated configuration at a much higher density.

Selectivity and Performance in Complex Samples

PSiO₂ biosensors modified with 6H7-aptamer have previously demonstrated high selectivity towards their target his-tagged protein and robustness against unspecific adsorption even in complex media with an abundance of non-target proteins (i.e. bacteria lysates)^{26, 30}. In the present study, we compare the behavior of the different biosensors upon exposure to non-target proteins (i.e., trypsin and bacteria lysate) and to complex media (bacteria lysate with a typical protein content of 1.8 mg mL⁻¹) spiked with the target tyrosinase. The optical response of the biosensors is summarized in Figure 5.1.4.

Biosensors functionalized with aptamers and oriented antibodies show high affinity towards their target with reproducible results. The biosensors selectively detect their target protein in a complex solution of bacteria lysate and the obtained EOT values are in good agreement with the values collected for tyrosinase in a buffer (see also Figure 5.1.3 and Figure S5.1.4 for the real-time optical response). Notably, both biosensors exhibit low nonspecific adsorption of non-target proteins. We note that the negative response of the aptasensor to trypsin and lysate solutions may be ascribed to conformational changes of the immobilized aptamers. The latter are often utilized as the sensing mechanism in various aptasensors^{365, 366}.

Contrary, biosensors in which the antibody is conjugated in a random orientation exhibit similar response to all studied solutions and poor reproducibility, as can be seen by the large deviations obtained upon exposure to trypsin or bacteria lysates. Thus, the signals obtained for samples containing the pure target protein are indiscernible from those collected for non-target proteins. The inconsistent behavior of antibody-regions other than the antigen binding sites is ascribed to the undirected immobilization, which may promote nonspecific adsorption onto the biosensor.

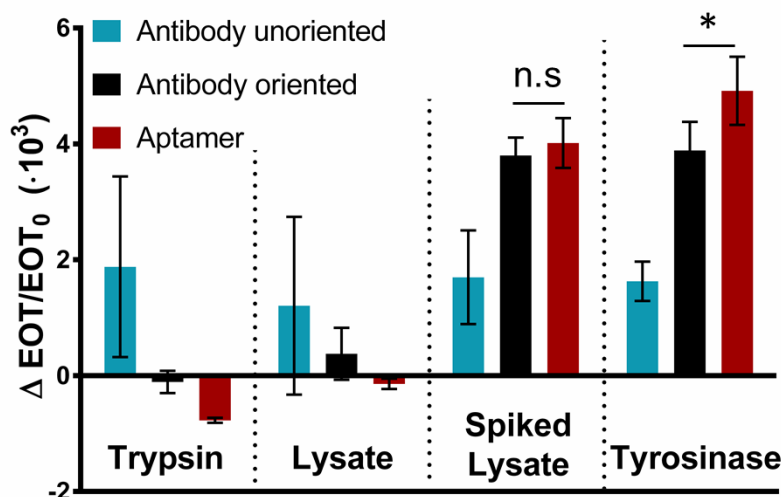


Figure 5.1.4. The biosensor response, expressed as the relative EOT change, collected after 1 h exposure to different samples: trypsin as a non-target protein (concentration $16.5 \mu\text{M}$), bacterial lysates (with a protein concentration of 1.8 mg mL^{-1}) and lysates spiked with $16.5 \mu\text{M}$ tyrosinase. The response of the biosensors to a pure tyrosinase (concentration $16.5 \mu\text{M}$) solution is presented for comparison. (n.s) or (*) Indicate non-significant or statistically significant difference, respectively, between the oriented antibody and aptamer-based biosensors (*t* test, $n \geq 3$, $p < 0.05$).

Biosensor Regeneration

One of the main advantages of DNA or RNA aptamers in comparison to antibodies is their ability to undergo reversible folding and unfolding, leading to a greater stability and a simpler elution of the bound target from the aptamer²⁵⁷. Thus, rendering aptamer-based biosensors as potentially recyclable^{317, 320, 367}. For the 6H7 aptamers, exposure to imidazole enables the release of the bound target protein, by a competitive interaction between the imidazole, his-tagged target and the aptamer, similarly to the purification procedure of his-tagged proteins by immobilized metal ion affinity chromatography (IMAC)^{26, 368}. Our previous report demonstrated the reusability of the 6H7 aptamer-functionalized PSiO₂ surface for up to 12 consecutive cycles by regenerating the biosensor surface in between these cycles by a short exposure to imidazole solution²⁶. Contrary, the regeneration of immunosensors for repetitive usage is more complicated since antibodies are prone to irreversible denaturation³⁴³. While for aptamers regeneration conditions can be predefined during their selection in the SELEX process³⁶⁹, for antibodies, regeneration must be investigated by a trial and error process for each antibody-antigen couple and biosensor platform^{342, 343}, owing to the different attractive forces defining each interaction and the stability of the transducer and signal to environmental changes³⁴³. Regeneration of immunosensors has been commonly achieved using acidic pH^{344, 345}, glycine/HCl^{342, 344, 346}, addition of detergents such as sodium dodecyl sulphate (SDS)³⁴⁷ or addition of dimethyl sulfoxide (DMSO)³⁴⁶. Table 5.1.1 summarizes the different regeneration protocols which were employed for the oriented-antibody functionalized PSiO₂. All regeneration attempts were carried out at a high tyrosinase concentration ($56 \mu\text{M}$) which poses the greatest challenge for regeneration. The relative EOT changes upon exposure of the immunosensor to the different regeneration conditions, following a biosensing experiment of $56 \mu\text{M}$ target protein, are presented in Figure S5.1.5. None of these conditions was found

Results

to result in full restoration of the initial baseline; however, incubation in solutions of 1 M imidazole, 10 mM glycine/HCl pH 2.5 or 100 mM HCl (at pH 2.0) had the best effect. Next, we studied the reusability of the immunosensor in three consecutive cycles, where the biosensor was regenerated for 30 min in between the cycles utilizing these three regeneration solutions, see Figure S5.1.6. It should be noted that we performed a 30 min exposure of the immunosensor to the regeneration solution for a proper comparison to the aptasensor. Nevertheless, a shorter regeneration of 5 min results in a similar regeneration performance, see Figure S5.1.7, indicating that the exposure time (in this solution) has a negligible effect. Baseline drift in successive experiments, i.e., incomplete return to the original EOT value following exposure to the regeneration solution, was observed for all studied conditions, as shown in Figure S5.1.6. It should be pointed out that despite the harsh regeneration conditions (combination of low pH and relatively long exposure of 30 min to the regeneration solution), a maximal EOT decrease of only ~56% is achieved (for the use of 1M imidazole), indicating that the protein target was only partially eluted. Moreover, this moderate decrease in the EOT values also suggests that possible elution of the antibody molecules, due to possible disruption of the IgG binding to the immobilized protein A³⁷⁰, is minor (the antibody molecular weight is ~5 times higher than that of the target protein and thus its elution should induce a pronounced decrease in the EOT value¹⁸⁹). Based on the results presented in Figure S5.1.6, the combination of 10 mM glycine/HCl pH 2.5 (see Figure S5.1.6-III) was used for our subsequent studies as the achieved biosensing performance, in terms of the attained new signal in comparison to that achieved during the first biosensing cycle, was found to be better. For example, 80% compared to 55% for 10 mM glycine/HCl pH 2.5 and 1M imidazole, respectively, for the second biosensing cycle compared to the first.

Figure 5.1.5 summarizes the results of the biosensors' regeneration experiments. Figure 5.1.5b presents the attained EOT signals (expressed as percent of the first biosensing cycle signal) of the oriented-antibody and the aptamer-immobilized PSiO₂ upon three consecutive biosensing experiments. The biosensors were exposed to a high concentration of the target protein (56 μM) followed by a regeneration step (using 10 mM glycine/HCl pH 2.5 for the immunosensor and 1 M imidazole for the aptasensor). The characteristic real-time biosensing curves for these experiments are depicted in Figures 5.1.5c and 5.1.5d. Following the first regeneration step, the aptasensor performance has decreased by ~10%, see Figure 5.1.5b. Yet, after this initial decrease, the biosensor response was highly reproducible upon subsequent cycles, demonstrating a fair recyclability. It should be noted that a full baseline restoration after each biosensing cycle is not achieved (see Figure 5.1.5c). This is in contrast to our previous report for the 6H7 aptasensor²⁶ and may be attributed to the high target concentration used here, as well as to the different protein targets (tyrosinase vs. lipase). It is well established that the high structural complexity of proteins allows aptamer binding in different modes through a variety of attractive forces, which in turn significantly affects the binding strength^{343, 354}. For the immunosensor, a greater activity loss of ~20% is observed in the second biosensing cycle, and by the third cycle, the collected signal is further decreased to 58±9%. Thus, regeneration of the immunosensor is not achieved

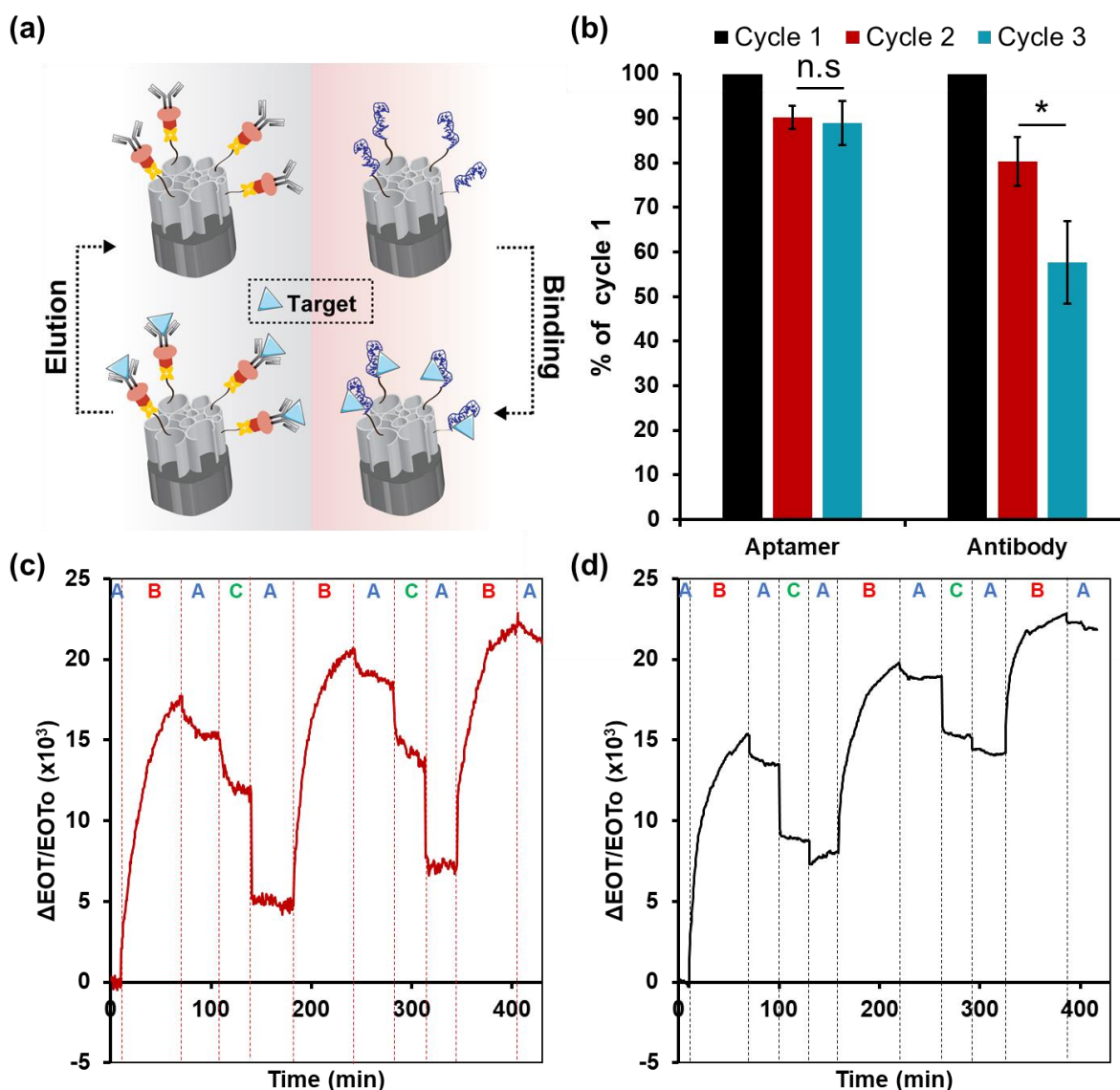


Figure 5.1.5. (a) Schematic illustration of the biosensor regeneration concept. (b) Relative signal (presented as % of the EOT signal collected in the first biosensing cycle) collected from the (oriented) antibody- and the aptamer- biofunctionalized P_{Si}O₂ upon three successive exposure cycles to 56 μ M tyrosinase. After each exposure to the protein, the biosensors were regenerated with solutions of 10 mM glycine/HCl pH 2.5 or 1 M Imidazole supplemented SB, for antibody or aptamer biosensors, respectively. (n.s) or (*) indicate non-significant or statistically significant difference, respectively, between the oriented antibody and aptamer-based biosensors (*t* test, $n \geq 3$, $p < 0.05$). Relative EOT changes vs. time upon exposure of the (c) aptamer and (d) oriented antibody-biofunctionalized P_{Si}O₂ to 56 μ M Tyrosinase in three consecutive biosensing cycles, utilizing a regeneration solution of 1M imidazole for the aptasensor and 10 mM glycine/HCl pH 2.5 for the immunosensor. A, B and C indicate incubation with SB or PBS buffers, with the target protein or with elution buffer, respectively.

using the common regeneration conditions studied here. This can be ascribed to the poor structural stability of the antibody following its denaturation, compared to the aptamers³²⁰, and may require a further tedious probing of different regeneration conditions for the immunosensor. The better performance of the aptasensor in the successive cycles can be also referred to the greater number of binding sites available for the target, due to the higher immobilization density of the aptamers. Thus, although full restoration of the biosensor is not achieved after each biosensing cycle, there are still

Results

sufficient binding sites for the target, at this high target concentration (56 μM). This makes the aptasensor reusable for at least three biosensing experiments of 56 μM tyrosinase, and could potentially be utilized for up to 12 consecutive biosensing cycles, according to our previous work ²⁶. It should be noted that in this work we have utilized imidazole as the eluting agent similarly to IMAC columns; however, aptamers can be also reversibly unfolded to release their target by a simple heat denaturation ³⁶⁹, which is not applicable for immunosensors. Thus, for potential practical application, the P*Si*-based aptasensors can be easily regenerated by heat treatment, which will further simplify the regeneration process.

Conclusions

This study presents a direct comparison for the specific detection of a model target protein, his-tagged tyrosinase, with antibody and aptamer capture probes, utilizing optical P*Si*-based biosensors. The 6H7 aptamer is compared to anti-his-tag antibodies, where the latter are immobilized onto the P*SiO*₂ nanostructure in a random or Fc-oriented configuration. The aptamer's smaller size allows surface immobilization at much higher density, resulting in a larger number of binding sites on a similar P*SiO*₂ surface. However, in practice, both the aptamer and the oriented antibody-based biosensors present a similar biosensing performance in terms of the dynamic detection range, measured detection limit, binding rate, and selectivity. Thus, the oriented conjugation route of the antibodies allows for similar performance even though the biosensor target binding capacity is smaller.

In contrast, a simple random immobilization of antibodies onto the P*SiO*₂ biosensors does not allow target detection. Although their surface density is comparable to that achieved by oriented immobilization, only ~10% of the randomly oriented antibodies were active. Thus, the laborious directed immobilization of the antibodies, even though decreasing the available free porous volume, and extending the fabrication time and costs, is required for successful target detection. Our main conclusion from the study is that by tailoring the immobilization chemistry and orientation of the bioreceptor, a similar biosensing performance can be achieved on the same transducer.

The aptasensor advantages are reflected in the practical fabrication, use and storage of the biosensor. The aptasensor fabrication is much faster and cost effective, compared to the immunosensor. Also, the high stability of the DNA aptamers allows for the aptasensor effective storage in dry conditions at room temperature before usage. Contrary, the immunosensor should be stored in a refrigerator in wet conditions, limiting its long-term storage. Importantly, the aptamer's ability to undergo reversible denaturation enables regeneration of the aptasensor for multiple uses. In contrast, the immunosensor cannot be regenerated without a significant activity loss after the first biosensing cycle.

It should be also pointed out that at lower target concentration, the sensitivity of both biosensors has been mainly limited by the P*Si* transducer, leading to a similar detection limit. Thus, the performance of both bioreceptors at the lower detection range could not be effectively compared. Our future work

Results

focuses on improving the limited sensitivity, while in the present work our main attention is directed to the comparison of the capture probes.

Supporting Information

Table S5.1.1 Characterization results of the oxidized PSi nanostructures by spectroscopic liquid infiltration method (SLIM) ($n=5$).

Porosity (%)	Thickness (nm)	Pore diameter* (nm)
73±3	5500±200	35-65

*Average pore diameter was evaluated with HR-SEM.

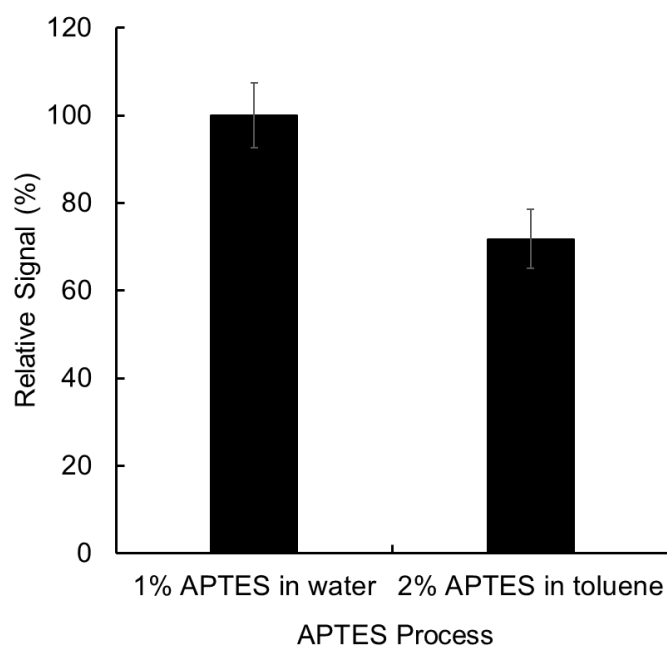


Figure S5.1.1. Comparison of the biosensing performance of the immunosensor upon exposure to 56 μM Tyrosinase, for two methods of APTES modification of the PSiO₂ film. The signal is normalized to the standard APTES method of the antibody immobilization process (1% APTES in water) ($n\geq 3$). Results indicate lower immunosensor performance, by 28%, upon APTES modification according to the aptamer immobilization process (2% APTES in toluene).

Results

Table S5.1.2. A summary of the applied amount, number of moles cleaved, the immobilized percentage and surface density of the aptamers and oriented and unoriented antibodies within the P_{SiO}₂ (n=3).

	Moles Applied (nmol)	Moles Cleaved (nmol)	Immobilization Percentage (%)	Surface Area (cm²)	Surface Density (cm⁻²)
Aptamer	3.75	1.89±0.02	50.3±0.5%		1.25·10 ¹²
Oriented IgG	0.067	0.045±0.002	67±3%	910	2.94·10 ¹⁰
Unoriented IgG	0.067	0.0430±0.0006	64.5±0.8%		2.83·10 ¹⁰

The bioreceptor densities within the P_{SiO}₂ were calculated by dividing the number of bioreceptor moles by the porous surface area. The latter was measured in a previous study ³⁴¹ by nitrogen adsorption isotherms and application of BET (Brunauer-Emmett-Teller) model for a similar P_{SiO}₂ nanostructure. Since the P_{SiO}₂ utilized in the present study was characterized with a smaller layer thickness (5500 nm vs. 7880 nm), the surface area was corrected according to the layer thickness ratio of both nanostructures. Thus, the surface area value utilized for the calculations was 684 cm² STP cm⁻² (expressed per unit area of P_{SiO}₂ sample). The area of the P_{SiO}₂ sample is 1.33 cm², resulting in a total surface area of 910 cm².

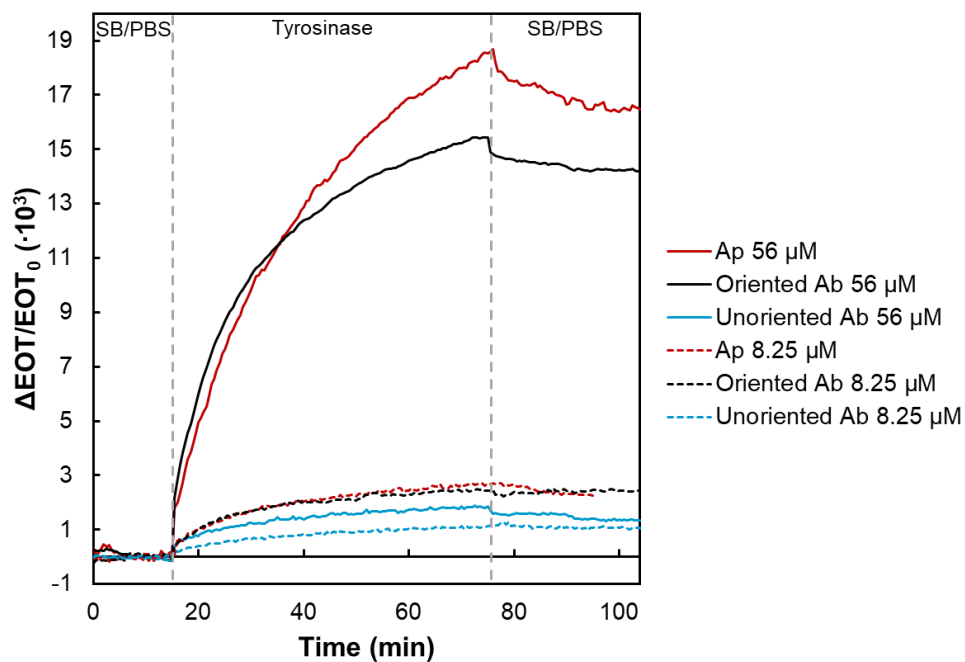


Figure S5.1.2. Real-time relative EOT changes for aptamer (Ap), oriented and unoriented antibody (Ab)-immobilized PSiO₂ upon exposure to 56 μM or 8.25 μM his-tagged tyrosinase (data represents an average of $n = 3$). SB denotes aptamer's selection buffer.

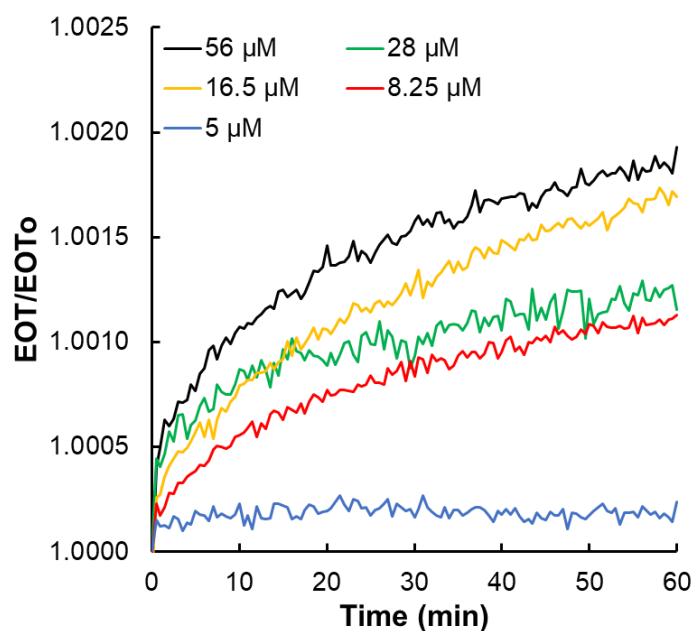


Figure S5.1.3. Relative EOT changes vs. time for randomly oriented antibody-biofunctionalized PSiO₂ upon exposure to different concentrations of his-tagged Tyrosinase (data represents an average of $n \geq 3$).

Results

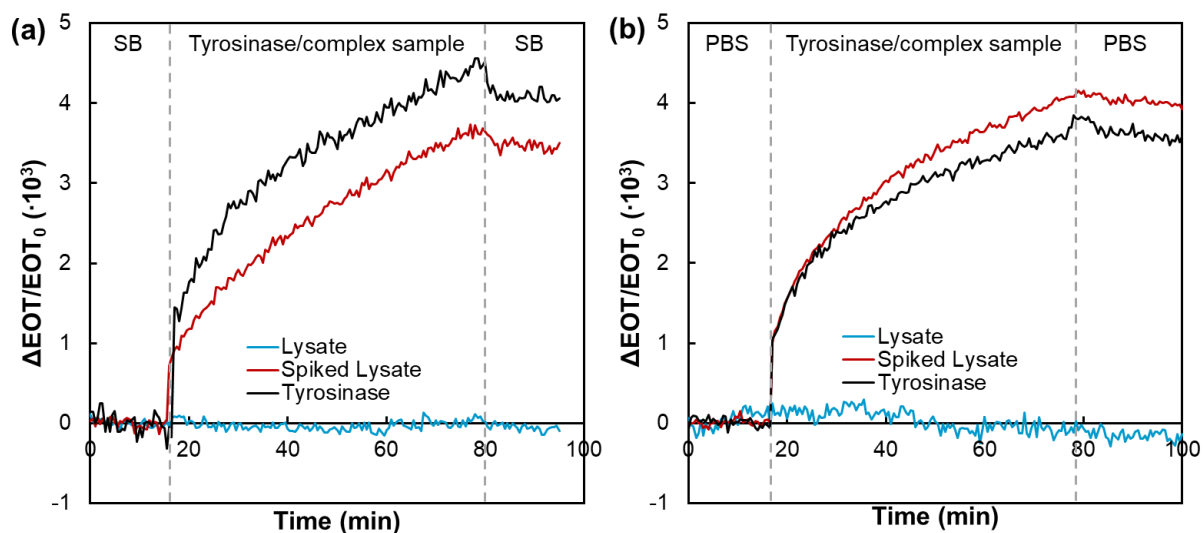


Figure S5.1.4. Characteristic relative EOT changes vs. time for the (a) aptasensor and (b) oriented-immunosensor upon exposure to neat bacterial lysate, bacterial lysate spiked with $16.5 \mu\text{M}$ tyrosinase and $16.5 \mu\text{M}$ tyrosinase in a buffer. SB denotes aptamer's selection buffer.

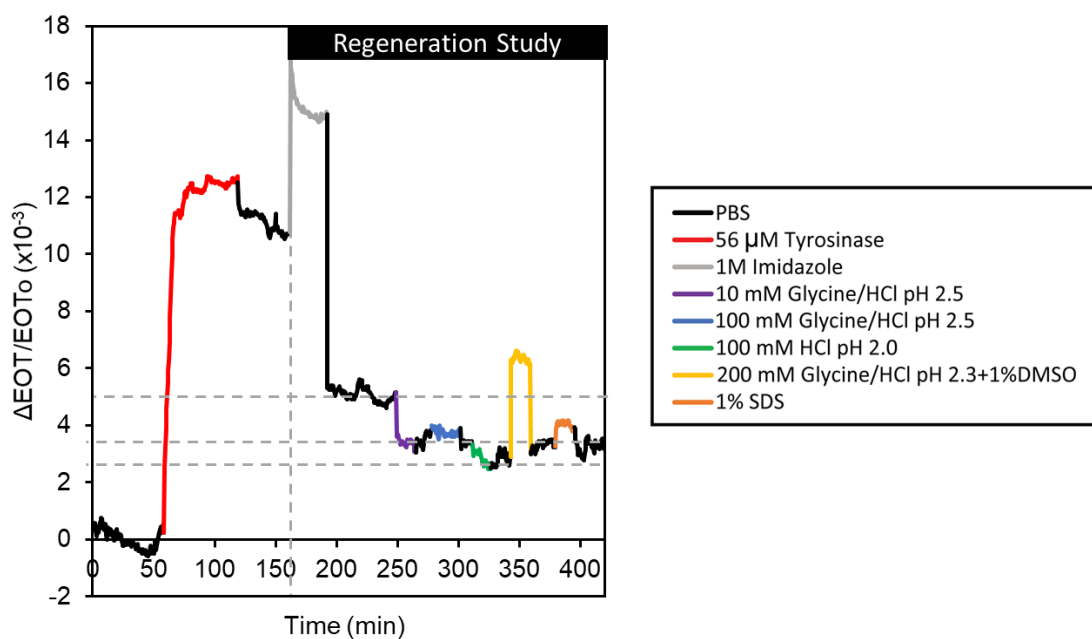


Figure S5.1.5. Relative EOT changes vs. time upon exposure of the oriented antibody-biofunctionalized PSiO_2 to $56 \mu\text{M}$ Tyrosinase, followed by washing with PBS and exposure to different regeneration solutions. Although complete regeneration to initial PBS baseline is not achieved, 1 M imidazole, 10 mM glycine/HCl pH 2.5 and 100 mM HCl pH 2.0 have the most significant regeneration effect.

Results

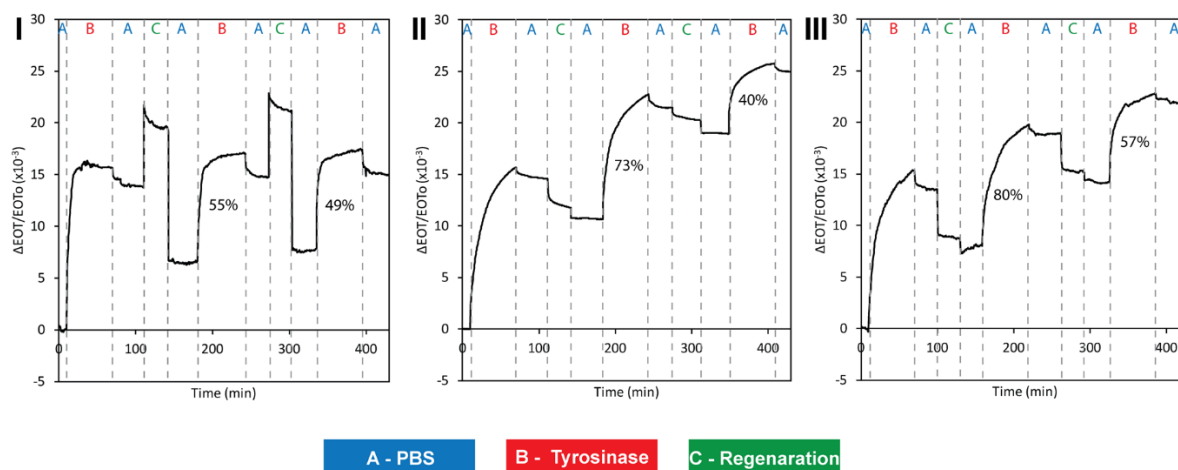


Figure S5.1.6. Relative EOT changes vs. time upon exposure of the oriented antibody-biofunctionalized $PSiO_2$ to $56 \mu M$ Tyrosinase in three consecutive biosensing cycles, utilizing a regeneration solution of (I) 1M imidazole, (II) 100 mM HCl pH 2.0 and (III) 10 mM glycine/HCl pH 2.5. Percentages represent biosensing signal (calculated after exposure to $56 \mu M$ Tyrosinase and wash with PBS) of the second and third cycles out of the first cycle.

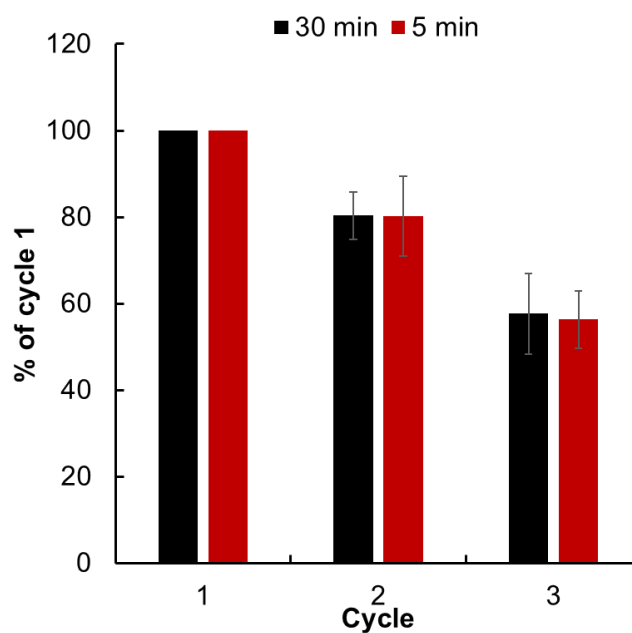
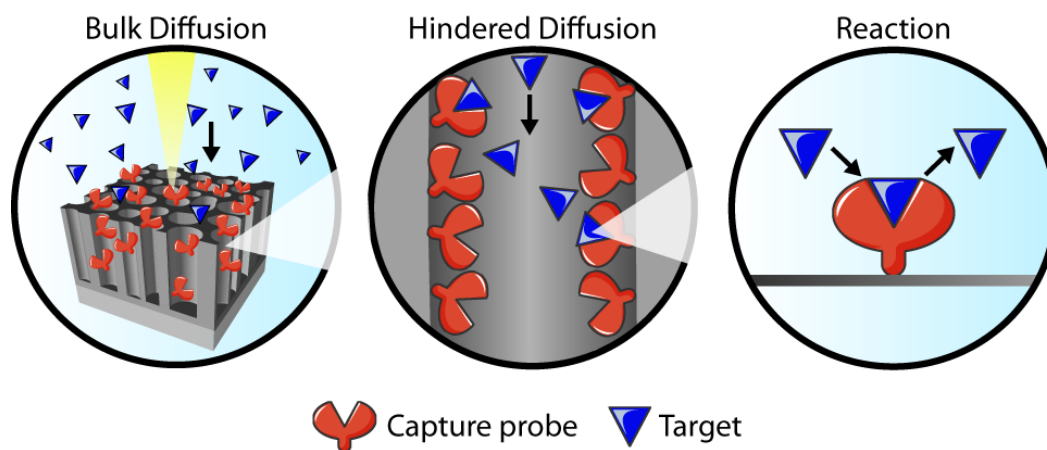


Figure S5.1.7. Comparison of a 30-min and a 5-min exposure time of the immunosensor to a regeneration solution of 10 mM glycine/HCl pH 2.5, presented as the relative signal for each biosensing cycle (presented as % of the EOT signal collected in the first biosensing cycle) ($n \geq 3$). Both regeneration periods result in similar regeneration performance.

5.2 Mass Transfer Limitations of Porous Silicon-Based Biosensors for Protein Detection

Sofia Arshavsky-Graham, Evgeniy Boyko, Rachel Salama, and Ester Segal

ACS Sensors 5 (10), 3058-3069 (2020).



Respective Table of Contents Image

Abstract

Porous silicon (PSi) thin films have been widely studied for biosensing applications, enabling label-free optical detection of numerous targets. The large surface area of these biosensors has been commonly recognized as one of the main advantages of the PSi nanostructure. However, in practice, without application of signal amplification strategies, PSi-based biosensors suffer from limited sensitivity, compared to planar counterparts. Using a theoretical model, which describes the complex mass transport phenomena and reaction kinetics in these porous nanomaterials, we reveal that the interrelated effect of bulk and hindered diffusion is the main limiting factor of PSi-based biosensors. Thus, without significantly accelerating the mass transport to and within the nanostructure, the target capture performance of these biosensors would be comparable, regardless of the nature of the capture probe-target pair. We use our model to investigate the effect of various structural and biosensor characteristics on the capture performance of such biosensors and suggest rules of thumb for their optimization.

Introduction

Biosensors monitor the binding between a target molecule and a capture probe, by various transducing methods, and surface-based detection, in which the capture probes are immobilized on the transducing surface, are among the most widespread bioanalytical tools¹⁰⁻¹⁴. The performance of surface-based planar biosensors based on surface capture is governed by the complex interplay between transport phenomena and reaction kinetics, as modelled by Squires *et al*³⁶. As such, numerous studies have been directed to optimize these systems and elucidating their limiting factors^{5, 38, 371-376}.

Porous silicon (PSi) has been widely studied as an optical transducing surface in various biosensing platforms, presenting low cost fabrication, chemically active surface and unique optical properties^{22, 332}. Specifically, employing interferometric Fourier transform spectroscopy (RIFTS) as the transduction mechanism enables real-time and label-free target detection¹⁵⁻¹⁸. In this method, a series of Fabry-Pérot interference fringes are produced from incident white light reflections from the top and bottom interfaces of a porous thin film and the fringe pattern depends on the thickness and averaged refractive index of the porous layer.

The porous nanostructure of PSi increases dramatically the surface area, which allows the immobilization of a greater amount of capture probe molecules compared to planar devices and potentially increase the detection sensitivity by orders of magnitude^{21, 25, 43, 147, 157, 332}. Nevertheless, common detection thresholds in such systems revealed an inferior performance, with micromolar detection limits for protein and DNA targets in direct and label-free optical detection¹⁹⁻²⁵. Therefore, many have focused on developing assays for improving the sensitivity and performance of such systems^{19, 20, 22, 24, 30, 42}, while others investigated the limiting characteristics of the platform and suggested solutions for overcoming these issues^{23, 188-190}. The latter includes mass transfer limitations, which are

Results

affected by the nanostructure characteristics such as pore size, length, porosity, surface area and roughness^{188-190, 377-382}. For example, studies on the impact of the pore size on the binding efficiency have been conducted^{381, 383} and a critical correlation between the molecule size and the pore diameter has been suggested to allow effective infiltration into the porous layer, in which the molecule must be at least five times smaller than the pore opening¹⁸⁹. To overcome mass transport limitations, flow through platforms have been developed^{23, 241}. Moreover, accurate quantitative determination of molecular binding kinetics was performed by analyzing dilute analyte solution at short binding times, avoiding capture probe saturation with the analyte¹⁶⁵. The many parameters affecting the performance of P*Si* biosensors challenge the experimental characterization of each factor. Thus, deriving theoretical models to describe the effect of each of the parameters is a facile way to study those complex systems. In mesoporous systems, as the size of the pore approaches that of the solute, a deviation from the diffusion kinetics predicted by Fick's law is observed, leading to an overestimation of the solute flux³⁸⁴⁻³⁸⁶. The diffusion within the porous nanostructure is hindered by steric and hydrodynamic interactions between the diffusing solute, the pore wall and the immobilized molecules and receptors on the pore wall^{384, 387-390}. The structural properties of the porous nanostructure, such as pore diameter and porous layer thickness, have also a tremendous effect, as the deviation from the bulk diffusion coefficient is more pronounced for smaller pores and thicker layer³⁹¹. The motion of the diffusing molecule is also highly dependent on structural defects, as revealed by single molecule diffusion analysis in a mesoporous silica^{392, 393}. Molecules transport and adsorption in porous materials have been investigated and models describing the hindered diffusion effect have been empirically derived^{386, 394}. Nevertheless, the spatial and time-resolved change in the diffusivity coefficient upon the filling of the pore has been often neglected to simplify the solution of the mass balances^{44, 46, 395}.

Further simplification of the mass transfer studies in porous biosensors has approximated the porous layer as a perfect collector, giving the large capacity of binding sites within the porous layer. Thus, the entry into the pores has been concluded as the rate limiting step, while the hindered diffusion effect has been neglected^{23, 45, 396}. Such modeling and analysis were derived for protein adsorption on a porous anodic aluminum oxide nanostructure, for a target solution flow over the nanostructure³⁹⁶ and for mass transfer analysis in P*Si*-based optical biosensors^{23, 45}. Nevertheless, for evaluation of the effect of mass transfer or reaction kinetics in P*Si*-based biosensors, the system cannot be assumed as a planar surface, and all transport phenomena as well as reaction between the target and the immobilized probes, should be considered.

In this work, we aim to determine the effect of each of the mass transport phenomena and reaction kinetics in P*Si*-based optical biosensors. In contrast to previous works, we develop a model which captures the complex mass transfer processes in porous materials, including the bulk diffusion, hindered diffusion, and capture probe-target binding kinetics. The model is solved numerically using parameters which are characteristic of typical P*Si* biosensors. Specifically, we compare our model results to biosensing experiments of several P*Si*-based aptasensors for targeting proteins, as well as to the

Results

common simplified “planar” model, which neglects the hindered diffusion within the porous layer. Importantly, we determine the limiting transport phenomena of PSi-based biosensors and the dependency of the target binding rate on various biosensor characteristics and conclude with directions for proper optimization of such biosensors.

Experimental

Materials

Heavily doped p-type Si wafers (<100>-oriented, 0.90-1.00 mΩ·cm resistivity) were purchased from Sil'tronix Silicon Technologies (France). Aqueous HF (48%), (3-Aminopropyl)triethoxysilane (APTES), ethyldiisopropylamine (DIEA), succinic acid, succinic anhydride, N-(3Dimethylaminopropyl)-N'-ethylcarbodiimide hydrochloride (EDC), N-Hydroxysuccinimide (NHS), glutaraldehyde 25% solution (GA), ethanolamine, acetonitrile (ACN), dimethyl sulfoxide (DMSO), sodium cyanoborohydride, sodium dodecyl sulfate (SDS), N-Succinimidyl 3-(2-pyridyldithio)propionate (SPDP), DL-Dithiothreitol (DTT), isopropyl alcohol (IPA) morpholinoethanesulfonic acid (MES), MES sodium salt, Tris base and all buffer salts were purchased from Merck (Israel). Ethanol absolute was supplied by Bio-Lab Ltd (Israel). All solutions were prepared with Milli-Q water (ddH₂O, 18.2 MΩ·cm). Anti-AGR2 aptamer sequence (5'-TCT-CGG-ACG-CGT-GTG-GTC-GGG-TGG-GAG-TTG-TGG-GGG-GGG-GTG-GGA-GGG-TT-3') was obtained from Wu *et al*³⁰⁴. Anti-his-tag aptamer 6H7 (5'- GCT ATG GGT GGT CTG GTT GGG ATT GGC CCC GGG AGC TGG C - 3') sequence was taken from U.S. patent 7329742³⁰³. These aptamers were purchased with a 5'-amino modification from Integrated DNA Technologies (USA). Anti-protein A aptamer, selected by Stoltenburg *et al*³⁰⁵, was used in truncated form PA#2/8[S1-58]: 5'- ATA CCA GCT TAT TCA ATT AGC AAC ATG AGG GGG ATA GAG GGG GTG GGT TCT CTC GGC T – 3', and purchased with a 3'-amino-C6 modification. AGR2 protein was purchased from MyBioSource Inc (USA). Mouse anti-his monoclonal antibody was obtained from Enco (Israel). Streptavidin, biotinylated protein A and recombinant protein A from human serum were purchased from Merck (Israel). 6xhis tyrosinase from *Bacillus megatherium* (recombinant, expressed in *Escherichia coli*) was generously supplied by Prof. Ayelet Fishman, Technion. His-tagged AbnA-D2 (from *Geobacillus stearothermophilus* T-6, expressed in *Escherichia coli*) (D2) was generously supplied by Prof. Yuval Shoham, Technion. 10 mM phosphate buffered saline (PBS) was composed of 137 mM NaCl, 2.7 mM KCl, 10 mM Na₂HPO₄ and 2 mM KH₂PO₄ (pH 7.5). AGR2 selection buffer was composed of 137 mM NaCl, 20 mM KCl, 10 mM Na₂HPO₄ and 2 mM KH₂PO₄ (pH 7.4). 6H7 selection buffer was composed of 50 mM K₂HPO₄, 150 mM NaCl, pH 7.4 and elution buffer was composed of 50 mM K₂HPO₄, 150 mM NaCl, and 1 M Imidazole (pH 7.4). Protein A aptamer selection buffer was composed of 20 mM Tris base, 100 mM NaCl, 5 mM KCl, 10 mM MgCl₂, and 1 mM CaCl₂. 0.5 M MES buffer was

Results

prepared from 0.27 M MES and 0.23 M MES sodium salt (pH 6.1) and Tris buffer was composed of 50 mM Tris base (pH 7.4).

Construction of P*Si*-based Biosensors

The studied biosensors include several P*Si*-based aptasensors and a representative immunosensor, as detailed in Table 5.2.1. All biosensors employed a similar P*Si* nanostructure as the optical transducer and capture probe molecules (aptamer or antibody) were immobilized onto the surface.

Table 5.2.1. Properties of the studied capture probe and target protein pairs and comparison of the theoretical and fitted K_D values.

Aptamer/Antibody	Target	Molecular Weight (kDa)	Literature K_D	Fitted K_D (μ M)
Anti-his tag aptamer	D2	60	$\sim 4.6 \mu\text{M}^{306}$	29 ± 8 ($R^2=0.9551$)
Anti-his tag aptamer	Tyrosinase	35		31 ± 7 ($R^2=0.9731$)
Anti-his tag antibody	Tyrosinase	35	$\sim 10 \text{ nM}^{307}$	24 ± 5 ($R^2=0.9420$)
Anti-AGR2 aptamer	AGR2	22	$\sim 13 \text{ nM}^{304}$	21 ± 1 ($R^2=0.9951$)
Anti-protein A aptamer	Protein A	45	$\sim 0.522 \mu\text{M}^{305}$	14 ± 1 ($R^2=0.9177$)

P*Si* Fabrication: P*Si* Fabry-Pérot thin films are fabricated from a highly doped p-type crystalline Si wafers, with a typical resistivity of 0.90-1.00 $\text{m}\Omega \cdot \text{cm}$, using a two-step anodic electrochemical etching process. A detailed description of the etching setup can be found elsewhere¹⁶. First, a sacrificial layer is etched at a constant current density of 300 mA cm^{-2} for 30 s for the anti-AGR2 system or 375 mA cm^{-2} for 30 s for the other systems, in a 3:1 (v/v) solution of aqueous HF (48%) and ethanol, respectively. The obtained porous layer is removed by introduction of 0.1 M NaOH, followed by exposure to a solution of 1:3:1 (v/v) HF, ethanol and ddH₂O, respectively. Next, a second etching is performed, at the same etching conditions as above. After each step, the silicon surface is thoroughly rinsed with ethanol and dried under a nitrogen stream. Subsequently, the freshly etched P*Si* is thermally oxidized in a tube furnace (Thermo Scientific, Lindberg/Blue M 1200°C Split-Hinge, USA) at 800 °C for 1 h in ambient air to create a chemically stable and hydrophilic oxidized P*Si* scaffold¹⁵⁹.

Results

Aptamers Immobilization: Amino-terminated aptamers are conjugated to the oxidized PSi films by carbodiimide coupling chemistry. The first two steps of the chemistry, amino-silanzation and carboxylation, slightly differ in solvents and materials for each sensing system. For the anti-AGR2 aptamer immobilization, the oxidized PSi film is amino-silanzed by incubation in 1% v/v APTES and 1% v/v DIEA in ddH₂O solution for 1 h, followed by washing with ddH₂O and ethanol and drying under a nitrogen stream. Subsequently, the amino-activated PSi samples are annealed at 100 °C for 15 min. Next, carboxylation is achieved by incubation in a solution of succinic anhydride (10 mg mL⁻¹) and 2% v/v DIEA in ACN for 3 h, followed by extensive rinsing with ACN and ddH₂O and drying under a nitrogen stream.

The anti-his-tag aptamer, 6H7, and the anti-protein A aptamer are immobilized by the method described by Urmann et al ^{26, 29}. Briefly, the oxidized PSi films are reacted with a solution of 42 mM APTES in toluene for 1 h, followed by a thorough rinsing with toluene, ethanol and acetone and drying under a nitrogen stream. A similar annealing step is then performed, as described above. The APTES-modified surface is then incubated in a solution of 100 mg of succinic acid in 4.7 mL of DMSO and 300 µL of 0.1 M NaHCO₃ (pH 9.4) for 30 min, followed by washing with DMSO and ddH₂O and dried under a stream of nitrogen.

Subsequently, for both systems, the carboxylated samples are reacted with EDC (10 mg mL⁻¹) in the corresponding selection buffer for 1 h, followed by introduction of 50 µM anti-AGR2 aptamer or 75 µM anti-his tag or anti-protein A aptamers in selection buffer, and incubation for 1 h. The samples are then washed with Tris buffer, to deactivate remaining reactive EDC groups on the surface. Finally, the aptamer-functionalized PSi is exposed to boiling ddH₂O for 2 min, and gently dried under a nitrogen stream, to unfold any secondary structures of the aptamer prior to further use.

Antibody Immobilization: The oxidized PSi surface is first amino-silanzed in 1% v/v APTES and 1% v/v DIEA in ddH₂O solution for 1 h, followed by washing with ddH₂O and ethanol and drying under a nitrogen stream. Subsequently, the surface is exposed to 2% aqueous GA solution for 30 min, washed with ddH₂O and dried under a nitrogen stream, followed by incubation with 50 mM sodium cyanoborohydride in HEPES for 30 min, in order to stabilize the Schiff base formed during reaction of the aldehyde groups with the amine groups ²⁴². Next, the surface is washed with HEPES and streptavidin (100 µL; 100 µg mL⁻¹ in PBS) is applied and incubated for 1 h. The surface is washed with PBS and stabilized again with sodium cyanoborohydride. Next, a blocking step with 0.3M ethanolamine in BBS buffer (0.15M borate buffered saline, pH 9.0) is carried out for 30 min, followed by washing with BBS and PBS buffers. Finally, the surface is reacted with biotinylated protein A (100 µL; 100 µg mL⁻¹ in PBS) for 1 h, rinsed with PBS and incubated with the antibody (50 µL; 100 µg mL⁻¹ in PBS; in humidity chamber) for 1 h at room temperature and then overnight at 8 °C. On the next day, the film is rinsed with PBS buffer prior to biosensing experiments.

Determination of Aptamer Concentration within PSi

Quantification of the immobilized aptamer concentration is carried out by the method described by Hu et al ⁴³, for the anti-AGR2 and anti-his tag aptasensors. We used aptamers with a thiol and FAM6 modification which are diluted in TE buffer (10 mM Tris and 1 mM EDTA, pH 8.0), supplemented with 30 mM DTT. Prior to use, the aptamer is cleaned in NAP-5 column (GE healthcare), in HEPES buffer (0.05M HEPES, pH 7.5) to remove the DTT reducing agent. After amino-silanization of the oxidized PSi films, the samples are reacted with SPDP (6.5 mM in ethanol) for 30 min, followed by washings with IPA and ddH₂O, three times. 50 μ M anti-AGR2 or 75 μ M 6H7 aptamers in HEPES buffer are then introduced to the samples and incubated for 1 h, followed by extensive washing with HEPES, to remove physisorbed aptamer molecules. As a control, oxidized PSi is similarly functionalized with SPDP, but without aptamer. The surface is washed until no fluorescence signal is detected in the collected washing solution, compared to the control.

For the anti-AGR2 aptamer, the aptamer-functionalized PSi is incubated with DTT solution (250 μ L; 25 mM in HEPES, pH 7.5) for 30 min, resulting in immediate aptamer cleavage from the surface, by disulfide bond reduction. The cleaved aptamer solution is collected and the absorbance is measured at 495 nm using a plate reader (Thermo Scientific Varioskan), as described by Hu et al ⁴³. For the anti-his tag aptamer, the aptamer cleavage from the surface is slower, attributed to the different amino silanization procedure. Thus, the aptamer functionalized surface is incubated with reducing solution for 24 h, followed by solution collection and replacement with a new reducing solution. This process is repeated until no fluorescence signal is observed in the collected solution (compared to the control). The fluorescence of the collected solutions is analyzed by a plate reader at excitation and emission wavelength values of 490 nm and 525 nm, respectively, enabling more sensitive determination of the slower cleavage process. The measured absorbance or fluorescence values are correlated to the respective aptamer concentrations using a calibration curve, which is constructed using known concentrations of FAM6-labeled aptamer (in 25 mM DTT in HEPES buffer).

Biosensing Experiments

Protein Targets: A 60 kDa his-tagged protein from the Arabinanase family, named D2, and a 35 kDa his-tagged tyrosinase from *B. megatherium* are used as targets for the anti-his tag 6H7 aptamer-functionalized PSi ²⁶. The his-tagged tyrosinase is also detected by an anti-his tag antibody-functionalized PSi. The 45 kDa recombinant protein A from *S. aureus* is used as a target for the anti-protein A aptamer ²⁹ and the 22 kDa AGR2 protein is detected by the anti-AGR2 aptamer functionalized PSi.

Optical Setup: RIFTS method is utilized for real-time monitoring of changes occurring within the porous nanostructure by detection of variations in the average refractive index of the porous layer ^{17, 18, 26}. The aptamer or antibody functionalized PSi sample is mounted in a custom-made Plexiglas cell, which is fixed during the experiments to ensure that the reflectivity is measured at the same spot

Results

throughout the experiment. Interferometric reflectance spectra are collected with a charge-coupled device (CCD) spectrometer (Ocean Optics, USB 4000) fitted with an objective lens coupled to a bifurcated fiber-optic cable. A tungsten light source is focused onto the center of the sample with a spot size of approximately 1 mm². Illumination and reflectivity detection are performed perpendicular to the surface. Reflectivity spectra are collected in real time in a wavelength range of 450-900 nm and analyzed by applying fast Fourier transformation (FFT), as previously described by Massad-Ivanir et al.¹⁷². The latter results in a single peak, which position along the x-axis equals the effective optical thickness (EOT) of the porous layer and is the product of average refractive index and the thickness of the porous layer.

Experimental Procedure: For the anti-his tag biosensor, the surface is first washed with elution buffer for 30 min to unfold the aptamer. Then and for all biosensing systems, the P*Si* biosensor is incubated with the baseline buffer, corresponding selection buffer for the aptasensors or PBS for the immunosensor, for at least 30 min and until a stable baseline is acquired. Next, the target protein, diluted in the baseline buffer, is introduced, and allowed to incubate for 1 h or until a steady state signal. Subsequently, the biosensor is extensively washed with the baseline buffer. Throughout the experiment, the reflectivity spectra are recorded every 15 s, while during buffer exchange and rinsing steps, reflectivity measurements are shortly paused.

Data Analysis: Reflectivity data are presented as relative ΔEOT , defined as

$$\frac{\Delta EOT_t}{EOT_0} = \frac{EOT_t - EOT_0}{EOT_0} \quad 5.2.1$$

where EOT_0 is the averaged EOT signal obtained during baseline establishment. For the binding curve, the EOT_t used is the averaged EOT signal at equilibration, following the wash of unbound proteins.

LOD is calculated as the protein concentration for which the optical signal equals $3 \cdot \sigma$, where, σ is the standard deviation between relative EOT values, measured during baseline establishment. Non-linear regression of obtained data was performed with GraphPad Prism software utilizing the model for specific binding with a hill slope, according to:

$$Y = \frac{B_{\max} \cdot X^h}{(K_D^h \cdot X^h)} \quad 5.2.2$$

B_{\max} is the interpolated concentration at which the maximum biosensor response is reached and K_D is the apparent dissociation constant, which is the target concentration needed to reach the half-maximum biosensing signal. h is the Hill coefficient, which gives information about the stoichiometry of the binding interaction^{314, 315}. Table 5.2.1 summarizes the fitted K_D values.

Numerical Simulations

We performed numerical simulations of the governing equations using finite differences. We first discretized the spatial derivatives using a second-order central difference approximation with uniform grid spacing, leading to a series of coupled ordinary differential equations. We then integrated forward in time the resulting set of ordinary differential equations using Matlab's routine ode15s (Matlab R2018sb, MathWorks, Inc.). For the simulation we used the parameters of the aptasensors, as summarized in Table S5.2.1 (Supporting Information): height of solution above the PSi of 0.001 m, porous layer thickness of $5.5 \cdot 10^{-6}$ m, average pore diameter of $50 \cdot 10^{-9}$ m, hydrodynamic radius of analyte of $5.3 \cdot 10^{-9}$ m, hydrodynamic radius of capture probe of $3.0 \cdot 10^{-9}$ m, protein bulk diffusivity of $7 \cdot 10^{-11} \text{ m}^2 \text{ s}^{-1}$, capture probe concentration within the PSi layer of $3.6 \cdot 10^{-3} \text{ M}$, capture probe surface density of $1.2 \cdot 10^{-8} \text{ mol m}^{-2}$, reaction association rate of $1.21 \cdot 10^3 \text{ M}^{-1} \text{ s}^{-1}$ and reaction dissociation rate of $6.32 \cdot 10^{-4} \text{ s}^{-1}$. For higher affinity interaction simulation, a reaction association rate of $1 \cdot 10^5 \text{ M}^{-1} \text{ s}^{-1}$ and reaction dissociation rate of $1 \cdot 10^{-4} \text{ s}^{-1}$ are used.

Results and Discussion

PSi-Based Biosensors for Protein Targets

PSi Fabry-Pérot thin film-based biosensors are widely studied for detection of various target molecules^{22, 332}. Over the past few years, we have established several such biosensors for detection of different protein targets^{26, 29} (see Table 5.2.1), using both antibodies and aptamers as recognition elements. All these biosensors are based on a similar oxidized PSi nanostructure, which is $\sim 5 \text{ }\mu\text{m}$ thick, and is characterized by interconnected cylindrical pores with an average diameter of 50 nm and a porosity of $>70\%$ ^{26, 29}, where capture probe molecules (amino-terminated DNA aptamers or antibodies) are immobilized via different techniques^{26, 29, 177, 302}.

Biosensing experiments are performed in a conventional cell setup, illustrated in Figure 5.2.1a-i, where the target protein solutions are introduced on top of the biosensor and incubated (without convection). Figure 5.2.1b presents characteristic biosensing results for an aptasensor upon incubation with different concentrations of the target protein, where the EOT changes are plotted as a function of time. As the target protein diffuses in the bulk solution towards the pore entry (Fig. 5.2.1a-ii), it infiltrates into the nanostructure, diffuses and simultaneously interacts with the immobilized aptamer molecules (Fig. 5.2.1a-iii and iv, respectively), resulting in an increase in the EOT signal with time. After the EOT signal reaches an equilibrium, the biosensor is washed with buffer solution to remove non-bound target molecules and the attained signal is used for constructing a binding curve. Figure 5.2.1c presents characteristic binding curves for several studied capture probe-target pairs and their corresponding curve fit, utilizing a model for specific binding with a Hill slope^{314, 315}. Surprisingly, all the investigated biosensors present a similar performance, with a dynamic range in the lower micromolars and a measured limit of detection (LOD) of $\sim 1 \text{ }\mu\text{M}$, regardless of the nature of the capture probe, the target

Results

protein, and their binding affinity. Moreover, the apparent dissociation constant (K_D) values, as calculated from the binding curves, are in the range of 14-31 μM , where these values are significantly higher by few orders of magnitude from those reported in the literature, see Table 5.2.1. These results may suggest that the major limiting factor of these biosensors is the porous platform and specifically the involved complex mass-transfer phenomena. As the binding behavior is similar regardless of the theoretical affinity between the capture probe and the target, we hypothesize that the effect of reaction kinetics is less pronounced. Yet, as any measurement is limited by the experimental setup, the signal

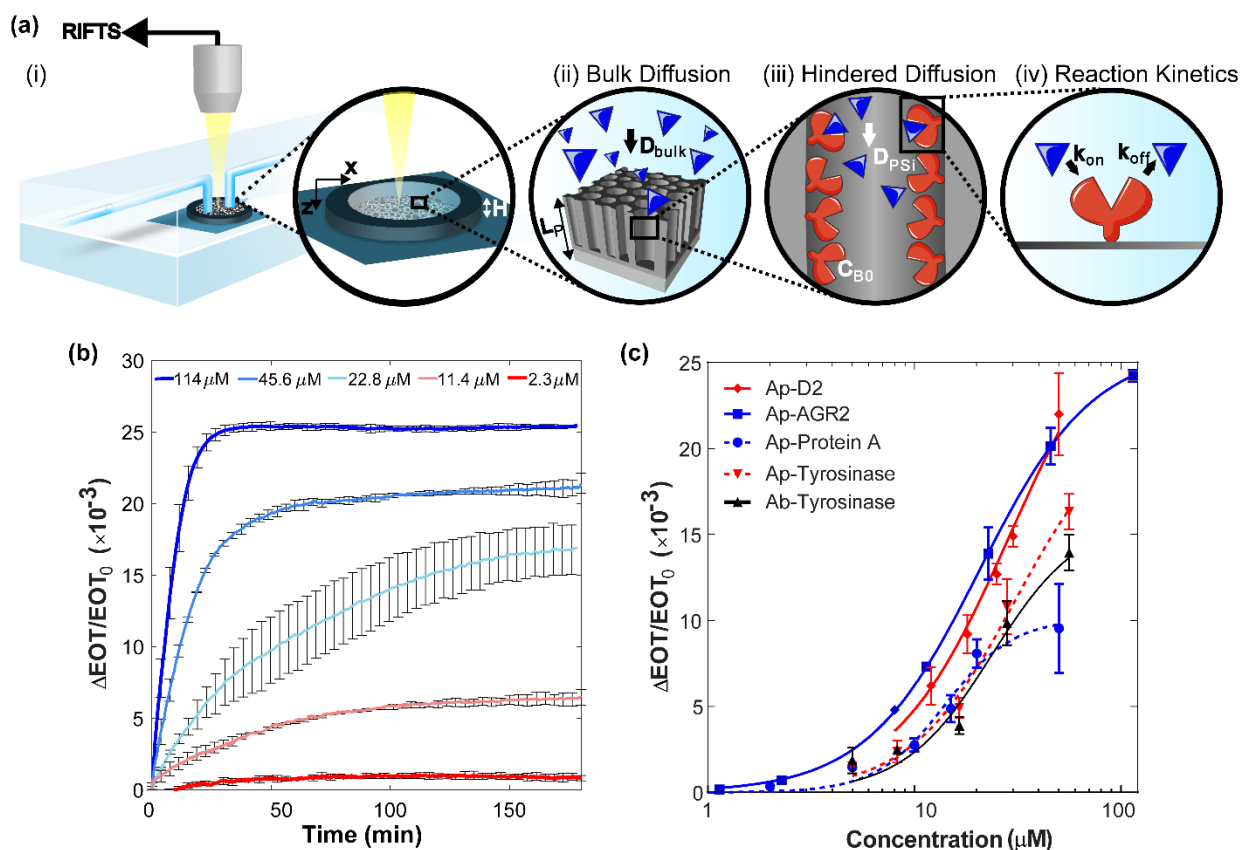


Figure 5.2.1. PSi biosensor setup and characteristic biosensing results for different capture probe-target pairs. (a) Schematic illustration of the PSi biosensing system: (i) A traditional cell setup used for the RIFTS biosensing experiments. The PSi-based biosensor is fixed in the cell with an O-ring, confining the introduced solution to a height of H . (ii) The target solution is introduced to the cell and target proteins diffuse to the PSi biosensor with a diffusivity D_{bulk} . (iii) As arriving to the pore entry, the proteins diffuse inside the porous nanostructure with a diffusivity D_{PSi} . The PSi is functionalized with capture probe molecules at a concentration of c_{B0} and the porous layer thickness is L_p . (iv) While diffusing, the target binds to the immobilized capture probe with kinetic parameters of k_{on} and k_{off} . (b) Characteristic biosensing results presenting the relative EOT changes with time for anti-AGR2 aptasensors upon incubation with different concentrations of AGR2 protein solutions ($n \geq 3$). The relative EOT increases with the infiltration and diffusion of the target protein into the porous layer, followed by binding to the immobilized aptamer probes. (c) Binding curves of different protein targets on aptamer (Ap) or antibody (Ab)-functionalized PSi-based biosensors, fitted with a specific binding model with a Hill slope. The curves present a similar behavior, independent of the target protein, capture probe and their corresponding theoretical binding affinity.

processing method and consequently the noise of the system, these also play a role, as has been recently suggested by Barillaro and coworkers. They applied a different signal processing technique (named Interferogram Average over Wavelength, IAW) instead of the common EOT calculation, which resulted in a significant improvement in the LOD of the P*Si* biosensors^{19,20}. Yet, in the present work we focus on the fundamental mass transfer phenomena in P*Si* biosensors and study their effect on the biosensing performance.

Mass Transfer and Reaction Kinetics Model

The theoretical models, which describe the mass transfer in porous biosensors, and specifically P*Si*-based biosensors, commonly apply a perfect collector assumption to the porous layer^{23,45,396}. As such, the rate limiting step is assumed as the entry into the pores, while the diffusion within the pores is neglected and the porous surface is modeled as a flat capturing surface, with a capture probe surface density of b_m , as schematically illustrated in Figure 5.2.2a^{23,396,397}. The derivation of such model, named in this work as the ‘planar model’, is detailed in the Supporting Information. Our aim is to investigate a complete model, which includes both transport phenomena (to and within the pores), as well as reaction, as illustrated in Figure 5.2.2b. To this end, we formulate a one-dimensional model, termed in this work as ‘porous model’, describing the concentration of the target analyte as a function of time. We refer to a conventional cell setup with a solution height H above the P*Si* biosensor, a porous layer of thickness L_p and an average pore diameter of d_p . For simplification, we assume that the pores are stacked to each other and we neglect the inter-pore distance (consistent with the high porosity of the P*Si*). The concentration of the immobilized capture probe molecules and the introduced analyte are c_{B0} and c_{A0} , respectively. We assume no convection and one-dimensional diffusion, directed in the z axis only.

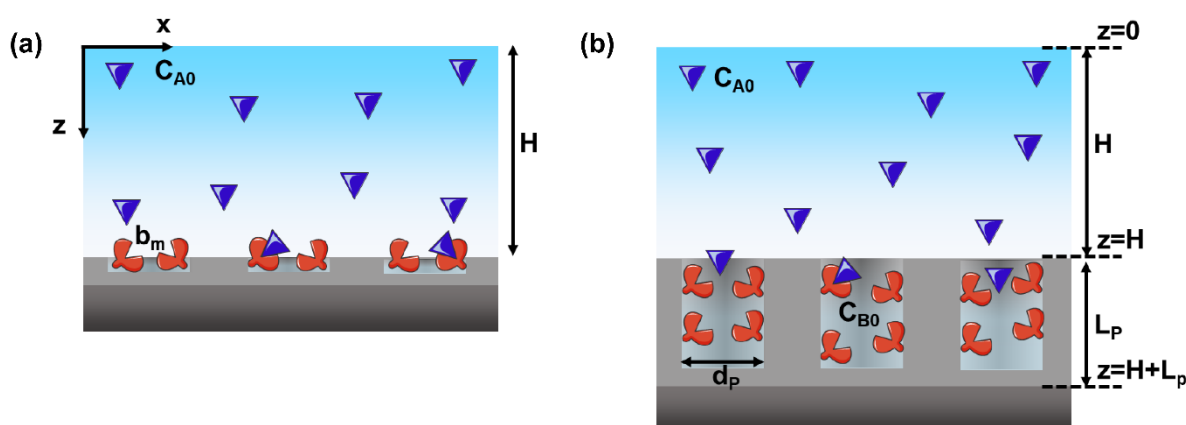


Figure 5.2.2. Schematic illustration of the (a) planar and (b) porous models, describing the mass transfer and reaction kinetic phenomena in the P*Si*-based biosensors. The P*Si* has a thickness of L_p and an average pore diameter of d_p . The solution height above the porous layer is H . Capture probes are immobilized at a concentration of c_{B0} and a density of b_m . The target analyte is introduced to the biosensor at a concentration of c_{A0} .

Results

In the bulk solution, the time evolution of the analyte concentration, $c_{A,bulk}(z, t)$, is governed by Fick's second law

$$\frac{\partial c_{A,bulk}}{\partial t} = D_{bulk} \frac{\partial^2 c_{A,bulk}}{\partial z^2} \quad 0 < z < H \quad 5.2.3$$

Subscripts of *bulk* refer to the bulk solution, where D_{bulk} is the analyte diffusivity coefficient in the bulk solution.

Within the porous layer, we describe the time evolution of analyte concentration, $c_{A,PSi}(z, t)$, by the diffusion-reaction equation

$$\frac{\partial c_{A,PSi}}{\partial t} = \frac{\partial}{\partial z} \left(\underset{\text{Diffusion}}{D_{PSi} \frac{\partial c_{A,PSi}}{\partial z}} \right) - \underset{\text{Reaction}}{k_{on} (c_{B0} - c_P) c_{A,PSi} + k_{off} c_P} \quad H < z < H + L_p \quad 5.2.4$$

Note that subscripts of *PSi* refer to the porous layer, where the analyte diffusivity coefficient is D_{PSi} . This is the main difference with respect to the planar model, in which the diffusion within the porous layer is neglected and the reaction is only considered at the PSi surface as a boundary condition (see Supporting Information).

We use the standard ligand-receptor model to describe the simultaneous reaction of the analyte with the immobilized capture probes, and accordingly the concentration of the bound analyte-probe complexes, $c_P(z, t)$, evolves as:

$$\frac{\partial c_P}{\partial t} = k_{on} (c_{B0} - c_P) c_{A,PSi} - k_{off} c_P, \quad 5.2.5$$

where k_{on} and k_{off} are the reaction association and dissociation rates, respectively.

The governing equations 5.2.3, 5.2.4 and 5.2.5 are subjected to the no-flux boundary conditions at the ceiling of the device, on top of the bulk solution ($z = 0$) and at the bottom of the pore ($z = H + L_p$) (see scheme in Figure 5.2.2), as well as the continuity of the concentration and the flux at the interface between the bulk and the pores ($z = H$),

$$\frac{\partial c_{A,bulk}}{\partial z} = 0 \quad \text{at} \quad z = 0, \quad 5.2.6$$

$$\frac{\partial c_{A,PSi}}{\partial z} = 0 \quad \text{at} \quad z = H + L_p, \quad 5.2.7$$

$$c_{A,bulk} = c_{A,PSi} \quad \text{at} \quad z = H, \quad 5.2.8$$

and

$$D_{bulk} \frac{\partial c_{A,bulk}}{\partial z} = D_{PSi} \frac{\partial c_{A,PSi}}{\partial z} \quad \text{at} \quad z = H. \quad 5.2.9$$

Results

We assume the initial analyte concentration in the bulk is c_{A0} , and that the initial concentration of the analyte and of the immobilized analyte-probe complexes within the porous layer are both zero,

$$c_{A,bulk}(z, t = 0) = c_{A0} \quad 0 \leq z \leq H, \quad 5.2.10$$

$$c_{A,PSi}(z, t = 0) = c_{A0}[(1 - \theta(z))] \quad H \leq z \leq H + L_p, \quad 5.2.11$$

$$c_p(z, t = 0) = 0, \quad 5.2.12$$

where the function $\theta(z)$ is defined as

$$\theta(z) = \begin{cases} 0 & z = H \\ 1 & z > H \end{cases}. \quad 5.2.13$$

The governing equations 5.2.3, 5.2.4 and 5.2.5 are coupled through the boundary conditions 5.2.6-5.2.9 and should be solved together to obtain the concentration in the bulk and in the porous layer.

Within the porous layer, the constrained space of the pore leads to hindered diffusion of the analyte molecules. Thus, the diffusivity coefficient of the analyte within the PSi, D_{PSi} , should be corrected according to the molecular and hindered diffusion phenomena, accounting for steric restriction, hindered Brownian motion and energetic interactions of pore-solvent-analyte³⁹⁰. Empirical models for D_{PSi} describe the hindered diffusivity as a function of the parameter α , defined as the ratio of the hydrodynamic diameter of the analyte d_A and the diameter of the average pore $d_p(z, t)$, i.e. $\alpha(z, t) = d_A / d_p(z, t)$. The diameter of the average pore $d_p(z, t)$ decreases upon binding of the analyte to the immobilized probes on the pore walls and can be related to the bound analyte concentration c_p through

$$d_p(z, t) = d_{p0} - 2 \left[\frac{c_p}{c_{B0}} d_A + d_B \right], \quad 5.2.14$$

where d_{p0} is the initial diameter of the pore, and d_B is the hydrodynamic diameter of the probe. Thus, the ratio α is given by

$$\alpha(z, t) = \frac{d_A}{d_{p0} - 2 \left[(c_p / c_{B0}) d_A + d_B \right]}. \quad 5.2.15$$

For our study, we utilize the comprehensive model derived by Dechadilok and Deen *et al*³⁹⁴ for cylindrical pores for the estimation of D_{PSi} :

$$D_{PSi}(z, t) = D_{bulk} \left[\begin{array}{l} 1 + \frac{9}{8} \alpha \ln \alpha - 1.56034 \alpha + 0.528155 \alpha^2 + 1.91521 \alpha^3 \\ -2.81903 \alpha^4 + 0.270788 \alpha^5 + 1.10115 \alpha^6 - 0.435933 \alpha^7 \end{array} \right] \quad 5.2.16$$

Comparison of Theoretical Models to Experimental Results

We solve the three coupled non-linear differential equations numerically, using parameters characteristic of actual PSi aptasensors, described in Table 5.2.1. Specifically, we use an average pore diameter value of 50 nm, a porous layer thickness of 5.5 μm , and a bulk solution height of 1 mm. A representative value of $\sim 7 \cdot 10^{-11} \text{ m}^2 \text{ s}^{-1}$ is applied for the protein bulk diffusivity coefficient, based on the relative protein sizes³⁹⁸. For the kinetic binding rate constants, we use those of the pair of anti-protein A aptamer and protein A, which were previously determined by SPR as $1.21 \cdot 10^3 \text{ M}^{-1} \cdot \text{s}^{-1}$ and $6.23 \cdot 10^{-4} \text{ s}^{-1}$ for the association and dissociation rates, respectively³⁰⁵. The aptamer and target protein diameters are 3 and 5.3 nm, respectively. Please see Table S5.2.1 (Supporting Information) for a comprehensive summary of all values used for the numerical simulations.

We have experimentally determined the concentration of the immobilized aptamers within the porous layer, by using a fluorescently-labelled aptamer and its subsequent cleavage. This method was applied for the anti-AGR2 and anti-his tag aptasensors and the resulting aptamer concentration ranges between $1.0 \pm 0.2 \text{ mM}$ and $6.28 \pm 0.06 \text{ mM}$, respectively (see Table S5.2.2 for detailed results, Supporting Information). These values provide an order of magnitude estimation for the probe concentration for all studied aptasensors and thus, for the numerical simulations a representative value is used, i.e. aptamer concentration of 3.6 mM.

Figure 5.2.3a and 5.2.3b depict the real-time experimental binding curves of the investigated aptasensors, for detection of the target proteins at concentrations of 50 and 10 μM , respectively, in comparison to results obtained by numerical simulations. We present the simulation results for the porous model as well as those obtained for a planar model, where the porous layer is assumed a perfect collector as is conventionally considered in the literature^{23, 45, 396}. For the planar model (see detailed derivation of the model in the Supporting Information), we applied the same reaction kinetic parameters and capture probe surface density, as for the porous model. For the experimental binding curves, the percentage of target binding was calculated by normalizing the EOT signal to the maximal EOT signal obtained at aptasensor saturation with the target. While our suggested porous model presents a relatively good fit to the experimental results at both studied target concentrations, the planar model highly overestimates the binding rate, even at a high target concentration where mass transfer limitations should be less pronounced (Figure 5.2.3a). Only at long enough times, the experimental and the model curves converge, while at (relatively) short times, the planar model greatly diverge. Moreover, these deviations intensify at low target concentrations, as shown in Figure 5.2.3b for a target concentration of 10 μM (and in Figure S5.2.1 for lower target concentrations of 1 μM and 0.5 μM , Supporting Information), mainly ascribed to the decrease in the concentration gradient, i.e., diffusion driving force, for lower target concentrations. It should be emphasized that the porous model fits the experimental results also when applying other reaction rates, while the overestimation of the planar model is still apparent, as shown in Figure S5.2.2 (Supporting Information). Our results demonstrate that hindered diffusion has a major impact on the binding rates of PSi-based biosensors and cannot be neglected.

Results

Thus, the porous model is essential for accurate representation of the binding behavior, especially when studying relevant target concentrations⁴, which are orders of magnitude lower than those presented here.

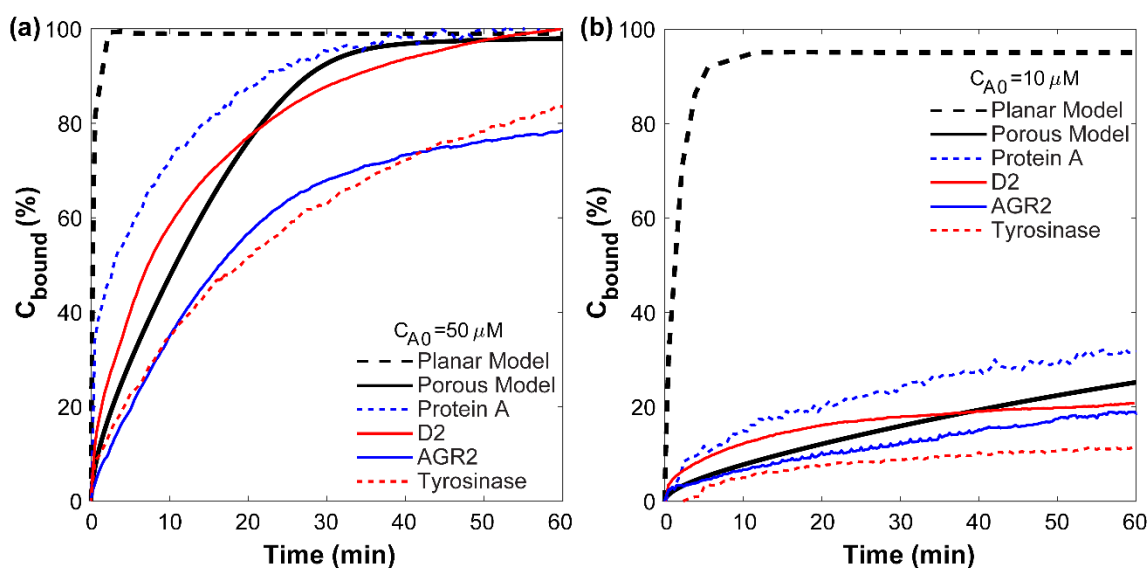


Figure 5.2.3. Comparison of experimental binding curves of the investigated aptasensors to numerical simulation results obtained for the porous and planar models, at target concentrations of (a) $50 \mu\text{M}$ and (b) $10 \mu\text{M}$. For the experimental data, the EOT signals for each aptasensor were normalized to the maximal EOT signal obtained upon aptasensor saturation with the target. For the simulated binding, the curves present the bound analyte, normalized to the probe concentration or density, at the bottom of the pore as a function of time.

To illustrate the significance of each of the diffusion phenomena, we present in Figure 5.2.4 the simulated distribution of the target concentration (in z axis) in the bulk solution and in the porous layer, at different time points. At the initial stage of binding, the target is rapidly depleted near the pore entry (to a value below 5% of the initial target concentration) and a diffusion boundary layer is formed, spanning deep into the bulk solution. With the progress of the diffusion of the target into the porous layer, the concentration gradient slowly diminishes, until equilibration is reached. In contrast, for a planar model, the depletion of the target at the biosensor surface is significantly lower, as shown in Figure S5.2.3 (Supporting Information). These results indicate that both diffusion processes, in the bulk and in the porous layer, are interrelated: the diffusion within the porous layer leads to a rapid and substantial formation of a diffusion boundary layer within the bulk solution. Thus, the similar binding behavior observed for the different studied biosensors (see Figure 5.2.1c) is ascribed to the mass transfer limitations and to the interconnected effect of both diffusion processes. These conceal the capture probe-target protein reaction and our main conclusion from this study is that without significantly accelerating the mass transfer rate, the contribution of higher affinity capture probes for improving the biosensing performance (i.e., sensitivity and detection time) will be imperceptible. It should be kept in mind that the system noise also plays a critical role in determining the biosensor performance and it should be

Results

minimized. Thus, when applying methods for mass transfer acceleration, the resulting LOD will also depend on their effect on the noise.

We further demonstrate the contribution of mass transfer acceleration to the enhancement of the apparent binding rate by application of mixing of the target solution on top of the biosensor. This results in a constant analyte concentration within the solution above the porous nanostructure, eliminating the diffusion gradient in the bulk solution and decreasing the diffusion pathlength to the porous layer⁵. Figure S5.2.4 (Supporting Information) compares biosensing results with and without target mixing (10-min mixing followed by incubation vs. incubation only). During mixing, the EOT signal is observed to rapidly increase and a significantly higher apparent binding rate (by >5 fold) is obtained in comparison to the non-mixed system; thus, demonstrating the profound effect of mass transfer acceleration on enhancing the target flux into the porous layer. It should be noted that we use a manual mixing in this work, while a better performance in terms of sample-to-sample reproducibility will be obtained upon mixing automation.

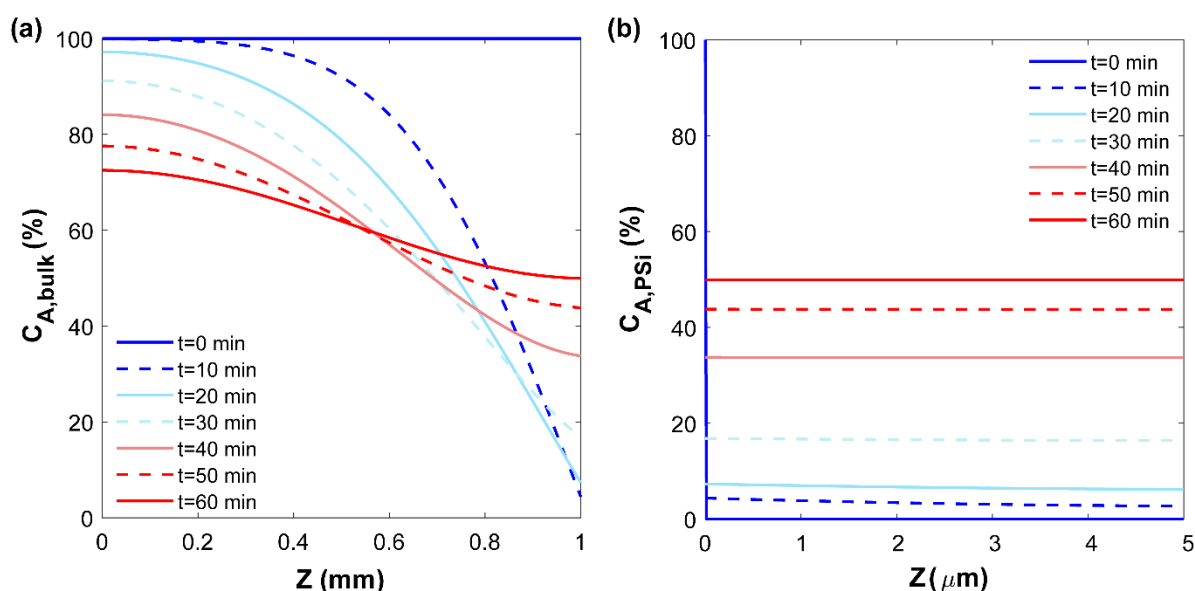


Figure 5.2.4. Simulation of the distribution of the target concentration in z axis at different time points in (a) the bulk solution and (b) the porous layer, obtained by the porous model. The target concentration is normalized to an initial target solution concentration of $50 \mu\text{M}$.

Effect of Biosensor Characteristics

We use the derived porous model to study the effect of important biosensor characteristics, which can be tailored during the biosensor construction, on the binding rate. The first parameter we examine is the capture probe surface density, which is considered of high importance for surface-based biosensors in general^{352, 399, 400} and PSi-based biosensors in particular^{21, 27, 43, 164}. While for both planar and porous surfaces an overall similar capture probe density may be attained, the large surface area of PSi allows immobilizing larger amounts of capture probes and their concentration within the nanoscale pores. This in turn reduces the binding time, affects the apparent off rate of the probe-analyte complexes and

Results

enhances the biosensor sensitivity, as has been previously suggested^{5, 21, 43}. In the present work we would like to investigate whether an excess of capture probes within the pores may lead to a counter effect on the mass transport rate. Figure 5.2.5a presents a simulation of the effect of capture probe surface density within the porous layer on the target binding rate, for different analyte concentrations. We apply in the simulations a capture probe density range of $\sim 10^{-11}$ to $\sim 10^{-8}$ mol m⁻², which has been utilized in P*Si*-based biosensors^{23, 27, 43}. Increasing the capture probe surface density results in higher binding rates until an optimal surface density value; above this value, the binding rate slightly decreases. For a higher affinity interaction (Figure 5.2.5b), with an association rate of 10^5 M⁻¹ s⁻¹ and dissociation rate of 10^{-4} s⁻¹, which is characteristic for antibody-ligand interactions^{165, 401}, increase in surface density results in a drastic decrease in the binding rate. We attribute this behavior to the decrease in the free porous volume available for the transport of the target. In addition, at a high probe density, a depletion region can rapidly build, which in turn will increase the thickness of the diffusion boundary layer in the bulk (adjacent to the pore entry)³⁹⁹, and as a result, both bulk and hindered diffusion rates will decrease. Our results suggest that mass transfer limitations require maintaining an optimum capture probe surface density, below a certain threshold, while considering immobilization levels that would produce a biosensor response with acceptable signal-to-noise ratio. This has also high significance for maintaining active probes while immobilized, avoiding steric crowding effects^{164, 351}.

Two additional key parameters which can be easily tailored for P*Si* biosensors are the porous layer thickness and pore diameter. These affect both the optical properties of the nanostructure and the hindered diffusion within the pores, as they dictate the available free porous volume for molecular transport^{18, 382, 383, 391}. Figure 5.2.5c presents the effect of porous layer thickness and pore diameter on the binding rate (as simulated at the bottom of the porous layer), while the capture probe and the analyte concentrations are kept constant. The results show a significant effect of the porous layer thickness on the binding rate, with the latter decreasing for increasing thickness. This agrees with other studies and is related to the increase in diffusion time inside the porous layer with increasing pore length, which scales as $t_d \propto L_p^2 / D_{P*Si*}$ ^{377, 378}. Thus, decreasing the P*Si* layer thickness will result in an improved biosensor sensitivity³⁷⁷. The impact of the pore diameter (in the range of 30-100 nm) on the binding rates is less pronounced. Yet, this result is valid for aptasensors, where the size of the capture probe is significantly lower than the diameter of the pores (see Table S5.2.2); whereas, for larger probes (e.g., antibodies) this pore diameter range will narrow^{164, 189}.

When higher affinity interaction parameters are used for the simulation (an association rate of 10^5 M⁻¹ s⁻¹ and dissociation rate of 10^{-4} s⁻¹, typical for antibody-ligand interactions), the effect of the layer thickness and pore diameter is intensified, see Figure 5.2.5d. The simulated binding rate decreases by orders of magnitude for thicker porous layer or smaller pore diameter. This is related to the impact of the mass transfer limitation in the bulk solution and the rapid formation of a depletion region at the pore entrance, owing to the fast uptake of the target. Thus, for biosensing interactions with higher affinity,

Results

the porous layer should be designed with smaller thickness and larger pore diameter, compared to lower affinity interactions. The number of pores in the PSi nanostructure, which can be correlated to the PSi porosity (see derivation in the Supporting Information), also characterizes the porous layer and influences the target capture rate. As the number of pores, and accordingly the porosity, decreases, a higher binding rate is observed, as presented in Figure S5.2.5 (Supporting Information). This is related to the higher diffusion flux into each pore. Nevertheless, the effect is less pronounced compared to the porous layer thickness and the pore diameter, even for a high affinity interaction (see Figure S5.2.5b, Supporting Information).

It should be kept in mind that the reflectivity of the PSi transducer, in terms of the intensity and number of fringes (for RIFTS), highly depends on the pore diameter and the thickness of the porous layer^{18, 382, 383}. Figure S5.2.6 (Supporting Information) shows the experimental reflectivity spectra for PSi films of different thicknesses, showing the decrease in the number of fringes for thinner porous films. This in turn affects the RIFTS signal processing, whereas the reflectivity of a layer with a thickness below 1 μm cannot be reliably analyzed. Thus, the porous layer thickness should be as low as possible to allow high binding rates and reflectance intensity, but this value should be optimized to yield sufficient number of fringes. The latter is also dependent on the pore diameter³⁸¹⁻³⁸³. The effect of the PSi structural characteristics on the optical properties is interrelated; thus their collective contribution should be considered upon nanostructure optimization^{16, 382}. To highlight the importance of a rational biosensor design, Figure S5.2.7 presents the simulated binding rate for various target concentrations, upon decreasing the porous layer thickness to 2 μm and the capture probe density to $2.3 \cdot 10^{-9} \text{ mol m}^{-2}$, compared to the original PSi aptasensor. These values have been chosen according to the simulation results of the effect of the PSi thickness and capture probe density on the target binding rate, as presented in Figure 5.2.5. A significantly enhanced binding rate is observed, suggesting that the LOD can be improved by at least 10-fold by simply adjusting the biosensor characteristics.

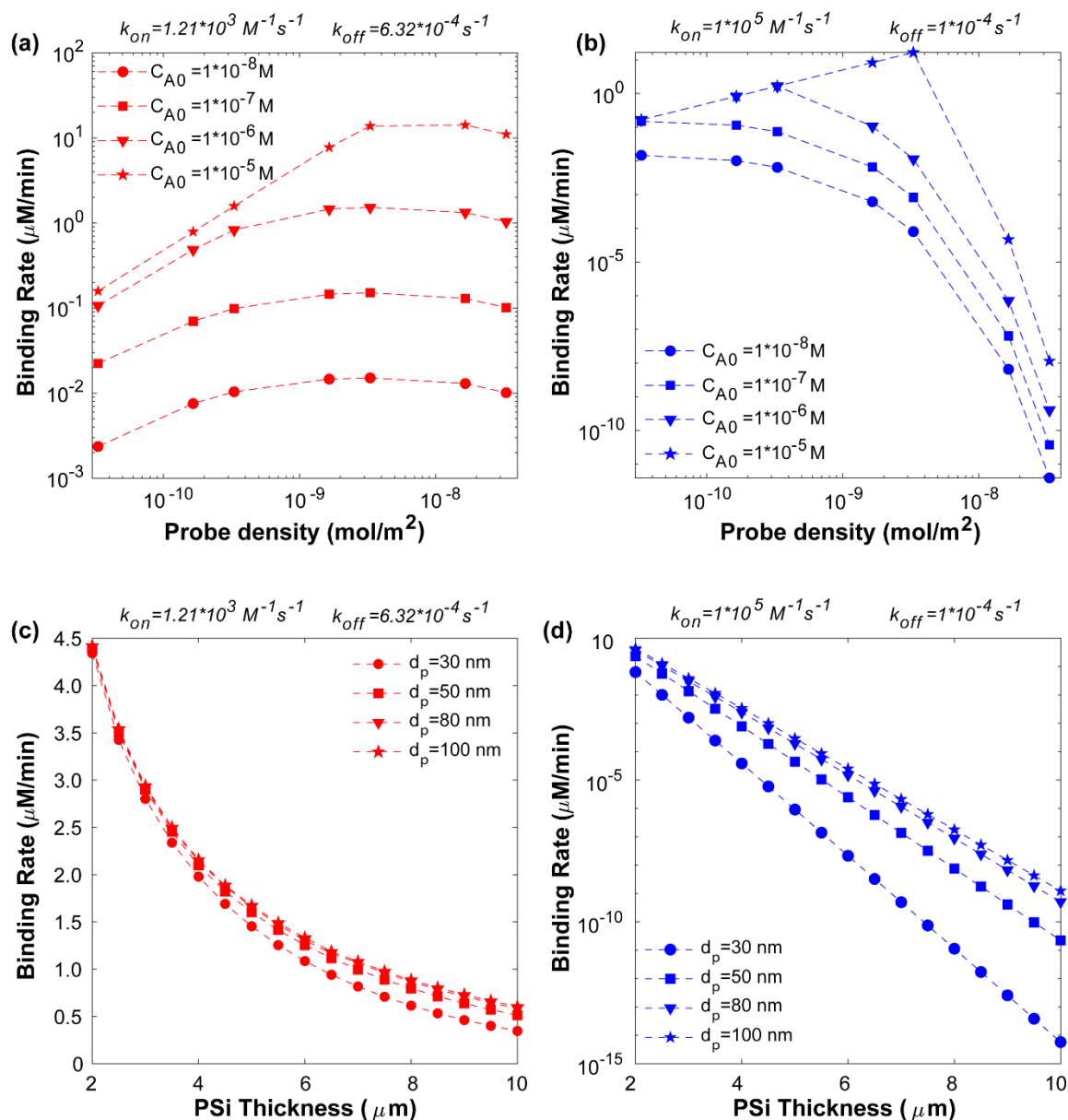


Figure 5.2.5. The effect of biosensor characteristics on the simulated target binding rate. (a, b) Effect of capture probe surface density for different target concentrations, for low ($k_{on} = 1.21 \cdot 10^3 \text{ M}^{-1} \text{ s}^{-1}$ and $k_{off} = 6.32 \cdot 10^{-4} \text{ s}^{-1}$) and high ($k_{on} = 10^5 \text{ M}^{-1} \text{ s}^{-1}$ and $k_{off} = 10^{-4} \text{ s}^{-1}$) affinity interactions, respectively. (c, d) Effect of porous silicon layer thickness for different pore diameters for a target concentration of $1 \mu\text{M}$, for low ($k_{on} = 1.21 \cdot 10^3 \text{ M}^{-1} \text{ s}^{-1}$ and $k_{off} = 6.32 \cdot 10^{-4} \text{ s}^{-1}$) and high ($k_{on} = 10^5 \text{ M}^{-1} \text{ s}^{-1}$ and $k_{off} = 10^{-4} \text{ s}^{-1}$) affinity interactions, respectively. The binding rate was calculated as the slope of bound target concentration vs. time curve, in a time frame of 60 min, at the bottom of the pore.

Conclusions

A theoretical model, in which the complex mass transfer processes involved in target capture within PSi-based transducers, is derived. The model considers the bulk diffusion of the target in the solution towards the biosensor surface, the hindered diffusion within the porous layer and simultaneous reaction

Results

with the immobilized capture probe molecules. We solve the model numerically using parameters which were derived experimentally and are characteristic of PSi-based biosensors. The model successfully captures the target binding rates of several PSi aptasensors designed for protein detection; while, the common-practiced model in which the PSi is assumed as a planar surface and thus neglects the hindered diffusion phenomenon, drastically overestimates the target binding rate. Numerical simulation results indicate an interrelated effect of both diffusion processes, in the bulk solution and in the porous layer, which cannot be separated. Thus, the diffusion within the porous layer should not be neglected and both diffusion phenomena are important to accurately represent the transport within PSi-based biosensors, especially at low target concentrations. The model results can explain ours and others encountered low sensitivity of PSi biosensors (in the micromolar range) and similar target capture regardless of the nature of the capture probe-target pair and their theoretical binding affinity. Thus, accelerating mass transport, while maintaining similar (or lower) noise levels, is essential to exploit the advantages of high affinity capture probes. It should be emphasized that while we focus in our work on mass transfer limitations, system noise and signal processing methods also affect the performance of the biosensor and should be considered for obtaining maximal enhancement of the biosensor.

The proposed theoretical model is used to investigate the effect of PSi biosensors characteristics, i.e., capture probe surface density, porous layer thickness and pore diameter, which can be tailored during biosensor construction, on the capture rate. Importantly, we show that the increased surface area of the PSi, which is one of the main advantages of these nanostructured transducers, can in turn lead to an excess of target binding sites. This results in further diffusion impedance in the bulk solution and the porous layer. Thus, the amount of immobilized capture probes and the corresponding surface density should be optimized to allow an efficient mass transfer rate, while still producing a biosensor response with a reliable signal-to-noise ratio. Porous layer thickness and pore diameter have also high impact on the binding rate; the latter decreasing for thicker PSi layers and smaller pore diameters. Yet, the pore diameter should be large enough to accommodate the bioreceptor and the target molecules, while the porous layer thickness should be thinned while allowing a reliable optical signal processing.

Supporting Information

Derivation of a Planar Model for the PSi-Based Biosensors (Perfect Collector Assumption)

The PSi biosensor is modelled as a perfect collector, as previously described by Lazzara *et al*³⁹⁶. One dimensional diffusion in the z direction is assumed. The analyte of interest is introduced to the PSi biosensor at an initial concentration c_{A0} and diffuses in the bulk solution towards the PSi surface with a diffusivity coefficient D_{bulk} . Bioreceptor molecules are immobilized on the PSi surface at a density of b_m . The change in analyte concentration in bulk solution is described by Fick's second law:

$$\frac{\partial c_{A,bulk}}{\partial t} = D_{bulk} \frac{\partial^2 c_{A,bulk}}{\partial z^2} \quad 0 < z < H \quad S5.2.1$$

with the following initial and no-flux boundary conditions:

$$c_{A,bulk}(z, t = 0) = c_{A0} \quad 0 \leq z \leq H \quad S5.2.2$$

$$\frac{\partial c_{A,bulk}}{\partial z} = 0 \quad \text{at } z = 0 \quad S5.2.3$$

At the PSi surface, the following boundary condition is applied, assuming continuity between the diffusive flux and reactive flux:

$$\frac{\partial b}{\partial t} = -\frac{d_p}{4L_p} D_{bulk} \frac{\partial c_{A,bulk}}{\partial z} \quad \text{at } z = H \quad S5.2.4$$

where b is the bound analyte-bioreceptor complex density on the PSi surface, d_p is the pore diameter and L_p is the porous layer thickness. Since both fluxes relate to a different area, equation S5.2.4

considers the area ratio between the pore entry area ($\frac{\pi d_p^2}{4}$) and the total area of the pore for reaction

($\frac{\pi d_p^2}{4} + \pi d_p L_p$), while assuming $d_p \ll L_p$:

$$\text{Ratio} = \frac{\frac{\pi d_p^2}{4}}{\frac{\pi d_p^2}{4} + \pi d_p L_p} = \frac{\frac{d_p}{4}}{\frac{d_p}{4} + L_p} \stackrel{d_p \ll L_p}{\approx} \frac{\frac{d_p}{4}}{L_p} = \frac{d_p}{4L_p}. \quad S5.2.5$$

The change in the bound complex density is described by:

Results

$$\frac{\partial b}{\partial t} = k_{on} (b_m - b) c_{A,bulk} |_{z=H} - k_{off} b, \quad \text{S5.2.6}$$

with initial condition:

$$b(z = H, t = 0) = 0. \quad \text{S5.2.7}$$

Comparison of Theoretical Models to Experimental Results*Table S5.2.1. Fitting parameters used for the numerical simulations, based on the properties of the different aptasensors.*

Parameter	Description	Units	Protein A	D2	Tyrosinase	AGR2	Simulation
H	Height of solution above PSi	m	0.001	0.001	0.001	0.001	0.001
L_p	Porous layer thickness	m	$5.5 \cdot 10^{-6}$	$5.5 \cdot 10^{-6}$	$5.5 \cdot 10^{-6}$	$5.0 \cdot 10^{-6}$	$5.5 \cdot 10^{-6}$
D_{bulk}	Analyte diffusivity in bulk	$\frac{m^2}{s}$	$7 \cdot 10^{-11}$	$7 \cdot 10^{-11}$	$7 \cdot 10^{-11}$	$7 \cdot 10^{-11}$	$7 \cdot 10^{-11}$
d_{p0}	Initial average pore diameter	m	$5 \cdot 10^{-8}$	$5 \cdot 10^{-8}$	$5 \cdot 10^{-8}$	$5 \cdot 10^{-8}$	$5 \cdot 10^{-8}$
d_A	hydrodynamic diameter of analyte	m	$\sim 5.3 \cdot 10^{-9}$	$\sim 6 \cdot 10^{-9}$	$\sim 4.0 \cdot 10^{-9}$	$\sim 5.0 \cdot 10^{-9}$	$\sim 5.3 \cdot 10^{-9}$
d_B	hydrodynamic diameter of probe	m	$\sim 3 \cdot 10^{-9}$	$\sim 3 \cdot 10^{-9}$	$\sim 3 \cdot 10^{-9}$	$\sim 3 \cdot 10^{-9}$	$\sim 3 \cdot 10^{-9}$
k_{on}	Reaction association rate	$\frac{1}{M \cdot s}$	$1.21 \cdot 10^3$ ³⁰⁵	n.a.	n.a.	n.a.	$1.21 \cdot 10^3$
k_{off}	Reaction dissociation rate	$\frac{1}{s}$	$6.32 \cdot 10^{-4}$ ³⁰⁵	n.a.	n.a.	n.a.	$6.32 \cdot 10^{-4}$
K_D	Dissociation constant	M	$0.522 \cdot 10^{-6}$ ³⁰⁵	$4.6 \cdot 10^{-6}$	$4.6 \cdot 10^{-6}$	$0.013 \cdot 10^{-6}$	-

*n.a. – values are not available

Table S5.2.2. Quantification of immobilized aptamer concentration and surface density on the P_{SiO}₂.

Aptasensor	P _{SiO} ₂ volume (cm ³)	P _{SiO} ₂ surface area (cm ²)	Moles of cleaved aptamer (nmol)	C _{B0} Concentration inside the P _{SiO} ₂ (mM)	b _m Density inside the P _{SiO} ₂ (mol m ⁻²)
Anti-AGR2	2.73·10 ⁻⁴	827	0.28±0.05	1.0±0.2	(3.3±0.6) · 10 ⁻⁹
Anti-his tag	3.01·10 ⁻⁴	910	1.89±0.02	6.28±0.06	(2.07±0.02) · 10 ⁻⁸

The concentration of the aptamer capture probes was experimentally determined for the anti-AGR2 and anti-his tag aptasensors, which slightly differ in the porous nanostructure characteristics, the aptamer concentration utilized for the immobilization, and the surface chemistry protocol (mainly the amino-silanization). Thus, the results give a reliable range for the immobilized aptamers for all studied aptasensors. Immobilized aptamer concentration and surface density are determined by dividing the cleaved aptamer moles from the surface by the total porous volume of area, respectively. The latter was measured in a previous study by nitrogen adsorption isotherms and application of BET (Brunauer-Emmett-Teller) model for a similar P_{SiO}₂ nanostructure³⁴¹. Since the P_{SiO}₂ utilized in the present study was characterized with a smaller layer thickness (5000-5500 nm vs. 7880 nm), the surface area was corrected according to the layer thickness ratio of both nanostructures. The area of the P_{SiO}₂ sample is 1.33 cm².

Results

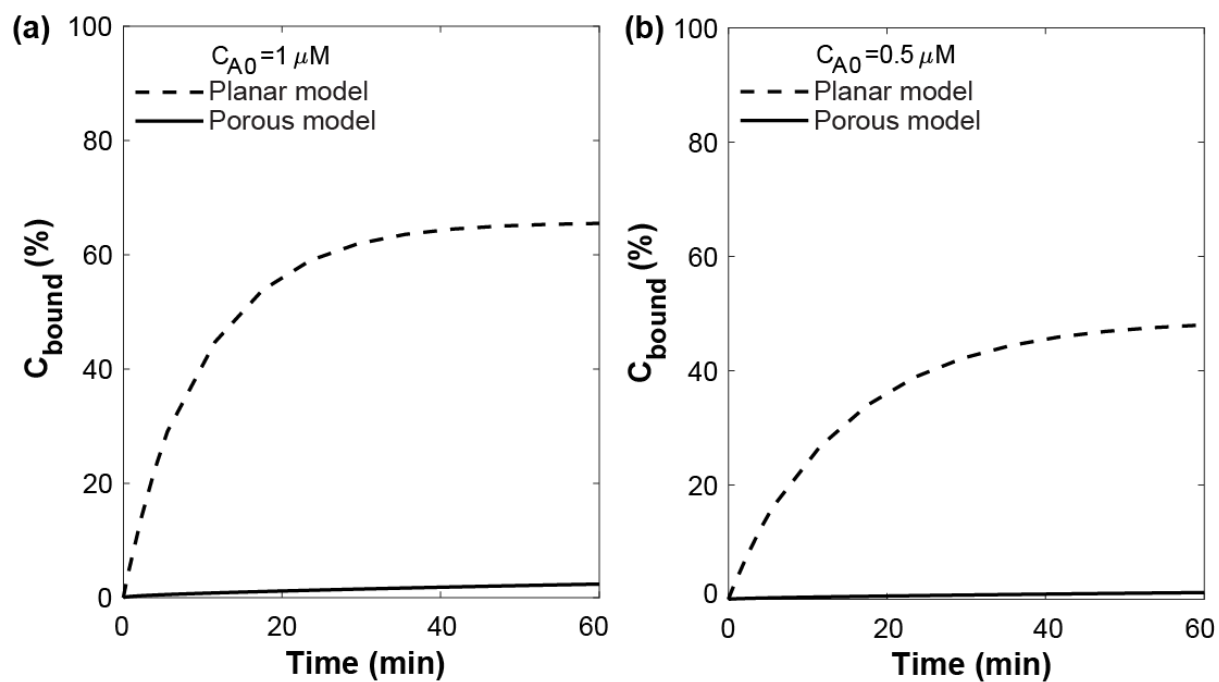


Figure S5.2.1. Simulated binding rates for the porous and planar models at target concentrations of (a) $1 \mu\text{M}$ and (b) $0.5 \mu\text{M}$. The curves present the bound analyte, normalized to the probe concentration, at the bottom of the pore as a function of time.

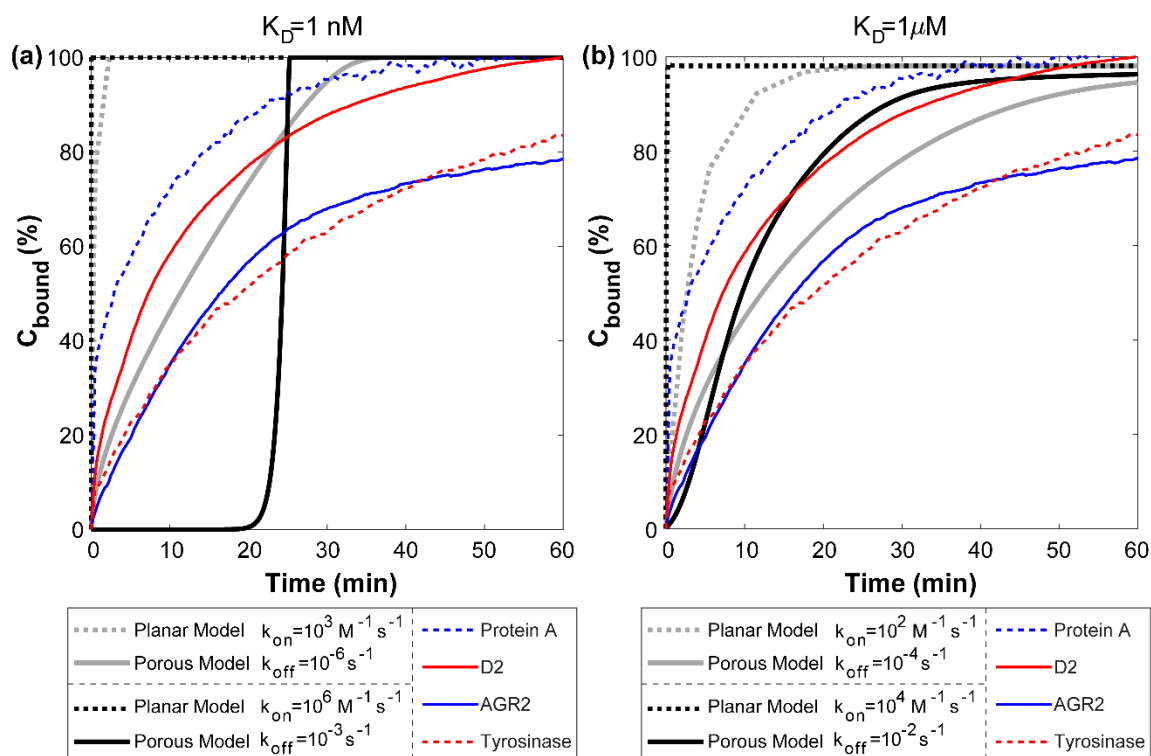


Figure S5.2.2. Comparison of experimental binding curves of the investigated aptasensors, at target concentration of $50 \mu\text{M}$ to numerical simulation results obtained for the porous and planar models, for two different binding affinity interactions with (a) $K_D=1 \text{ nM}$ and (b) $K_D=1 \mu\text{M}$. For the experimental data, the EOT signals for each aptasensor were normalized to the maximal EOT signal obtained upon aptasensor saturation with the target. For the simulated binding, the curves present the bound analyte concentration at the bottom of the pore as a function of time.

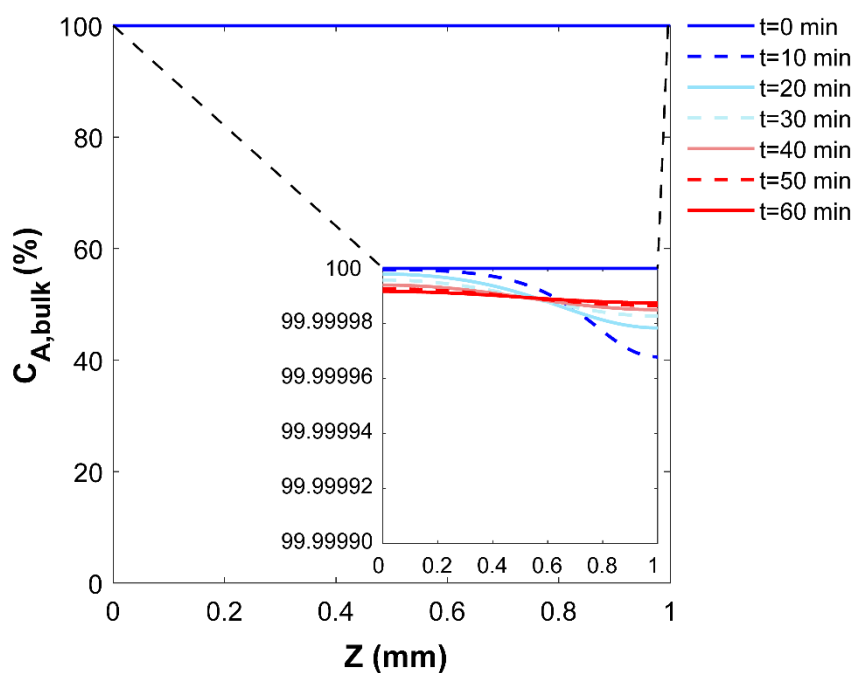


Figure S5.2.3. Change in target concentration in z axis in the bulk solution at different time points, simulated by the planar model. The aptasensor parameters were applied for the simulation and the concentration is normalized to the initial target concentration solution of $50 \mu\text{M}$.

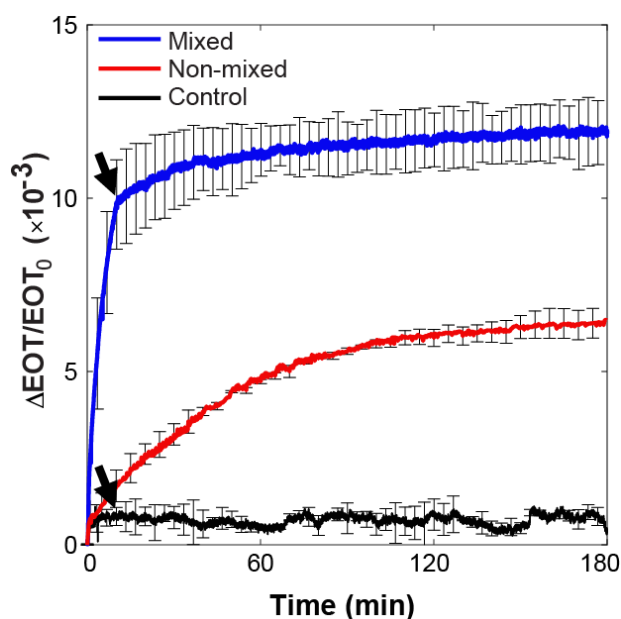


Figure S5.2.4. Relative EOT changes as a function of time for 10 min-mixed and non-mixed AGR2 ($11.4 \mu\text{M}$) biosensing experiments on anti-AGR2 aptasensor. As a control, the protein dilution buffer is mixed on the aptasensor for 10 min. Black arrows indicate the transfer from mixing to incubation. The results show the significant enhancement in binding rate and total signal obtained upon mixing.

The Effect of the PSi Porosity on the Binding Rate

The PSi porosity affects the boundary condition requiring a diffusion flux continuity between the bulk solution and the porous layer at the pore entry:

$$A_1 \cdot D_{bulk} \frac{\partial c_{A,bulk}}{\partial z} = A_2 \cdot D_{PSi} \frac{\partial c_{A,PSi,single}}{\partial z} \quad \text{at } z = H \quad \text{S5.2.8}$$

where A_1 is the surface area of the cell chamber, given by $A_1 = \frac{\pi d_{cell}^2}{4}$, where d_{cell} is the cell diameter.

A_2 is the surface area of the pore entries, given by $A_2 = N_{pores} \cdot \frac{\pi d_p^2}{4}$, where N_{pores} is the number of pores and d_p is the average pore diameter. The ratio of A_2 and A_1 is the porosity of the porous layer, termed P . Thus, the boundary condition is given by

$$D_{bulk} \frac{\partial c_{A,bulk}}{\partial z} = P \cdot D_{PSi} \frac{\partial c_{A,PSi,single}}{\partial z} \quad \text{at } z = H \quad \text{S5.2.9}$$

The effect of the porosity (and accordingly the number of pores) is presented in Figure S5.2.5, demonstrating higher binding rates for decreasing porosities.

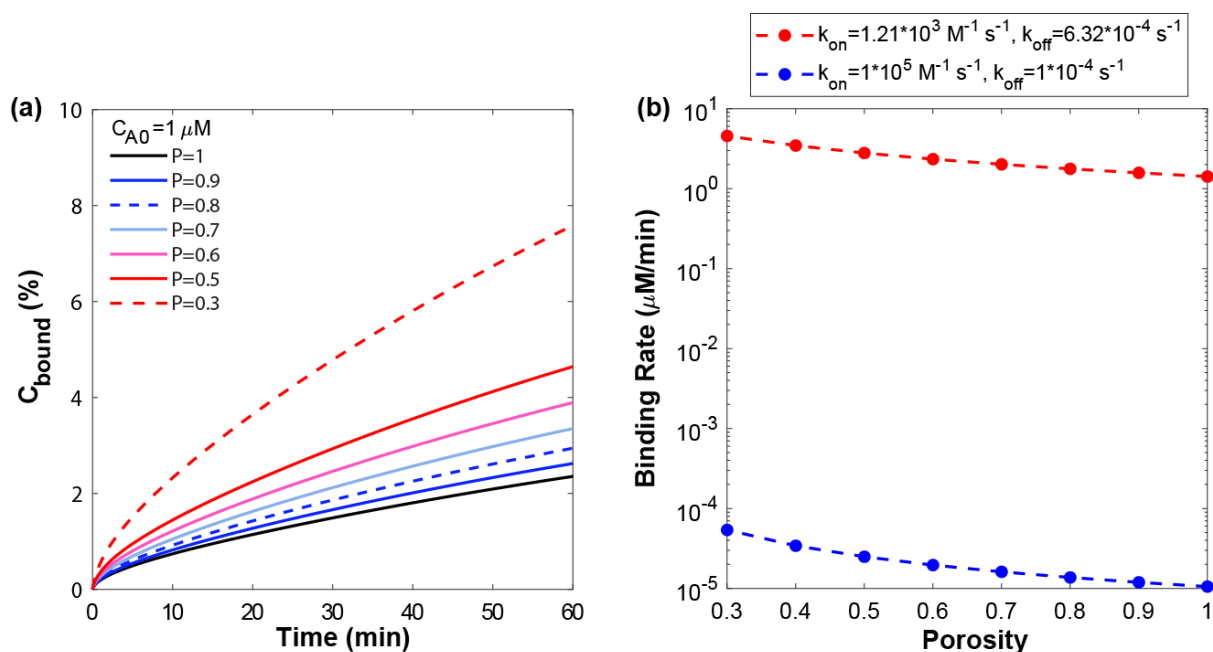


Figure S5.2.5. (a) Simulated binding rate for the porous model, for different PSi porosity values (P), at a target concentration of $1 \mu\text{M}$. The curves present the bound analyte, normalized to the probe concentration, at the bottom of the pore as a function of time. (b) Simulated effect of the PSi porosity on the target binding rate for a target concentration of $1 \mu\text{M}$, for low ($k_{\text{on}} = 1.21 \cdot 10^3 \text{ M}^{-1} \text{ s}^{-1}$ and $k_{\text{off}} = 6.32 \cdot 10^{-4} \text{ s}^{-1}$) and high ($k_{\text{on}} = 10^5 \text{ M}^{-1} \text{ s}^{-1}$ and $k_{\text{off}} = 10^{-4} \text{ s}^{-1}$) affinity interactions, respectively. The binding rate was calculated as the slope of bound target concentration vs. time curve, in a time frame of 60 min, at the bottom of the pore.

Characterization of PSi with Different Layer Thicknesses

PSi thin films were electrochemically etched at 375 mA cm^{-2} for different time periods, to create layers with different thicknesses. The porosity and layer thickness of each nanostructure were determined by spectroscopic liquid infiltration method (SLIM), as previously described ¹⁶. The results are presented in Table S5.2.3.

Table S5.2.3. Etching time and characterization results by SLIM.

Etching Time (s)	Porosity (%)	Thickness (μm)
60	72 \pm 1	11.3 \pm 0.3
30	77 \pm 1	5.5 \pm 0.2
10	73 \pm 4	1.92 \pm 0.01
5	-	~0.9*

*The PSi layer fabricated by electrochemical etching for 5 s could not be analyzed by SLIM. Thus, the thickness was determined by cross section imaging with high-resolution scanning electron microscopy (HRSEM).

Figure S5.2.6 presents HRSEM (Carl Zeiss Ultra Plus, at an accelerating voltage of 1 keV) top view micrographs of the different PSi films, as well as the reflectivity spectrum, measured in air. The pore diameter and porosity are similar for the different layers; thus, the differences in the reflectivity spectrum are attributed to the different thicknesses of the films.

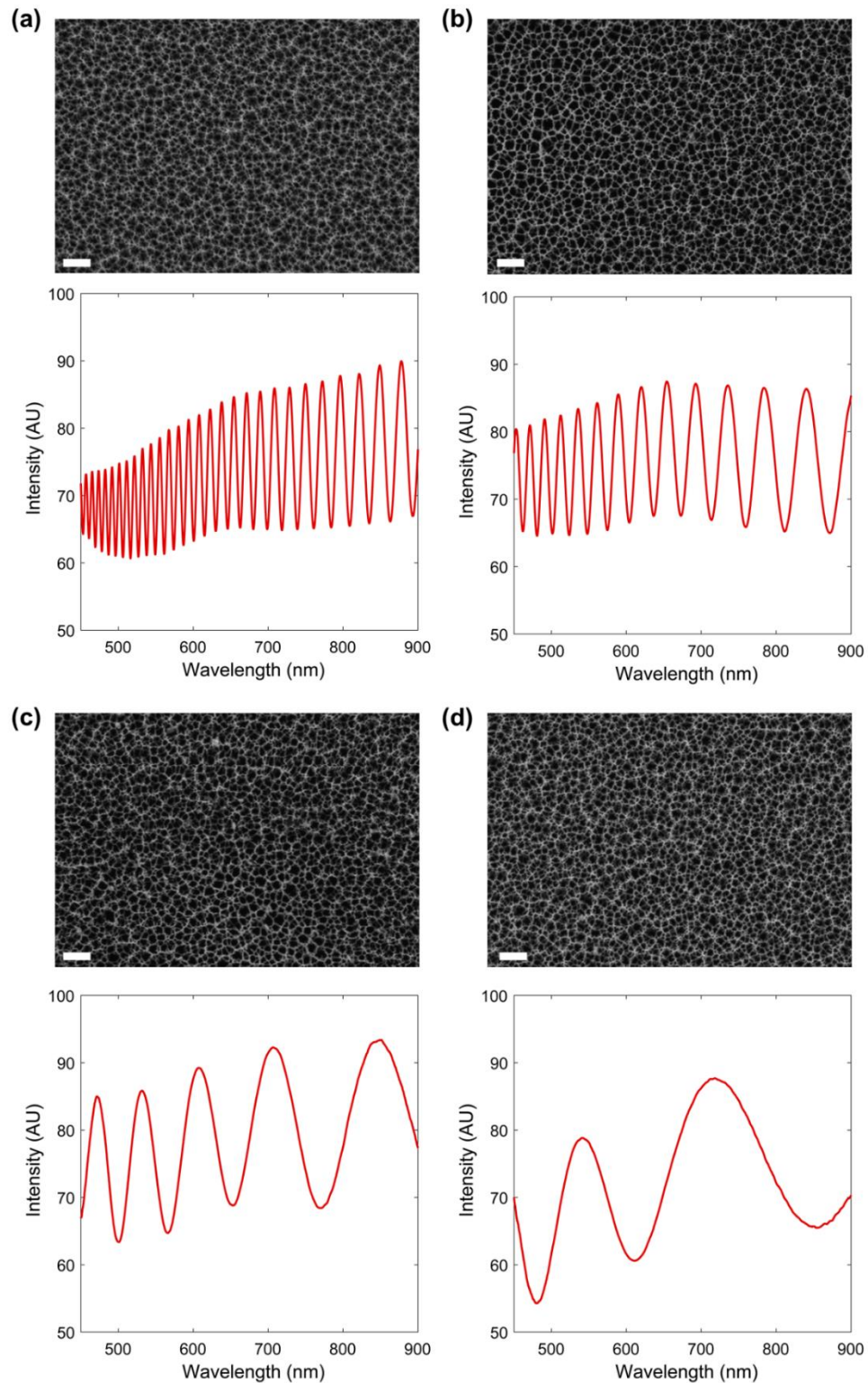


Figure S5.2.6. Top view SEM micrographs and reflectivity spectra of PSi with different layer thicknesses: (a) $11.3 \pm 0.3 \mu\text{m}$; (b) $5.5 \pm 0.2 \mu\text{m}$; (c) $1.92 \pm 0.01 \mu\text{m}$ and (d) $\sim 0.9 \mu\text{m}$. For (a-c) the thickness was determined by SLIM analysis, while the reflectivity spectrum of structure (d) could not be reliably analyzed by FFT. Thus, the thickness of a cross section was evaluated by SEM. The scale bar is 200 nm.

Results

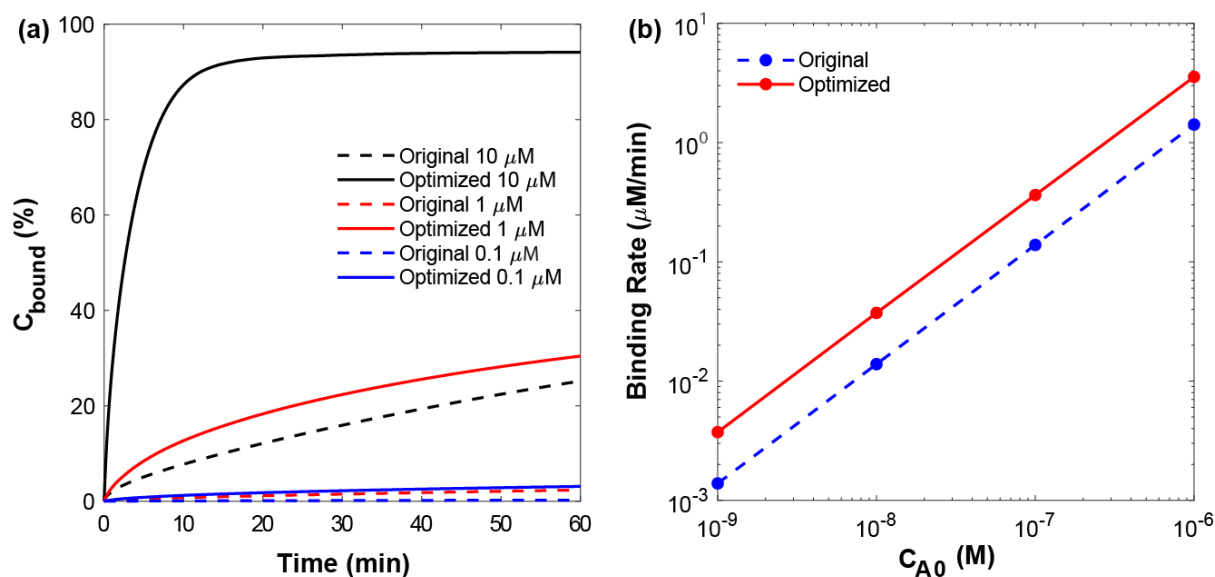
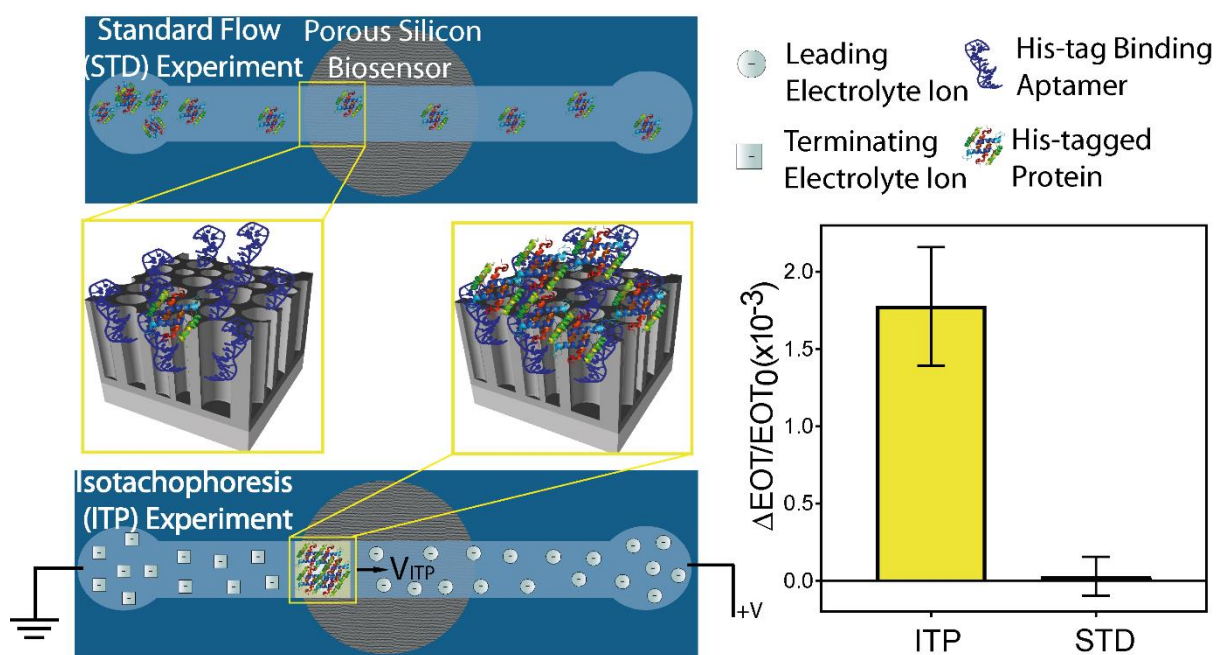


Figure S5.2.7. (a) Simulated binding rates for the porous model for an optimized aptasensor (porous layer thickness of 2 μm and capture probe density of $2.3 \cdot 10^{-9} \text{ mol m}^{-2}$) vs. the original aptasensor (porous layer thickness of 5.5 μm and capture probe density of $1.2 \cdot 10^{-8} \text{ mol m}^{-2}$), for different target concentrations. The optimized parameters were chosen according to the numerical simulation results of the effect of the PSi thickness and capture probe density on the target binding rate. Specifically, for the thickness, this value ensures a reliable analysis of the optical signal. The curves present the bound analyte, normalized to the probe concentration, at the bottom of the pore as a function of time. (b) Comparison of the simulated binding rates for the optimized and original aptasensors as a function of target concentration. The binding rate was calculated as the slope of bound target concentration vs. time curve, in a time frame of 60 min, at the bottom of the pore. Kinetic parameters were set to $k_{\text{on}} = 1.21 \cdot 10^3 \text{ M}^{-1} \text{ s}^{-1}$ and $k_{\text{off}} = 6.32 \cdot 10^{-4} \text{ s}^{-1}$.

5.3 On Chip Protein Pre-Concentration for Enhancing the Sensitivity of Porous Silicon Biosensors

Sofia Arshavsky-Graham, Naama Massad-Ivanir, Federico Paratore, Thomas Scheper, Moran Bercovici and Ester Segal

ACS Sensors 2 (12), 1767-1773 (2017)



Respective Table of Contents Image

Abstract

Porous silicon (PSi) nanomaterials have been widely studied as label-free optical biosensors for proteins detection. However, these biosensors' performance, specifically in terms of their sensitivity (which is typically in the micromolar range), is insufficient for many applications. Herein, we present a proof-of-concept application of the electrokinetic isotachopheresis (ITP) technique for real-time pre-concentration of a target protein on a PSi biosensor. With ITP, a highly concentrated target zone is delivered to the sensing area, where the protein target is captured by immobilized aptamers. The detection of the binding events is conducted in a label-free manner by reflective interferometric Fourier transformation spectroscopy (RIFTS). Up to 1000-fold enhancement in local concentration of the protein target and the biosensor's sensitivity are achieved, with a measured limit of detection of 7.5 nM. Furthermore, the assay is successfully performed in complex media, such as bacteria lysate samples, while the selectivity of the biosensor is retained. The presented assay could be further utilized for other protein targets, and to promote the development of clinically useful PSi biosensors.

Introduction

Since the seminal work of Sailor and coworkers in 1997¹⁵, porous silicon (PSi) nanomaterials have been extensively studied as optical transducers in a variety of biosensing schemes^{144, 159, 402, 403}. Different PSi-based optical structures, such as Fabry-Pérot thin films^{15, 160}, Bragg mirrors⁴⁰⁴, rugate filters^{153, 405} and microcavities^{406, 407}, have been exploited for detection of small molecules^{192, 252, 253, 255}, DNA^{15, 175, 184, 187}, proteins^{26, 29}, enzymes^{174, 231} and whole cells^{33, 172, 330, 408}. In these biosensors, selective capture of a target analyte within the PSi nanostructure, by surface-immobilized receptors, induces measurable shifts in the reflectivity spectrum^{15, 17, 18} allowing for real-time and label-free detection and quantification of the target in a simple yet reliable manner^{15-18, 26}. Despite the significant advantages of PSi biosensors, their application is limited due to their relatively low sensitivity, attributed mainly to the hindered diffusion of analytes into the porous matrix^{23, 42, 159, 189, 396}. Thus, most of the reports to date present measurements in the micromolar range for both DNA^{187, 278} and protein^{21, 26, 29, 186, 229, 402} targets. Significant research efforts have been directed towards improving the sensitivity of PSi-based biosensors. Several label-free strategies have been proposed for enhancing the sensitivity. Recently, Barillaro and co-workers presented a new signal processing technique which relies on the calculation of the average value spectral interferograms over wavelength, demonstrating detection of 150 pM bovine serum albumin (BSA) by non-specific adsorption in a PSi Fabry-Pérot thin film²⁰. In a later study, this methodology was applied for the detection of a protein biomarker of inflammation and sepsis at a concentration as low as 3 nM¹⁹. Weiss and co-workers developed a PSi microcavity membrane for a flowthrough biosensing platform, which improves the analyte transport into the pores and enables the detection of 500 nM streptavidin within 20 min²³.

Results

Several recent studies have demonstrated the potential in using isotachopheresis (ITP) focusing to enhance surface-based reactions^{245, 409-411}. ITP is a well-established electrophoretic method that utilizes a discontinuous buffer system for simultaneous extraction, separation and concentration of ionic species, based on their effective electrophoretic mobility⁴¹²⁻⁴¹⁴. Yet, as all the reported assays are based on fluorescence detection of the target, they require target labeling or utilization of a labeled secondary capture probe. In recent work, we have demonstrated the interfacing the PSi Fabry-Pérot interferometer with ITP to achieve highly sensitive and label-free detection of nucleic acids⁴². In the present work, we extend the applicability of this platform for a real-time pre-concentration of a protein target. As a model biosensing system, we utilize a PSi-based aptasensor for detection of his-tagged proteins, which is a characterized biosensor with a micromolar-range sensitivity²⁶. An oxidized PSi (PSiO₂) thin film, with an insulating oxide layer, is chemically functionalized with polyhistidine tag (his-tag) binding aptamers^{26, 303, 306, 333}, and integrated with a microfluidic system. ITP is then applied to focus the target protein into a highly concentrated protein zone and deliver it to the PSi biosensor. By holding this concentrated protein zone stationary on top of the biosensor via counter-flow⁴², the target protein is able to diffuse into the porous layer and interact with the capturing aptamers. The binding events are monitored throughout the entire ITP process with reflective interferometric Fourier transformation spectroscopy (RIFTS) method. We demonstrate detection of the target protein at concentrations as low as 7.5 nM and up to 1000-fold enhancement in sensitivity. Importantly, we show that this assay can be successfully applied in complex biological fluids such as bacterial lysate samples.

Experimental

Materials

Highly doped p-type Si wafers (B-doped, <100>-oriented, 0.95-0.98 mΩ·cm resistivity) were purchased from Sil'tronix Silicon Technologies. Aqueous HF (48%) was supplied by Merck. Ethanol absolute, toluene and isopropyl alcohol were supplied by Bio-Lab Ltd. Dimethyl sulfoxide (DMSO) was purchased from Carlo Erba Reagents. (3-Aminopropyl)triethoxysilane (APTES), succinic acid, *N*-(3-Dimethylaminopropyl)-*N'*-ethylcarbodiimide hydrochloride (EDC), Bis(2-hydroxyethyl)amino-tris(hydroxymethyl)methane (Bis-Tris), *N*-[Tris (hydroxymethyl) methyl] glycine (Tricine), and all buffer salts were purchased from Sigma-Aldrich Chemicals. All solution were prepared with Milli-Q water (18.2MΩ·cm). Anti-His Tag aptamer 6H7 (5'-GCT ATG GGT GGT CTG GTT GGG ATT GGC CCC GGG AGC TGG C-3') sequence was obtained from the U.S patent specification U.S. 7329742³⁰³. Aptamers were purchased with a 5'-amino modification from Integrated DNA Technologies. Alexa Fluor® 488 Succinimidyl Ester was purchased from ThermoFisher Scientific. Sylgard® 184 Silicon Elastomer kit (PDMS) was purchased from Dow Corning. Target his-tagged protein domain 4 of extracellular endo-α-(1→5)-L-arabinanase 1 (AbnA(D4)) was generously supplied by Prof. Yuval Shoham. *E. coli* K12 was generously supplied by Prof. Sima Yaron. Luria-Bertani (LB) medium was

Results

prepared by dissolving 5 g of NaCl, 5 g of yeast extract, and 10 g of tryptone in 1 L of deionized water. 5 mM phosphate buffered saline (PBS) was composed of 68.5 mM NaCl, 1.35 mM KCl, 5 mM Na₂HPO₄ and 1 mM KH₂PO₄ (pH 7.4). Selection buffer (SB) was composed of 50 mM K₂HPO₄ and 150 mM NaCl (pH 7.4). Elution buffer was composed of 50 mM K₂HPO₄, 150 mM NaCl and 1 M Imidazole (pH 7.4). LE buffer was composed of 200 mM Bis-Tris, 150 mM NaCl and 100 mM HCl and TE buffer was composed of 20 mM Bis-Tris and 10 mM Tricine.

Bacteria Lysate Preparation and Protein Labelling

A freeze culture of *E. coli* K12 was cultivated in a sterile LB medium (5 mL) overnight at 37 °C, under continuous shaking. The resulting culture was spun down in a standard lab centrifuge (2-16P, Sigma Laboratory Centrifuges) at 4500 rpm for 10 min, replacing the supernatant with 5 mL of TE buffer for the spiked lysate samples or with 0.1M NaHCO₃ (pH 8.3) buffer for the labelling process. After additional resuspension, the culture was ultrasonicated on ice, at 4 °C at a constant amplitude of 40% by using a Vibra cell VCX 750 instrument (Sonics & Materials Inc.). The culture was ultrasonicated for 2 min, with 30 s pulses and 30 s pauses in-between to avoid temperature rise. Cell debris were then removed by ultracentrifugation at 4 °C for 30 min at 12000 g (1-15K, Sigma Laboratory Centrifuges) and the supernatant was then used as the bacteria lysate samples.

The target protein (AbnA(D4)) and bacteria lysate for negative control experiments were fluorescently labelled with Alexa Fluor® 488 succinimidyl ester. The target protein or lysate samples were mixed with the dye at a ratio of 1:5 (molar ratio for the protein and weight ratio for the lysate) in NaHCO₃ buffer for 1 hr. Then the labelled proteins were separated from the free dye by PD SpinTrap G-25 (GE Healthcare Life Sciences) and eluted with PBS buffer. All concentrations were determined with NanoDrop instrument (NanoDrop 2000 spectrophotometer, Thermo Scientific). After addition of 10% glycerol, the labelled samples were aliquoted and stored at -20 °C until further use.

Bacteria lysate, fluorescently labelled and non-labelled, were analyzed with a standard SDS-PAGE. Briefly, the analysis was performed on a discontinuous buffer system³¹³, using 15% separating gel and 4% stacking gel. 30 µL bacteria lysate samples were mixed with 10 µL sample buffer (4x) and heated for 10 min at 95 °C. The gel was stained with 0.25% Coomassie brilliant blue (R-250) in 50% ethanol and 10% acetic acid and destained in 20:10:70 (v/v/v) methanol:acetic acid:water.

Fabrication and Characterization of Oxidized Porous Silicon Thin Film

Highly doped p-type crystalline Si wafers (0.95-0.98 mΩ·cm) were cleaned in an ultrasonic bath (Elmasonic S 10, Elma Schmidbauer GmbH) in isopropyl alcohol for 15 min, rinsed with ethanol and dried under nitrogen stream. Then, an electrochemical etching process was conducted to create the porous silicon thin film, using a solution of aqueous HF and ethanol. **Caution:** HF is a highly corrosive liquid and thus should be handled with extreme care! A detailed description of the etching setup can be found elsewhere²⁶. The electrochemical etching process was conducted in two steps. First, a sacrificial

Results

layer was etched at a constant current density of 375 mA cm^{-2} for 30 s, in a 3:1 (v/v) solution of aqueous HF and ethanol, respectively. The obtained porous layer was removed by exposure to 0.1M NaOH for 2 min, followed by exposure to a solution of 1:3:1 (v/v) HF, ethanol, and deionized water, respectively, for 2 min. Next, a second etching was performed, at the same etching conditions as above. After each step, the silicon surface was thoroughly rinsed with ethanol and dried under nitrogen stream. The freshly etched PSi was then thermally oxidized in a tube furnace (thermolyne) at $1000 \text{ }^\circ\text{C}$ for 46 h under constant oxygen flow of 0.5 L min^{-1} . High resolution scanning electron microscopy (HRSEM) was used for structural characterization of the oxidized PSi (PSiO_2) nanostructure, utilizing a Carl Zeiss Ultra Plus microscope, at an accelerating voltage of 1 keV.

Fabrication and Integration with Microfluidic Device

PDMS microchannels were fabricated based on an SU8 template. The template was constructed by standard lithography at Stanford Microfluidic Foundry (Stanford University, Stanford, CA, <http://www.stanford.edu/group/foundry/>)³¹⁰. Using the template, the microfluidic channels were fabricated in-house from PDMS at 10:1 ratio of polymer and cross-linker, respectively, followed by curing at $100 \text{ }^\circ\text{C}$ for 3 h. The PDMS microchannels were attached to the SiO_2 chip (containing both planar and porous SiO_2 regions), by exposure of the inner surface of the PDMS to oxygen plasma for 40 s, using a laboratory corona treater (BD-20V Electro-Technic Products), followed by baking at $100 \text{ }^\circ\text{C}$ for 3 h.

Functionalization of Oxidized Porous Silicon Thin Film

Immobilization of amino-modified 6H7 aptamers to PSiO_2 was performed as reported by Urmann *et al*²⁶. Briefly, prior to integration with the PDMS microchannels, the PSiO_2 samples were incubated with a solution of 42 mM APTES in toluene for 1 h, followed by a thorough rinsing with toluene, ethanol and acetone and drying under a nitrogen stream. The APTES-modified surface was then incubated in a solution of 100 mg of succinic acid in 4.7 mL of DMSO and 300 μL of 0.1 M NaHCO_3 (pH 9.4) for 30 min. The surface was then thoroughly washed with DMSO and deionized water and dried under stream of nitrogen. Subsequent chemical modification steps were carried out after attachment of PDMS microchannels, adjacent to the biosensing experiments. All solutions were introduced into the microchannels using a vacuum pump; however the reactions were performed under stationary conditions, without flow. First, the microchannel was washed with 70% aqueous ethanol solution and SB, followed by incubation with a 52 mM EDC in SB, for 1 h. Subsequently, a solution of 75 μM aptamer in SB was introduced into the microchannel and incubated for 1 h. Then, a thorough washing with 50 mM Tris buffer (pH 7.4) was performed, followed by washing and incubation with elution buffer for 30 min and SB for 30 min.

Measurement of Interferometric Reflectance Spectra and Fluorescence Imaging

To collect both interferometric reflectance spectra and fluorescent signal, a customized Zeiss upright microscope equipped with an Ocean Optics charge-coupled device (CCD) USB 4000 spectrometer, was utilized. A two-port adapter was used to selectively transmit the light either to the microscope camera (Axio Cam MRc, Zeiss) or to the collimator, coupled to a fiber optic. An additional two-port adapter was used to switch between light from a halogen source (halogen100 illuminator, Zeiss) and XCite® 120Q excitation light source (Excelitas Technologies). The PSiO₂-microfluidic device was fixed to the microscope stage, under the objective. For the reflectance spectra measurements, the PSiO₂ region of the microchannel was illuminated with light from a halogen source, focused through an A-Plan objective (10x magnification, 0.25 NA, Zeiss). The size of the illumination spot was controlled by the microscope iris and adjusted to the microchannel width of 350 μm. The reflectivity spectra were collected using the CCD spectrometer and analyzed by applying FFT, as previously reported by Massad-Ivanir *et al*³³⁰. The optical data is presented as relative ΔEOT, defined as

$$\frac{\Delta EOT_t}{EOT_0} = \frac{EOT_t - EOT_0}{EOT_0}$$

where the term EOT₀ refers to the averaged EOT recorded during the initial baseline of the optical experiment.

For the fluorescence imaging, the illumination was switched to a light coming from X-Cite® 120Q excitation light source. The imaging was conducted with the camera, at a constant exposure time of 100 ms, concurrently to the reflectance measurements.

Standard and ITP-based Biosensing Experiments

The biosensing experiments were conducted immediately after preparation of the PSiO₂-microfluidic device. In the standard experiment, an EOT baseline was obtained with a mixture of LE and TE buffer, at a ratio of 2:1, respectively. This buffer composition was utilized to simulate the buffer conditions at the ITP peak, at the LE/TE interface. Subsequently, the protein solution (diluted in 2:1 LE-TE) was introduced using a vacuum pump and incubated for 30 min. Reflectivity spectra were recorded under static conditions, with no flow, every 15 s. The microchannel was then thoroughly washed with 2:1 LE-TE.

For the ITP-based biosensing experiment, a similar protocol as recently reported by Vilensky *et al.*⁴² was utilized. Briefly, the microchannel's east reservoir and the microchannel itself were filled with LE buffer using a vacuum pump and an EOT baseline was obtained. The measuring site was maintained constant throughout the whole experiment. Then, the microchannel's west reservoir was rinsed with deionized water several times and filled with the protein sample, diluted in TE. To initiate ITP, a constant voltage of 350 V was applied across the channel, using a high-voltage power supply (model PS375, Stanford Research Systems, Inc.). The location of the ITP peak was visualized by the

Results

fluorescence microscope camera and its locations was controlled by applying a pressure driven counter-flow, produced by an external water column connected to the east reservoir. For the counter-flow ITP mode, once the ITP focusing zone arrived to the P_{SiO}₂ measuring site, it was kept stationary by applying a positive pressure to counter electromigration with the water column, for as long as the ITP plug was stable or for a maximum voltage time of 30 min. During this time, the reflectance spectra were recorded and analyzed in real-time, concurrently to monitoring the position of the ITP plug with the microscope camera. The reflectivity acquisition was not performed in fixed time intervals, but upon stabilization of the ITP plug on top of the biosensor. Next, the voltage was turned off and the ITP plug was pushed back to the west reservoir by negative pressure. The channel was then rinsed thoroughly with LE buffer using a vacuum pump, to remove any unbound proteins. For all the baseline and rinsing steps, the reflectance spectra were recorded every 15 s.

For the pass-over ITP mode, the reflectance spectra were recorded continuously, every 1 s, and analyzed in real-time. As the ITP plug electromigrated above the measuring site, with an approximate velocity of $\sim 20 \mu\text{m s}^{-1}$ (without applying any counter pressure), the voltage was turned off and the channel was washed with LE buffer.

For the control experiments of ITP without protein, the experiment was conducted as for the pass-over ITP mode. To prevent arrival of TE buffer to the measuring site, a total voltage time of 15-20 min was measured, before the voltage was turned off and the channel was rinsed with LE buffer.

Results and Discussion

A schematic illustration of the biosensor design and corresponding assay is presented in Figure 5.3.1a. The biosensor is constructed from a P_{Si} Fabry-Pérot thin film, used as an optical transducer, and aptamers specifically binding the his-tag sequence of proteins (6H7 aptamer) are conjugated to the porous nanostructure^{26, 303, 306, 333}. This biosensor, previously developed by our group²⁶, is adapted as a model system for demonstrating the applicability of ITP for pre-concentration of proteins on P_{Si}. As the behavior of aptamers may vary drastically when conjugated to a surface³⁵¹, working with a well-characterized system is important for proper characterization of the biosensor. The P_{Si} nanostructure is fabricated by anodization of a heavily-doped p-type crystalline Si wafer at a constant current density of 375 mA cm⁻² for 30 s. The resulting porous film is thermally oxidized at 1000°C for 46 h under oxygen flow to create a robust insulating oxide layer that can withstand the high voltage applied during ITP⁴². High-resolution scanning electron microscopy of the oxidized film reveals that the integrity of the delicate porous nanostructure is maintained during the harsh oxidation step and interconnecting cylindrical pores with an average diameter of 45±10 nm are observed (Figure S5.3.1, Supporting Information). The porous nanostructure thickness is 4.8 μm and a 780-nm-thick planar SiO₂ layer is observed beneath the P_{SiO}₂ layer. Figure S5.3.1 also presents the raw reflectivity data and corresponding FFT spectra of the planar and porous SiO₂ layers. Following oxidation, subsequent silanization and carbodiimide coupling steps are used to conjugate the amine-terminated 6H7 aptamers

Results

to the porous surface²⁶ and successful immobilization is confirmed by RIFTS (Figure S5.3.2). The biosensor is integrated with polydimethylsiloxane (PDMS) microchannels, as illustrated in Figure 5.3.1a. The PDMS microchannel, 3 cm in length, 350 μm in width and 25 μm in depth, is attached to the PSiO_2 by plasma activation. It should be noted that the aptamer immobilization step is carried out following the assembly with the microchannel and adjacent to the biosensing experiments.

One of the main considerations in designing an ITP assay is proper choice of a discontinuous buffer system, comprising a leading electrolyte ion (LE) and terminating electrolyte ion (TE), having higher and lower electrophoretic mobility than the target, respectively⁴¹⁵. The buffer system should be chosen according to the charge of the target and optimized to allow maximal ITP focusing, proper functionality of the biological capture probe and suitability to the PSiO_2 substrate, which may be affected by buffers with a high pH value²⁴⁵. In the present work, the target is a 24 kDa his-tagged protein from the arabinanase family. This protein possesses a theoretical isoelectric point of 5.45 (calculated based on its amino acid sequence) and is accordingly characterized by a net negative charge at a neutral pH. Thus, an anionic ITP is applied and LE and TE buffers are chosen accordingly. Cl^- was used as a leading ion, Tricine as a terminating ion and Bis-Tris as the counterion. This buffer system was recently demonstrated for anionic protein focusing with ITP²⁴⁵. In addition, proper function of the aptamers as capture probes is dependent on their correct 3D folding and typically requires performing the binding reactions in the buffer used in their selection process (i.e., selection buffer)^{26, 29, 33, 351}. Herein, the pH value of the chosen buffer system (~ 7) resembles that of the 6H7 aptamer's selection buffer, and the LE buffer is further supplemented with 0.15 M NaCl. The latter is not only ideal for the aptamer-protein interaction, but also improves the ITP focusing ratio²⁴⁵. Furthermore, prior to ITP, the selection buffer is introduced into the microchannel to ensure the proper folding and functionality of the immobilized aptamer. As presented in Figure 5.3.1a, upper panel, in a typical ITP-based biosensing experiment, the microchannel and the East reservoir are first filled with LE buffer, while the West reservoir is filled with the target protein, mixed in TE buffer. Voltage is then applied along the channel and a sharp electric field gradient is formed at the LE-TE interface where the target protein focuses. The target continuously accumulates at the LE-TE interface and a highly-concentrated protein zone is formed. This zone, referred to as the ITP peak, electromigrates along the channel toward the PSiO_2 biosensor region where the target protein is captured by the 6H7 aptamers (Figure 5.3.1a, lower panel). At this stage, two different ITP assay modes, pass-over and counter-flow, are tested, presented in Figure 5.3.1b as raw fluorescence images of the target protein ITP peak. In the pass-over ITP mode, the ITP peak passes over the PSiO_2 biosensor without stopping. The interaction of the ITP peak with the sensing area is minimal and only a few seconds in time. In the counter-flow ITP mode, as the ITP peak arrives to the biosensor, it is held stationary for up to ~ 25 min, by applying a pressure driven flow, which counters the electromigration. Target infiltration into the porous layer and capture by the 6H7 aptamers are monitored in real-time during the ITP assay by RIFTS, and changes in the effective optical thickness (EOT), which is the product of the average refractive index and the thickness of the porous layer, are

Results

computed. It should be noted that the protein is fluorescently labelled in the assay only to allow visualization of the ITP peak location, but no labelling is required for the biosensing experiments. Although not tested herein, the presence of the ITP peak on top of the biosensor could be also controlled by real-time analysis of the EOT signal. Figure 5.3.1c summarizes the relative ΔEOT changes for biosensing experiments of 750 nM target protein under counter-flow and pass-over ITP modes. For comparison, the obtained signal for a similar experiment using a standard (no ITP) biosensing experiment is also presented. While no change in the EOT signal is observed under standard conditions, a significant EOT increase is obtained when ITP is applied, with both ITP assay modes. Furthermore, a ~ 5.4 -fold signal enhancement is observed when counter-flow ITP mode is applied, in comparison to the pass-over mode. This is ascribed to the enhanced diffusion flux of the target protein into the porous nanostructure as well as sufficient interaction time to allow binding of the protein to the immobilized aptamers in the counter-flow assay²⁴⁵. Thus, the counter-flow mode is further utilized in this work as will be described next.

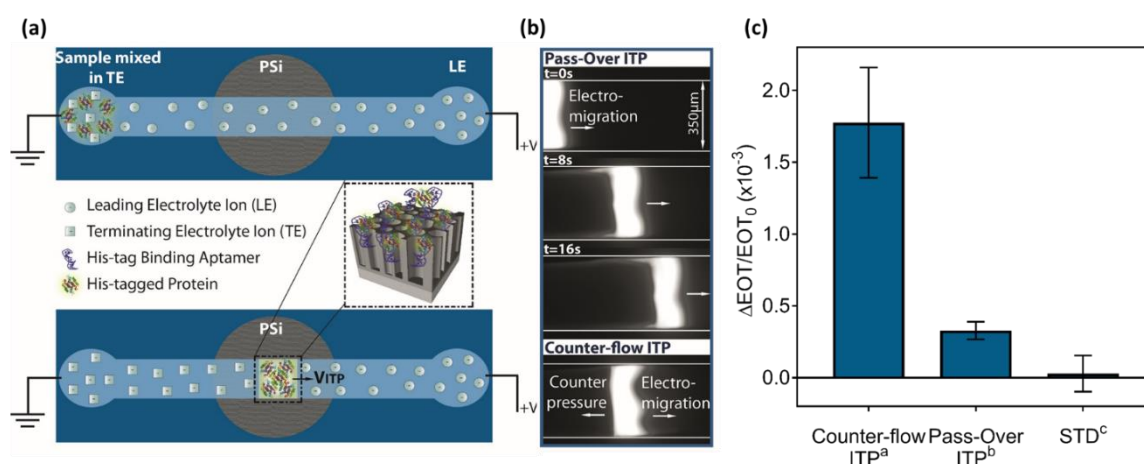


Figure 5.3.1. (a) Schematic illustration of the PSiO₂ biosensor setup and an ITP-based biosensing experiment. Upper panel: the target protein sample is mixed with TE buffer in the west reservoir, while the channel and the east reservoir are filled with LE buffer. Lower panel: as voltage is applied, the target protein focuses at the LE-TE interface and electromigrates along the channel toward the PSiO₂ sensing area where it is captured by the targeting aptamers. (b) Raw fluorescence images of the target protein, focusing under different modes of ITP assay. (c) Averaged relative ΔEOT signal for counter-flow ITP, pass-over ITP and standard (STD) configurations for 750 nM target protein, demonstrating the profound increase in signal upon counter-flow ITP mode ($n \geq 2$ for each data set). ^{a,b,c}Different superscript letters indicate a statistically significant difference (*t* test, $p < 0.05$).

Figure 5.3.2a compares relative ΔEOT changes during time for typical ITP-based and standard biosensing experiments of 750 nM target protein. First, an EOT baseline is acquired in LE buffer for ITP-based experiment, and a mixture of 2:1 LE and TE, respectively, for standard experiment. This buffer mixture is utilized to simulate the buffer conditions in the ITP peak. Then, for the ITP-based experiment, a 350 V voltage is applied, and ITP is initiated. As the concentrated protein zone arrives to

Results

the PSiO₂ biosensor region, it is held stationary and the reflectivity spectra are recorded. For the standard experiment, the protein sample is introduced and incubated in the channel for 30 min. It should be noted that the reflectivity spectra in these experiments are recorded under static conditions, with no flow. For both assays a gradual EOT increase is observed until saturation is attained. This increase is attributed to the infiltration of the protein molecules into the pores and binding to the immobilized aptamer. The noisy signal during this step stems from the basic experimental setup (pressure driven flow produced by a water column) used for controlling the location of the ITP focusing zone over the PSiO₂ biosensor region and the concurrent reflectivity measurements. Since the stabilization is manual, slight movements of the ITP plug occur during the reflectivity measurements, which result in the observed fluctuations in the signal during this step. Next, the microchannel is thoroughly washed with the baseline buffers and a rapid decrease in the EOT signal is observed for both experiments, as unbound proteins are washed away. Accordingly, this steady state EOT shift is ascribed to the surface-bound targets and constitutes the relevant readout signal of the assay. The attained relative ΔEOT value in the ITP-based assay is $2.8 \cdot 10^{-3}$ (corresponding a net EOT shift of 41 nm) in comparison to only $0.15 \cdot 10^{-3}$ (corresponding a net EOT shift of 2.5 nm) in the standard mode, demonstrating a significant signal improvement by ITP. Qualitatively, the change in the EOT as a function of time observed during ITP resembles that of a standard biosensing experiment in which the concentration target protein is 7.5 μM (see Figure S5.3.3).

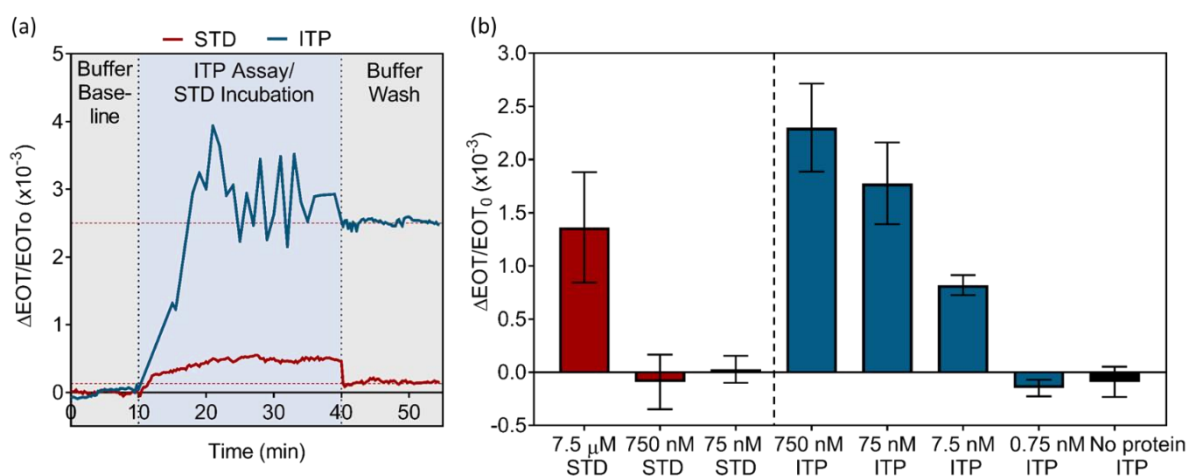


Figure 5.3.2. (a) Relative ΔEOT changes vs. time of the constructed biosensor during typical ITP-based (blue line) and standard (STD) (red line) biosensing experiments with 750 nM target protein. (b) Averaged relative ΔEOT signal for different concentrations of the target protein under STD and ITP conditions. Biosensing experiments are also conducted without target protein as a negative control ($n \geq 3$ for each concentration).

Sensitivity enhancement and improvement in LoD are studied by exposure of the biosensor to different concentrations of the target protein (0.75 nM – 7.5 μM) under ITP and standard configurations. The results are summarized in Figure 5.3.2b, presenting the averaged relative ΔEOT changes for each concentration (summarizing $n \geq 3$ repeats for each). For standard conditions, an EOT signal is only

Results

observed for protein concentrations $\geq 7.5 \mu\text{M}$, while for lower concentrations of 750 nM and 75 nM no EOT shifts are detected. These results are in agreement with the micromolar detection range observed by Urmann *et al.*²⁶. When applying ITP, EOT changes are already detected at a target concentration of 7.5 nM, demonstrating a significant enhancement in sensitivity of the biosensor and an improvement in the LoD by more than 100-fold and up to 1000-fold (a typical ITP experiment with 7.5 nM target is presented in Figure S5.3.4, and raw reflectivity data and respective FFT spectra are depicted in Figure S5.3.5). It should be pointed out that the dissociation constant of the 6H7 aptamer is only $4.6 \mu\text{M}$ ³⁰⁶. Thus, the presented assay allows overcoming the limited binding affinity of the capture probe by detection of the protein with initial concentration far below the dissociation constant. In standard experiments, the target delivery to the biosensor is governed by diffusion and reaction kinetics. For protein concentrations of 750 and 75 nM (which are below the K_d of the aptamer), the reaction kinetics is limited by the reaction off-rate, which dominates this concentration regime and is characterized by single-molecule binding and de-binding events³⁶. ITP, which increases the local target concentration above the biosensor, affects both diffusion and reaction kinetics. The former is accelerated due to the higher concentration gradient, while the latter is enhanced by pushing the reaction to a regime dominated by the reaction on-rate. Additional contribution of counter-flow ITP assay is by introducing sample mixing in the ITP plug⁴¹⁶, which further enhances the target flux to the biosensor. The poor performance of ITP at a protein concentration of 0.75 nM may be attributed to dispersion, which arises from electroosmotic flow (EOF). Note that no EOF suppressing agents, such as polyvinylpyrrolidone, were used in the present study, as our previous work has shown that the polymer may affect the integrity of the optical readout⁴². Yet, effects ascribed to reduction in fluorescence signal (see Figure 5.3.3a) possibly due to fluorophore adsorption to the PDMS microchannel and photobleaching may be also considered as they result in loss of peak visualization and consequently significant reduction in interaction time (to ~ 10 min, in comparison to ~ 25 min for higher protein concentrations). As the ITP assay involves a complex buffer system, the biosensor response to the buffers (no target protein) is also characterized. Figure S5.3.6 presents the relative ΔEOT changes during time for these experiments, where the electromigration of the LE-TE interface is monitored by real-time analysis of the EOT changes and exploits the significant difference in refractive index between LE and TE buffers. No EOT changes are detected during these experiments (Figure 5.3.2b), confirming that the optical signal is only ascribed to binding events occurring within the porous nanostructure.

Results

The actual target protein concentration within the ITP peak is estimated by analysis of the target fluorescence intensity. Figure 5.3.3a presents raw fluorescence images of the ITP peak of different concentrations of the target protein. The analysis of the fluorescence signal is conducted for the lower concentration range (Figure 5.3.3a, upper panel) due to signal saturation for protein concentrations of 750 nM and 75 nM (Figure 5.3.3a, lower panel). Figure 5.3.3b compares the maximal fluorescence intensity of the ITP peak for target concentrations of 7.5 nM and 0.75 nM to the fluorescence values observed under standard experiment with the protein at 7.5 μ M and 0.75 μ M. No significant difference (t-test, $p > 0.05$) in fluorescence intensity of the target protein is observed between 7.5 nM ITP peak and 7.5 μ M standard experiment, and 0.75 nM ITP peak and 0.75 μ M standard experiment. These results suggest a 1000-fold increase in the local target concentration within the ITP peak, compared to the initial concentration of the sample, for the corresponding concentrations. Furthermore, for 0.75 nM target protein, the actual concentration within the ITP peak is estimated to be 0.75 μ M, far below the dissociation constant of the 6H7 aptamer, suggesting that for protein's concentrations lower than 7.5 nM, the sensitivity is limited by the aptamer's affinity and not by the ITP assay. Thus, by utilizing different capture probes with lower dissociation constants, higher sensitivity and lower LoD may be achieved.

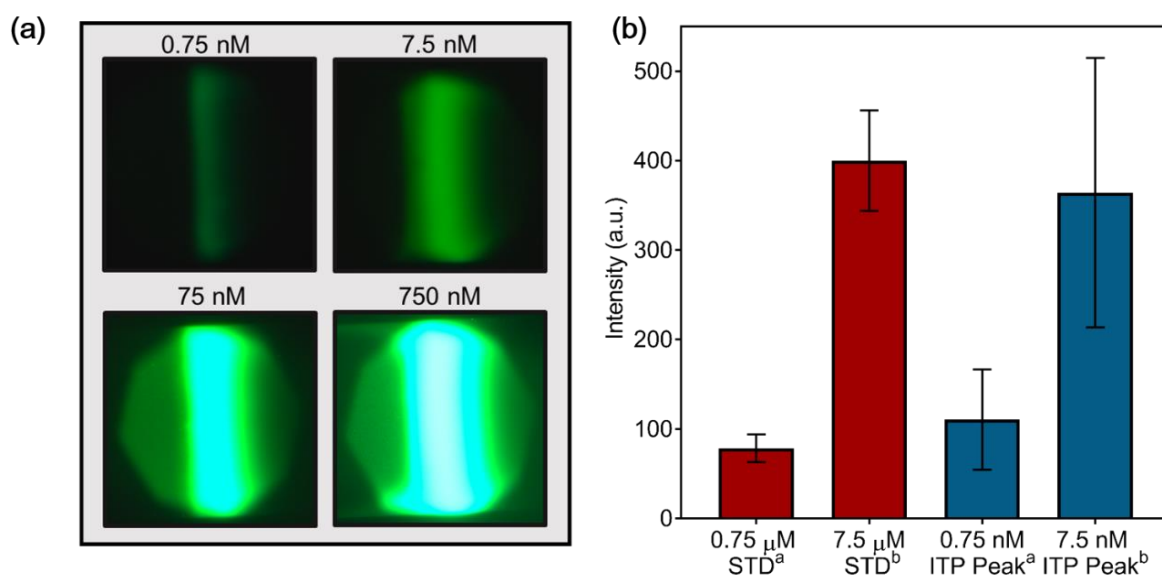


Figure 5.3.3. (a) Raw fluorescence images of the ITP peak for different concentrations of the labeled target protein. (b) Comparison of the fluorescence intensity values of the labeled protein measured during standard (STD) vs. ITP biosensing experiments ($n \geq 3$ for each data set). ^{a,b}Different superscript letters indicate a statistically significant difference (t test, $p < 0.05$).

The selectivity of the biosensor under ITP and its performance in complex media, rich with proteins, are studied by introduction of *E. coli* lysate suspension (with protein concentration of 20 μ g mL⁻¹) spiked with 18 μ g mL⁻¹ of the target protein (corresponding to 750 nM). This complex sample is rich in non-target proteins, with different molecular weights, as presented in the SDS-PAGE analysis in Figure

Results

S5.3.7. Figure 5.3.4a depicts the relative ΔEOT changes vs. time in this set of experiments in comparison to behavior of a neat lysate (no target protein). For both experiments, a gradual increase in the EOT signal is observed, as the target and non-target proteins infiltrate into the porous layer. However, upon a washing step with LE buffer, as the non-target proteins are washed away, the EOT signal rapidly decreases for lysate sample to its original EOT value, while for the spiked lysate sample, a profound relative ΔEOT signal of $1.94 \cdot 10^{-3}$ (corresponding to a net ΔEOT value of 33 nm) is observed. This signal is attributed to the selective binding of the target protein by the 6H7 aptamers from a diverse concentrated mixture of non-target proteins. Figure 5.3.4b compares the averaged relative ΔEOT changes for neat target protein, *E. coli* lysate spiked with the target protein and neat lysate (no target protein) upon ITP biosensing experiments. A similar EOT signal (t-test, $p > 0.05$) is obtained for a neat target protein and the target protein within the lysate sample, demonstrating the excellent performance of the constructed biosensor in detecting the target protein upon ITP, even in a highly complex sample overabundant with non-target proteins and shorter interaction time. The ITP peak in the presence of the lysate sample, overloaded with a diversity of proteins, could not be held stably stationary above the sensing area, resulting in reduction of interaction time to ~ 10 min, in comparison to ~ 25 min with a neat protein sample. This may be ascribed to dispersion due to EOF. Additionally, this suggests that reduction in assay time without significantly affecting the EOT signal may be possible. For neat lysate samples, a significantly lower EOT signal (t-test, $p < 0.05$) is observed, attributed to a minimal

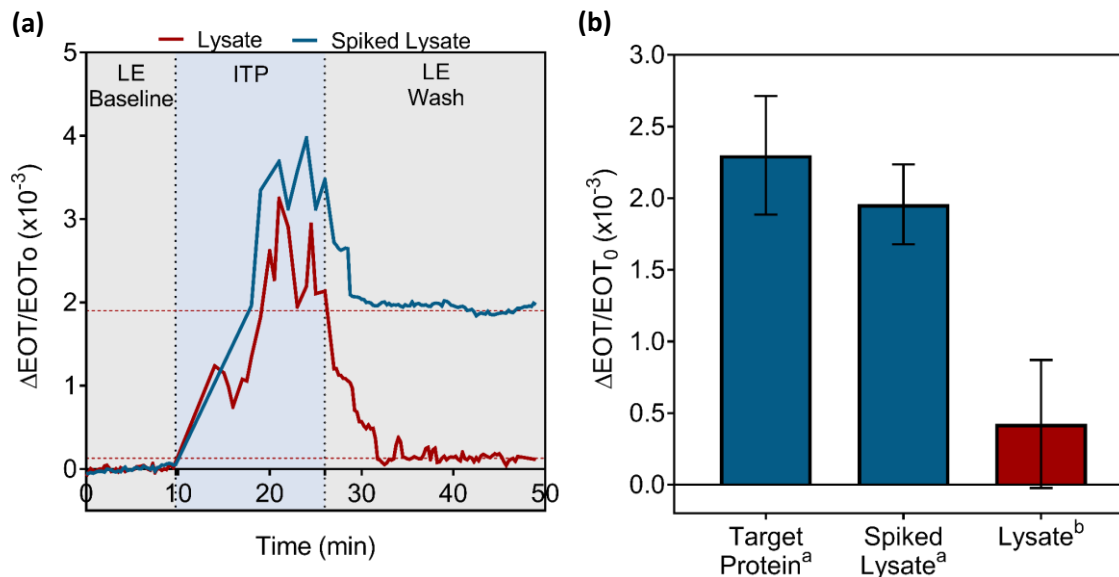


Figure 5.3.4. (a) Relative ΔEOT changes vs. time of the aptamer-based biosensor during a typical ITP experiment with *E. coli* lysate suspension (with protein concentration of $20 \mu\text{g mL}^{-1}$) spiked or non-spiked with $18 \mu\text{g mL}^{-1}$ of the target protein (corresponding to 750 nM). (b) Averaged relative ΔEOT signal for ITP biosensing experiments of neat target protein, *E. coli* lysate spiked with the target protein and neat *E. coli* lysate (no target protein), demonstrating great performance and selectivity of the assay in a highly complex media ($n=4$ for each data set). Note: for neat lysate samples, a fluorescently-labeled lysate is utilized, while for spiked samples, a non-labeled lysate is used. ^{a,b} Different superscript letters indicate a statistically significant difference (t test, $p < 0.05$).

Results

nonspecific adsorption of non-target proteins. Additional feature of ITP is its ability to separate the ionic species within the sample, based on their effective electrophoretic mobility. This is demonstrated in Figure S5.3.8, presenting the sample separation by ITP of a target-spiked lysate. Although not investigated extensively herein, this feature has the potential to further improve the specificity of the biosensor, separating the target from other interfering species and creating a neat target plug. This is especially valuable when analyzing complex biological fluids, loaded with non-target molecules.

In this proof-of-concept work we have demonstrated the applicability of ITP for protein focusing on PSi biosensor. Utilizing ITP, we were able to enhance the local target protein concentration at the sensing area by 1000-fold and maximize the optical signal. A nanomolar LoD is demonstrated in less than 50 min assay time. Furthermore, the successful performance in highly complex bacteria lysate samples demonstrates the tremendous potential of the assay for constructing clinically relevant biosensing schemes. This is the first time that ITP has been applied for protein focusing on PSi biosensors, as well as the utilization of immobilized aptamers as capture probes in an ITP assay. This assay is independent of other signal amplification techniques and could be combined with other strategies to further enhance the sensitivity of PSi biosensors.

Supporting Information

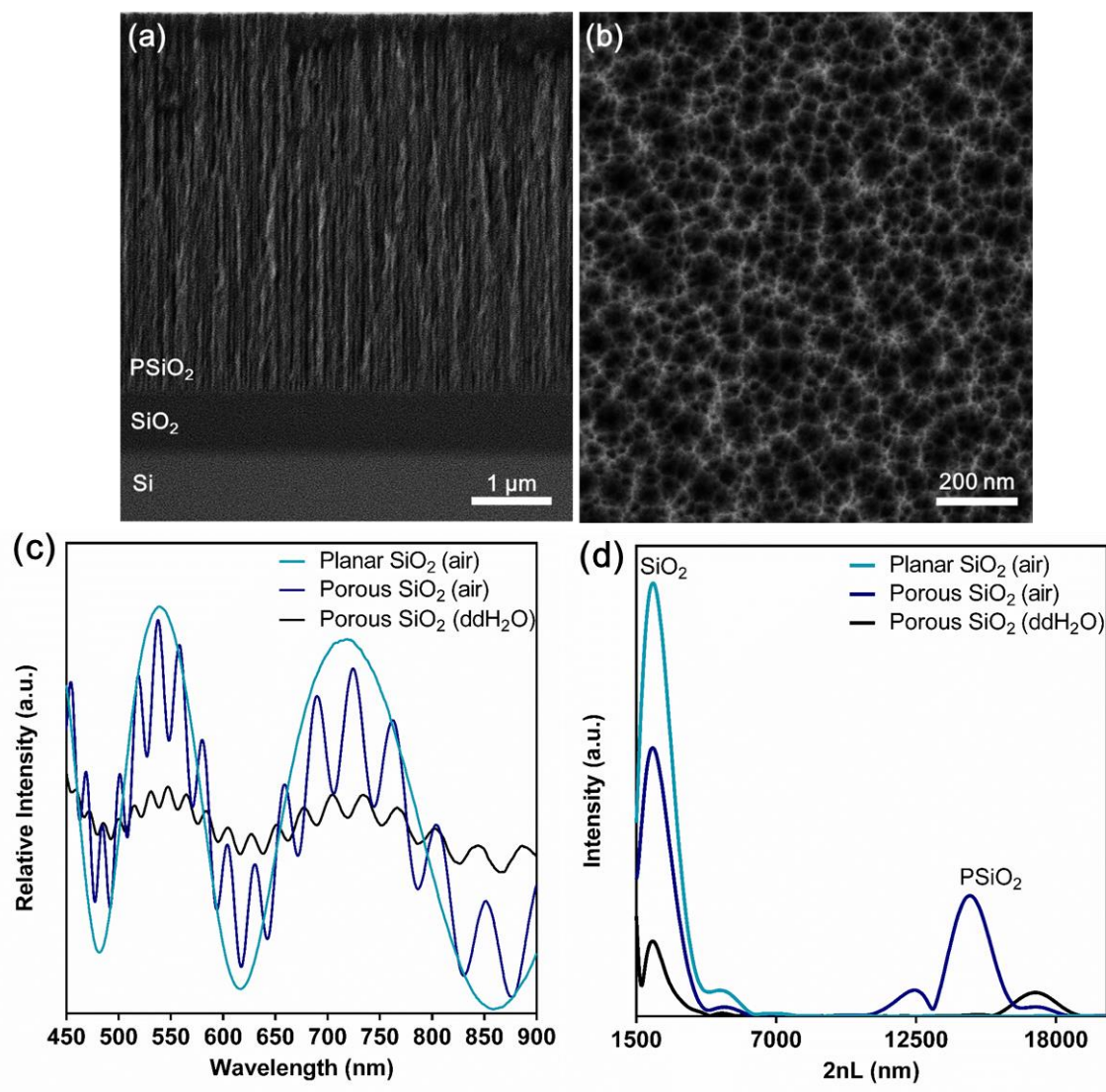
HRSEM Characterization and Reflectivity Spectra of the P SiO_2 Nanostructure

Figure S5.3.1. Characterization of the P SiO_2 nanostructure; High resolution scanning electron microscopy images (a) cross-sectional view and (b) top-view. (c) Reflectivity spectra and (d) corresponding FFT peaks of planar SiO₂ and porous SiO₂ in air and porous SiO₂ in ddH₂O (oxidized at the same conditions). While no EOT (2nL) shift is observed for SiO₂ FFT peak upon introduction of ddH₂O, a clear red-shift is observed for P SiO_2 FFT peak due to the water filling of the pores and the corresponding change in the average refractive index of the porous layer.

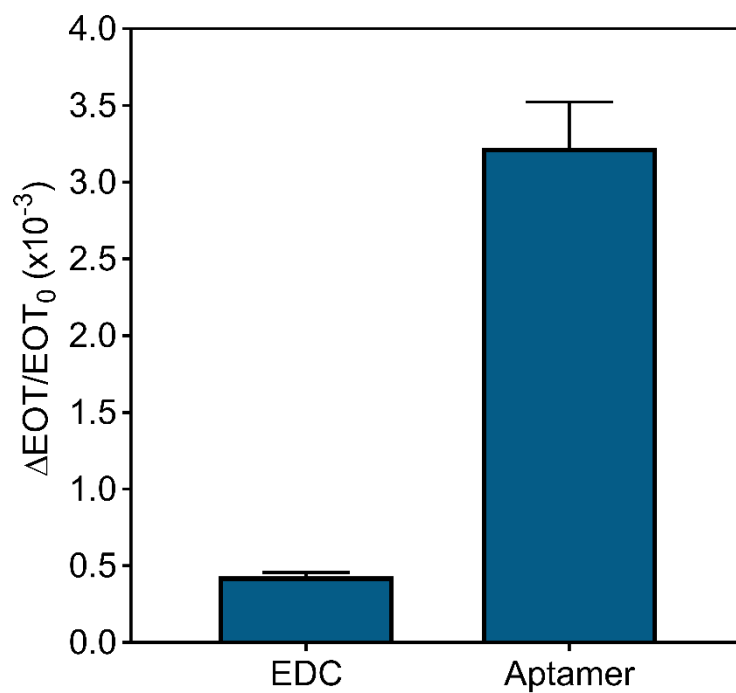
RIFTS Analysis of Aptamer Immobilization on the P_{Si}O₂

Figure S5.3.2. Relative ΔEOT signal for activation of carboxylated P_{Si} surface with EDC followed by conjugation of amino-terminated 6H7 aptamers. The increase in EOT in each step confirms the successful immobilization of the 6H7 aptamers to the P_{Si}O₂. Note: the ΔEOT values are normalized to the EOT value of the carboxylated P_{Si} surface.

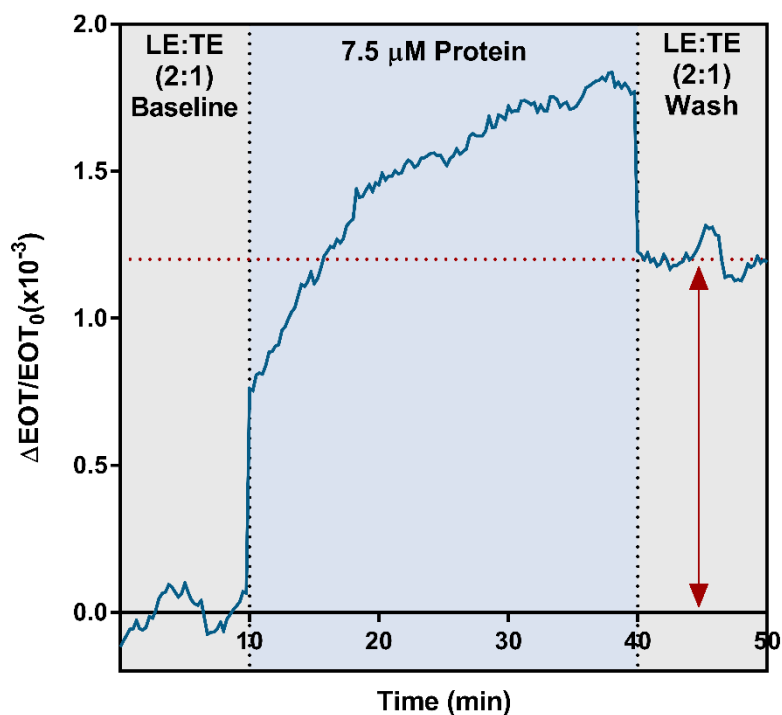
Standard Biosensing Experiment with 7.5 μM Target Protein

Figure S5.3.3. Relative ΔEOT changes vs. time of the constructed biosensor during standard biosensing experiment with the target protein. First, a baseline is acquired in a 2:1 mixture of LE-TE. This composition was utilized to simulate the conditions in the ITP peak interface. Then, 7.5 μM target protein is introduced and a gradual increase in the signal is observed as the protein infiltrates into the porous layer and interacts with the capturing aptamers. After 30 min of incubation with the protein, a thorough washing with the LE-TE mixture is performed until a stable signal is attained. The final increase in the signal in comparison to the initial baseline demonstrates binding of the target protein to the constructed biosensor.

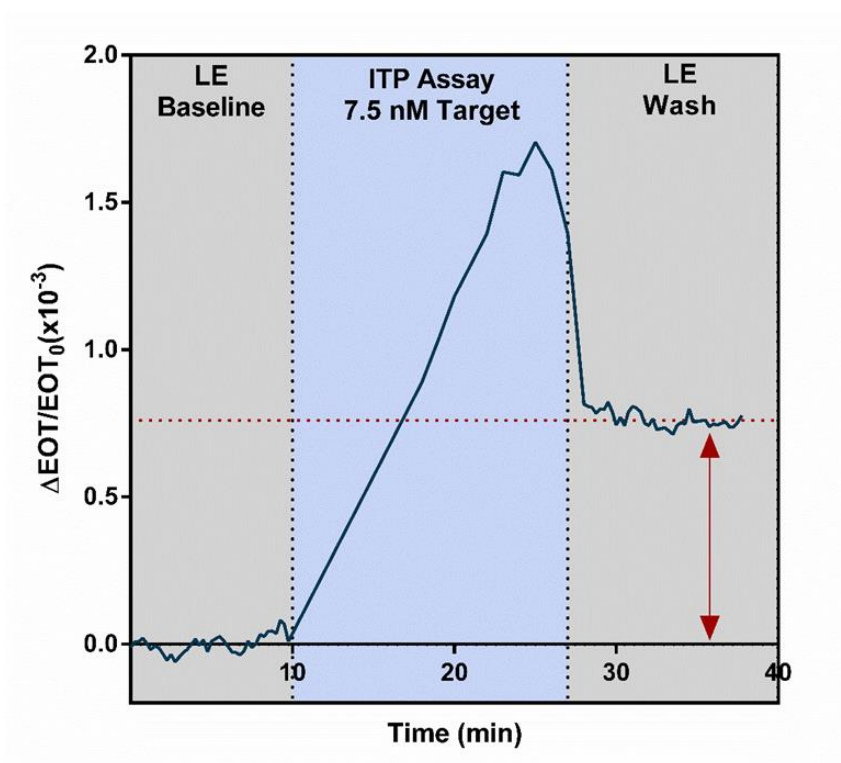
ITP Biosensing Experiment with 7.5 nM Target Protein

Figure S5.3.4. Relative ΔEOT changes vs. time of the constructed biosensor during ITP biosensing experiment with target protein at a concentration of 7.5 nM.

Raw Reflectivity Spectra and FFT Peaks of ITP Biosensing Experiments

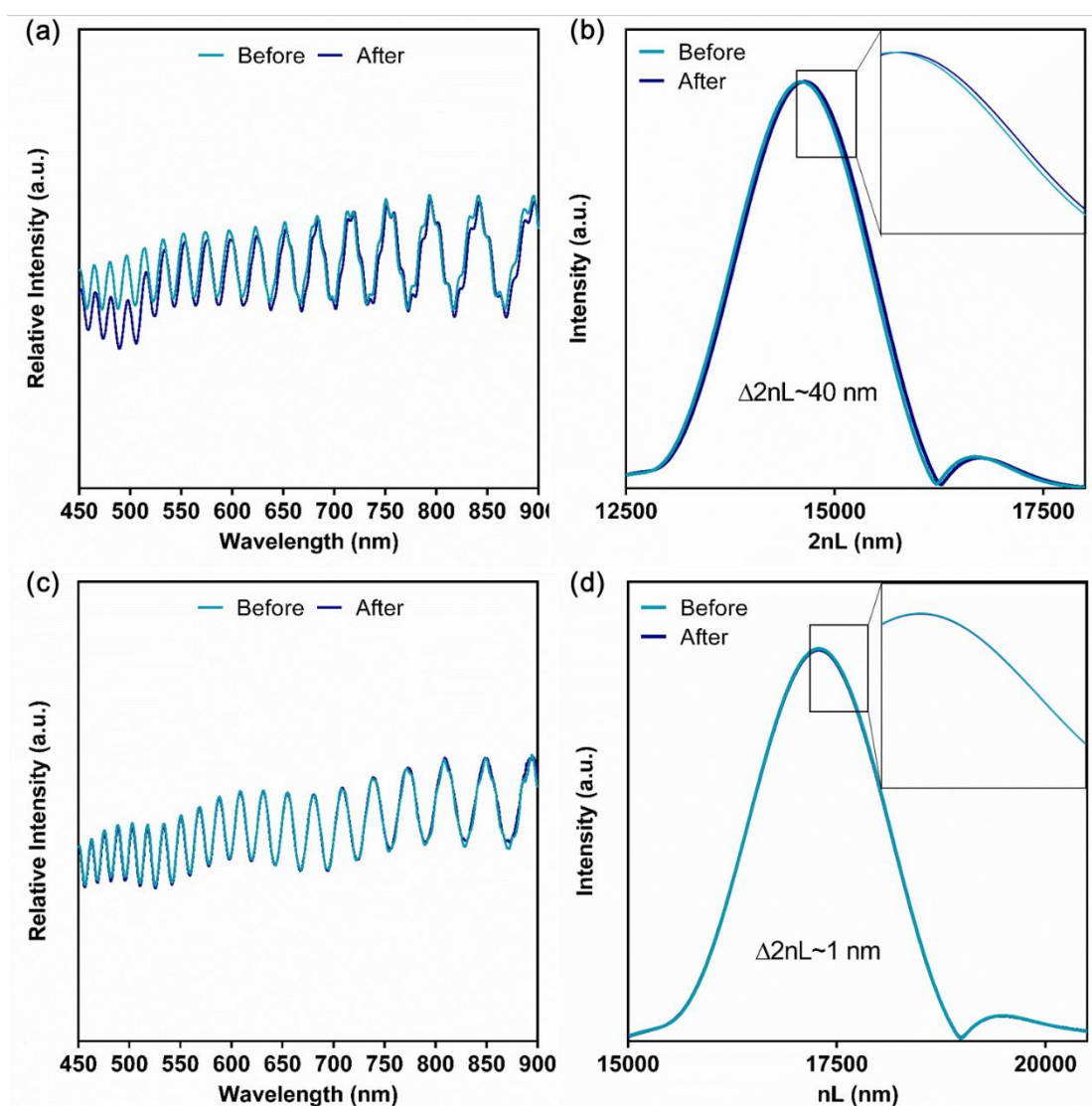


Figure S5.3.5. Raw reflectivity spectra and the corresponding FFT peaks of the biosensor before and after exposure to the target protein upon ITP biosensing experiments; (a) reflectivity spectra and (b) FFT peaks for ITP biosensing experiment of 750 nM target; (c) reflectivity spectra and (d) FFT peaks for ITP biosensing experiment of 0.75 nM target. Note: Since the spectrometer in each experiment was calibrated on planar SiO₂ (oxidized at the same conditions), the SiO₂ FFT peaks are not visualized in the spectrum. Additionally, the bending in the reflectivity spectrum at ~450-550 nm after exposure to target upon ITP experiment with a concentration of 750 nM is attributed to the fluorescence signal of the labelled target.

Control Experiments of ITP without Protein, with or without Exposure to TE

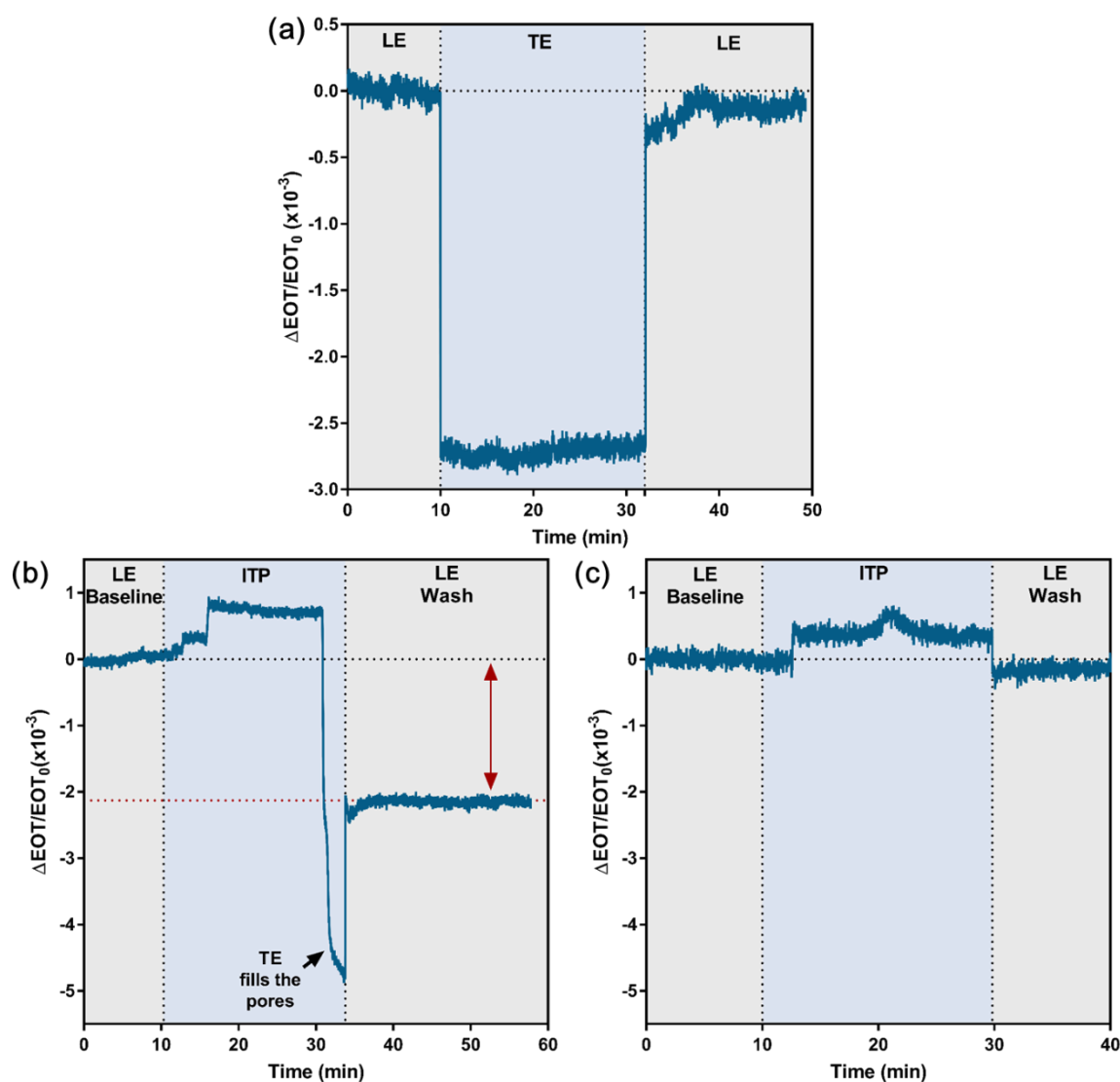


Figure S5.3.6. (a) Relative ΔEOT changes vs. time of the constructed biosensor during standard introduction of LE and TE buffers into the microchannel (reflectivity spectra are recorded in static conditions, with no flow). First, a baseline is acquired in LE buffer. Then, the channel is washed with TE buffer and a sharp decrease in the signal is observed, indicating the significant difference in the refractive index between both buffers, which could be utilized for real-time monitoring of the LE-TE interface electromigration during ITP. Subsequently, the channel is washed with LE buffer and the signal returns to its original baseline, demonstrating that the optical properties of the constructed biosensor are not affected by LE or TE buffers. (b) Relative ΔEOT changes vs. time of the constructed biosensor during ITP experiment with no protein. Initially, the channel and the east reservoir are washed with LE and a baseline is acquired. Subsequently, the west reservoir is washed with DI water, filled with TE buffer and a constant voltage of 350 V is applied. After ~ 2.5 min and ~ 6 min an increase in the optical signal is observed, which is attributed to impurities concentrating at the LE-TE interface. After ~ 20 min, a sharp decrease in the signal is observed, indicating the arrival of the TE buffer, with lower refractive index, to the measuring site. The voltage is then turned off and the channel is rinsed with LE buffer. The signal increases, however, does not return to its original baseline. A significant net negative EOT signal is observed, suggesting a change in the optical properties of the biosensor upon exposure to TE buffer, under applied voltage. As the aptamer molecules are negatively charged, this negative signal may be ascribed to changes in aptamer's conformation and folding upon the applied

Results

voltage and the drastic change in the buffer conditions from LE to TE during ITP. Nevertheless, throughout ITP with the target protein, the biosensor surface is exposed to LE buffer and the ITP peak solely and not to a pure TE buffer and thus these significant negative EOT changes are not observed. (c) Relative Δ EOT changes vs. time of the constructed biosensor during ITP experiment with no protein, without exposure to TE. The experiment is conducted as above, however the voltage is turned off before the biosensor surface is exposed to TE buffer, without modifying significantly the assay time (after ~20 min of running ITP). In this case, upon rinsing the channel with LE, the optical signal returns to its initial baseline. Hence, the control experiments of ITP without the target protein are conducted in this manner, without exposing the biosensor to pure TE buffer, similarly to ITP experiments with the target protein.

SDS-PAGE Analysis of Fluorescently Labelled/Non-Labelled Bacteria Lysate

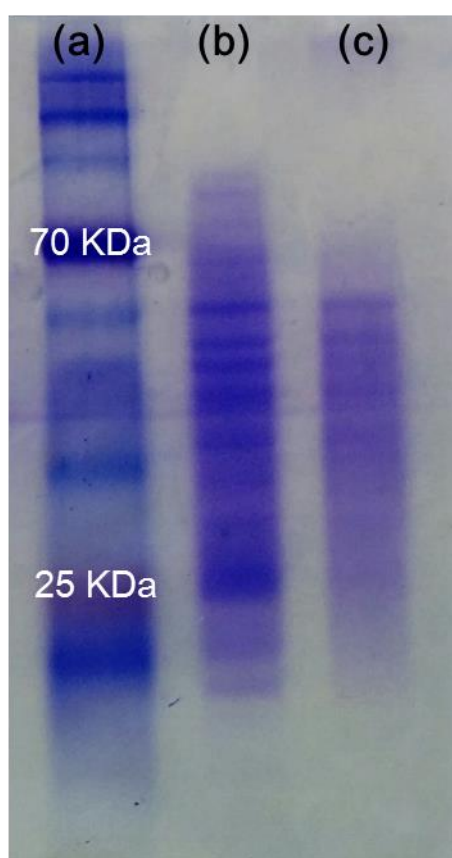


Figure S5.3.7. SDS-PAGE analysis of bacteria lysates used for the biosensing experiments, demonstrating high diversity of non-target proteins. (a) molecular size marker; (b) non-labelled bacteria lysate, used for the biosensing experiments with bacteria lysate spiked with the target protein; (c) fluorescently labelled bacteria lysate used for the control biosensing experiments. Note: different concentrations of labelled and non-labelled bacteria lysate were used for the SDS-PAGE analysis.

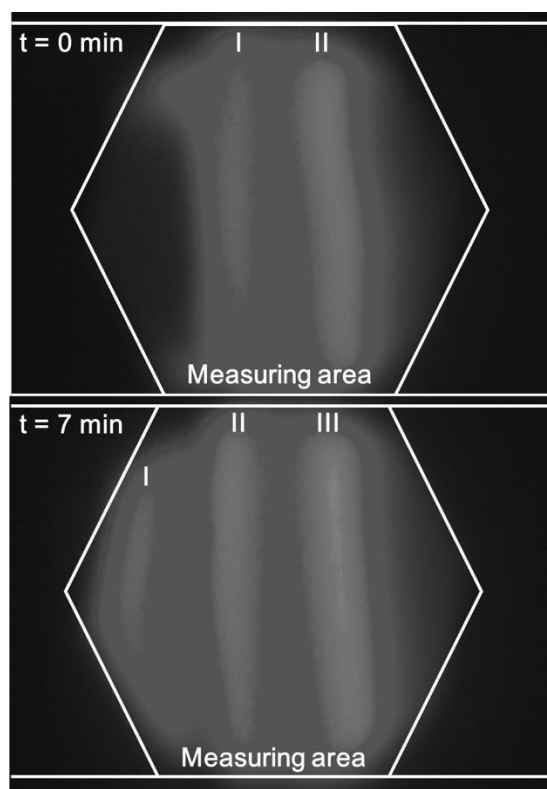
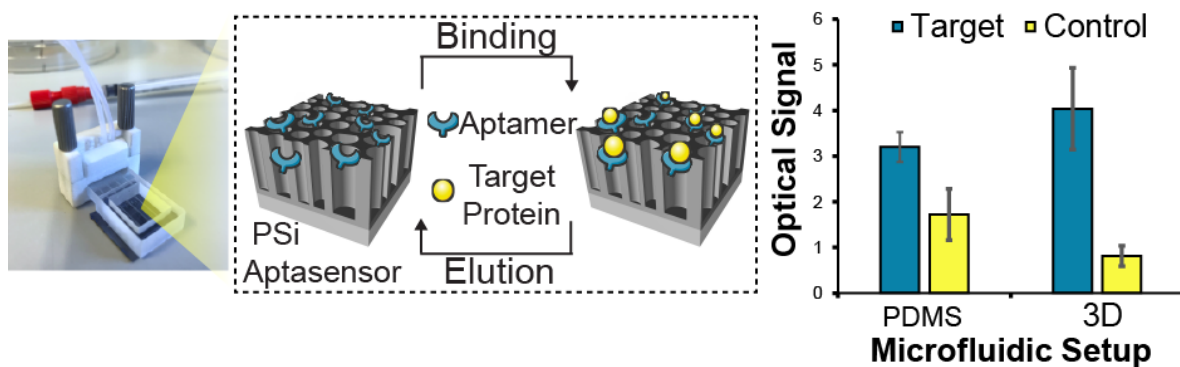
Sample Separation and Accumulation Over Time During ITP

Figure S5.3.8. Raw fluorescence images of the ITP peak of a target-spiked lysate sample, demonstrating sample separation and accumulation over time. ITP enables separation of the ionic species based on their effective electrophoretic mobility, while the infinite injection mode in ITP causes a continuous species accumulation at the LE-TE interface over time. The former can be observed already at the initial arrival of the ITP peak to the measuring area ($t = 0$ min), with the presence of two separate fluorescent plugs. The latter is characterized by increased fluorescent intensity and appearance of additional ITP plug at $t = 7$ min. The multiple ITP plugs observed are ascribed to the fluorescent protein target and residues of free fluorescent dye, which can focus under ITP by itself or react with other species in the protein lysate mixture. The separation feature of ITP has the potential to further improve the specificity of the biosensor, separating the target from other interfering species and creating a neat target plug.

5.4 3D-Printed Microfluidics Integrated with Optical Nanostructured Porous Aptasensors for Protein Detection

Sofia Arshavsky-Graham, Anton Enders, Shanny Ackerman, Janina Bahnemann and Ester Segal

Microchimica Acta 188, 67 (2021).



Respective Table of Contents Image

Abstract

Microfluidic integration of biosensors enables improved biosensing performance and sophisticated lab-on-a-chip platform design for numerous applications. While soft lithography and polydimethylsiloxane-based microfluidics are still considered the gold standard, 3D-printing has emerged as a promising fabrication alternative for microfluidic systems. Herein, a 3D-printed polyacrylate-based microfluidic platform is integrated for the first time with a label-free porous silicon (PSi)-based optical aptasensor via a facile bonding method. The latter utilizes a UV-curable adhesive as an intermediate layer, while preserving the delicate nanostructure of the porous regions within the microchannels. As a proof-of-concept, a generic model aptasensor for label-free detection of his-tagged proteins is constructed, characterized, and compared to non-microfluidic and polydimethylsiloxane (PDMS)-based microfluidic setups. Detection of the target protein is carried out by real-time monitoring reflectivity changes of the PSi, induced by the target binding to the immobilized aptamers within the porous nanostructure. The microfluidic-integrated aptasensor is successfully used for detection of a model target protein, in the range of 0.25 μM to 18 μM , with a good selectivity and an improved limit of detection, when compared to a non-microfluidic biosensing platform (0.04 μM vs. 2.7 μM respectively). Furthermore, a superior performance of the 3D-printed microfluidic aptasensor is observed, compared to a conventional PDMS-based microfluidic platform with similar dimensions.

Introduction

Microfluidic systems and their integration with biosensors are extensively studied for construction of lab-on-a-chip platforms^{417,418}. The miniaturization of such systems reduces sample and reagent volume, shortens the analysis time, and enables high-throughput detection, portability, and reduced costs^{417,418}. Importantly, microfluidics improves the mass transfer to the biosensor surface, resulting in a higher sensitivity compared to traditional biosensing setups³⁶⁻³⁸. Nowadays, polydimethylsiloxane (PDMS) is the most used polymer for microfluidics fabrication. It is commonly constructed by casting on a master template featuring the microfluidic design, which is fabricated by soft lithography techniques. Thus, it requires sophisticated instrumentation and high costs, while the translation to commercial scale is challenging^{40, 419}. Importantly, a change in the microfluidic design cannot be performed without repeating the whole fabrication process, which poses a significant barrier for rapid prototyping^{40, 419}. The technological advancement of 3D-printing, which facilitates rapid and fully digital prototyping of complex 3D microstructures in a one-step process, has positioned it as a promising alternative to traditional manufacturing methods⁴²⁰. 3D printing also lowers the costs and the manufacturing time compared to soft lithography and enables the fabrication of multiple devices at the same time^{40, 420}. This facilitates a flexible investigation of microfluidic device designs for any desired application^{40, 421}. For integrating 3D-printed microfluidics with biosensors, one must consider the resolution of the printer (often on the range of tens of microns), the resulting surface roughness of the printed device, its

Results

deformation and resistance to harsh conditions⁴²⁰. Thus, bonding to a biosensor surface can be achieved by indirect methods, via an intermediate layer, which can be performed at comparatively mild conditions at a lower surface quality^{422, 423}. As an intermediate layer, UV-curable adhesives are most commonly used, since they require only a short UV irradiation for curing and can be operated at ambient conditions⁴²³. The adhesive can be applied to the substrates by means of capillary forces^{424, 425}, scaffold micro-pillars⁴²⁶, or by stamping technique⁴²⁷⁻⁴³⁰. In the stamping technique, a thin layer of the adhesive is first spun on a flat wafer. Then, the microfluidic part is stamped on the adhesive-coated wafer, resulting in adhesive transfer to the microfluidic part, which can be then bonded to a second sealing part^{427, 428}. This method allows for the creation of a thin (<3 μm) adhesive intermediate layer that does not interfere with the microchannel area and was successfully applied for relatively smooth and even surfaces (such as glass, silicon, and SU-8)^{422, 427, 430}. Yet, for biosensing applications, this method was only demonstrated with microfluidic glass chips used for surface Plasmon resonance⁴²⁸.

To date, there are only a handful of reports that combine 3D-printed microfluidics with aptasensors⁴³¹⁻⁴³³ and herein, we present for the first time the integration of a 3D-printed microfluidic device with a generic label-free optical porous silicon (PSi) aptasensor. The nanostructured PSi scaffold is used as the optical transducer, and binding of the target analyte to surface-immobilized aptamers, used as capture probes, is detected in real time by monitoring reflectivity changes^{18, 19, 22, 31, 32, 332}. To date, PSi-based optical biosensors have been only integrated with PDMS-based microfluidics, fabricated by soft lithography^{23, 30, 42-44, 46, 434}. In the present work, we develop a straightforward and low-temperature bonding method for the integration of the PSi-based aptasensor with 3D-printed polyacrylate-based microfluidics, utilizing a UV-curable adhesive as an intermediate layer. The method is derived from the stamping technique and creates a thin adhesive layer. It should be emphasized that in contrast to previous works, in the present work we are integrating a relatively rough surface of a 3D-printed polyacrylate microchannels with a delicate highly-porous nanostructure. As a proof-of-concept to demonstrate the biosensing capabilities of the platform, we use a model aptasensor: oxidized PSi Fabry-Pérot thin films are functionalized with an anti-his tag aptamer, and a 60 kDa his-tagged protein is used as a target. The aptasensor sensitivity is evaluated and the selectivity is characterized by exposure to several non-target proteins as well as to bacteria lysate samples. Importantly, we compare the aptasensor performance in the 3D-printed device to that of PDMS microchannels with similar dimensions, as well as to non-microfluidic setups.

Experimental

Materials

Heavily doped p-type Si wafers (<100>-oriented, ~0.95 mΩ·cm resistivity) were purchased from Sil'tronix Silicon Technologies (Archamps, France). Ethanol absolute was supplied by Bio-Lab ltd (Jerusalem, Israel). Aqueous HF (48%), (3-Aminopropyl)triethoxysilane (APTES), succinic acid,

Results

dimethylsulfoxide (DMSO), N-(3-Dimethylaminopropyl)-N'-ethylcarbodiimide hydrochloride (EDC), Tris base, and all buffer salts were purchased from Merck (Darmstadt, Germany). All solutions were prepared with Milli-Q water (ddH₂O, 18.2 MΩ·cm). Polydimethylsiloxane (PDMS) was prepared from Sylgard® 184 Silicon Elastomer kit, purchased from Dow Corning (Midland, USA). Anti-His Tag aptamer 6H7 (5'-GCT ATG GGT GGT CTG GTT GGG ATT GGC CCC GGG AGC TGG C-3')³⁰³ was purchased with a 5'-amino modification from Integrated DNA Technologies (Coralville, USA). Recombinant his tagged protein, domain 2 of extracellular endo- α -(1→5)-L-arabinanase 1 (from *Geobacillus stearothermophilus* T-6) (D2), and a non-target version without his tag (named D2N), were both produced and purified using *E. coli* BL21 cells. Trypsin from porcine pancreas was obtained from Merck, and *E. coli* K12 was generously supplied by Prof. Sima Yaron, Technion. Luria-Bertani (LB) medium was prepared by dissolving 5 g of NaCl, 5 g of yeast extract, and 10 g of tryptone in 1 L of ddH₂O. Selection buffer (SB) was composed of 50 mM K₂HPO₄, and 150 mM NaCl (pH 7.4) and elution buffer was composed of 50 mM K₂HPO₄, 150 mM NaCl, and 1 M Imidazole (pH 7.4).

Fabrication of Oxidized PSi Nanostructures

PSi Fabry-Pérot thin films were fabricated from a highly doped p-type crystalline Si wafers, using a two-step anodic electrochemical etching process, as previously described⁴³⁵. The electrochemical etching was performed at a constant current density of 375 mA cm⁻² for 30 s in a 3:1 (v/v) solution of aqueous HF (48%) and ethanol, respectively, followed by thermal oxidation at 800 °C for 1 h in ambient air. For further details, please see Supplementary Information and Table S5.4.1.

Design and Fabrication of 3D-Printed Microfluidic Devices

The microfluidic device was designed in SolidWorks software (Dassault Systèmes) and contained two separate microchannels, with dimensions of 200 μm in height and 500 μm in width, spaced 2.5 mm apart. The microchannel length to be in contact with the PSi was 7 mm, while the rest passed within the device. Above the contact area a measurement window was created, reducing the thickness of the device by 2.8 mm, see Figure 5.4.1. The designed devices were printed using 3D Systems Projet MJP 2500 Plus multijet printer. Polyacrylate-based photopolymer material (VisiJet M2R-CL, 3D Systems, Rock Hill, USA) and hydroxylated wax (VisiJet M2 Sup, 3D Systems, Rock Hill, USA) were used as the printing and support materials, respectively. The microchannels were located at the bottom layer of the printing plane and in parallel to the printing direction. The printer resolution was 32 μm and a deviation of 10% in size was reported for features with sizes of 100 μm to 200 μm⁴³⁶. After printing, the devices were subjected to several post processing steps, as previously described (see Supplementary Information for more details)^{40, 309}.

Integration of PSi Films with 3D-Printed Polyacrylate Microfluidic Devices

Prior to bonding the 3D-printed device to the PSi film, the devices were first gently polished with a standard grid paper (1000 grit), washed with water and soap, and flattened at 60 °C by applying a pressure of ~38 kPa for 1 h. During this step, the measurement window was filled with a fitting square that ensures the alignment of the microchannel bonding area to the PSi. Next, UV curable adhesive (Norland Optical Adhesive 72, Norland Products Inc, Cranbury, USA) (50 µL) was spread on a transfer wafer with a K hand coater no. 2 (Printcoat Instruments, Litlington, UK) and the printed device was placed on top of the adhesive layer two times for the glue transfer. Finally, the device was carefully placed on top of carboxylated PSi films, followed by UV curing at 365 nm (1.5 mW cm⁻²) for 30 min (VL-6.LC UV lamp 365/254 nm 6 W, Vilber Lourmat, Collégien, France).

Integration of PSi Films with PDMS Microchannels

PDMS microchannels were fabricated based on a 3D-printed polyacrylate template, with 200 µm high and 500 µm wide microchannels. PDMS was prepared by mixing the polymer and the cross-linker at a 10:1 ratio, respectively, followed by curing at 100 °C for 3 h. Then, the inner surface of the PDMS microchannels was treated with corona for 40 s, using a laboratory corona treater (BD-20V Electro-Technic Products, Chicago, USA). The activated PDMS was then placed on top of carboxylated PSi films, followed by baking at 90 °C for 4 h^{30, 42}.

Characterization of Integrated Devices

The 3D-printed microfluidic devices, integrated with the PSi, were characterized by several methods. Standard food color solutions (E124 and E133) were introduced into the microchannels to visualize possible leakage. It should be noted that these dyes could be successfully removed by flushing the microchannels with water and no microchannel staining was apparent. The integrated devices were imaged with an upright optical microscope Olympus BX51 (Olympus). Cross-sections of the integrated devices were characterized by Carl Zeiss Ultra Plus high-resolution scanning electron microscope (HRSEM), at an accelerating voltage of 1 keV. The cross sectioned samples were prepared by embedding the devices in epoxy (EpoFix resin, Struers, Cleveland, USA), which was refilled several times under vacuum (1 torr) to remove any air, followed by curing at room temperature for 48 h. The cured epoxy block was sectioned using a IsoMet™ low speed saw (Buehler, Illinois, USA) and polished in EcoMet™ 3 variable speed grinder-polisher (Buehler, Illinois, USA) with sandpaper with increasing grit, as well as an Alumina Suspension (50 nm Neutral, Akasel, Denmark). Finally, the cross-sectioned samples were sputtered with carbon.

Functionalization of Oxidized PSi Films

Amino-terminated anti his tag aptamers, 6H7, were grafted onto the oxidized PSi films using carbodiimide coupling chemistry²⁶. Briefly, the oxidized PSi films were incubated for 1 h in APTES

Results

solution (in toluene, 42 mM), followed by a thorough rinsing with toluene, ethanol, and acetone. Next, an annealing step was performed at 100 °C for 15 min. The P*Si* film was cooled down to room temperature and subsequently incubated in a solution of succinic acid (0.17 M) and NaHCO₃ (6 mM) in DMSO for 30 min, followed by washing with DMSO and ddH₂O and drying it under a stream of nitrogen. After this step, the carboxylated P*Si* was integrated in the microfluidic device, and the remaining functionalization steps were carried out inside the microchannels.

The microchannels were first washed with EtOH (50 % v/v) in ddH₂O for 5 min to remove any air bubbles inside the channels, followed by subsequent washing with SB buffer at 100 μL min⁻¹ for 10 min. Next, EDC in SB buffer (10 mg mL⁻¹) was introduced at 30 μL min⁻¹ for 30 min, followed by introduction of aptamer (75 μM, 250 μL) at 30 μL min⁻¹. The aptamer was then allowed to react with the surface for 1 h without flow. Subsequently, the microchannel was washed with Tris (50 mM, pH 7.4) at 30 μL min⁻¹ for 15 min to deactivate any remaining reactive EDC groups on the surface.

Protein Production and Purification

The target his tagged protein, abnA-D2 (from *Geobacillus stearothermophilus T-6*) (D2), and the non-target version without his tag (named D2N), were both produced and purified using the following method. *E. coli* BL21 cells, transformed with an abnA-D2 gene, were grown overnight at 37 °C on LB plates with appropriate antibiotic. The cells were transferred to a TB (Terrific Broth) medium for overnight growth in a shaker (230 rpm) at 37 °C. The cells were then cooled on ice for 15 min, harvested by centrifugation, and re-suspended in binding buffer (20 mM imidazole, 0.5 M NaCl, and 20 mM phosphate buffer, pH 7.4). Subsequently, the cells were disrupted by two passages through an Avestin Emulsiflex C3 Homogenizer, 1500 psi (Avestin, Ottawa, Canada) at room temperature, and centrifuged at 7000 rpm for 30 min. The supernatant was then heated at ~50 °C for 30 min and centrifuged again. The his-tagged protein was purified by fast protein liquid chromatography (FPLC) using the ÄKTA Avant-25 chromatography system (GE Healthcare Life Sciences) equipped with HisTrap column (1- or 5-ml column volume, GE Healthcare Life Sciences). The protein was eluted with a 10 CV gradient of elution buffer that contained 0.5 M imidazole, 0.5 M NaCl, and 20 mM phosphate buffer, pH 7.4. The protein D2N, without the his-tag, was purified via gel filtration using a Superdex 200 26/60 column, ÄKTA Avant (GE Healthcare Life Sciences), running at 2.5 ml/min with 50 mM Tris-HCl buffer pH 7.0, 100 mM NaCl and 0.02% sodium azide. Injected samples volumes were ~14 ml (~5% column volume).

Preparation of *E. coli* Lysates

E. coli K12 was cultivated in LB medium overnight under continuous shaking at 37 °C. The culture was spun down in a standard lab centrifuge (2-16P, Sigma Laboratory Centrifuges, Sigma-Aldrich) at 4500 rpm for 10 min, and the supernatant was replaced with SB buffer. This step was repeated twice. Subsequently, the culture was ultrasonicated on ice in a Vibra cell VCX 750 instrument

Results

(Sonics & Materials Inc., Newtown, Connecticut, USA) for 2 min, with 30 s pulses and 30 s pauses in between. The temperature and the amplitude were set to 4 °C and 40%, respectively. Cell debris were removed by ultracentrifugation at 4 °C for 30 min at 12000 g (1-15K, Sigma Laboratory Centrifuges, Sigma-Aldrich), and the supernatant was analyzed for protein content in NanoDrop instrument (NanoDrop 2000 spectrophotometer, Thermo Scientific), assuming 1 ABS=1 mg mL⁻¹. For the experiments, the lysate was diluted for protein content of 1 mg mL⁻¹.

Biosensing Experiments

For biosensing experiments, the microfluidic integrated PSi was fixed on a motorized linear translation stage (Thorlabs, Inc., New Jersey, USA) and four different spots, all spaced out at 1.5 mm apart, were monitored on each microchannel in every experiment. A syringe pump (Fusion 200, Chemyx, Texas, USA) was used to control the flow rate. The 3D-printed microfluidic device was connected to tubes through a Dolomite 4-way microfluidic connector and a 4 mm top interface (The Dolomite Center Ltd., Royston, UK). Female-to-male Luer Assy and flangeless fittings (IDEX Health and Science LLC, Middleboro, USA) were used to connect the tubes to a syringe. For the cell setup, the PSi aptasensor was fixed in a custom-made plexiglass cell, using an O-ring.

RIFTS method was used to monitor in real time the reflectivity changes of the PSi-based aptasensor^{18, 26}; the latter presenting a Fabry-Pérot interference fringe pattern attained from light reflecting from the top and bottom interfaces of the PSi. The fringe maxima are described by the Fabry-Pérot relationship:

$$m\lambda=2nL$$

where m is the spectral order, λ is the wavelength of the incident light, n is the average refractive index (RI) of the porous layer and L is the thickness of the porous layer. The term $2nL$ is referred to as the effective optical thickness (EOT) and is only a function of the average RI of the porous layer, as the thickness is constant. A schematic illustration of the method is presented in Figure S5.4.1.

Interferometric reflectance spectra were collected with a charge-coupled device (CCD) spectrometer (Ocean Optics, USB 4000) fitted with an objective lens and coupled to a bifurcated fiber-optic cable. A tungsten light source was focused on the microchannel or sample with a spot size of approximately 1 mm², perpendicular to the surface. The experimental setup is presented in Figure S5.4.2 (Supplementary Information). The spectral acquisition and the stage movement were controlled with a LabView software (National Instruments). The spectra were acquired at an integration time of 30 ms and with a scan average of 160, every ~1.1 min. Fast Fourier transformation (FFT) was performed at a wavelength range of 450-900 nm, as previously described by Massad-Ivanir *et al*⁴³⁷. This results in a single peak, wherein position along the x-axis equals the EOT of the porous layer and is linearly correlated to the RI changes of the PSi. For the flow experiments, the microchannel was washed with elution buffer for 30 min, followed by a 1 h wash with SB buffer, to allow the aptamer to properly fold to its active 3D structure. Next, the protein samples (0.25 μM to 18 μM, in SB buffer) or lysate (with a protein content of 1 mg mL⁻¹) were introduced for 1 h, after which the surface was washed with SB for 30 min. To

Results

regenerate the surface for additional experiment, elution buffer was introduced for 30 min, followed by SB wash for 30 min. Each microchannel was used for two biosensing cycles. Flow rate was kept at 30 $\mu\text{L min}^{-1}$ for all steps. For the static experiment in the cell setup, the buffers (~5 mL) were introduced to the cell with a syringe and allowed to incubate for the same amount of time. Protein sample (100 μL of 1 μM in SB) was injected to the cell with a pipette and allowed to incubate for 1 h. The buffer washing steps were performed with 10 mL of the buffers.

The data is presented as relative ΔEOT , defined as

$$\frac{\Delta\text{EOT}_t}{\text{EOT}_0} = \frac{\text{EOT}_t - \text{EOT}_0}{\text{EOT}_0}$$

where EOT_0 is the average EOT signal at the baseline acquisition with SB buffer prior to protein introduction, and EOT_t is the average EOT signal at the last 5 min of protein incubation/flow phase. Calibration curve was fitted with a sigmoidal curve, according to the equation:

$$R = R_{\max} \frac{[C]}{[C] + K_D}$$

where R is the relative EOT signal, $[C]$ is the target concentration, R_{\max} is the maximal response signal attained for $[C] \rightarrow \infty$, and K_D is the apparent dissociation constant. R_{\max} and K_D are equal to $(7.7 \pm 0.3) \times 10^{-3}$ (as $\Delta\text{EOT}/\text{EOT}_0$) and $0.9 \pm 0.1 \mu\text{M}$, respectively.

The signal-to-noise ratio (SNR) values are calculated as the ratio of the relative EOT signal to the standard deviation (σ) of the baseline in SB prior to protein introduction. The latter equals to 0.08×10^{-3} , 0.07×10^{-3} and 0.09×10^{-3} (as $\Delta\text{EOT}/\text{EOT}_0$) for the cell setup, PDMS and 3D-printed microfluidic setups for 1 μM protein experiments, respectively. Limit of detection (LoD), the lowest target concentration which can be reliably distinguished from the background noise, is calculated by extrapolation from the fitted curve of the concentration when the optical signal is equal to $3 \cdot \sigma$. For 3D-printed microfluidic setup, the average σ for all experiments is equal to 0.11×10^{-3} (as $\Delta\text{EOT}/\text{EOT}_0$). Limit of quantification (LoQ) is calculated as the concentration which yields an optical signal equal to $10 \cdot \sigma$. Relative standard deviation (%RSD) is calculated for each experimental set as the standard deviation divided by the averaged relative EOT change.

Statistical analysis

In the microfluidic setups, repeats were performed on at least two independent microchannels, in which four different spots were measured. For the cell setup, repeats were performed on at least three different aptasensors. All data is presented as the mean of $n \geq 3$ with standard deviation of the mean. For statistical evaluation, unpaired t-test was performed with two-tailed distribution and unequal variance. p values below 0.05 were considered for significant difference between two groups.

Results and Discussion

Microfluidic Design and Integration with PSi Films

The 3D-printed polyacrylate microfluidic device design is presented in Figure 5.4.1a. Each device contains two separate microchannels, spaced out at 2.5 mm apart, with a width of 500 μm and height of 200 μm . Out of the total microchannel length (55.6 mm), only 7 mm are in contact with the PSi to minimize the required bonding area with the highly porous surface, while allowing for multi-spot optical measurements along the channel. A measurement window is created above the contact area to reduce the thickness of the polyacrylate material in the optical measurement area.

The preferable direct bonding of the microfluidic device to the PSi is not feasible owing the combination of the rough surface of the 3D-printed polyacrylate and the delicate porous nanostructure. The latter is characterized by a high porosity of $\sim 75\%$ and cylindrical pores with a diameter of ~ 50 nm, as depicted in the high-resolution scanning electron microscopy (HRSEM) micrographs in Figure 5.4.1b (and summarized in Table S5.4.1, Supplementary Information) Thus, we use an intermediate-layer bonding approach, derived from the stamping technique⁴²⁷, utilizing a UV-curable adhesive as the intermediate. The latter is used as these adhesives only require a short UV irradiation for curing and as such avoid harsh conditions, which may damage the fragile silicon scaffold. Prior to the bonding process, the 3D-

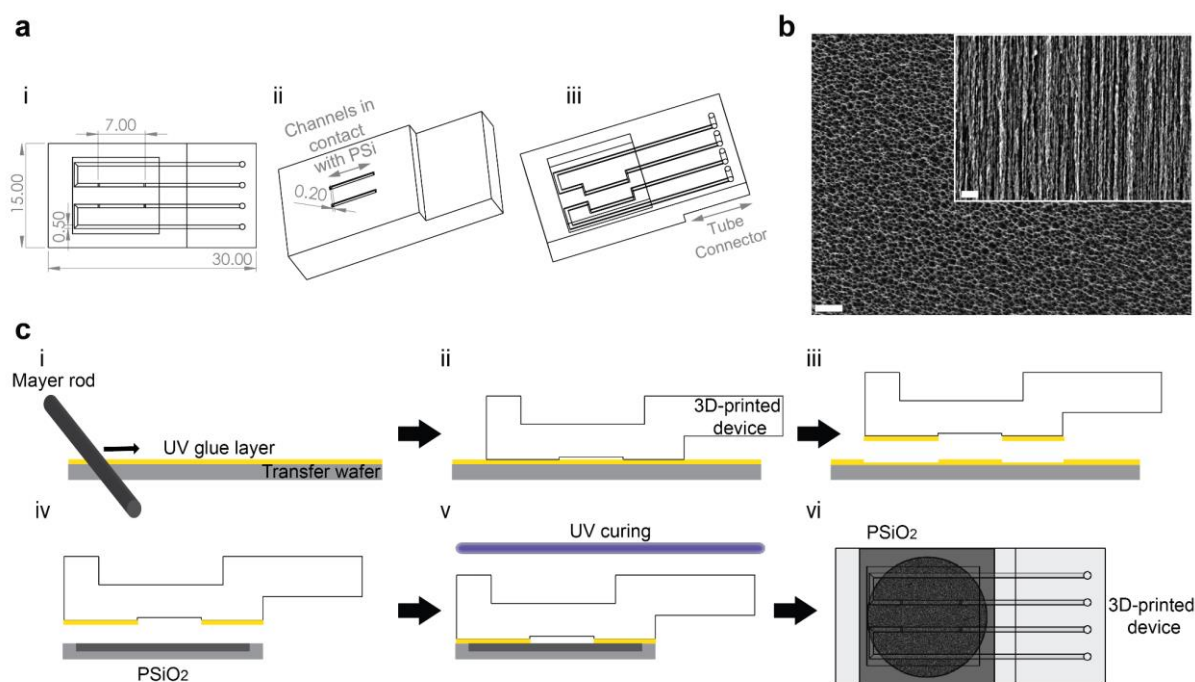


Figure 5.4.1 The microfluidic design, the PSi nanostructure, and the bonding method. (a) The 3D-printed microfluidic device design presented in (i) top-side; (ii) bottom-side and (iii) top-side views. Dimensions are in mm units. (b) Top view and cross-section HRSEM micrographs of an oxidized PSi nanostructure (the inset presents a cross-section view; scale bars are 400 nm). (c) The bonding method of the 3D-printed microfluidic device and the PSi: (i) a UV-curable adhesive is spread on a transfer wafer with a Mayer rod; (ii) the 3D-printed device is placed on top; (iii) the glue transfers to the device; (iv) the microfluidic device is carefully placed on top of the PSi chip; (v) the combined device is UV cured for 30 min; and (vi) the resulting integrated device.

Results

printed device, which often suffers from bending and a roughened surface due to the printing resolution^{40, 309}, is subjected to several alignment steps for its flattening. These include gentle gridding and flattening by applying a pressure of ~ 38 kPa at 60°C for 1 h.

Figure 5.4.1c presents the multi-step integration process; first, the UV-curable adhesive is spread on a transfer wafer with a Mayer rod (Figure 5.4.1c-i), which creates a thin and uniform adhesive layer with a thickness of $12\ \mu\text{m}$. In the next step, the microfluidic device is placed on top of the coated transfer wafer (Figure 5.4.1c-ii) and the glue is observed to spread throughout the device (Figure 5.4.1c-iii). This step is repeated twice, and then the microfluidic device is carefully placed on top of the P*Si* chip (Figure 5.4.1c-iv), followed by UV curing for 30 min (Figure 5.4.1c-v). It should be noted that the UV curing duration was not optimized and can be potentially shortened. No leakage or microchannel clogging are observed upon introduction of a dyed solution into the microchannels (Figure 5.4.2a), confirming successful bonding of the substrates. The effect of the bonding method on the microchannels and the porous regions is characterized by HRSEM imaging of the device cross-section, illustrated in Figure 5.4.2b. Outside of the microchannel, a continuous $5\pm 2\ \mu\text{m}$ thick adhesive layer is observed between the porous layer and the top polyacrylate device, see Figure 5.4.2c-i. The microchannel is completely free from adhesive, even in the interface regions of the channel's edges (Figure 5.4.2c-ii and iii, respectively). Notably, the integrity of the bonding between the layers is maintained through the harsh cross-sectioning procedure for the HRSEM, as well as >1 -year post bonding (see Figure S5.4.3, Supplementary Information). These demonstrate the bonding strength and suggest that the bonding method does not limit the long-term stability of the integrated devices. Thus, the latter is dictated by the aptasensor characteristics, i.e., capture probe and its immobilization chemistry. The relatively thick adhesive layer^{422, 427, 428} is required to ensure a good contact between the porous substrate and the 3D-printed device. The layer printing technique and the $32\text{-}\mu\text{m}$ resolution of the printer result in a rough polyacrylate surface, as can be seen in Figure 5.4.2d. Yet, this adhesive layer thickness is negligible compared to the current channel height and is compatible with the lowest microchannel dimensions allowed by the printer ($64\ \mu\text{m}$, data not shown). The presented bonding method is straightforward compared to other reported techniques⁴²², and can be readily performed and adapted to other device configurations.

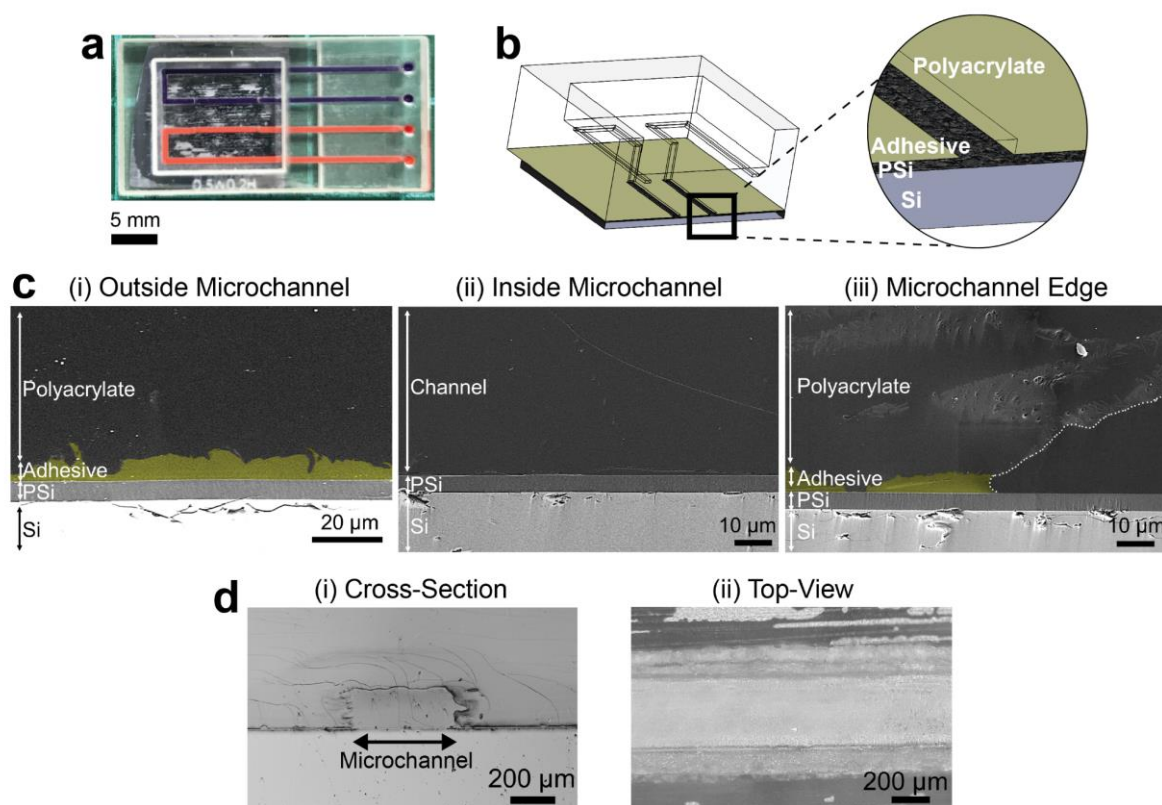


Figure 5.4.2 Characterization of the 3D-printed microfluidic-integrated PSi device: (a) Leakage study by dye flow in the microchannels; (b) illustration of the integrated device cross-section, showing its different layers; (c) HRSEM images of a cross-sectioned device, presenting an area (i) outside the microchannel; (ii) inside the microchannel and (iii) the microchannel edge, which is marked in white dashed line. No adhesive is found inside the microchannel, whereas a continuous $5 \pm 2 \mu\text{m}$ thick adhesive layer can be observed outside of the microchannel, between the PSi and the polyacrylate device. Note: for clarity, the adhesive layer is false-colored in yellow. (d) (i) Cross-section and (ii) top-view optical micrographs of the integrated device, demonstrating the roughness of the polyacrylate material at the microchannel edges.

Biosensing Experiments and Performance

In order to study the biosensing performance of the integrated platform, we use a model aptasensor, which we thoroughly characterized in our previous work, to allow a proper comparison of the biosensing results^{26, 435}. An anti-his tag aptamer, 6H7^{26, 435} is immobilized onto the PSi film by the standard amino-silanization and carbodiimide coupling chemistry, as we previously described^{26, 435}. The amino-silanization and carboxylation steps are performed prior to microfluidic device bonding, whereas the subsequent immobilization stages should be executed inside the microchannel. The UV curing during the bonding process is found to affect the functionality of the aptamers as capture probes (see Figure S5.4.4, Supplementary Information), possibly due to modification of DNA bases⁴³⁸.

For the biosensing experiments, a 60 kDa his-tagged protein from the Arabinanase family (termed as D2) is used as the target. The protein solution is introduced into the microchannels using a custom-designed 3D-printed tube connector and the reflectivity from the PSi is collected throughout the experiment from four different spots along the channel, as presented in Figure 5.4.3a (see Figure S5.4.2,

Results

Supplementary Information, for a complete description of the experimental setup). Figure 5.4.3b displays the results of two consecutive biosensing cycles with increasing protein concentrations, performed on the same aptasensor, where changes in the relative EOT values are plotted vs. time. Initially, the aptamer's selection buffer (SB) is introduced into the microchannel to allow proper folding of the aptamers and to acquire the initial EOT baseline. Upon the introduction of the D2 protein (0.25 μM), the relative EOT signal increases to a value of $(1.6\pm 0.2)\times 10^{-3}$ (as $\Delta\text{EOT}/\text{EOT}_0$) (equivalent to a net EOT change of 27 ± 2 nm), corresponding to the protein infiltration into the porous layer and binding to the immobilized aptamers. The signals collected from the different spots along the microchannel present a similar behavior, with a deviation of $< 9\%$. This suggests that a uniform bonding of the 3D-printed microfluidic device to the PSi is achieved, whereas the observed deviation is attributed to the variation of the PSi nanostructure along the microchannel, resulting from the anodization reaction, as well as the manual adjustment of the reflectivity measurement position from each spot. Nevertheless, no correlation is found between the sequential location of the spot along the microchannel and the optical signal value.

To release the bound protein, the aptasensor surface is washed with an elution buffer containing imidazole; the latter serves as a competitive agent, replacing the his-tagged proteins bound to the tethered aptamers³⁶⁸. Indeed, the EOT signal is observed to rapidly decrease, indicating the release of the bound proteins. Yet, it should be noticed that the signal decreases below the initial baseline possibly due to conformational changes of the immobilized aptamers. Aptamers 3D folding greatly depends upon their environment and as such saturating the biosensor with imidazole molecules, replacing the large proteins, may lead to prominent changes in the aptamer 3D structure, as we previously encountered³⁰. The aptasensor is then successfully reused for an additional biosensing cycle of the D2 protein at a higher concentration (0.5 μM), and a greater relative EOT increase of $(2.3\pm 0.4)\times 10^{-3}$ (as $\Delta\text{EOT}/\text{EOT}_0$) (corresponding to a net EOT change of 37 ± 7 nm) is observed.

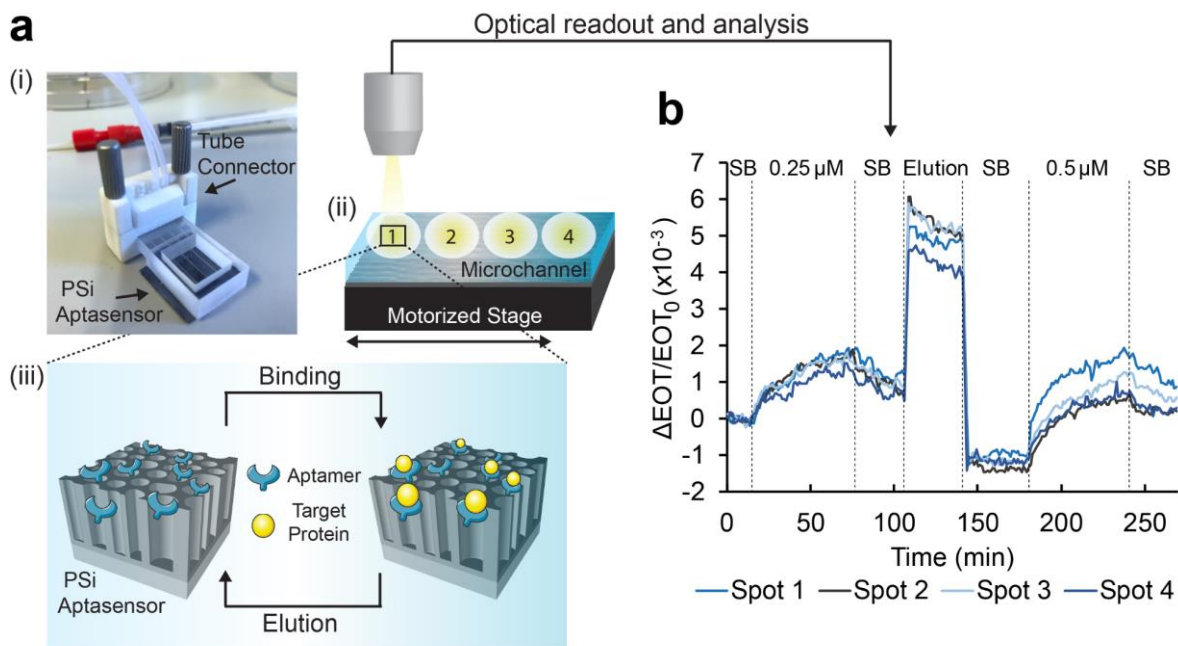


Figure 5.4.3 Biosensing experiments using the 3D-printed microfluidic-integrated PSi aptasensor. (a) (i) The microfluidic device is connected to tubes with a designated tube connector; (ii) it is fixed on a motorized stage, enabling optical monitoring of four different spots along a single microchannel. (iii) The anti-his tag PSi-based aptasensor is used to detect the target D2 protein and can be easily regenerated for several subsequent uses by exposure to elution buffer, containing imidazole. (b) Relative EOT changes vs. time of upon introduction of D2 protein solutions. First, a baseline is acquired in selection buffer (SB), followed by introduction of $0.25 \mu\text{M}$ protein at a flow rate of $30 \mu\text{L min}^{-1}$ for 1 h, and wash with SB. Subsequently, the biosensor is washed with an elution buffer, resulting in the aptasensor regeneration for a subsequent experimental cycle, using a protein concentration of $0.5 \mu\text{M}$.

Figure 5.4.4a presents the averaged relative EOT changes for the target D2 protein at a concentration range of $0.25 \mu\text{M}$ to $18 \mu\text{M}$. The lowest measured concentration is $0.25 \mu\text{M}$ with a relative EOT increase of $(1.8 \pm 0.3) \times 10^{-3}$ (as $\Delta\text{EOT}/\text{EOT}_0$) with a signal-to-noise (SNR) value of 19 ± 7 . The curve is fitted with a sigmoidal curve ($R^2=0.915$) and accordingly the K_D , the apparent dissociation constant, is estimated as $0.9 \pm 0.1 \mu\text{M}$ and is on the same order of magnitude as previous reports (K_D of $4.6 \mu\text{M}$ ²⁶).

Table 5.4.1 summarizes the analytical performance of the integrated aptasensor and provides a comparison to a non-microfluidic system (in which the same aptasensor is used for detection of a different his-tag protein). Notably, a significant improvement of ~ 70 -fold in the limit of detection is achieved in the 3D-printed microfluidic system. This is mainly attributed to the microfluidic integration and the flow configuration during the biosensing experiment, as discussed in the next section. The different target may also influence the performance, with a better accessibility of the histidine sequence in the protein structure for the binding aptamer.

Results

Table 5.4.1. Analytical results of the 3D-printed microfluidic-integrated aptasensor; compared to a similar aptasensor in a non-microfluidic setup (cell). Assay time is similar in both systems to allow proper comparison.

	3D-Printed Microfluidic Setup	Non-Microfluidic (cell) Setup
Detection Range (μM)	0.25-18	5-56
SNR*	19 \pm 7	16 \pm 6
LOD (μM)	0.04	2.7
LOQ (μM)	0.16	5.5
%RSD	12-22	6-27

*For lowest measured target concentration

Figure 5.4.4b compares the averaged relative EOT signal for the target D2 protein to non-target proteins. While 1 μM of the target protein induce a relative EOT change of $(4.0\pm 0.9)\times 10^{-3}$ with SNR value of 41 ± 17 , exposure of the biosensor to a similar protein with no his-tag group (D2N) results in a significantly lower signal of only $(0.8\pm 0.2)\times 10^{-3}$, with a lower SNR value of 13 ± 6 . This demonstrates that the optical signal obtained for the target D2 is ascribed mainly to specific binding of the his-tag sequence of the protein to the tethered aptamers. Exposure of the aptasensor to a higher concentration of trypsin, and importantly *E. coli* lysates (a complex protein mixture, which simulates best a control for his-tagged protein purification applications) with a substantial non-target protein content of 1 mg mL^{-1} , induce even lower signal changes [$(0.4\pm 0.6)\times 10^{-3}$ and $(0.1\pm 0.4)\times 10^{-3}$, respectively]. These results demonstrate that the selectivity of the aptasensor is not compromised by the integration with the printed microchannels when compared to our previous study²⁶.

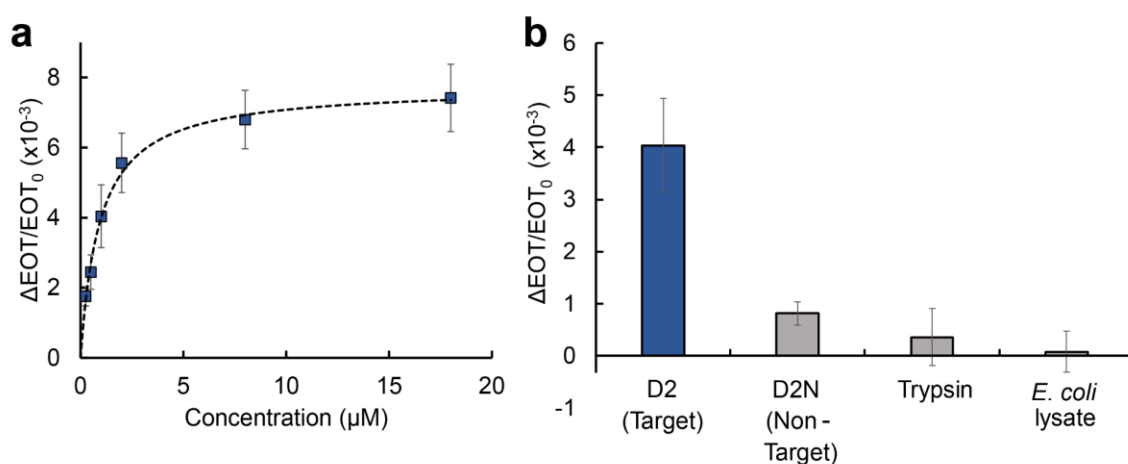


Figure 5.4.4 Averaged relative EOT changes upon exposure of the 3D-printed microfluidic-integrated aptasensor to (a) different concentrations of the target D2 protein; (b) D2 and non-target proteins. Protein concentrations are 1 μM for D2 and D2N (D2 without a his tag), 9 μM for trypsin and 1 mg mL^{-1} protein content in the *E. coli* lysates.

Comparison to Conventional Experimental Setups

The aptasensor performance in the 3D-printed microfluidic setup is compared to that observed when integrated in conventional experimental setups. The latter include a traditional cell setup^{18, 26, 28} and PDMS microchannels with similar dimensions, as illustrated in Figure 5.4.5a. The averaged relative EOT changes upon exposure to D2 and D2N proteins collected from the aptasensors, integrated in the different experimental setups, are presented in Figure 5.4.5b. Results are presented for one protein concentration (1 μM), but are characteristic also of other concentrations. The 3D-printed microfluidic platform presents the highest signal for detection of the target D2 protein with a SNR ratio of 41 ± 17 . Yet, its main advantage is in its selectivity, particularly when compared to the PDMS-microfluidic setup, the latter presenting a 2.5-fold higher relative EOT signal for the non-target D2N control ($p < 0.05$). This suggests higher non-specific adsorption in the PDMS microfluidic setup, which also questions the aptamer functionality in this system. It should be noted that in both microfluidic systems, the aptamer immobilization step is performed in the microchannel, prior to the biosensing experiment. Table S5.4.2 (Supplementary Information) compares point by point the construction process and performance of the 3D-printed and PDMS-based microfluidic aptasensors. For the PDMS microfluidic setup, aptamer immobilization in the microchannel significantly increases the EOT signal for both the target and non-target proteins, compared to aptamer immobilization prior to microchannel integration, see Figure S5.4.5 (Supplementary Information). Moreover, the signal in the former case, does not reach equilibrium within the time frame of the experiment. This behavior suggests different aptamer density within the PSi upon the two immobilization approaches and may be partly ascribed to the aptamer adsorption on the PDMS surface⁴³⁹. This in turn results in a lower aptamer density within the PSi upon aptamer immobilization in the PDMS microchannels, which exposes a larger surface area of the non-modified PSi nanostructure to non-specific adsorption of proteins²⁶. Thus, although a similar signal is obtained for the target in the 3D-printed and PDMS microfluidic systems, in the PDMS channels, it is ascribed in part to non-specific protein adsorption on the PSi surface. The integration process of the PSi and the PDMS, including corona surface treatment and high temperature curing, may also affect the surface chemistry of the PSi. This emphasizes the advantage of the 3D-printed microfluidic platform and the developed bonding method, which avoids harsh conditions. It should be noted that the negative charge of the polyacrylate-based material used for the 3D printing may induce nonspecific adsorption of positively charged biomolecules on its surface. Yet, as aptamers are negatively charged, they are not adsorbed to the 3D-printed microchannels and thus the aptasensor fabrication is not affected.

Our results also demonstrate the significant role of convection in these aptasensors, as target flow induces a higher signal in all systems, compared to a cell system without flow (see Figure 5.4.5b and Table 5.4.1). The induced convection improves the mass transfer of the target to the aptasensor surface^{36, 38}, which can reach up to 25-fold higher target flux compared to a diffusion-based system, based on a theoretical calculation (see detailed calculation in the Supplementary Information). This correlates

Results

with the ~70-fold enhancement in LOD compared to previous work⁴³⁵, whereas further enhancement is ascribed to the smaller microchannel dimensions and the microchannel uneven edges of the 3D-printed platform (see Figure 5.4.2c). The latter may contribute to solution mixing in the microchannel on top of the aptasensor, thus further improving the mass transfer³⁷.

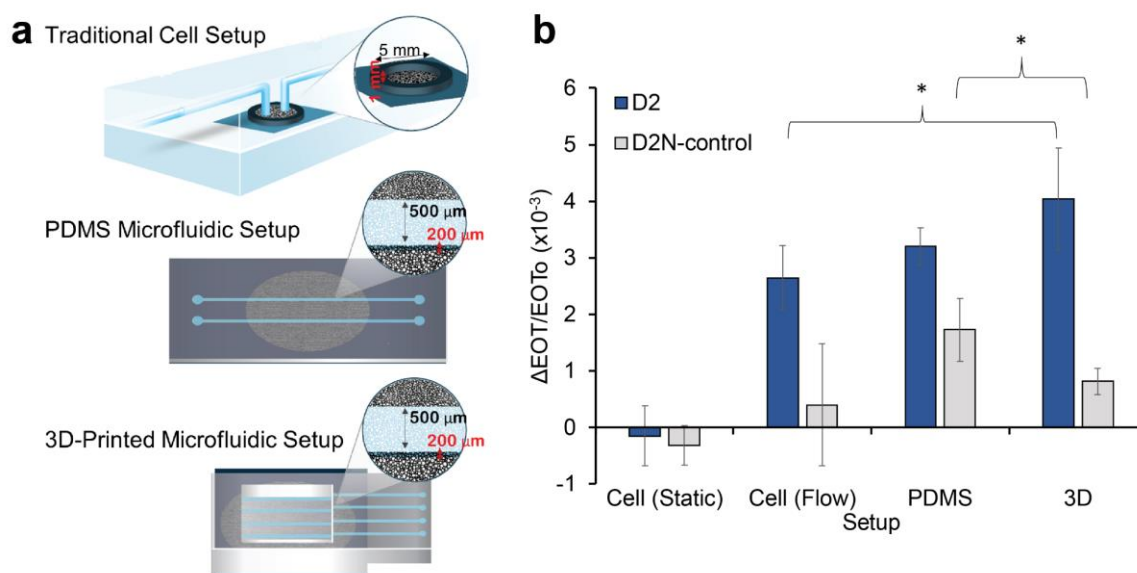


Figure 5.4.5 Comparison of the PSi aptasensor performance when integrated in different devices. (a) Schematics of the three experimental setups: 3D-printed microfluidics, PDMS microfluidics, and conventional cell (non-microfluidic); (b) Averaged relative ΔEOT changes for detection of 1 μM D2 or D2N proteins in the three experimental setups. For the cell setup, biosensing experiments are performed in static (no flow) or flow configurations. (*) indicates a statistically significant difference (t test, $n \geq 3$, $p < 0.05$).

Conclusions

In this work we present a simple and facile method for the integration of PSi-based aptasensors with 3D-printed polyacrylate microfluidics. The integration of both materials is based on a stamping technique with a UV-curable adhesive at room temperature. Successful bonding of the two substrates is demonstrated with a thin adhesive layer (~5 μm) in between; while the delicate porous regions within the microchannel remain clean and intact. As a proof-of-concept, we successfully immobilize a well-characterized anti-his tag aptamer as capture probe within the porous nanostructure, integrated in the microfluidic device, and demonstrate selective detection of a model target protein, compared to several non-target proteins, as well as complex *E. coli* lysate samples. The sensitivity of the integrated aptasensor, with a calculated LOD of 40 nM, is improved by ~70-fold compared to previous work. Thus, the developed bonding method does not impair the performance of the constructed biosensor. Furthermore, the resulting biosensor exhibits a superior selectivity and a higher detection signal for the

Results

target while integrated in the 3D-printed microfluidics, in comparison to the gold standard PDMS-based microfluidic setup with equal microchannel dimensions. For the latter, non-specific binding of the aptamer capture probe to the PDMS impairs the biosensors selectivity. Yet, the resolution of 3D printers, which dictates the microchannel dimensions, is currently on the range of tens of microns and much larger than applicable for PDMS-based microfluidics fabricated by soft lithography techniques. Moreover, the bonding method may also require adjustment to lower dimension microchannels or complex microstructures, due to the rough surface of the 3D-printed material, obtained due to the printer resolution. Nevertheless, 3D printing technology is rapidly advancing, the resolution keeps improving and there are already printers with a resolution in the lower micrometer range.

The superior performance of the 3D-printed microfluidic-integrated aptasensor in combination with its straightforward design and construction pave the way towards a more flexible approach to designing and investigating sophisticated microfluidic platforms integrated with PSi-based biosensors. For example, the presented microfluidic design could be adapted for multiplexed analyte detection, and integrated with different 3D-printed functional elements, such as pumps, valves and mixing components, which facilitate device automation, portability, and high-throughput⁴⁴⁰. These can be readily coupled with PSi aptasensors using the presented bonding method, where these aptasensors can be designed for detection of various target molecules simply by changing the aptamer capture probe, promoting the platform applicability in medical diagnostics^{31,441}, food quality and safety⁴⁴², as well as environmental monitoring.

Supporting Information

Additional Information Regarding Experimental Procedure

Fabrication of Oxidized PSi Nanostructures

PSi Fabry-Pérot thin films were fabricated from a highly doped p-type crystalline Si wafers, using a two-step anodic electrochemical etching process, as previously described¹⁶. First, a sacrificial layer was etched at a constant current density of 375 mA cm⁻² for 30 s in a 3:1 (v/v) solution of aqueous HF (48%) and ethanol, respectively. The resulting porous layer was removed by exposure to 0.1 M NaOH for 2 min, followed by a 1 min exposure to a solution of 1:3:1 (v/v) HF, ethanol and ddH₂O, respectively. Next, a second etching was conducted, at the same etching conditions as above. After each step, the silicon surface was thoroughly rinsed with ethanol and dried under nitrogen stream. The freshly etched PSi was thermally oxidized in a tube furnace (Thermo Scientific, Lindberg/Blue M™ 1200 °C Split-Hinge) at 800 °C for 1 h in ambient air, resulting in an oxidized PSi scaffold¹⁵⁹.

Post Processing of 3D-Printed Microfluidic Devices

Following printing, after the devices were cooled down, they were placed in a heat steam bath (EasyClean unit, 3D Systems, Rock Hill, USA) at 65 °C for 30 min and were subsequently immersed

Results

in hot biological oil bath (EasyClean unit, 3D Systems, Rock Hill, USA) at 65 °C for 30 min, to remove the support material. Next, hot oil was introduced into the channels using a syringe to remove any residues of support material. Finally, the devices were sonicated at 60 °C for 30 min in deionized water with detergent (Fairy Ultra Plus, Procter and Gamble, CT, USA) in an ultrasonic bath (Bandelin electronic, Berlin, Germany), followed by wash with 70% EtOH.

Experimental Setup

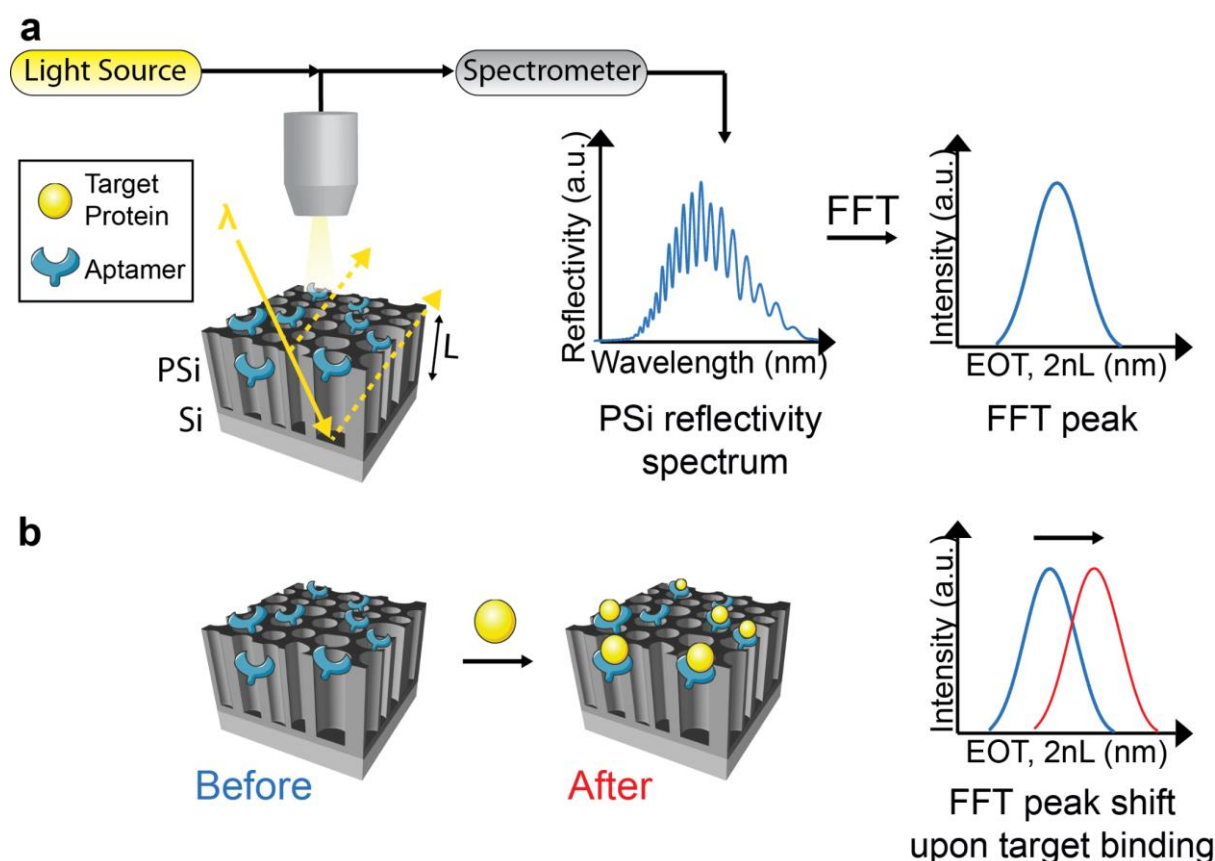


Figure S5.4.1. A schematic of the optical signal acquisition and analysis. (a) The PSi film is illuminated with white light from a broadband light source and the reflectivity is monitored with a spectrometer, presenting in a Fabry-Pérot fringe pattern due to interference from the two reflective interfaces of the PSi film. Application of Fast Fourier transformation (FFT) to the reflectivity spectrum results in a single peak, which position along the x axis equals to the effective optical signal (EOT) of the porous layer and linearly correlates to its average refractive index (n). (b) Upon target binding, an increase in the average refractive index of the PSi is obtained, observed as a shift of the FFT peak along the x-axis towards higher EOT values.

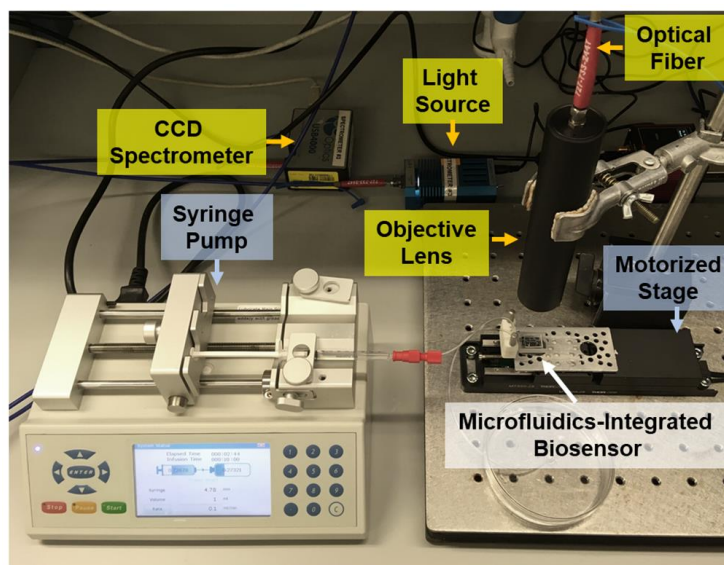


Figure S5.4.2. Image of the 3D-printed microfluidic experimental setup.

Porous Silicon Nanostructure Characterization

Porous layer thickness and porosity are evaluated by spectroscopic liquid infiltration method (SLIM). Briefly, the interferometric reflectance spectrum of the porous film is measured in air and while immersed in ethanol and acetone, having refractive indices of 1.359 and 1.357, respectively. The refractive index of the silicon oxide portion is assumed to be 1.455. The optical parameters from the reflectance spectra are then fitted to a Bruggeman effective medium approximation, yielding the thickness and the porosity of the porous layer.

Table S5.4.1. Oxidized PSi nanostructure fabrication and characterization with SLIM (n=5)

Wafer Resistivity (mΩ cm)	Current Density (mA cm ⁻²)	Etching Time (s)	Porosity (%)	Porous Layer Thickness (μm)
0.90-1.00	375	30	73±3	5.5±0.2

Integrity of Bonded Devices

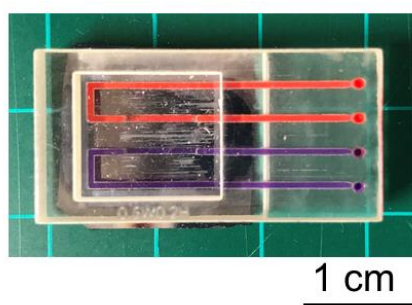


Figure S5.4.3. The integrated 3D-printed microfluidic aptasensor with a dyed solution flowed within the microchannels >1-year post bonding, demonstrating the integrity of the device.

Aptamer Immobilization

Aptamer immobilization can be conducted in two paths: either prior to microfluidic integration, or inside the microchannel following the integration. Figure S5.4.4 presents a comparison of the optical signal of the two chemical immobilization paths, for the target D2 protein and the non-target D2N control (D2 without his-tag). When the aptamer immobilization is carried out inside the microchannel, a good signal is observed for the target protein compared with the non-target control. By contrast, when performing the immobilization prior to microfluidic integration, a similar biosensing signal is observed for both proteins. We ascribe this to a non-specific binding to the modified PSi surface, due to a poor aptamer functionality upon exposure to UV light during the microfluidic integration process.

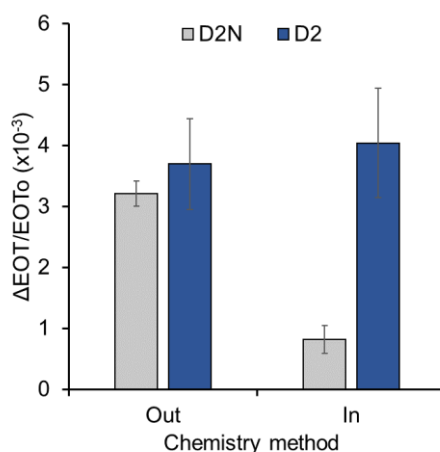


Figure S5.4.4. Averaged relative EOT changes for the detection of 1 μM D2 (target) and D2N (non-target) proteins in the 3D-printed microfluidic integrated aptasensor, where the aptamer molecules are immobilized prior (chemistry out) or after (chemistry in) the microfluidic integration.

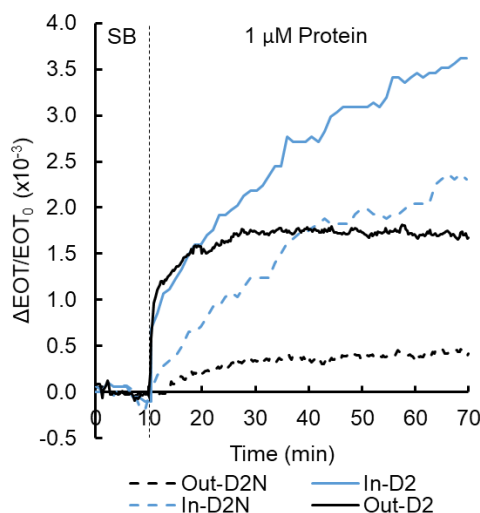


Figure S5.4.5. Real time relative EOT changes upon introduction of D2 (target) or D2N (non-target) protein solutions (1 μM) to the PDMS microfluidic setup, in which the aptamer is immobilized prior to microfluidic integration (out) or within the microchannel (in).

Derivation of Analyte Flux to the PSi Biosensor Surface in Static and Flow Experiments

The analyte flux to the PSi biosensor surface is calculated based on the thorough derivation of Squires *et al.*³⁶ and Lynn *et al.*³⁸. In our calculation, we consider only the diffusion and convection in the bulk solution towards the surface. The microchannel system is characterized with a microchannel height (H) of $200 \cdot 10^{-6}$ m and a microchannel width (W) of $500 \cdot 10^{-6}$ m. The length from the inlet to the PSi biosensor (L) is 0.017 m. The target diffuses in the bulk solution with a diffusion coefficient (D) of $7 \cdot 10^{-11}$ $\text{m}^2 \text{s}^{-1}$ ³⁹⁸. The flow rate (Q) used for the experiments is $5 \cdot 10^{-10}$ $\text{m}^3 \text{s}^{-1}$. At steady state, an analyte concentration boundary layer with a thickness δ is formed above the biosensor surface. At a distance greater than δ , the analyte will have no interaction with the surface and will be swept away, while only molecules below δ will interact with the surface. While assuming the fluid flow can be approximated as a one-dimensional pressure-driven flow between two flat plates, the following relation for δ is obtained, as derived by Lynn *et al.*³⁸:

$$1) \quad \delta \approx L \left(\frac{DH^2W}{6L^2Q} \right)^{1/3}$$

and the flux of the analyte towards the biosensor surface is given by:

$$2) \quad J_{\text{Diffusion+convection}} \approx C_{A,0} \left(\frac{6D^2Q}{LH^2W} \right)^{1/3}$$

Where $C_{A,0}$ is the introduced analyte concentration. This expression gives an upper limit for the flux at the biosensor surface since it neglects the diffusion within the porous layer. For the flow experimental

Results

system, with introduced analyte concentration of $1 \cdot 10^{-6}$ M, the boundary layer thickness, δ , is estimated as $2 \cdot 10^{-5}$ m and the analyte $J_{\text{Diffusion+convection}}$ is estimated as $3.5 \cdot 10^{-9}$ mol m⁻² s⁻¹.

For a system without convection, where the analyte solution is statically incubated on top of the biosensor, the flux can be simplified and described by^{36, 38}:

$$3) \quad J_{\text{Diffusion}} \approx D(C_{A,0} - C_{A,s}) / \delta(t)$$

where $C_{A,s}$ is the analyte concentration at the sensor surface. δ in that case is not constant; it increases with the progress of analyte binding by the biosensor and scale as $\delta \sim \sqrt{Dt}$ ³⁶. We will assume that $C_{A,s}$ is zero for simplification, thus resulting in an upper limit for the flux, not considering the diffusion within the porous layer. Thus, the analyte flux at the biosensor surface in a static experiment will be:

$$4) \quad J_{\text{Diffusion}} \approx \frac{DC_{A,0}}{\sqrt{Dt}}$$

By comparing equations (2) and (4), the time when the fluxes will be equal in both systems can be derived, as:

$$5) \quad t \approx \frac{D}{\left(\frac{6D^2Q}{LH^2W}\right)^{2/3}}$$

which in our system equals to 5.7 s. For longer times, the flux in the static system will substantially decrease in comparison to the flow system. For instance, after 60 min of incubation with the analyte, which is the binding time used in our system, the bulk diffusion flux in the static system will be $1.4 \cdot 10^{-10}$ mol m⁻² s⁻¹, more than an order of magnitude lower compared to the flow system.

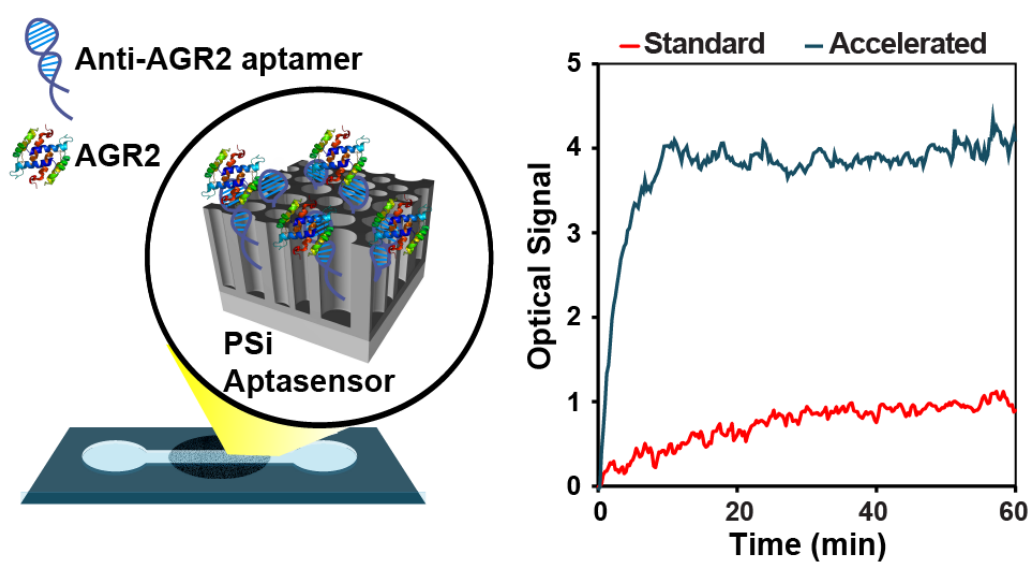
Comparison of 3D-printed and PDMS-based microfluidic integrated aptasensors**Table S5.4.2.** Overview of the construction of 3D-printed and PDMS-based microfluidic-integrated aptasensors and their biosensing performance.

	3D-Printed	PDMS
Template	No template	3D-printed
Resolution	32 μm (lowest microchannel dimensions 64 μm)	Similar upon 3D-printed template. Better for photolithographed template (lowest microchannel dimensions <10 μm)
Pre-bonding steps	Post printing processing steps, 2.5 h	PDMS curing at 60°C overnight
Bonding to PSi	Room temperature UV curing for 30 min	Corona treatment Baking at 90°C for 4 h
Aptamer immobilization	Within microchannels	Within microchannels
Average system noise ($\Delta\text{EOT}/\text{EOT}_0 \times 10^3$)	0.09	0.07
Optical signal for 1 μM target protein ($\Delta\text{EOT}/\text{EOT}_0 \times 10^3$)	4.0 \pm 0.9	3.2 \pm 0.3
SNR	41 \pm 17	53 \pm 12
%RSD	22	10
Optical signal for 1 μM non-target protein ($\Delta\text{EOT}/\text{EOT}_0 \times 10^3$)	0.8 \pm 0.2	1.7 \pm 0.6

5.5 Porous Silicon-Based Aptasensors: Towards Cancer Protein Biomarker Detection

Sofia Arshavsky-Graham, Simon J. Ward, Naama Massad-Ivanir, Thomas Scheper, Sharon M. Weiss, and Ester Segal

Submitted to ACS Measurement Science Au



Respective Table of Contents Image

Abstract

Anterior gradient homolog-2 (AGR2) protein is an attractive biomarker for various types of cancer. In pancreatic cancer it is secreted to the pancreatic juice by pre-malignant lesions, which would be an ideal stage for diagnosis. Thus, designing assays for sensitive detection of AGR2 would be highly valuable for potential early diagnosis of pancreatic and other types of cancer. Herein, we present a biosensor for label-free AGR2 detection and investigate approaches for enhancing the aptasensor sensitivity by acceleration of the target mass transfer rate and reduction of the system noise. The biosensor is based on a nanostructured porous silicon thin film, which is decorated with anti-AGR2 aptamers, where real-time monitoring of the reflectance changes enables detection and quantification of AGR2, as well as studying the diffusion and target-aptamer binding kinetics. The aptasensor is highly selective for AGR2 and can detect the protein in simulated pancreatic juice, where its concentration is outnumbered by orders of magnitude by numerous proteins. The biosensor limit of detection is optimized by increasing the diffusion flux to and within the nanostructure by applying isotachopheresis for pre-concentration of the AGR2 on the aptasensor, mixing, or integration with microchannels. By combining these approaches with a new signal processing technique that employs Morlet wavelet filtering and phase analysis, we achieve a limit of detection of 15 nM, without compromising the biosensor's selectivity and specificity.

Introduction

The aim of biosensors for medical diagnostic applications is to detect biomarker molecules in body fluids at clinically relevant levels. In many cases, sub-picomolar detection limits are required to meet the clinical criteria ⁴, as well as a sufficient sensitivity (i.e., the ability to discriminate between small changes in analyte concentrations) at low background noise. This should be accompanied by high selectivity and a fast response time ⁵⁻⁸. These three benchmarks are the main challenges to develop a successful biosensor for the clinic and should be carefully considered. For instance, overcoming the sensitivity challenge is related to maximizing the signal from a low number of analyte molecules, by more sensitive transducers or amplification schemes; the latter related to the signal or the number of target molecules ^{5, 8, 443}. Fast response time can be achieved by accelerating the mass transport of the analyte molecule to the biosensor surface, where the diffusion distance should be minimized ⁵⁻⁷. Finally, selectivity, which addresses the ability to detect the presence of the biomarker when it is outnumbered by several orders of magnitude by non-target species, should be enhanced by minimizing cross reactivity. This can be achieved by the proper choice of high-affinity capture probes, their density within the biosensor, as well as tailoring surface chemistry to minimize non-specific adsorption, or by pretreatment of the complex biological sample to remove interfering components ⁵.

Detection of protein biomarkers in body fluids for diagnosis and prognosis of various diseases enables the development of minimally invasive and point-of-care assays. For example, screening of protein

Results

biomarkers for various types of cancer is highly valuable for cancer management and monitoring^{4, 444, 445}. An increasing interest has been devoted towards the protein anterior gradient homolog-2 (AGR2) over the past decade, due to its diagnostic and prognostic value for pancreatic, breast, ovarian, prostate and colorectal cancer⁴⁴⁶⁻⁴⁵¹. Specifically, in pancreatic cancer, which is one of the most lethal types of cancer, AGR2 has been suggested to play an important role in cancer initiation and development. Moreover, AGR2 has been found to be elevated, at a concentration in the sub-nanomolar range, in the pancreatic juice of patients with high-grade pancreatic intraepithelial neoplastic (PanIN) lesions, which are precursors to invasive pancreatic cancer⁴⁵²⁻⁴⁵⁴. This would be an ideal stage for diagnosis, as a time point when surgical resection can potentially prevent the progression to malignancy⁴⁵⁴. To date AGR2 detection has been demonstrated by traditional laboratory-based analytical methods, such as enzyme linked immunosorbent assay (ELISA)⁴⁵⁵ and mass spectrometry (MS)⁴⁵⁶. Aptamer-based optical biosensors (aptasensors) for sensitive AGR2 detection have been successfully constructed, relying on rather complex competitive reaction schemes^{457, 458}.

In this work we aim to develop a label-free biosensor for the direct detection of the protein AGR2 in body fluids. The biosensor is constructed from porous silicon (PSi) Fabry-Pérot thin films, which enable target detection, via real-time monitoring of the PSi reflectance changes. Despite the significant advantages of such biosensors, their application has been rather limited due to insufficient sensitivity, usually in the micromolar range for proteins^{21, 26, 29, 186, 229, 332, 459}. To the best of our knowledge, their use for detection of cancer protein biomarkers, usually present in the picomolar range, has not yet been demonstrated. Their inferior performance is mainly attributed to mass transfer limitations^{23, 42, 159, 189, 396}, and several strategies have been implemented for sensitivity enhancement, while still detecting the analyte in a direct and label-free manner. These include the optimization of the porous nanostructure and surface chemistry^{19, 27, 32, 460}, design of a flow-through PSi biosensor^{23, 241}, microfluidic integration^{44, 46}, decoration of the PSi with gold nanoparticles for improved optical signal^{461, 462}, signal amplification⁴⁶³, application of an electrokinetic focusing of the target on top of the biosensors^{42, 464}, as well as novel signal processing techniques^{20, 465}. Specifically, we have demonstrated the integration of PSi biosensors with isotachopheresis (ITP) technique for on-chip analyte preconcentration and demonstrated a nanomolar detection limit for both DNA and protein targets^{42, 464}. Furthermore, we have recently presented a novel signal processing technique, which reduces system noise by application of Morlet wavelet convolution to filter spectra, resulting in an improved limit of detection⁴⁶⁵.

Herein, we investigate different avenues for enhancing the sensitivity of PSi and address the three key benchmarks for developing a successful biosensor⁵. The selectivity of the biosensor is achieved by the immobilization of an anti-AGR2 aptamer³⁰⁴ within the PSi and analyzed by exposure of the biosensor to non-target proteins in a buffer solution, as well as to a simulated pancreatic juice. The sensitivity and response time of the biosensor are investigated by real-time mass transfer imaging and several strategies for improving the protein flux to the biosensor are studied and compared. Furthermore, a new signal processing technique is investigated to reduce the experimental noise.

Experimental

Materials

Heavily doped p-type Si wafers (<100>-oriented, 0.90-0.95 mΩ·cm resistivity) were purchased from Sil'tronix Silicon Technologies. Aqueous HF (48%), (3-Aminopropyl)triethoxysilane (APTES), diisopropylethylamine (DIEA), succinic anhydride, N-(3-Dimethylaminopropyl)-N'-ethylcarbodiimide hydrochloride (EDC), N-Hydroxysuccinimide (NHS), acetonitrile (ACN), morpholinoethanesulfonic acid (MES), MES sodium salt, Tris base and all buffer salts were purchased from Merck. Ethanol absolute was supplied by Bio-Lab Ltd. All buffer solutions were prepared with Milli-Q water (ddH₂O, 18.2 MΩ·cm). Polydimethylsiloxane (PDMS) was prepared from Sylgard® 184 Silicon Elastomer kit, purchased from Dow Corning. Anti-AGR2 aptamer sequence was obtained from Wu *et al*³⁰⁴ and used with a 17-bases long spacer at the 5' terminus: 5'-TCT-CGG-ACG-CGT-GTG-GTC-GGG-TGG-GAG-TTG-TGG-GGG-GGG-GTG-GGA-GGG-TT-3'. The aptamers were purchased with a 5'-amino modification or 5'-amino modification and 3'-Cy5 fluorescent dye modification from Integrated DNA Technologies. AGR2 protein was purchased from MyBioSource Inc. Pancreatin from porcine pancreas (4x USP), N_α-benzoyl-L-arginine ethyl ester (BAEE), Trypsin and BSA were purchased from Merck. Rabbit Immunoglobulin G (IgG) was purchased from Jackson ImmunoResearch Labs Inc. 10 mM phosphate buffered saline (PBS) was composed of 137 mM NaCl, 2.7 mM KCl, 10 mM Na₂HPO₄ and 2 mM KH₂PO₄ (pH 7.0). Selection buffer (SB) was composed of 137 mM NaCl, 20 mM KCl, 10 mM Na₂HPO₄ and 2 mM KH₂PO₄ (pH 7.4). 0.5 M MES buffer was prepared from 0.27 M MES and 0.23 M MES sodium salt (pH 6.1) and Tris buffer was composed of 50 mM Tris base (pH 7.4).

Aptasensor Construction

Fabrication of oxidized PSi nanostructures: PSi Fabry-Pérot thin films are fabricated from a highly doped p-type crystalline Si wafers, with a typical resistivity of 0.90-0.95 mΩ·cm, using a two-step anodization process. A detailed description of the etching setup can be found elsewhere¹⁶. First, a sacrificial layer is etched at a constant current density of 300 mA cm⁻² for 30 s, in a 3:1 (v/v) solution of aqueous HF (48%) and ethanol, respectively. Subsequently, the obtained porous layer is dissolved in 0.1 M NaOH and removed. Finally, a second etching is conducted under similar conditions and the resulting freshly-etched PSi is thermally oxidized in a tube furnace (Thermo Scientific, Lindberg/Blue M™ 1200°C Split-Hinge, USA) at 800 °C for 1 h in ambient air¹⁵⁹.

Nanostructure characterization with scanning electron microscopy: The oxidized PSi nanostructure, pore diameter and film thickness are characterized by high-resolution scanning electron microscopy (Carl Zeiss Ultra Plus), at an accelerating voltage of 1 keV.

Results

Immobilization of anti-AGR2 aptamers: Amino-terminated aptamers are conjugated to the oxidized PSi films by amino silanization and carbodiimide coupling chemistry^{26, 302}. Initially, the oxidized PSi film is amino-silanized by incubation in a solution of 1% v/v APTES and 1% v/v DIEA in ddH₂O for 1 h, followed by washing with ddH₂O and ethanol and drying under a nitrogen stream. Subsequently, the PSi samples are annealed at 100 °C for 15 min. Next, carboxylation is achieved by incubation in a solution of succinic anhydride (10 mg mL⁻¹) and 2% v/v DIEA in ACN for 3 h, followed by extensive rinsing with ACN and ddH₂O and drying under a nitrogen stream. The samples are then reacted with EDC (10 mg mL⁻¹) and NHS (5 mg mL⁻¹) in MES buffer for 1 h, after which, the samples are rinsed with MES buffer and gently dried under nitrogen stream. Subsequently, aptamer solution (50 μM in PBS) is applied and incubated for 1 h, followed by rinsing with Tris buffer, to deactivate remaining reactive NHS and EDC groups on the surface. Finally, the aptamer-functionalized PSi is exposed to boiling ddH₂O for 2 min, and gently dried under a nitrogen stream, to unfold any secondary structures of the aptamer prior to further use.

Chemistry characterization with Fourier transform infrared (FTIR) spectroscopy: Chemical modification of the PSi is studied with attenuated total reflectance FTIR (ATR-FTIR) spectroscopy, utilizing a Thermo 6700 FTIR instrument, equipped with a Smart iTR diamond ATR device.

Chemistry characterization with confocal laser scanning microscopy: Cy5-labeled aptamer is immobilized onto the PSi, followed by scanning with a confocal laser scanning microscope (LSM 700, Carl Zeiss, Inc.), linked to a Zeiss inverted microscope equipped with a Zeiss X63 oil immersion objective. PSi photoluminescence and Cy5-labeled aptamers are excited with laser lines of 405 nm and 639 nm, respectively. For three-dimensional image projection of the porous structure, z-scans in 0.4 μm increments over a depth of ~12 μm are taken and projected with a standard Carl Zeiss software (ZEN 2009). Further image analysis is performed by Imaris Bitplane scientific software.

PDMS Microchannels

PDMS microchannels, 3 cm in length, 100-350 μm in width and 20 μm in depth, are fabricated in-house based on an SU8 template, which was constructed by standard lithography at Stanford Microfluidic Foundry (Stanford University, Stanford, CA, <http://www.stanford.edu/group/foundry/>)³¹⁰. PDMS polymer and cross-linker are mixed at a 10:1 ratio, respectively, followed by curing at 100 °C for 3 h. The microchannels are attached to the aptamer-functionalized PSi by exposure of the inner surface of the PDMS to corona treatment for 40 s, using a laboratory corona treater (BD-20V Electro-Technic Products), followed by baking at 100 °C for 3 h.

Time-Resolved Mass Transfer Visualization

Infiltration of a fluorescently-labeled AGR2 protein (Atto-647N dye) in the aptasensor is monitored in real time by confocal laser scanning microscopy (CLSM). The scanning is conducted with a LSM 510 confocal laser-scanning microscope (Carl Zeiss, Inc.), linked to a Zeiss upright microscope equipped

Results

with a Zeiss X63 oil immersion objective. PSi photoluminescence and Atto-647N-labeled AGR2 are excited with laser lines of 458 nm and 633 nm, respectively. For three-dimensional image projection of the porous structure, z-scans in 0.73 μm increments over a depth of ~ 15 μm are taken, every 30 s, and projected with a standard Carl Zeiss software (ZEN 2010). Initially, the photoluminescence and AGR2 fluorescence signals are scanned within the aptasensor with 10 μL of SB buffer for 10 min. Then, a 1 μM solution of Atto-647N-labeled AGR2 in SB (40 μL) is introduced and the photoluminescence and AGR2 fluorescence are measured continuously for additional 50 min. We use a relatively low AGR2 concentration for the measurements to obtain a time-resolved visualization of the protein infiltration before signal saturation is reached. Image analysis is performed by Imaris Bitplane scientific software.

Isotachopheresis (ITP) Assay

For application of ITP, the freshly etched PSi is thermally oxidized in a tube furnace (Thermolyne) at 1000 $^{\circ}\text{C}$ for 46 h under constant oxygen flow of 0.5 L min^{-1} . These harsh oxidation conditions are employed to ensure an insulating oxide layer, capable to withstand high voltage values^{42, 464}. Following aptamer immobilization, PDMS microchannels are attached (350 μm in width and 20 μm in height) as described above. A fluorescently-labeled AGR2 is used to visualize the protein focusing, where the protein is labeled via amine groups with Atto-647N dye, to maintain its natural charge. In the standard cationic ITP assay, the microchannel and its east reservoir are filled with a leading electrolyte (LE) buffer using a vacuum pump, while the microchannel's west reservoir is filled with the fluorescently-labeled AGR2, diluted in a terminating electrolyte (TE) buffer, see schematic illustration in Figure S5.5.1 (Supporting Information). A constant voltage of 350 V is then applied across the microchannel, utilizing a high-voltage power supply (model PS375, Stanford Research Systems, Inc.). The fluorescence signal is monitored with a customized Zeiss upright microscope, equipped with a camera (Axio Cam MRc, Zeiss), at a constant exposure time of 100 ms. X-Cite® 120Q excitation light source (Excelitas Technologies) is used for illumination. The LE and TE buffer compositions are detailed in Table S1 (Supporting Information). For the indirect anionic ITP assay, the LE is composed of 200 mM Bis-Tris, 100 mM KCl and 100 mM HCl and TE buffer is composed of 20 mM Bis-Tris, 10 mM Tricine and 0.2 mM KCl. The fluorescently-labeled AGR2 is reacted with the anti-AGR2 aptamer at a ratio of 1:10, respectively, in TE buffer for 1 h, prior to the ITP assay.

Biosensing Experiments

The aptasensor is mounted in a custom-made Plexiglas cell and a tungsten light source is focused onto the center of the sample with a spot size of approximately 1 mm^2 . Interferometric reflectance spectra are collected with a charge-coupled device (CCD) spectrometer (Ocean Optics, USB 4000) fitted with an objective lens coupled to a bifurcated fiber-optic cable, see Figure S5.5.2a (Supporting Information) for additional details. For experiments in microchannels, a customized Zeiss upright microscope equipped with a CCD spectrometer is utilized. The aptasensor is fixed to the microscope stage, under

Results

the objective, and illuminated with light from a halogen source (halogen100 illuminator, Zeiss), focused through an A-Plan objective (10x magnification, 0.25 NA, Zeiss). The size of the illumination spot is controlled by the microscope iris and adjusted to the microchannel width (the experimental setup is shown in Figure S5.5.2b, Supporting Information).

Illumination and reflectivity detection are performed perpendicular to the surface and the reflectance spectra are recorded in real time at a wavelength range of 450-900 nm. The collected spectra are analyzed by reflective interferometric Fourier transformation spectroscopy (RIFTS)^{17, 18, 26} in which taking the fast Fourier transformation (FFT) of the raw spectra results in a peak that corresponds to the dominant frequency of the Fabry-Pérot interference fringes. The position of this peak along the x-axis equals the effective optical thickness (EOT) of the porous layer and is the product of the average refractive index and the thickness of the porous layer. Reflectance spectra are recorded every 15 s throughout the experiments and the data is presented as a relative EOT, defined as

$$\frac{\Delta EOT_t}{EOT_0} = \frac{EOT_t - EOT_0}{EOT_0}$$

where EOT_0 is the averaged EOT signal obtained during baseline establishment.

In all biosensing experiments, a baseline is first acquired in SB and the protein solution (in SB or in a simulated pancreatic juice) is introduced and incubated for 1 h. The protein solution is removed and the aptasensor is extensively washed with SB. Please note that the purchased AGR2 stock (1 mg mL⁻¹) is diluted in 20 mM Tris-HCl, 1 mM DTT, 1 mM EDTA and 10% glycerol (pH 8.0) buffer. Thus, its dilution in SB contains residues of these components. Biosensing experiments with non-target proteins were carried out with the same dilution procedure to eliminate variability due to buffer composition. For experiments with simulated pancreatic juice, pancreatin is utilized. It is diluted according to its trypsin activity to provide 100 *p*-toluene-sulfonyl-L-arginine methyl ester units per mL³¹¹. The trypsin activity of 0.45 μm filtered pancreatin in SB is determined by a standard BAEE assay³¹² and diluted accordingly. The total protein amount within this sample is determined with NanoDrop instrument (NanoDrop 2000 spectrophotometer, Thermo Scientific) and the sample is analyzed by a standard SDS-PAGE. In some experiments, mixing is applied by manual pipetting of the AGR2 solution over the aptasensor for 10 min, followed by an incubation without mixing. As a control, the buffer used for the dilution of the AGR2 protein stock was mixed for the same time on top of the aptasensor.

The limit of detection (LOD) is calculated based on the standard deviation of the relative EOT signal while the aptasensor is incubated with the baseline buffer, prior to protein introduction. We use the lowest standard deviation values in each of the experimental setups, which are equal to $\sigma=0.03$, $\sigma=0.01$ and $\sigma=0.04$ (as $\Delta EOT/EOT_0 \times 10^{-3}$) for the cell, mixing and microchannel setups, respectively. LOD is commonly determined as the concentration at which the signal equals to $3.3 \times \sigma$, thus centering the noise floor around 0; however, this assumes that the intercept of the line of the best fit is 0, which is not always the case due to baseline drift or nonspecific adsorption. This may result in an undefined LOD when the intercept is outside the noise floor. Thus, we apply a more accurate and robust approach by

Results

centering the noise floor around the intercept, and calculating the LOD as the concentration at which the signal exceeds its intercept by $3.3 \cdot \sigma$ in the linear fit of the data ⁴⁶⁵. It should be noted that AGR2 is present in a dimer-monomer equilibrium ⁴⁶⁶ and thus we utilize a molecular mass of a dimer to convert between $\mu\text{g L}^{-1}$ and M units.

The apparent dissociation constant (K_D) is calculated based on a non-linear regression of the obtained data utilizing the model for specific binding with a hill slope, according to:

$$Y = \frac{B_{\max} \cdot X^h}{(K_D^h \cdot X^h)}$$

B_{\max} is the concentration at which the maximum biosensor response is reached and h is the Hill coefficient, which gives information about the stoichiometry of the binding interaction ^{314,315}. GraphPad Prism software is used for the fitting.

Signal processing based on Morlet wavelet filtering and average phase difference (Morlet wavelet phase method)

The acquired reflectance spectra are processed using the recently-introduced Morlet wavelet phase method ⁴⁶⁵. The requisite steps are depicted in Figure S5.5.3 and include the application of complex Morlet wavelet band pass filtering to the reflectance vs. wavenumber spectrum. The Morlet wavelet parameters are determined based on the width and center frequency of the dominant peak in the FFT, obtained using a rectangular window. The phase of the resulting complex filtered spectrum is extracted and unwrapped. In this manner, the unwrapped phase is calculated for a reference spectrum, during aptasensor incubation with the baseline buffer prior to protein or complex sample introduction, and for each subsequent time point. The resulting Morlet wavelet phase signal is the average of the difference between the unwrapped phase of the reference spectrum and that of the spectrum collected at each time point.

Statistical analysis

For all experimental sets, $n \geq 3$ and values are presented as the mean and standard deviation of the mean. For statistical analysis, a Student's t-test with a minimum confidence level of 0.05 for statistical significance, assuming unequal sample sizes and unequal variance, is performed.

Results and Discussion

Aptasensor Construction

PSi is fabricated by contact-current anodization of Si to yield a nanostructured porous film ($\sim 4.9 \mu\text{m}$ thick) with characteristic interconnected cylindrical pores (with a diameter of 40-60 nm), as presented in Figure 5.5.1a. The porous film is thermally oxidized and functionalized with amine terminated anti-AGR2 aptamers ³⁰⁴ using NHS/EDC coupling chemistry ³⁰²; where the aptamer is modified with a 17

Results

bases-long spacer sequence at its 5' terminus to increase the distance of the binding region from the solid surface^{334,467}. The oxidized PSi is amino silanized and ATR-FTIR spectrum depicts a peak at 1640 cm^{-1} (see Figure 5.5.1b), attributed to the bending of the primary amines^{302, 348}. Subsequent carboxylation with succinic anhydride results in two strong peaks at 1557 and 1637 cm^{-1} , which are ascribed to amide II and amide I bonds, respectively, and a peak at 1406 cm^{-1} is assigned to the carboxylic acid groups^{302,348}. After the activation with coupling agents, EDC and NHS, 3 peaks at 1736, 1785 and 1820 cm^{-1} are observed, characteristic of the NHS ester groups on the surface^{302, 348, 468}. The latter diminish following the conjugation of the aptamer, while the peaks of the amide I and II bonds intensify. We have also monitored the changes in the reflectance spectra of the PSi film throughout the aptamer immobilization process, and the relative EOT values after each modification step are presented in Figure 5.5.1c. Upon immobilization of the different chemical groups and aptamer, the average refractive index of the porous layer increases as evidenced by the increasing EOT values^{16, 18}. Aptamer conjugation is further characterized by confocal laser scanning microscopy (CLSM) and Figure 5.5.1d presents 3D projection images of the PSi film following conjugation with Cy5-labeled aptamer. When utilizing the complete conjugation chemistry of the labeled aptamer, a strong fluorescence signal from the labeled aptamer is observed to be uniformly distributed throughout the entire porous nanostructure (Fig. 5.5.1d-I). As a control, the activation step of the carboxylated surface with NHS and EDC is omitted, and no fluorescence from the Cy5-labeled aptamer is detected, indicating that no conjugation of the aptamers to the carboxylated surface has occurred (Fig. 5.5.1d-II). Thus, these results confirm the successful immobilization of the aptamer within the PSi nanostructure.

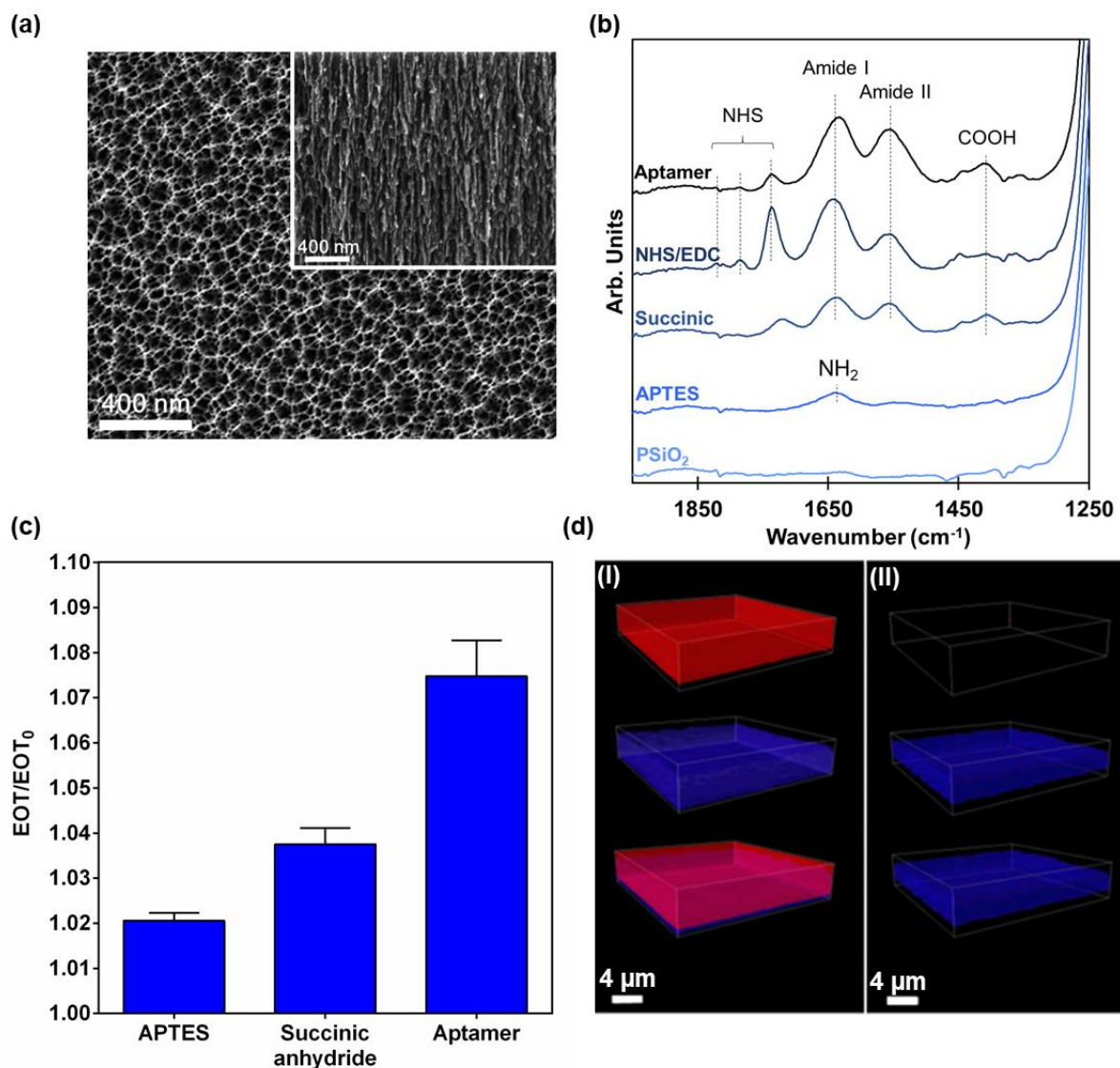


Figure 5.5.1. PSi aptasensor construction: (a) Top-view and cross-section electron micrographs of the oxidized PSi film, fabricated by anodization at 300 mA cm^{-2} for 30 s; (b) ATR-FTIR spectra and (c) Relative EOT values of the PSi film following the synthetic steps for the aptamer immobilization: amino-silanization with APTES, carboxylation with succinic anhydride, activation with NHS/EDC, and coupling of amino-terminated aptamer. Note that the ATR-FTIR spectra are normalized to the Si-O-Si stretching peak, which is the maximal peak value for each spectrum, and that the EOT values are normalized to the EOT of a neat oxidized PSi film (no aptamer). Since NHS and EDC serve as leaving groups, replaced by the aptamers, the EOT of the porous layer after NHS/EDC activation is not presented. (d) CLSM 3D projection images of PSi film conjugated with Cy5-labeled aptamer: (I) full conjugation chemistry; (II) control experiment - no activation of the carboxylated surface with coupling agents, NHS and EDC. Top row represents the fluorescence signal of Cy5-labeled aptamer, middle row represents the photoluminescence of the PSi nanostructure and bottom row is the merged view of top and middle rows.

Biosensor Selectivity

Figure 5.5.2a presents the real-time relative EOT changes of the PSi aptasensor upon introduction of the target (AGR2) and non-target (Trypsin) proteins. The two proteins present a similar molecular

Results

weight and charge, while trypsin is highly abundant in the gastrointestinal body fluids³¹¹. The aptasensor is initially washed with SB to allow the aptamer's proper folding and to establish the initial EOT baseline. Following the introduction of AGR2, the EOT signal is observed to gradually increase due to the protein infiltration into the porous layer and binding to the tethered aptamers, as manifested by the slope of this curve. In contrast, for the non-target trypsin only a low increase in the EOT signal is observed, which remains relatively steady throughout the incubation step. This is also observed for other relevant non-target proteins, including BSA and IgG (see Figure S5.5.4), and was also reported for other porous aptasensors^{26, 435, 469}. While the slope of the real-time EOT signal cannot differentiate between infiltration and molecular binding phenomena⁴⁷⁰, the net increase in the relative EOT (obtained upon the wash step with SB intended for removal of unbound and adsorbed proteins) is used to study apparent protein binding within the PSi. Figure 5.5.2b summarizes both the averaged net EOT values and the slopes obtained in these experiments, where only minor changes are observed for the non-target proteins, demonstrating the outstanding selectivity of the biosensor.

Pancreatic juice is a highly complex fluid, rich with different proteins and digestive enzymes⁴⁷¹. Given that pancreatic juice is secreted by the pancreas, it serves as an opportune medium for studying pancreatic cancer-related proteins, and specifically early cancer stage-related proteins, such as AGR2⁴⁷¹⁻⁴⁷³. Thus, the aptasensor is challenged with pancreatin, which is a simulated pancreatic juice from pigs. It is composed of a mixture of several digestive enzymes, such as amylase, trypsin, lipase, ribonuclease and protease, produced by the exocrine cells of the porcine pancreas³¹¹. The total protein concentration is $19 \pm 1 \text{ mg mL}^{-1}$ and the abundancy of non-target proteins within this sample is shown in an SDS-PAGE analysis in Figure S5.5.5 (Supporting Information). The aptasensor response in terms of the net EOT change to neat and AGR2-spiked pancreatin is presented in Figure 5.5.2c. Pancreatin induces only a small increase in the net relative EOT, suggestive of non-specific binding, while the spiked samples result in a 9-fold higher EOT changes (t-test, $p=0.0002$). This further highlights the selectivity of the aptasensor, where the AGR2 is selectively bound, while outnumbered by >100-fold of non-target proteins. Yet, it should be noted that the response to the spiked pancreatin is lower than that obtained for AGR2 in buffer (Fig. 5.5.2c). This result may be ascribed to pancreatin components interfering with the aptamer-AGR2 binding, which is highly dependent on the proper folding of the aptamer⁴⁶⁷.

The calculated slopes (see Fig. 5.5.2d) also present the selectivity of the biosensor towards AGR2: the AGR2-spiked pancreatin induces a 2-fold higher slope compared to neat pancreatin (t-test, $p=0.02$). Yet, the attained slope signal in neat pancreatin is rather high and the coefficient of variation between readouts is prominent compared to the net relative EOT change (Fig. 5.5.2c). The different behavior of these two signal analysis approaches stems from their origin; while the slope characterizes the protein infiltration and apparent binding rate, the net relative EOT signal represents the total binding within the porous layer. Thus, in contrast to the biosensor performance in a single protein solution (Fig. 5.5.2b), upon overwhelming the aptasensor with pancreatin, some of the components of this concentrated

Results

complex protein mixture diffuse into the porous nanostructure and non-specifically adsorb on the pore walls, resulting in a higher slope as shown in Figure 5.5.2d. This can be observed in Figure S5.5.6 (Supporting Information), presenting the real-time increase in the relative EOT during neat pancreatin introduction. Yet, after ~ 25 min of incubation the signal reaches a plateau, whereas, for the spiked sample, the signal continues to increase throughout the incubation period, resembling the real-time response of the aptasensor to AGR2 in a buffer. Once the aptasensor is washed with SB, the EOT decreases by ~ 6 nm for both the neat and spiked pancreatin (corresponding to a relative EOT decrease of $\sim 0.4 \Delta EOT/EOT_0 \times 10^{-3}$), indicating a similar extent of removal of adsorbed and non-specifically bound proteins from the porous layer. As such, due to the wash step, the net EOT change (presented in Fig. 5.5.2c) is less affected by reversible adsorption and nonspecific binding.

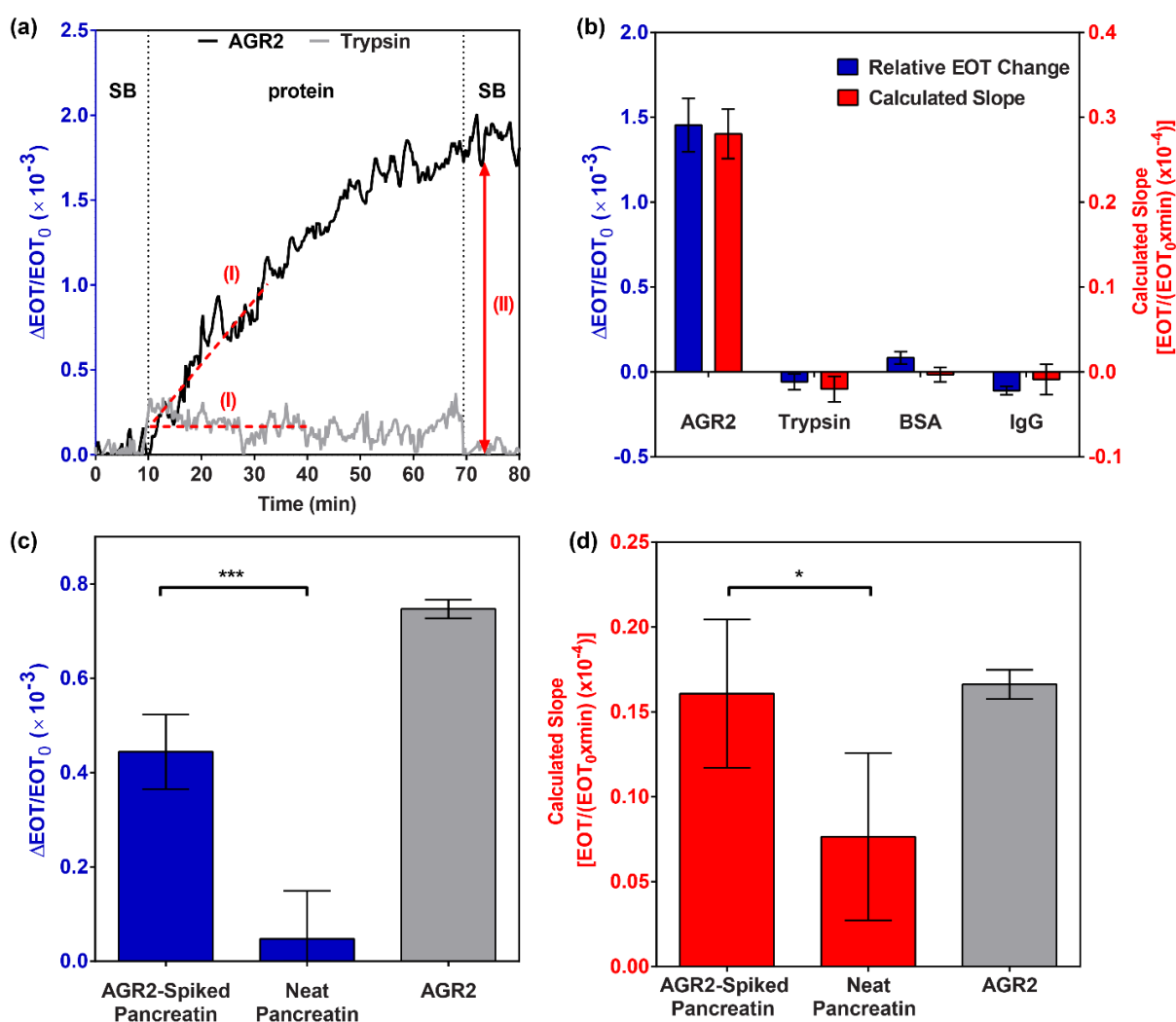


Figure 5.5.2. Aptasensor response to AGR2 in solution and in pancreatin. (a) Real-time relative EOT changes upon aptasensor incubation with AGR2 or trypsin protein solutions ($200 \mu\text{g mL}^{-1}$). Baseline is acquired in the aptamer's selection buffer (SB), followed by introduction of the protein solution and incubation for 1 h. The slope of the real-time EOT curves at the initial 30 min of protein incubation (I) is used to study the protein infiltration rate into the porous layer and binding. The solution is removed, and the biosensor is washed with SB and the attained signal (II) is referred to as the net relative EOT

change. (b) Net relative EOT changes and calculated slopes upon exposure of the aptasensor to AGR2 and different non-target proteins solutions (trypsin, BSA and IgG, a similar concentration of $200 \mu\text{g mL}^{-1}$ is used in all experiments, $n=3$). (c) Net relative EOT changes and (d) calculated slopes for pancreatin spiked with $100 \mu\text{g mL}^{-1}$ AGR2, neat pancreatin and $100 \mu\text{g mL}^{-1}$ AGR2 in a buffer. ***/* Significantly different (t test, $n=3$ for neat AGR2 and $n=5$ for experiments with pancreatin, $p=0.0002$ for relative EOT changes and $p=0.02$ for calculated slopes).

Limit of Detection

Figure 5.5.3 presents the averaged net relative EOT changes and calculated slopes upon exposure of the biosensor to different concentrations of AGR2. The linear detection range of the biosensor is between 0.05 and 2 mg mL^{-1} , based on both signal analysis methods, with a good linear correlation ($R^2=0.9957$ for the relative EOT changes and $R^2=0.9919$ for the calculated slope). For the net relative EOT signal, a concentration of $50 \mu\text{g mL}^{-1}$ is detected with an average signal-to-noise ratio (SNR) of 4.5 and the theoretical LOD value is calculated as $9.2 \mu\text{g mL}^{-1}$ ($\sim 0.2 \mu\text{M}$). Nevertheless, in practice, an AGR2 concentration of $25 \mu\text{g mL}^{-1}$ does not result in a reliable signal and cannot be differentiated from the background noise. Furthermore, the apparent dissociation constant is $\sim 21 \mu\text{M}$, which is several orders of magnitude higher than the reported value for the anti-AGR2 aptamer (determined to be in the nanomolar range by flow cytometry analysis in solution)³⁰⁴. This is in accordance with our previous report, where the protein diffusion was found to have a profound effect on its capture rate, resulting in micromolar apparent dissociation constants and detection limits, regardless of the capture probe and the protein target pair⁴⁷⁰.

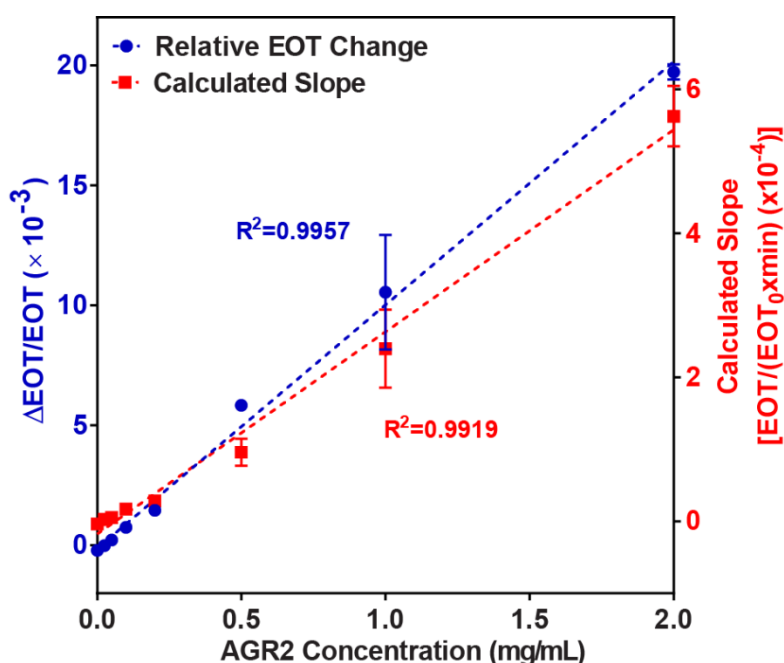


Figure 5.5.3. Net relative EOT changes and calculated slopes upon exposure of aptamer-functionalized PSi to different concentrations of AGR2, presenting linear correlation to both signal parameters ($n=3$).

Results

Herein, we experimentally demonstrate this phenomenon by real-time confocal laser scanning microscopy (CLSM) imaging of the diffusion process of a fluorescently-labeled AGR2 into an aptamer-functionalized PSi. We monitor the real-time fluorescence signal of the labeled protein with respect to the intrinsic photoluminescence (PL) signal of the PSi skeleton^{151,474}, allowing us to spatially correlate the labeled protein molecules with respect to the porous nanostructure^{163,219,302}. Figure 5.5.4a presents CLSM 3D projection images of the aptasensor, prior and 1-min after introduction of the fluorescently-labeled AGR2. The images are acquired by stacking 0.73 μm CLSM cross sections and present both the porous layer region, as well as the solution above the pores. These demonstrate that 1-min after the introduction of AGR2, the protein fluorescence signal is observed mainly above the porous layer, with a lower intensity signal within the porous layer. Figure 5.5.4b presents the distribution of the AGR2 fluorescence signal and the PSi PL signal with depth, in a segment of $\sim 11 \mu\text{m}$. The location of the porous layer, which is $\sim 4.9 \mu\text{m}$ thick (according to SEM measurements), is estimated based on the PL peak maximum, attributed to the top region of the PSi. Thus, the region of $< 3 \mu\text{m}$ represents the solution phase, above the pore entry. The fluorescence intensity of the protein increases with time in the imaged region and varies with depth within the PSi layer. A distinct gradient is observed at all studied time points, where the highest signal is measured at the bulk solution (above the pore entry) and the lowest at the bottom of the porous layer. These results qualitatively illustrate the target's concentration gradient and indicate that equilibration is not reached within 40 min. This is in agreement with the results of the biosensing experiments, where the EOT signal does not reach saturation in this time frame, see Figure 5.5.2a. Thus, we can conclude that molecular diffusion processes affect protein delivery to the porous layer, for at least 40 min after initial protein introduction to the biosensor, and that mass transport acceleration is mandatory for improving the biosensor response time and accordingly its sensitivity in this time frame.

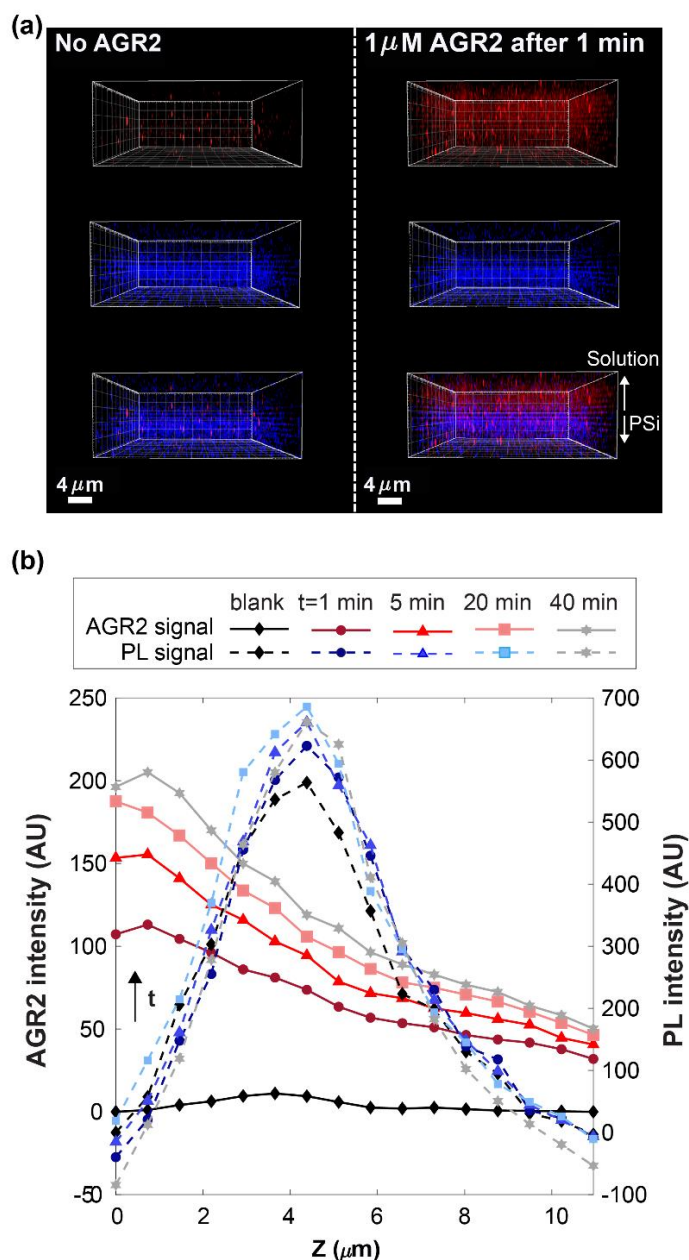


Figure 5.5.4. Time-resolved confocal laser scanning microscopy (CLSM) imaging of AGR2 diffusion within the aptasensor. (a) 3D projection images of the aptasensor before and 1-min after introduction of fluorescently-labeled AGR2 (1 μM). 3D images are obtained from stacking of CLSM cross sections; Top row represents the fluorescence signal of the fluorescent protein, middle row represents the photoluminescence (PL) signal of the PSi nanostructure, and the bottom row is the merged view of top and middle rows. (b) Variation with time of both AGR2 fluorescence and PL intensity as a function of depth (Z) above and within the porous nanostructure. The PSi region is estimated at the peak maximum of the PL signal, while the solution phase is located in the region of $<3 \mu\text{m}$. The gradient in the AGR2 intensity signal demonstrates that equilibration is not reached within the studied time frame.

Mass Transfer Acceleration

The target flux to the biosensor surface is governed by Fick's laws of diffusion and is correlated to the target concentration gradient and inversely proportional to the diffusion pathlength. Thus, increasing

Results

the target concentration gradient and decreasing the diffusion pathlength will result in enhanced diffusion flux. In our previous work⁴⁶⁴, we incorporated isotachopheresis (ITP) technique for on-chip and real-time concentration of a target protein in the sample, thus locally increasing the target concentration gradient on top of the aptasensor and consequently improving its flux. This resulted in up to 1000-fold improvement in the LOD to the lower nanomolar range (measured values). In ITP, a discontinuous buffer system is used, comprised of a leading electrolyte (LE) and a terminating electrolyte (TE), having higher and lower electrophoretic mobility than the target, respectively. Upon voltage application, a sharp electric field gradient is formed at the LE-TE interface and any species having an intermediate electrophoretic mobility will focus at this interface. This results in the concentration of the target into a highly-focused peak at the LE-TE interface⁴¹⁵. The proper choice of the LE and TE buffer system is crucial for the success of the method and is highly dependent on the target characteristics, mainly its charge²⁴⁵, and the capture probe properties to ensure its functionality. While in our previous work, anionic ITP was applied for concentrating a negatively-charged protein⁴⁶⁴, in the present work, as AGR2 is theoretically characterized by a basic isoelectric point (based on its amino-acid sequence), a cationic ITP is applied. As most proteins are negatively-charged at physiological conditions⁴⁷⁵, cationic ITP assays exist⁴⁷⁵⁻⁴⁸¹ but are less prevalent.

Figure 5.5.5a presents the concept of the ITP assay for focusing AGR2. The PSi aptasensor is incorporated in PDMS microchannels, 350 μm in width and 20 μm in height. A fluorescent AGR2 (labeled via amine groups) is utilized for visualizing the protein focusing within the microchannel. We have investigated several buffer compositions of cationic ITP for the focusing and accumulation of AGR2 at the LE-TE interface, see Table S-1 (Supporting Information). The microchannel is initially filled with LE buffer, while the labeled AGR2 is mixed with the TE buffer in the reservoir. Voltage application results in the migration of the LE-TE interface towards the PSi aptasensor, as evidenced by the electric field and RIFTS measurements (data not shown). Yet, none of the studied conditions has led to a formation of a fluorescent protein peak. Thus, in an effort to improve the AGR2 electrophoretic behavior, we have allowed the negatively-charged anti-AGR2 aptamer to interact with the protein (prior to voltage application), resulting in a complex with a predicted total negative charge. Indeed, when utilizing established anionic ITP buffer composition^{245, 464}, a fluorescent peak is observed at the buffer interface (see Figure 5.5.5b), suggesting the successful focusing of the protein. Nevertheless, the fluorescence intensity observed is weak and the peak formed is unstable for a relatively high AGR2 concentration (50 nM), compared to our previous work⁴⁶⁴, impeding the efficiency of the method. This emphasizes the main challenge of the ITP method, which should be carefully tailored for each target protein and capture probe pair⁴⁸². We note that further study and optimization of the buffer composition may eventually allow for successful ITP-assisted concentration of AGR2.

Another strategy for enhancing the target flux to the biosensor is to reduce the diffusion length to the biosensor surface, resulting in a decrease in the diffusion time, according to the following relation

Results

$$t \propto L^2 / D$$

where L is the diffusion length and D is the target diffusion coefficient^{5,377,378}. In the first approach, we apply mixing of the target solution on top of the biosensor, which eliminates the diffusion gradient in the bulk solution. Thus, a constant target concentration, equal to the applied solution concentration, can be assumed in the bulk solution, and the diffusion length is reduced to the porous layer thickness only. Figure 5.5.5c presents characteristic biosensing results for the aptasensor upon exposure to $100 \mu\text{g mL}^{-1}$ AGR2 and compares between mixed and non-mixed systems. During mixing, a significantly higher apparent infiltration and binding rate (by ~ 6.5 fold) is obtained in comparison to the non-mixed system and the relative EOT signal reaches $\sim 90\%$ of the maximal signal obtained at equilibration (after 1 h). Following the 10 min of mixing, the apparent binding rate sharply decreases, and minimal target capture is observed during the following incubation period. This is attributed to the decrease in the AGR2 concentration gradient, which is the driving force for diffusion, suggesting that the assay time can be reduced to the 10 min of mixing with similar results. Figure 5.5.5d summarizes the averaged net relative EOT values upon exposure to different AGR2 concentrations, for mixed and non-mixed systems. A signal enhancement of >3 -fold is realized by target mixing for all studied AGR2 concentrations, and specifically, AGR2 concentration of $25 \mu\text{g mL}^{-1}$ is detected with an average SNR of 16. The calculated LOD is reduced by ~ 5 -fold to $2.1 \mu\text{g mL}^{-1}$ (~ 47 nM). Analysis of the slope during the mixing allows us to study the apparent infiltration and binding kinetics and its comparison to the non-mixed system is presented in Figure 5.5.5e, where a substantial enhancement by >13 -fold for the mixed system is observed, underscoring the prominent effect of the enhanced target flux on the binding kinetics.

In the second approach, we decrease the characteristic diffusion length by integrating the P*Si* aptasensor with PDMS microchannels. Specifically, we decrease the solution height above the porous layer from 1 mm to $20 \mu\text{m}$ (as illustrated in Fig. 5.5.5f). This in turn accelerates the target capture rate, where the EOT signal is observed to reach equilibration almost instantly, as shown in the real-time relative EOT curve in Figure 5.5.5g. Figure 5.5.5h compares the averaged net relative EOT changes for AGR2 detection in the cell and the microchannels, where for the latter 3 to 6-fold increase in the EOT signal is observed, compared to a cell setup. The calculated LOD in the microfluidic set up is $5.7 \mu\text{g mL}^{-1}$ (~ 129 nM) and importantly, AGR2 can be reliably detected at a lower concentration of $12.5 \mu\text{g mL}^{-1}$ with an average SNR of 9, compared to a cell setup or mixing experiments. Note that due to the insufficient time resolution of the optical measurements at the initial protein introduction into the microchannel (see Figure S5.5.7, Supporting Information), we do not analyze the binding slope of the real-time EOT curves.

The binding enhancement achieved by the two presented strategies emphasizes the limiting effect of diffusion in these porous biosensors. Further acceleration of the mass transfer rate can be achieved by optimization of the porous nanostructure, e.g., carefully adjusting the thickness of the porous layer (i.e., the use of thinner porous layers is beneficial as it reduces the diffusion length, but it also affects the

Results

reflectance and as a result may hamper the accuracy of the optical signal)⁴⁷⁰, by introducing convection by the target flow in the system, and by the optimization of the microchannel dimensions and geometry^{5, 483}. Additional improvement in the LOD can be achieved by stabilization of the aptasensor surface to reduce any negative signal drifting events, which are occasionally observed upon overtime measurements.

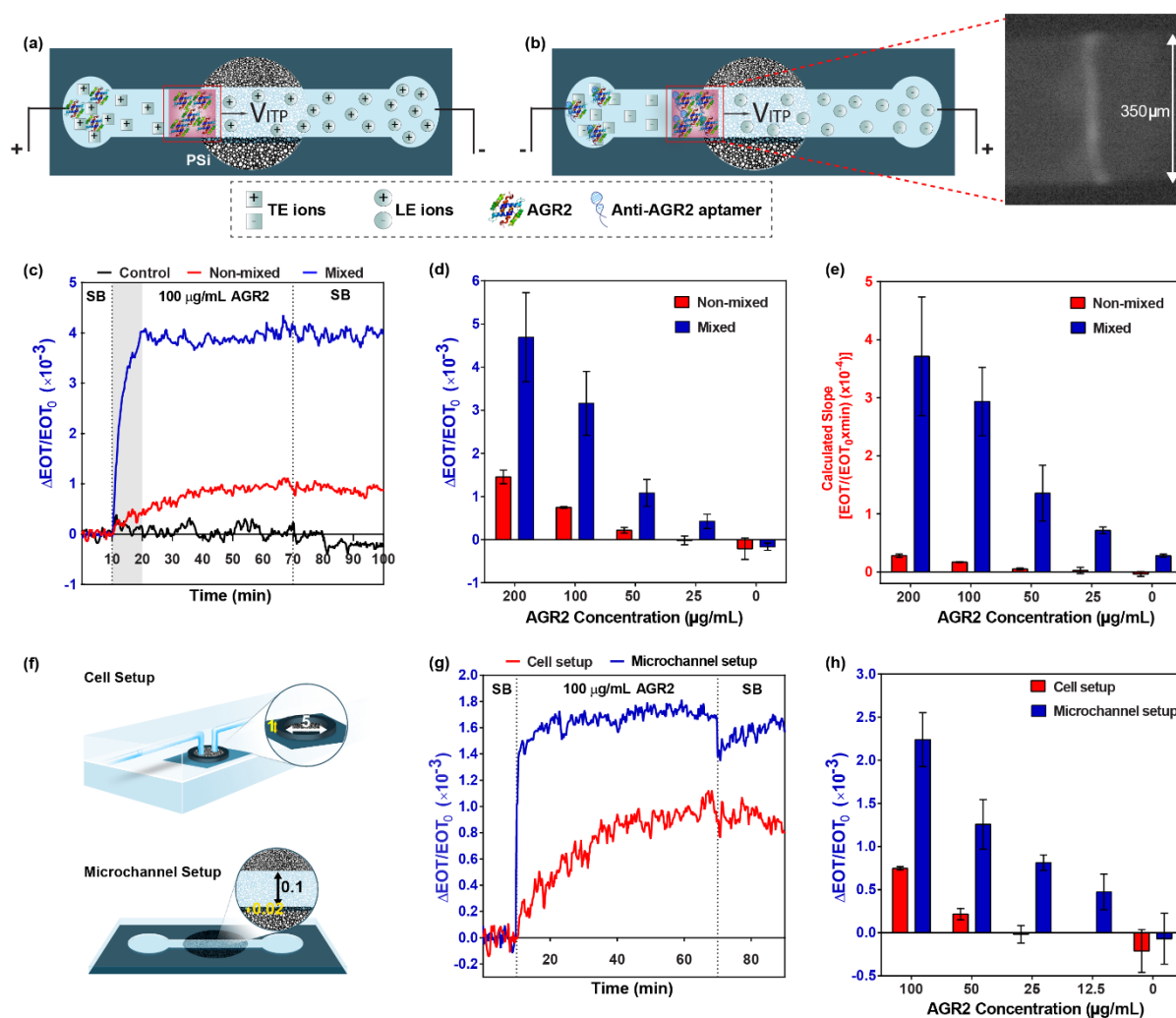


Figure 5.5.5. Strategies for enhancing the sensitivity, by mass transfer acceleration via ITP, target mixing and integration with microchannels. (a) Schematic illustration of a cationic ITP assay for AGR2 on-chip concentration; (b) Schematic illustration and raw fluorescence image of AGR2 (50 nM) and anti-AGR2 aptamer complex focusing under anionic ITP conditions; (c) Characteristic relative EOT changes as a function of time for 10 min-mixed and non-mixed AGR2 (100 µg mL⁻¹) biosensing experiments. As a control, selection buffer (SB) is mixed on the aptasensor for 10 min. Grey area indicates the mixing phase. (d) Averaged net relative EOT changes and (e) Calculated slopes for detection of different concentrations of AGR2 in a mixed and non-mixed biosensing experiments (n=3). (f) Schematic illustration of the PSi aptasensor integrated in the conventional cell setup and PDMS microchannel setup. Dimensions are in mm units. (g) Characteristic real-time relative EOT changes upon aptasensor incubation with 100 µg mL⁻¹ AGR2 in SB, in a cell setup or in a microchannel setup.

(h) Averaged net relative EOT changes for detection of different concentrations of AGR2 in both experimental setups ($n=3$).

Improved Signal Processing

The aptasensor performance is also determined by the experimental setup, the signal processing technique and consequently the noise of the system. To reduce the latter, we apply a different signal processing technique instead of RIFTS, named Morlet wavelet phase⁴⁶⁵. In this method, Morlet wavelet convolution is applied to the P*S*i reflectance spectra in order to filter out typical noise signatures. This results in enhanced noise immunity and consequently lower LOD values. In our recent study, we demonstrated that Morlet wavelet phase enables one order of magnitude improvement in LOD for BSA adsorption on a P*S*i thin film, compared to RIFTS and other commonly used signal processing techniques^{19, 20, 465}. Figure 5.5.6 presents the real time changes in the Morlet wavelet phase signal, compared to the RIFTS signal, for the lowest studied AGR2 concentrations in each of the different experimental setups, i.e., mixing, microchannel or cell setups. Morlet wavelet phase analysis results in a significant reduction in the signal noise, which consequently improves the SNR between 3 to 6-fold, compared to RIFTS (Figure 5.5.6a and 5.5.6b). Accordingly, the calculated LOD is improved for the mixing and microchannel experiments to $0.66 \mu\text{g mL}^{-1}$ ($\sim 15 \text{ nM}$) and $0.97 \mu\text{g mL}^{-1}$ ($\sim 22 \text{ nM}$), respectively, where further improvement could be realized by optimizing the Morlet wavelet parameters to filter measured reflectance spectra more effectively. Importantly, the selectivity of the biosensor is maintained while utilizing Morlet wavelet phase analysis, see Figure S5.5.8. Yet, as the platform is limited by the mass transfer rate, Morlet wavelet phase does not enable detection of AGR2 at a concentration of $25 \mu\text{g mL}^{-1}$ in a cell setup (Figure 5.5.6c), where no signal was obtained with RIFTS as well. Thus, the lowest measured target concentration is unchanged upon Morlet wavelet phase analysis and mass transfer acceleration is mandatory for practical improvement in the biosensor sensitivity, where Morlet wavelet phase presents a complementary approach to improve the detection reliability.

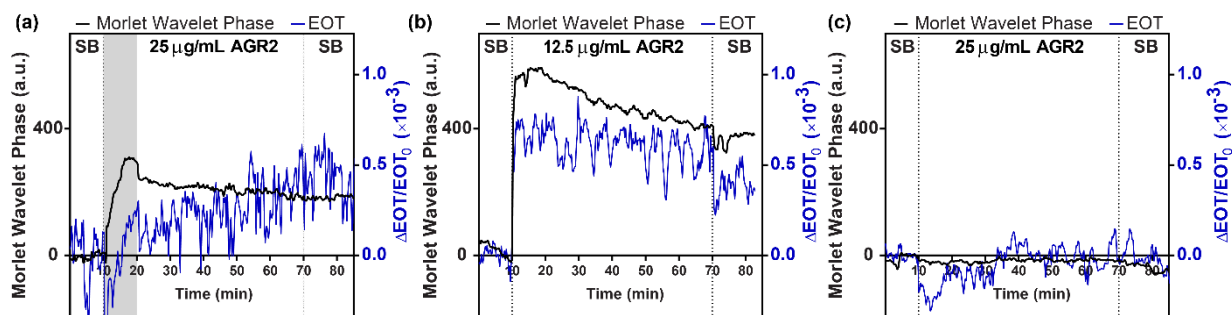


Figure 5.5.6. Characteristic changes in relative Morlet wavelet phase and net EOT signals as a function of time for the lowest measured AGR2 concentrations in (a) mixing, (b) microchannel and (c) cell setups,

Results

demonstrating that the Morlet wavelet phase signal processing technique reduces the signal noise and improves the SNR. Grey area indicates the mixing phase.

Conclusions

We constructed a label-free PSi-based biosensor for detection of AGR2, a cancer biomarker, and studied different approaches for enhancing its sensitivity. Anti-AGR2 aptamer is used as a capture probe and is immobilized within the nano-scale pores of the PSi thin film, which is utilized as an optical transducer. Detection of AGR2 by the aptamer-functionalized PSi film is carried out by real-time monitoring of the reflectance changes of the PSi nanostructure. AGR2 captured by the aptasensor is confirmed by the net EOT signal increase, and the apparent infiltration and binding rate is calculated based on the analysis of the slope of the real-time EOT curves. Both signal analysis methods linearly correlate to the AGR2 concentration and enable the selective AGR2 detection in a buffer and in a simulated pancreatic juice, where the AGR2 is outnumbered by >100-fold of non-target proteins. The LOD of the aptasensor is limited to $9.2 \mu\text{g mL}^{-1}$ ($0.2 \mu\text{M}$) attributed to the slow diffusion rate to and within the porous layer. Thus, we apply several strategies to improve the target flux to the PSi aptasensor. The ITP technique, which allows to preconcentrate the target based on its electrophoretic mobility, is investigated for real-time focusing of the protein on top of the aptasensor. However, focusing of the positively-charged AGR2 while maintaining the immobilized aptamer functionality was not successful. Two approaches are studied for reducing the diffusion length to the aptasensor, including target solution mixing on top of the biosensor and aptasensor integration in microchannels. Both methods successfully reduce the LOD of the aptasensor by up to 5-fold and improve its response time from 1 h to several minutes. To further improve the detection reliability, the Morlet wavelet phase signal processing technique is applied instead of RIFTS, resulting in a substantial reduction in the measurement noise, which reduces the LOD down to $0.66 \mu\text{g mL}^{-1}$ (15 nM). We acknowledge that the current LOD is not sufficient for AGR2 detection in real clinical samples; however, it can be improved by further optimization work of the microfluidic architecture and filtering parameters of the Morlet wavelet phase method, or introduction of convection into the system⁴⁸³.

Supporting Information

ITP Assay

A cationic ITP assay is studied due to the basic isoelectric point of AGR2 protein (8-8.5 based on its amino acid sequence), as schematically illustrated in Figure S5.5.1. The anti-AGR2 aptamer forms a G-quadruplex and its structure stability and binding affinity is highly-dependent on potassium ions¹. Thus, the latter is used as the leading electrolyte ion in the assay, while we study a decrease in the pH to increase the positive charge of AGR2. The different buffer compositions are detailed in Table S5.5.1.

Results

An established anionic buffer composition^{2,3} is also tested for the direct AGR2 focusing. The assay is applied for several AGR2 concentrations ranging from 50 nM to 5 μ M and as a control a successful focusing of the free positively-charged fluorescent dye is demonstrated (data not shown).

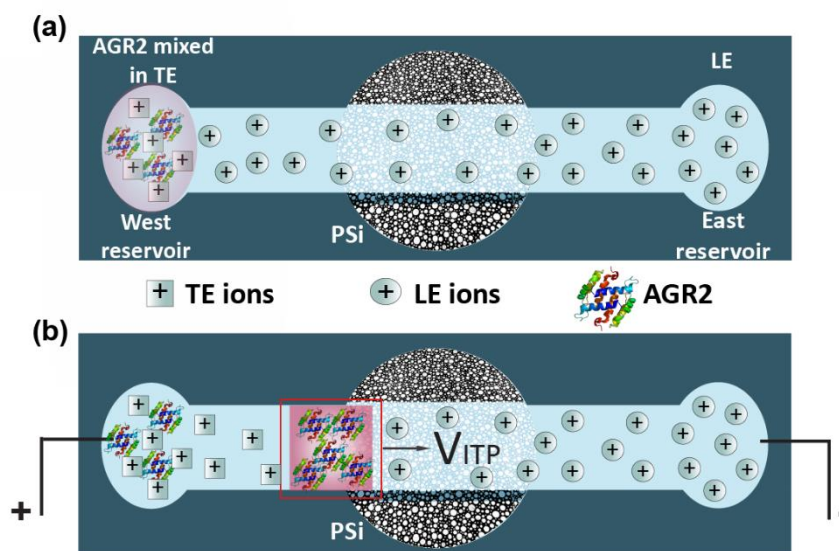


Figure S5.5.1. Schematic illustration of the cationic ITP assay. (a) The microchannel and the east reservoir are initially filled with LE buffer, while the fluorescently labelled AGR2 is mixed with the TE buffer in the west reservoir. (b) Upon voltage application, the labelled-protein focuses at the LE-TE interface and migrates towards the PSi aptasensor.

Table S5.5.1. Leading electrolyte (LE) and terminating electrolyte (TE) buffer compositions studied for AGR2 focusing on the aptasensor via cationic ITP technique

ITP	LE	TE
Cationic	200/100 mM HEPES/KOH	20/10 mM HEPES/Pyridine
Cationic	200/100 mM HEPES/KOH	20/10 mM HEPES/BisTris
Cationic	200/100 mM MOPS/KOH	20/10 mM HEPES/BisTris
Cationic	200/100 mM MES/KOH	20/10 mM HEPES/BisTris
Cationic	200/100/80 mM HEPES/KOH/HCl (pH 6.4)	20/10/7 mM HEPES/BisTris/HCl (pH 5.9)
Cationic	200/100 mM HEPES/KOH (pH 7.4)	20/10/7 mM HEPES/BisTris/HCl (pH 5.9)
Anionic	200/150/100mM BisTris/NaCl/HCl	20/10 mM BisTris/Tricine

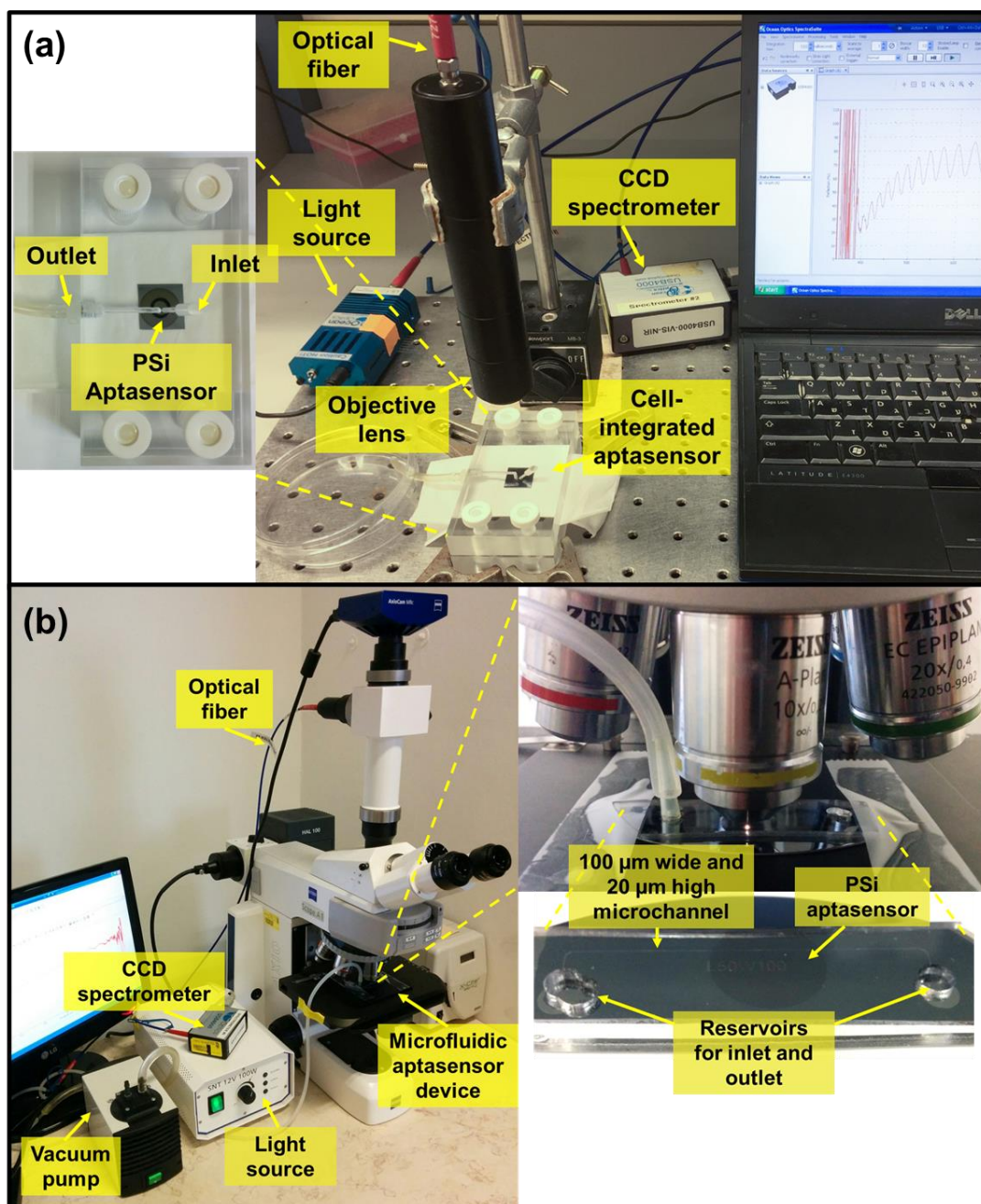


Figure S5.5.2. Images of the experimental setups. (a) Cell setup in which the PSi aptasensor is mounted in a Plexiglas cell; (b) microfluidic setup in which the microchannel-integrated PSi aptasensor device is fixed to a stage of a microscope, equipped with a CCD spectrometer.

Results

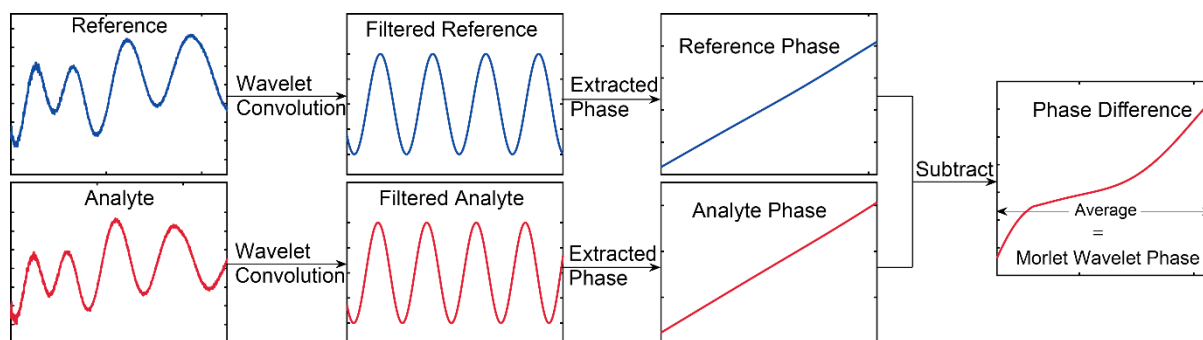


Figure S5.5.3. Schematic illustration of the Morlet wavelet phase signal analysis method.

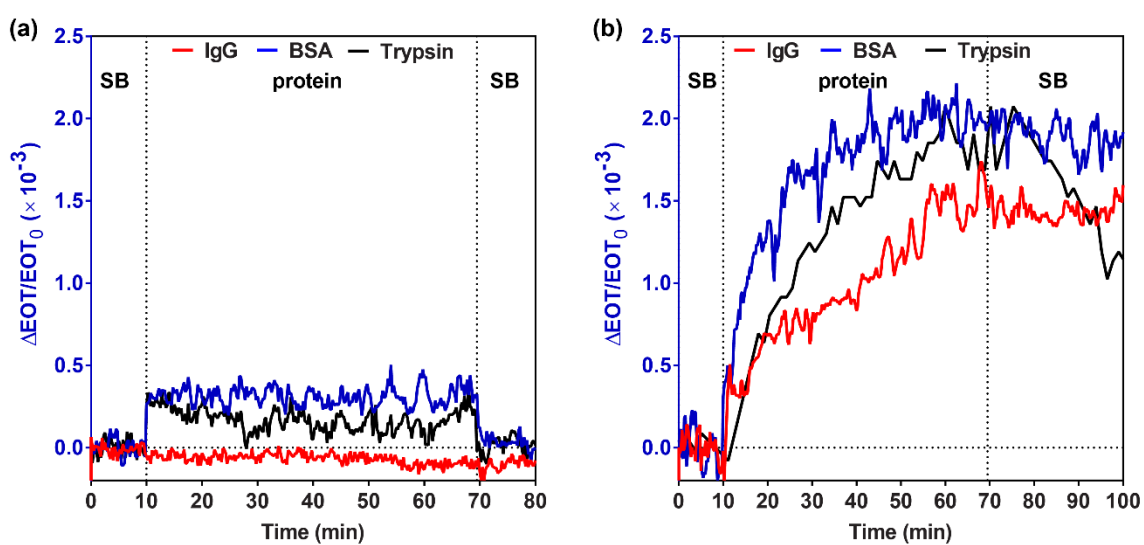


Figure S5.5.4. Characteristic relative EOT changes as a function of time for the (a) aptasensor and (b) neat oxidized PSi upon incubation with $200 \mu\text{g mL}^{-1}$ Trypsin, BSA or IgG in SB.

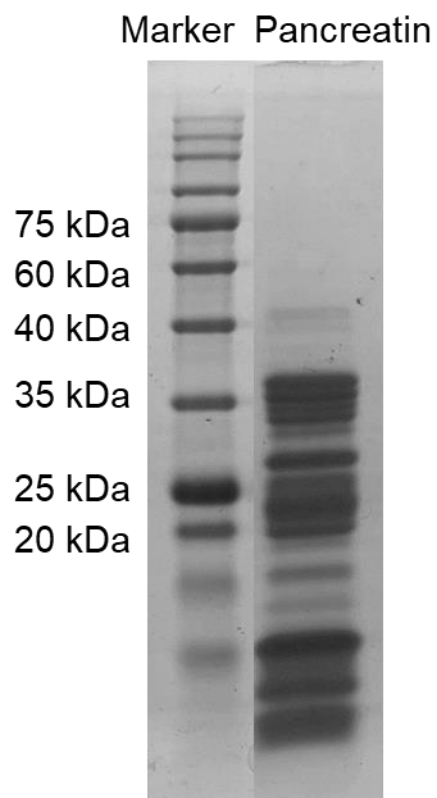


Figure S5.5.5. SDS-PAGE characterization of pancreatin at the concentration used for the biosensing experiments.

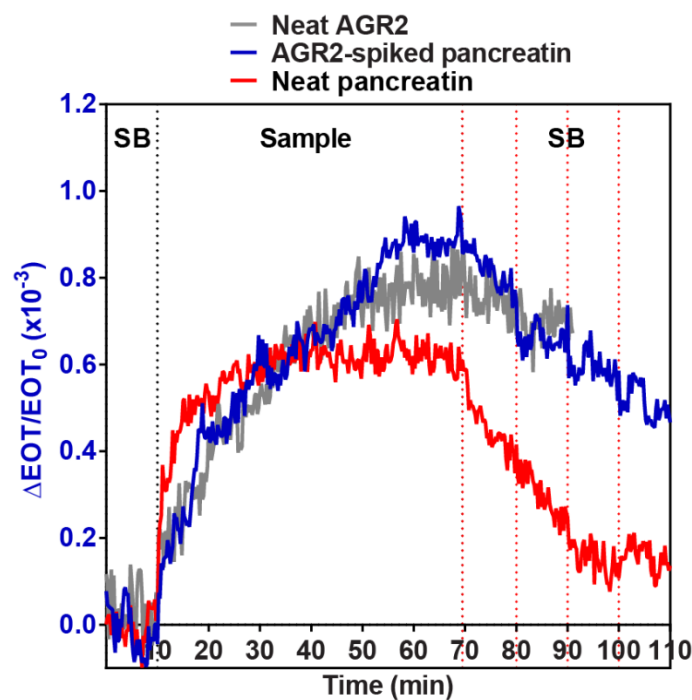


Figure S5.5.6. Characteristic relative EOT changes as a function of time upon aptasensor incubation with $100 \mu\text{g mL}^{-1}$ AGR2 in a buffer, pancreatin spiked with $100 \mu\text{g mL}^{-1}$ AGR2 and neat pancreatin. Baseline is acquired in the aptamer's selection buffer (SB), after which the samples are introduced and incubated for 1 h. Subsequently, the aptasensor is washed with 10 mL SB every 10 min (indicated by the red dashed lines).

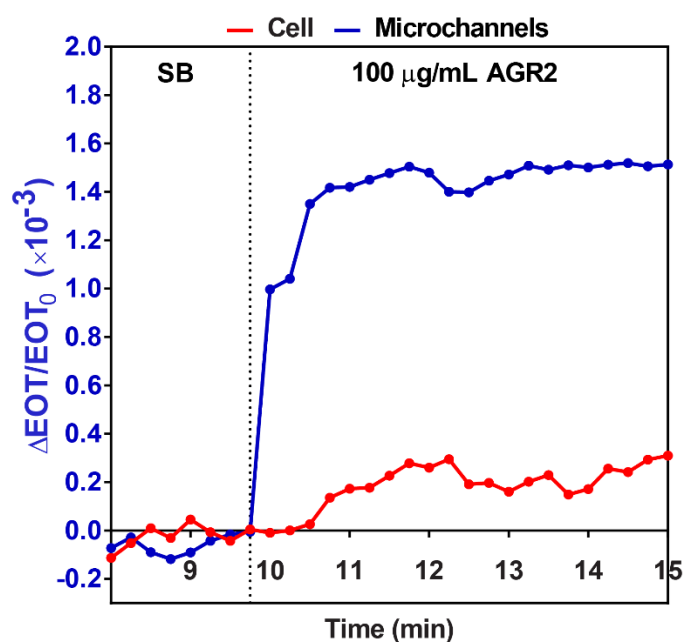


Figure S5.5.7. Characteristic relative EOT changes as a function of time upon aptasensor incubation with $100 \mu\text{g mL}^{-1}$ AGR2 in SB, in a cell setup or in PDMS microchannels, demonstrating the resolution of the measurements at the initial protein introduction.

Results

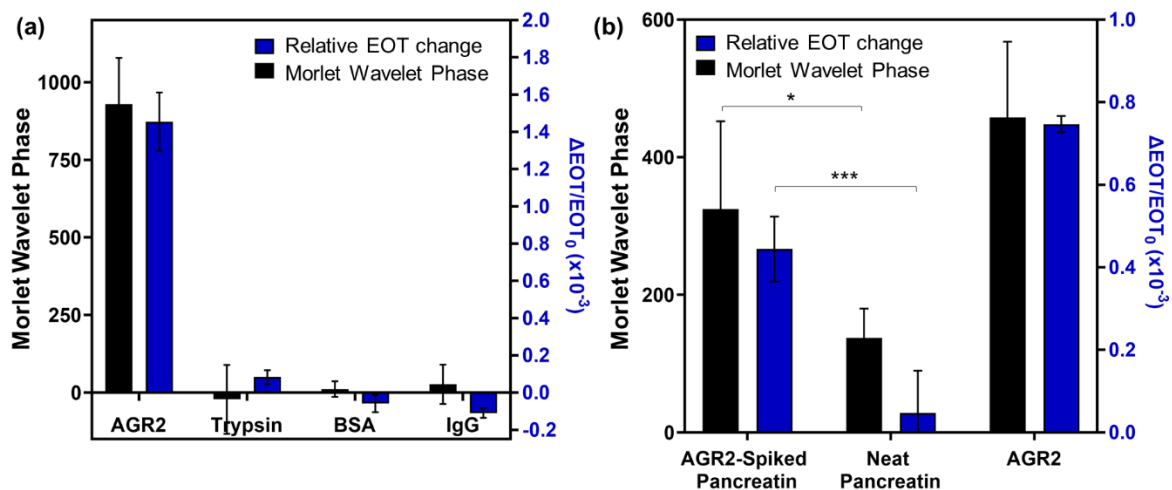


Figure S5.5.8. Aptasensor selectivity upon Morlet wavelet phase and RIFTS signal processing techniques. Averaged net relative EOT and Morlet wavelet phase changes upon aptasensor exposure to (a) AGR2 and non-target proteins (at a concentration of 200 $\mu\text{g mL}^{-1}$); (b) pancreatin spiked with 100 $\mu\text{g mL}^{-1}$ AGR2, neat pancreatin and 100 $\mu\text{g mL}^{-1}$ AGR2 in a buffer. ***/* Significantly different (*t* test, $p=0.0002$ for relative EOT changes and $p=0.03$ for Morlet wavelet phase).

6. Discussion

The following section summarizes the main results and achievements of this research:

Fabrication of PSi Fabry-Pérot Thin Films and Conjugation with Aptamers Specific for Target Proteins

In this work we investigated several different PSi biosensors, which are all based on PSi Fabry-Pérot thin films, as a model porous transducer. The latter is the simplest and most robust PSi nanostructure, which is easily fabricated by electrochemical etching. The resulting porous layer characteristics depend on the etching parameters, such as the Si resistivity, applied current density, and etching time. The applied etching conditions in this research were adapted from previous work^{26,29} and were similar for the different studied biosensors. The resulting films are highly porous (~75%), 5.0-5.5 μm thick comprising of cylindrical pores with an average diameter of 50 nm. These characteristics allow the efficient infiltration of aptamers and proteins, which sizes are 10-fold smaller than the pore diameter, into the porous layer.

To allow selective detection of target proteins, capture probes are immobilized within the porous layer. Here we utilize DNA aptamers, which are single-stranded oligonucleotides folding into a 3D structure for specific binding of their target. Aptamers are synthetically produced at relatively low costs, they can be chemically modified to allow their facile conjugation, and are ~10 times smaller than antibodies allowing their immobilization at a high-density^{215,216}. The integration of aptamers as capture probes in PSi transducers has been pioneered by the Segal group, demonstrating advantages of biosensor stability and reusability²⁶. Since then, aptamers have been successfully utilized in several PSi-based biosensors for various target molecules^{19,27-33}. Nevertheless, antibodies are still considered the gold-standard capture probes for biosensors and the advantages of aptamers over antibodies are still controversial in the scientific community. Thus, in the first publication (Section 5.1) we present a direct comparison of aptamers and antibodies as capture probes for the same target protein using the same PSi transducer. Aptamers, targeting the his-tag sequence of proteins, are immobilized onto an amino-silanized PSi surface via carbodiimide coupling of amine-terminated aptamers. This chemical path has been adapted from our previous work²⁶ and naturally results in an oriented conjugation of the aptamers onto the surface due to their single functional chemical group. Anti-his tag antibodies are immobilized onto the PSi by two routes: (i) direct covalent immobilization through amine groups via a glutaraldehyde crosslinker, which results in a random orientation of the antibodies on the PSi surface; and (ii) immobilization via a protein A layer which results in a Fc-oriented conjugation of the antibodies on the surface. We experimentally determine the surface density of all capture probes by their cleavage from the surface and demonstrate the significantly higher density of the aptamers, by two orders of magnitude, compared to the antibodies. This is attributed to the smaller size of the aptamers, compared to the antibodies. The latter are immobilized in a similar density by the two different conjugation routes

(see Figure 5.1.2). The aptamer-based biosensor (aptasensor) is compared to the random and oriented antibody-based biosensors (immunosensors) for detection of a model his-tagged protein and the dynamic detection range, target capture rate, limit of detection (see Figure 5.1.3) and selectivity (see Figure 5.1.4) are studied. The aptasensor and oriented-immunosensor are found to exhibit a similar performance, while the random immunosensor presents poor binding of the target, suggesting that only 10% of the randomly-immobilized antibodies are active. Thus, we conclude that by optimizing the capture probe immobilization (i.e., oriented immobilization of the antibodies), a similar performance can be realized for the same transducer. The advantages of the aptamers are found in the practical construction, use and storage of the biosensor. The construction of the aptasensor is more rapid and cost-effective compared to the immunosensor due to the low cost of the aptamers. Also, the aptasensor can be stored dry at room temperature, which facilitates long-term storage. Importantly, while the aptasensor can be easily regenerated for multiple uses, where the regeneration conditions are predefined and tailored in the aptamer's selection process, the antibody-based biosensor could not be efficiently regenerated by several common regeneration conditions (see Figure 5.1.5) and tedious work of probing different conditions is required.

Theoretical Modelling of the Governing Phenomena of Target Capture by PSi-Based Biosensors

Label-free PSi-based optical biosensors have been widely studied in the past two decades. However, in practice, their sensitivity and response time were not sufficient for clinical application; the former ranging in the micromolar range for protein and DNA targets. In fact, we found a similar performance for various aptamer- and antibody-based PSi biosensors for different target proteins, in terms of their dynamic detection range and sensitivity. This is regardless of the characteristic affinity of capture probe to its target protein, as represented by the theoretical K_D values, and the obtained apparent K_D values diverged by orders of magnitude (see Table 5.2.1. and Figure 5.2.1c). The porous nanostructure of the PSi is highly advantageous for increasing the biosensor surface area but can also lead to hindered diffusion phenomena of the target in the porous layer. This is accompanied by the target diffusion towards the biosensor surface and its interaction with the immobilized capture probes (see illustration in Figure 5.2.1a). These phenomena, which dictate the target capture rate, are dependent on various characteristics of the biosensor and should be all considered. Thus, in the second publication (Section 5.2) we derive a mathematical model to describe this complex system. We focus on a diffusion-based target capture (no convection) and compare the derived model to a commonly used model in the literature, which assumes the porous layer is a perfect collector and thus neglects the hindered diffusion within (termed in this work as the 'planar model'). We solve both models numerically, utilizing parameters characteristic of the PSi aptasensors, and compare them to experimental results of the studied aptasensors. Whereas our comprehensive model presents a good fit to experimental results, the commonly practiced model is found to highly overestimate the target capture rate in these biosensors

(see Figure 5.2.3). These results emphasize the impact of hindered diffusion in the porous layer on the target capture rate. Examination of the target concentration profile in the bulk solution on top of the biosensor and in the porous layer (see Figure 5.2.4) suggests an interrelated effect of both diffusion processes; the diffusion within the porous layer leads to a rapid and substantial formation of a diffusion boundary layer within the bulk solution, which significantly impedes the target mass transfer. Our main conclusion from this study is that PSi-based biosensors are limited by mass transfer phenomena, which conceal the effect of capture probe-target protein reaction kinetics. Thus, mass transfer acceleration is mandatory to exploit advantages of higher affinity capture probes in these biosensors.

Our derived model, accompanied by numerical simulations, can be utilized to guide the optimization of PSi biosensors and we present rule of thumbs for the process. While excess of capture probes on the surface has been commonly suggested to improve the biosensor sensitivity, our results indicate that above a certain threshold, increasing the capture probe density will decrease the target capture rate (see Figures 5.2.5a and 5.2.5b). This is attributed to a rapid depletion of the target at the bulk solution, resulting in a diffusion boundary layer, which impedes the diffusion rate. Additionally, we demonstrate that the porous layer thickness should be minimized, and the pore diameter maximized to improve the mass transfer rate (see Figures 5.2.5c and 5.2.5d). These should be tailored in accordance with their effect on the optical properties to allow a reliable signal processing. Considering these results, we simulate at least 10-fold improvement in sensitivity by nanostructure and capture probe density optimization (see Figure S5.2.7).

Design and Study of Methods for Performance Enhancement of PSi-Based Biosensors

To enhance the sensitivity and response time of PSi-based biosensors, we study methods that accelerate the mass transport rate of the target to the biosensor surface. The third publication (Section 5.3) presents the application of isotachopheresis (ITP) technique for real-time preconcentration of the target protein on the PSi biosensor. ITP has been successfully applied on a PSi biosensor for a DNA target⁴²; however, protein targets pose a greater challenge due to their heterogeneity and higher sensitivity and as such the biosensing assay should be tailored for each protein. This includes the ITP buffer system, the leading electrolyte (LE) and the terminating electrolyte (TE), where the protein target, having an intermediate electrophoretic mobility, focuses in between upon application of electric field. The buffer composition should be tailored according to the protein charge, the capture probe functionality, and the stability of the transducer surface.

The compatibility of PSi with ITP is achieved by a complete oxidation of the surface to create an insulating oxide layer, which will allow the current to pass through the buffer solution and not the PSi nanostructure. The PSi is integrated with PDMS microchannels for convenient ITP application and anti-his tag aptamers are immobilized within the PSi and utilized as a model biosensor for detection of a 24 kDa negative his-tagged protein. During ITP application, the protein focuses between the LE and TE buffers and migrates according to the electric field along the microchannel, towards the PSi

Discussion

biosensor region (see illustration in Figure 5.3.1a). Upon arrival to the biosensor, the protein plug is stopped on top by applying a counter pressure with a water column and allowed to interact with the surface-immobilized aptamers. Visualization of the target protein plug migration along the microchannel is achieved by its fluorescent labelling; however, its detection by the PSi biosensor is carried out by monitoring the reflectance changes of the PSi nanostructure, where no labelling is required. ITP results in a significant enhancement in sensitivity by up to 1000-fold, improving the LOD from the micromolar to the nanomolar range (see Figure 5.3.2). This is ascribed to the significant concentration by 1000-fold of the target protein in the ITP plug on top of the PSi (see Figure 5.3.3). This in turn increases the protein concentration gradient, i.e., the diffusion driving force, on top of the biosensor, resulting in a higher target flux to the biosensor surface. Additionally, the local concentration increase allows to detect target protein concentrations which are orders of magnitude below the aptamer-protein K_D value. Importantly, we show that the assay can successfully perform in complex media, such as bacteria lysates (Figure 5.3.4). Success of the ITP assay results in a substantial enhancement of sensitivity. Nevertheless, its limitation is depicted in Section 5.5, where application of ITP for a different target protein, which is positively-charged, was not successful. Tedious probing of different LE and TE buffers did not result in a formation of a stable target plug (see Figure 5.5.5a and 5.5.5b).

The complexity of the ITP assay led us to investigate simpler methods for mass transfer acceleration, focusing on decreasing the diffusion path length. This is achieved by applying mixing of the target on top of the biosensor, which reduces the diffusion barrier in the bulk solution and decreases the diffusion length to the porous layer only. Manual mixing of the target for 10 min resulted in reduction of the LOD by 5-fold and a substantial decrease in the biosensor response time (see Figure 5.5.5c to 5.5.5e). Additional strategy to improve the target flux to the biosensor surface is by integration with microchannels, where the diffusion length is decreased to the micrometer scale. Integration of the biosensor with PDMS microchannels, with a 20 μm height, resulted in a 2-fold improvement in the LOD (see Figure 5.5.5f to 5.5.5g).

Microfluidic integration is also highly advantageous for translation of biosensors for point-of-care settings. It reduces sample and reagent volumes, shortens the analysis time, and enables high-throughput detection, portability, and potentially reduced costs. PDMS is the main polymer used for microfluidic fabrication; however, it requires a template, usually fabricated by soft-lithography techniques, which are expensive, laborious and time consuming. Thus, in Section 5.4 we present a facile integration of a PSi biosensor with 3D-printed microfluidics. 3D printing is rapidly advancing, and it enables rapid and fully digital prototyping of complex microfluidic devices in a one-step process. Nevertheless, the lower resolution of 3D printing compared to the one achieved by soft lithography combined with surface roughness pose a challenge in its integration with the delicate nanostructure of PSi. Thus, we develop a straightforward bonding method between 3D-printed polyacrylate microchannels and PSi, utilizing a UV-curable adhesive as an intermediate layer. The 3D-printed devices are first subjected to several

simple polishing and alignment steps to reduce the bending and roughness of the devices and are then bonded to the PSi by a stamping technique (see Figure 5.4.1). This creates a ~ 5 μm thin adhesive between both substrates, which does not interfere with the microchannel biosensor area or the delicate PSi nanostructure (see Figure 5.4.2). The PSi biosensor is constructed by immobilization of anti-his tag aptamers, as a model system, within the polyacrylate microchannels. Utilizing a motorized stage, multiple spots are optically-monitored along a single microchannel in the microfluidic-integrated aptasensor in real-time (see Figure 5.4.3a). Also, the 3D-printed polyacrylate microfluidic device enables its integration with a convenient tube connector, which is much more robust compared to tubing in PDMS-based microfluidics. We demonstrate selective detection of the target protein, with a 40-fold improvement in sensitivity, compared to previous work (see Figure 5.4.4). This is mainly attributed to the flow configuration in the biosensing experiments, as well as to the smaller dimensions of the microchannels, compared to a non-microfluidic setup. Importantly, we compare the 3D-printed microfluidic device to the conventional PDMS, with similar microchannel dimensions (see Figure 5.4.5). We demonstrate a comparable detection signal and an improved selectivity in the 3D-printed microfluidics, attributed to non-specific binding of the aptamer capture probe to the PDMS. The novel integration of both substrates enables the application of the advantages of 3D printing to PSi biosensors. For instance, a flexible design process to investigate the impact of different microfluidic structures on the biosensing performance, as well as adaptation to point of care settings. Currently, the main limitation lies in the 3D printing resolution, which is tens of micrometers; however, it is anticipated to improve with the rapid advancement of the field.

Application for Cancer Biomarker Detection

In Section 5.5 we present the construction of a PSi-based aptasensor for detection of the protein anterior gradient homolog-2 (AGR2), a cancer biomarker associated with various types of cancer. For example, in pancreatic cancer this protein is secreted from pre-malignant lesions to the pancreatic juice and thus would be ideal for early detection of this lethal cancer. Anti-AGR2 aptamers are immobilized within the porous layer and AGR2 detection is carried out by monitoring the reflectivity changes of the PSi, followed by application of the standard RIFTS method. We analyze both the total protein binding within the porous layer, as well as the protein binding rate and both signal analysis methods correlate to the AGR2 concentration. We focus on the selectivity of the biosensor and challenge it with relevant non-target protein solutions, as well as a simulated pancreatic juice in which the target is outnumbered by >100 fold of non-target proteins (see Figure 5.5.2). The successful detection of AGR2 in this complex media demonstrates the stability and selectivity of the aptamer capture probe.

The LOD of the biosensor is found in the micromolar range, as typical to these biosensors (see Figure 5.5.3) and is ascribed to mass transfer limitations, as previously discussed in this thesis. We experimentally demonstrate the slow diffusion of a fluorescently-labelled AGR2 within the porous layer by time-resolved confocal microscopy imaging (see Figure 5.5.4), which correlates with the real-time

Discussion

optical signal during the biosensing experiments. Since the obtained sensitivity is not sufficient for a clinical application, where AGR2 is found in sub-nanomolar concentrations within pancreatic juice, we apply mass transfer acceleration methods as described above (see Figure 5.5.5). Finally, the LOD is reduced to the nanomolar range via the simple integration in microchannels or target mixing on top of the aptasensor, and application of an improved signal processing technique. Although not reaching the clinical sensitivity, this work presents a significant improvement in the sensitivity of label-free PSi biosensors, without compromising the label-free and direct detection of the target. Further enhancement in sensitivity can be achieved by optimization of the PSi nanostructure, applying convection to the system and optimization of the microchannel geometry.

7. Conclusions

The main achievements of this work are:

- For the first time, a careful and thorough comparison between aptamers and antibodies as capture probes is carried out. The latter are immobilized onto P*Si* transducers, with a similar characteristic, and binding of the target protein molecules to the tethered capture probes is investigated under similar conditions. We demonstrate that the biosensing performance is comparable when the immobilization of these capture probes, i.e., oriented immobilization, is practiced. We show that the advantages of the aptamers as capture probes are mainly in the facile fabrication, storage, and usage of the biosensor, due to the aptamer stability and low cost.
- For the first time, a comprehensive mathematical model for description of mass transport and reaction kinetics phenomena in P*Si* biosensors is derived; the model properly captures target binding rate in these biosensors, in contrast to previous models used in the literature. We decipher the limiting factors of P*Si*-based biosensors and the orders of magnitude deviations between experimental and theoretical target-capture probe binding affinities. Also, we present rule of thumbs for optimization of P*Si*-based biosensors, in terms of nanostructure characteristics and capture probe surface density.
- We present several techniques for mass transfer acceleration and sensitivity enhancement of P*Si*-based biosensors. For the first time, ITP method is applied for a protein target pre-concentration on top of a P*Si*-based biosensor, resulting in up to 1000-fold reduction in LOD. We also present up to 5-fold reduction in LOD by simple target mixing on top of the biosensor and basic microfluidic integration.
- For the first time, P*Si* biosensor is integrated in 3D-printed polyacrylate microfluidic device. We developed a straightforward method for bonding the rough surface of the 3D-printed device with the delicate nanostructure of P*Si*. We demonstrate successful and selective detection of a model target protein, improved performance compared to the gold-standard PDMS microfluidics, as well as sensitivity enhancement compared to previous work.
- A P*Si* biosensor for detection of a relevant protein cancer biomarker is constructed and highly-selective detection of the target within simulated pancreatic juice is demonstrated. We were able to enhance the sensitivity, reaching a LOD of ~15 nM, which is a significant improvement compared to previous studies.

8. References

1. Turner, A. P. F., Biosensors: sense and sensibility. *Chemical Society Reviews* **2013**, *42* (8), 3184-3196.
2. Sanjay, S. T.; Fu, G.; Dou, M.; Xu, F.; Liu, R.; Qi, H.; Li, X., Biomarker detection for disease diagnosis using cost-effective microfluidic platforms. *Analyst* **2015**, *140* (21), 7062-7081.
3. Gonzalez-Guerrero, A. B.; Maldonado, J.; Herranz, S.; Lechuga, L. M., Trends in photonic lab-on-chip interferometric biosensors for point-of-care diagnostics. *Analytical Methods* **2016**, *8* (48), 8380-8394.
4. Kelley, S. O., What Are Clinically Relevant Levels of Cellular and Biomolecular Analytes? *ACS Sensors* **2017**, *2* (2), 193-197.
5. Wu, Y.; Tilley, R. D.; Gooding, J. J., Challenges and Solutions in Developing Ultrasensitive Biosensors. *Journal of the American Chemical Society* **2019**, *141* (3), 1162-1170.
6. Kelley, S. O.; Mirkin, C. A.; Walt, D. R.; Ismagilov, R. F.; Toner, M.; Sargent, E. H., Advancing the speed, sensitivity and accuracy of biomolecular detection using multi-length-scale engineering. *Nature Nanotechnology* **2014**, *9* (12), 969-980.
7. Gooding, J. J.; Gaus, K., Single-Molecule Sensors: Challenges and Opportunities for Quantitative Analysis. *Angewandte Chemie International Edition* **2016**, *55* (38), 11354-11366.
8. Giljohann, D. A.; Mirkin, C. A., Drivers of biodiagnostic development. *Nature* **2009**, *462* (7272), 461-464.
9. Soper, S. A.; Brown, K.; Ellington, A.; Frazier, B.; Garcia-Manero, G.; Gau, V.; Gutman, S. I.; Hayes, D. F.; Korte, B.; Landers, J. L.; Larson, D.; Ligler, F.; Majumdar, A.; Mascini, M.; Nolte, D.; Rosenzweig, Z.; Wang, J.; Wilson, D., Point-of-care biosensor systems for cancer diagnostics/prognostics. *Biosensors and Bioelectronics* **2006**, *21* (10), 1932-1942.
10. Janshoff, A.; Galla, H.-J.; Steinem, C., Piezoelectric Mass-Sensing Devices as Biosensors—An Alternative to Optical Biosensors? *Angewandte Chemie International Edition* **2000**, *39* (22), 4004-4032.
11. McPhillips, J.; Murphy, A.; Jonsson, M. P.; Hendren, W. R.; Atkinson, R.; Höök, F.; Zayats, A. V.; Pollard, R. J., High-Performance Biosensing Using Arrays of Plasmonic Nanotubes. *ACS Nano* **2010**, *4* (4), 2210-2216.
12. Guo, X., Surface plasmon resonance based biosensor technique: A review. *Journal of Biophotonics* **2012**, *5* (7), 483-501.
13. Länge, K.; Rapp, B. E.; Rapp, M., Surface acoustic wave biosensors: a review. *Analytical and Bioanalytical Chemistry* **2008**, *391* (5), 1509-1519.
14. Fan, X.; White, I. M.; Shopova, S. I.; Zhu, H.; Suter, J. D.; Sun, Y., Sensitive optical biosensors for unlabeled targets: A review. *Analytica Chimica Acta* **2008**, *620* (1), 8-26.
15. Lin, V. S.-Y.; Motesharei, K.; Dancil, K.-P. S.; Sailor, M. J.; Ghadiri, M. R., A Porous Silicon-Based Optical Interferometric Biosensor. *Science* **1997**, *278* (5339), 840-843.
16. Sailor, M. J., *Porous silicon in practice: preparation, characterization and applications*. John Wiley & Sons: 2012.
17. Pacholski, C.; Yu, C.; Miskelly, G. M.; Godin, D.; Sailor, M. J., Reflective Interferometric Fourier Transform Spectroscopy: A Self-Compensating Label-Free Immunosensor Using Double-Layers of Porous SiO₂. *Journal of the American Chemical Society* **2006**, *128* (13), 4250-4252.
18. Pacholski, C.; Sartor, M.; Sailor, M. J.; Cunin, F.; Miskelly, G. M., Biosensing Using Porous Silicon Double-Layer Interferometers: Reflective Interferometric Fourier Transform Spectroscopy. *Journal of the American Chemical Society* **2005**, *127* (33), 11636-11645.
19. Mariani, S.; Pino, L.; Strambini, L. M.; Tedeschi, L.; Barillaro, G., 10 000-Fold Improvement in Protein Detection Using Nanostructured Porous Silicon Interferometric Aptasensors. *ACS Sensors* **2016**, *1* (12), 1471-1479.
20. Mariani, S.; Strambini, L. M.; Barillaro, G., Femtomole Detection of Proteins Using a Label-Free Nanostructured Porous Silicon Interferometer for Perspective Ultrasensitive Biosensing. *Analytical Chemistry* **2016**, *88* (17), 8502-8509.
21. DeLouise, L. A.; Kou, P. M.; Miller, B. L., Cross-Correlation of Optical Microcavity Biosensor Response with Immobilized Enzyme Activity. Insights into Biosensor Sensitivity. *Analytical Chemistry* **2005**, *77* (10), 3222-3230.
22. Arshavsky-Graham, S.; Massad-Ivanir, N.; Segal, E.; Weiss, S., Porous Silicon-Based Photonic Biosensors: Current Status and Emerging Applications. *Analytical Chemistry* **2019**, *91* (1), 441-467.
23. Zhao, Y.; Gaur, G.; Retterer, S. T.; Laibinis, P. E.; Weiss, S. M., Flow-Through Porous Silicon Membranes for Real-Time Label-Free Biosensing. *Analytical Chemistry* **2016**, *88* (22), 10940-10948.
24. Mariani, S.; Robbiano, V.; Strambini, L. M.; Debrassi, A.; Egri, G.; Dähne, L.; Barillaro, G., Layer-by-layer biofunctionalization of nanostructured porous silicon for high-sensitivity and high-selectivity label-free affinity biosensing. *Nature Communications* **2018**, *9* (1), 5256.

25. Mariani, S.; Strambini, L. M.; Barillaro, G., Electrical Double Layer-Induced Ion Surface Accumulation for Ultrasensitive Refractive Index Sensing with Nanostructured Porous Silicon Interferometers. *ACS Sensors* **2018**, *3* (3), 595-605.
26. Urmann, K.; Walter, J.-G.; Scheper, T.; Segal, E., Label-Free Optical Biosensors Based on Aptamer-Functionalized Porous Silicon Scaffolds. *Analytical Chemistry* **2015**, *87* (3), 1999-2006.
27. Terracciano, M.; De Stefano, L.; Borbone, N.; Politi, J.; Oliviero, G.; Nici, F.; Casalino, M.; Piccialli, G.; Dardano, P.; Varra, M.; Rea, I., Solid phase synthesis of a thrombin binding aptamer on macroporous silica for label free optical quantification of thrombin. *RSC Advances* **2016**, *6* (90), 86762-86769.
28. Chhasatia, R.; Sweetman, M. J.; Harding, F. J.; Waibel, M.; Kay, T.; Thomas, H.; Loudovaris, T.; Voelcker, N. H., Non-invasive, in vitro analysis of islet insulin production enabled by an optical porous silicon biosensor. *Biosensors and Bioelectronics* **2017**, *91*, 515-522.
29. Urmann, K.; Reich, P.; Walter, J. G.; Beckmann, D.; Segal, E.; Scheper, T., Rapid and label-free detection of protein a by aptamer-tethered porous silicon nanostructures. *J Biotechnol* **2017**, *257*, 171-177.
30. Arshavsky-Graham, S.; Massad-Ivanir, N.; Paratore, F.; Scheper, T.; Bercovici, M.; Segal, E., On Chip Protein Pre-Concentration for Enhancing the Sensitivity of Porous Silicon Biosensors. *ACS Sensors* **2017**, *2* (12), 1767-1773.
31. Terracciano, M.; Rea, I.; Borbone, N.; Moretta, R.; Oliviero, G.; Piccialli, G.; De Stefano, L., Porous Silicon-Based Aptasensors: The Next Generation of Label-Free Devices for Health Monitoring. *Molecules* **2019**, *24* (12), 2216.
32. Chhasatia, R.; Sweetman, M. J.; Prieto-Simon, B.; Voelcker, N. H., Performance optimisation of porous silicon rugate filter biosensor for the detection of insulin. *Sensors and Actuators B: Chemical* **2018**, *273*, 1313-1322.
33. Urmann, K.; Arshavsky-Graham, S.; Walter, J. G.; Scheper, T.; Segal, E., Whole-cell detection of live lactobacillus acidophilus on aptamer-decorated porous silicon biosensors. *Analyst* **2016**, *141* (18), 5432-40.
34. Choi, S.; Goryll, M.; Sin, L. Y. M.; Wong, P. K.; Chae, J., Microfluidic-based biosensors toward point-of-care detection of nucleic acids and proteins. *Microfluidics and Nanofluidics* **2011**, *10* (2), 231-247.
35. Rivet, C.; Lee, H.; Hirsch, A.; Hamilton, S.; Lu, H., Microfluidics for medical diagnostics and biosensors. *Chemical Engineering Science* **2011**, *66* (7), 1490-1507.
36. Squires, T. M.; Messinger, R. J.; Manalis, S. R., Making it stick: convection, reaction and diffusion in surface-based biosensors. *Nat Biotechnol* **2008**, *26* (4), 417-26.
37. Lynn, N. S.; Bocková, M.; Adam, P.; Homola, J., Biosensor Enhancement Using Grooved Micromixers: Part II, Experimental Studies. *Analytical Chemistry* **2015**, *87* (11), 5524-5530.
38. Lynn, N. S.; Šípová, H.; Adam, P.; Homola, J., Enhancement of affinity-based biosensors: effect of sensing chamber geometry on sensitivity. *Lab on a Chip* **2013**, *13* (7), 1413-1421.
39. Whitesides, G. M.; Ostuni, E.; Takayama, S.; Jiang, X.; Ingber, D. E., Soft Lithography in Biology and Biochemistry. *Annual Review of Biomedical Engineering* **2001**, *3* (1), 335-373.
40. Enders, A.; Siller, I. G.; Urmann, K.; Hoffmann, M. R.; Bahnemann, J., 3D Printed Microfluidic Mixers—A Comparative Study on Mixing Unit Performances. *Small* **2019**, *15* (2), 1804326.
41. Bhattacharjee, N.; Urrios, A.; Kang, S.; Folch, A., The upcoming 3D-printing revolution in microfluidics. *Lab on a Chip* **2016**, *16* (10), 1720-1742.
42. Vilensky, R.; Bercovici, M.; Segal, E., Oxidized Porous Silicon Nanostructures Enabling Electrokinetic Transport for Enhanced DNA Detection. *Advanced Functional Materials* **2015**, *25* (43), 6725-6732.
43. Hu, S.; Zhao, Y.; Qin, K.; Retterer, S. T.; Kravchenko, I. I.; Weiss, S. M., Enhancing the Sensitivity of Label-Free Silicon Photonic Biosensors through Increased Probe Molecule Density. *ACS Photonics* **2014**, *1* (7), 590-597.
44. Rea, I.; Orabona, E.; Lamberti, A.; Rendina, I.; Stefano, L. D., A microfluidics assisted porous silicon array for optical label-free biochemical sensing. *Biomicrofluidics* **2011**, *5* (3), 034120.
45. Wei, X.; Mares, J. W.; Gao, Y.; Li, D.; Weiss, S. M., Biomolecule kinetics measurements in flow cell integrated porous silicon waveguides. *Biomed. Opt. Express* **2012**, *3* (9), 1993-2003.
46. De Stefano, L.; Orabona, E.; Lamberti, A.; Rea, I.; Rendina, I., Microfluidics assisted biosensors for label-free optical monitoring of molecular interactions. *Sensors and Actuators B: Chemical* **2013**, *179*, 157-162.
47. Sorger, P. K., Microfluidics closes in on point-of-care assays. *Nature Biotechnology* **2008**, *26* (12), 1345-1346.
48. Lee, J.; Lee, S.-H., Lab on a chip for in situ diagnosis: From blood to point of care. *Biomedical Engineering Letters* **2013**, *3* (2), 59-66.
49. Gubala, V.; Harris, L. F.; Ricco, A. J.; Tan, M. X.; Williams, D. E., Point of Care Diagnostics: Status and Future. *Analytical Chemistry* **2012**, *84* (2), 487-515.
50. Jung, W.; Han, J.; Choi, J.-W.; Ahn, C. H., Point-of-care testing (POCT) diagnostic systems using microfluidic lab-on-a-chip technologies. *Microelectronic Engineering* **2015**, *132*, 46-57.

51. Kost, G. J., Guidelines for point-of-care testing. Improving patient outcomes. *Am J Clin Pathol* **1995**, *104* (4 Suppl 1), S111-27.
52. Lippa, P. B.; Müller, C.; Schlichtiger, A.; Schlebusch, H., Point-of-care testing (POCT): Current techniques and future perspectives. *TrAC Trends in Analytical Chemistry* **2011**, *30* (6), 887-898.
53. Whitesides, G. M., The origins and the future of microfluidics. *Nature* **2006**, *442* (7101), 368-373.
54. Zhang, Z.; Nagrath, S., Microfluidics and cancer: are we there yet? *Biomedical Microdevices* **2013**, *15* (4), 595-609.
55. Volpatti, L. R.; Yetisen, A. K., Commercialization of microfluidic devices. *Trends in Biotechnology* **2014**, *32* (7), 347-350.
56. Haeberle, S.; Zengerle, R., Microfluidic platforms for lab-on-a-chip applications. *Lab on a Chip* **2007**, *7* (9), 1094-1110.
57. Schumacher, S.; Nestler, J.; Otto, T.; Wegener, M.; Ehrentreich-Förster, E.; Michel, D.; Wunderlich, K.; Palzer, S.; Sohn, K.; Weber, A.; Burgard, M.; Grzesiak, A.; Teichert, A.; Brandenburg, A.; Koger, B.; Albers, J.; Nebling, E.; Bier, F. F., Highly-integrated lab-on-chip system for point-of-care multiparameter analysis. *Lab on a Chip* **2012**, *12* (3), 464-473.
58. Eicher, D.; Merten, C. A., Microfluidic devices for diagnostic applications. *Expert Review of Molecular Diagnostics* **2011**, *11* (5), 505-519.
59. Koczula, Katarzyna M.; Gallotta, A., Lateral flow assays. *Essays in Biochemistry* **2016**, *60* (1), 111-120.
60. Anfossi, L.; Di Nardo, F.; Cavallera, S.; Giovannoli, C.; Baggiani, C., Multiplex Lateral Flow Immunoassay: An Overview of Strategies towards High-throughput Point-of-Need Testing. *Biosensors* **2018**, *9* (1), 2.
61. Hemmig, E.; Temiz, Y.; Gökçe, O.; Lovchik, R. D.; Delamarche, E., Transposing Lateral Flow Immunoassays to Capillary-Driven Microfluidics Using Self-Coalescence Modules and Capillary-Assembled Receptor Carriers. *Analytical Chemistry* **2020**, *92* (1), 940-946.
62. Carrell, C.; Kava, A.; Nguyen, M.; Menger, R.; Munshi, Z.; Call, Z.; Nussbaum, M.; Henry, C., Beyond the lateral flow assay: A review of paper-based microfluidics. *Microelectronic Engineering* **2019**, *206*, 45-54.
63. Yetisen, A. K.; Akram, M. S.; Lowe, C. R., Paper-based microfluidic point-of-care diagnostic devices. *Lab on a Chip* **2013**, *13* (12), 2210-2251.
64. Gong, M. M.; Sinton, D., Turning the Page: Advancing Paper-Based Microfluidics for Broad Diagnostic Application. *Chemical Reviews* **2017**, *117* (12), 8447-8480.
65. Channon, R. B.; Nguyen, M. P.; Scorzelli, A. G.; Henry, E. M.; Volckens, J.; Dandy, D. S.; Henry, C. S., Rapid flow in multilayer microfluidic paper-based analytical devices. *Lab on a Chip* **2018**, *18* (5), 793-802.
66. Magro, L.; Escadafal, C.; Garneret, P.; Jacquelin, B.; Kwasiborski, A.; Manuguerra, J.-C.; Monti, F.; Sakuntabhai, A.; Vanhomwegen, J.; Lafaye, P.; Tabeling, P., Paper microfluidics for nucleic acid amplification testing (NAAT) of infectious diseases. *Lab on a Chip* **2017**, *17* (14), 2347-2371.
67. Tian, T.; Bi, Y.; Xu, X.; Zhu, Z.; Yang, C., Integrated paper-based microfluidic devices for point-of-care testing. *Analytical Methods* **2018**, *10* (29), 3567-3581.
68. Gervais, L.; de Rooij, N.; Delamarche, E., Microfluidic Chips for Point-of-Care Immunodiagnosics. *Advanced Materials* **2011**, *23* (24), H151-H176.
69. Song, Y.; Lin, B.; Tian, T.; Xu, X.; Wang, W.; Ruan, Q.; Guo, J.; Zhu, Z.; Yang, C., Recent Progress in Microfluidics-Based Biosensing. *Analytical Chemistry* **2019**, *91* (1), 388-404.
70. Apple, F. S.; Christenson, R. H.; Valdes, R., Jr.; Andriak, A. J.; Berg, A.; Duh, S.-H.; Feng, Y.-J.; Jortani, S. A.; Johnson, N. A.; Koplen, B.; Mascotti, K.; Wu, A. H., Simultaneous Rapid Measurement of Whole Blood Myoglobin, Creatine Kinase MB, and Cardiac Troponin I by the Triage Cardiac Panel for Detection of Myocardial Infarction. *Clinical Chemistry* **2020**, *45* (2), 199-205.
71. Clark, T. J.; McPherson, P. H.; Buechler, K. F., The Triage Cardiac Panel: Cardiac Markers for the Triage System. *Point of Care* **2002**, *1* (1), 42-46.
72. Wang, J.; Ahmad, H.; Ma, C.; Shi, Q.; Vermesh, O.; Vermesh, U.; Heath, J., A self-powered, one-step chip for rapid, quantitative and multiplexed detection of proteins from pinpricks of whole blood. *Lab on a Chip* **2010**, *10* (22), 3157-3162.
73. Gökçe, O.; Castonguay, S.; Temiz, Y.; Gervais, T.; Delamarche, E., Self-coalescing flows in microfluidics for pulse-shaped delivery of reagents. *Nature* **2019**, *574* (7777), 228-232.
74. Liu, H.; Crooks, R. M., Three-Dimensional Paper Microfluidic Devices Assembled Using the Principles of Origami. *Journal of the American Chemical Society* **2011**, *133* (44), 17564-17566.
75. Chen, C.-A.; Yeh, W.-S.; Tsai, T.-T.; Li, Y.-D.; Chen, C.-F., Three-dimensional origami paper-based device for portable immunoassay applications. *Lab on a Chip* **2019**, *19* (4), 598-607.
76. Liu, L.; Yang, D.; Liu, G., Signal amplification strategies for paper-based analytical devices. *Biosensors and Bioelectronics* **2019**, *136*, 60-75.

77. Bishop, J. D.; Hsieh, H. V.; Gasperino, D. J.; Weigl, B. H., Sensitivity enhancement in lateral flow assays: a systems perspective. *Lab on a Chip* **2019**, *19* (15), 2486-2499.
78. Moghadam, B. Y.; Connelly, K. T.; Posner, J. D., Isotachophoretic Preconcentration on Paper-Based Microfluidic Devices. *Analytical Chemistry* **2014**, *86* (12), 5829-5837.
79. Guo, S.; Schlecht, W.; Li, L.; Dong, W.-J., Paper-based cascade cationic isotachopheresis: Multiplex detection of cardiac markers. *Talanta* **2019**, *205*, 120112.
80. Moerland, C. P.; van Ijzendoorn, L. J.; Prins, M. W. J., Rotating magnetic particles for lab-on-chip applications – a comprehensive review. *Lab on a Chip* **2019**, *19* (6), 919-933.
81. Chircov, C.; Grumezescu, A. M.; Holban, A. M., Magnetic Particles for Advanced Molecular Diagnosis. *Materials* **2019**, *12* (13), 2158.
82. van Reenen, A.; de Jong, A. M.; den Toonder, J. M. J.; Prins, M. W. J., Integrated lab-on-chip biosensing systems based on magnetic particle actuation – a comprehensive review. *Lab on a Chip* **2014**, *14* (12), 1966-1986.
83. Ríos, Á.; Zougagh, M., Recent advances in magnetic nanomaterials for improving analytical processes. *TrAC Trends in Analytical Chemistry* **2016**, *84*, 72-83.
84. Masud, M. K.; Na, J.; Younus, M.; Hossain, M. S. A.; Bando, Y.; Shiddiky, M. J. A.; Yamauchi, Y., Superparamagnetic nanoarchitectures for disease-specific biomarker detection. *Chemical Society Reviews* **2019**, *48* (24), 5717-5751.
85. Hernández-Neuta, I.; Pereiro, I.; Ahlford, A.; Ferraro, D.; Zhang, Q.; Viovy, J.-L.; Descroix, S.; Nilsson, M., Microfluidic magnetic fluidized bed for DNA analysis in continuous flow mode. *Biosensors and Bioelectronics* **2018**, *102*, 531-539.
86. Lacharme, F.; Vandevyver, C.; Gijs, M. A. M., Full On-Chip Nanoliter Immunoassay by Geometrical Magnetic Trapping of Nanoparticle Chains. *Analytical Chemistry* **2008**, *80* (8), 2905-2910.
87. Xiong, Q.; Lim, C. Y.; Ren, J.; Zhou, J.; Pu, K.; Chan-Park, M. B.; Mao, H.; Lam, Y. C.; Duan, H., Magnetic nanochain integrated microfluidic biochips. *Nature Communications* **2018**, *9* (1), 1743.
88. Hwang, H.; Choi, E.; Han, S.; Lee, Y.; Choi, T.; Kim, M.; Shin, H.; Kim, J.; Choi, J., MESIA: Magnetic force-assisted electrochemical sandwich immunoassays for quantification of prostate-specific antigen in human serum. *Analytica Chimica Acta* **2019**, *1061*, 92-100.
89. Sebba, D.; Lastovich, A. G.; Kuroda, M.; Fallows, E.; Johnson, J.; Ahouidi, A.; Honko, A. N.; Fu, H.; Nielson, R.; Carruthers, E.; Diédhiou, C.; Ahmadou, D.; Soropogui, B.; Ruedas, J.; Peters, K.; Bartkowiak, M.; Magassouba, N. F.; Mboup, S.; Ben Amor, Y.; Connor, J. H.; Weidemaier, K., A point-of-care diagnostic for differentiating Ebola from endemic febrile diseases. *Science Translational Medicine* **2018**, *10* (471), eaat0944.
90. Kim, M. S.; Kweon, S. H.; Cho, S.; An, S. S. A.; Kim, M. I.; Doh, J.; Lee, J., Pt-Decorated Magnetic Nanozymes for Facile and Sensitive Point-of-Care Bioassay. *ACS Applied Materials & Interfaces* **2017**, *9* (40), 35133-35140.
91. Jacinto, M. J.; Trabuco, J. R. C.; Vu, B. V.; Garvey, G.; Khodadady, M.; Azevedo, A. M.; Aires-Barros, M. R.; Chang, L.; Kourentzi, K.; Litvinov, D.; Willson, R. C., Enhancement of lateral flow assay performance by electromagnetic relocation of reporter particles. *PLoS ONE* **2018**, *13*, e0186782.
92. Tamanaha, C. R.; Mulvaney, S. P.; Rife, J. C.; Whitman, L. J., Magnetic labeling, detection, and system integration. *Biosensors and Bioelectronics* **2008**, *24* (1), 1-13.
93. Kojima, T.; Takei, Y.; Ohtsuka, M.; Kawarasaki, Y.; Yamane, T.; Nakano, H., PCR amplification from single DNA molecules on magnetic beads in emulsion: application for high-throughput screening of transcription factor targets. *Nucleic Acids Research* **2005**, *33* (17), e150-e150.
94. Berensmeier, S., Magnetic particles for the separation and purification of nucleic acids. *Applied Microbiology and Biotechnology* **2006**, *73* (3), 495-504.
95. Zhao, Y.; Chen, F.; Li, Q.; Wang, L.; Fan, C., Isothermal Amplification of Nucleic Acids. *Chemical Reviews* **2015**, *115* (22), 12491-12545.
96. Duan, R.; Lou, X.; Xia, F., The development of nanostructure assisted isothermal amplification in biosensors. *Chemical Society Reviews* **2016**, *45* (6), 1738-1749.
97. Deng, H.; Gao, Z., Bioanalytical applications of isothermal nucleic acid amplification techniques. *Analytica Chimica Acta* **2015**, *853*, 30-45.
98. Ali, M. M.; Li, F.; Zhang, Z.; Zhang, K.; Kang, D.-K.; Ankrum, J. A.; Le, X. C.; Zhao, W., Rolling circle amplification: a versatile tool for chemical biology, materials science and medicine. *Chemical Society Reviews* **2014**, *43* (10), 3324-3341.
99. Nilsson, M.; Gullberg, M.; Dahl, F.; Szuhai, K.; Raap, A. K., Real-time monitoring of rolling-circle amplification using a modified molecular beacon design. *Nucleic Acids Research* **2002**, *30* (14), e66-e66.
100. Garbarino, F.; Minero, G. A. S.; Rizzi, G.; Fock, J.; Hansen, M. F., Integration of rolling circle amplification and optomagnetic detection on a polymer chip. *Biosensors and Bioelectronics* **2019**, *142*, 111485.
101. Minero, G. A. S.; Cangiano, V.; Garbarino, F.; Fock, J.; Hansen, M. F., Integration of microbead DNA handling with optomagnetic detection in rolling circle amplification assays. *Microchimica Acta* **2019**, *186* (8), 528.

102. Gorkin, R.; Park, J.; Siegrist, J.; Amasia, M.; Lee, B. S.; Park, J.-M.; Kim, J.; Kim, H.; Madou, M.; Cho, Y.-K., Centrifugal microfluidics for biomedical applications. *Lab on a Chip* **2010**, *10* (14), 1758-1773.
103. Tang, M.; Wang, G.; Kong, S.-K.; Ho, H.-P., A Review of Biomedical Centrifugal Microfluidic Platforms. *Micromachines* **2016**, *7* (2), 26.
104. Burger, R.; Amato, L.; Boisen, A., Detection methods for centrifugal microfluidic platforms. *Biosensors and Bioelectronics* **2016**, *76*, 54-67.
105. Strohmeier, O.; Keller, M.; Schwemmer, F.; Zehnle, S.; Mark, D.; von Stetten, F.; Zengerle, R.; Paust, N., Centrifugal microfluidic platforms: advanced unit operations and applications. *Chemical Society Reviews* **2015**, *44* (17), 6187-6229.
106. Piccolo Xpress. <https://www.abaxis.com/medical/piccolo-xpress> (accessed 10/02).
107. Zhu, Y.; Meng, X.; Chen, Y.; Li, J.; Shao, H.; Lu, Y.; Pan, L.; Xu, Y.; Cheng, J., Self-served and fully automated biochemical detection of finger-prick blood at home using a portable microfluidic analyzer. *Sensors and Actuators B: Chemical* **2020**, *303*, 127235.
108. Amasia, M.; Cozzens, M.; Madou, M. J., Centrifugal microfluidic platform for rapid PCR amplification using integrated thermoelectric heating and ice-valving. *Sensors and Actuators B: Chemical* **2012**, *161* (1), 1191-1197.
109. Czilwik, G.; Messinger, T.; Strohmeier, O.; Wadle, S.; von Stetten, F.; Paust, N.; Roth, G.; Zengerle, R.; Saarinen, P.; Niittymäki, J.; McAllister, K.; Sheils, O.; O'Leary, J.; Mark, D., Rapid and fully automated bacterial pathogen detection on a centrifugal-microfluidic LabDisk using highly sensitive nested PCR with integrated sample preparation. *Lab on a Chip* **2015**, *15* (18), 3749-3759.
110. Oh, S. J.; Seo, T. S., Combination of a centrifugal microfluidic device with a solution-loading cartridge for fully automatic molecular diagnostics. *Analyst* **2019**, *144* (19), 5766-5774.
111. Cao, X.; deMello, A. J.; Elvira, K. S., Enhanced versatility of fluid control in centrifugal microfluidic platforms using two degrees of freedom. *Lab on a Chip* **2016**, *16* (7), 1197-1205.
112. Zhu, Y.; Chen, Y.; Meng, X.; Wang, J.; Lu, Y.; Xu, Y.; Cheng, J., Comprehensive Study of the Flow Control Strategy in a Wirelessly Charged Centrifugal Microfluidic Platform with Two Rotation Axes. *Analytical Chemistry* **2017**, *89* (17), 9315-9321.
113. Li, L.; Miao, B.; Li, Z.; Sun, Z.; Peng, N., Sample-to-Answer Hepatitis B Virus DNA Detection from Whole Blood on a Centrifugal Microfluidic Platform with Double Rotation Axes. *ACS Sensors* **2019**, *4* (10), 2738-2745.
114. Kanchi, S.; Sabela, M. I.; Mdluli, P. S.; Inamuddin; Bisetty, K., Smartphone based bioanalytical and diagnosis applications: A review. *Biosensors and Bioelectronics* **2018**, *102*, 136-149.
115. Liu, J.; Geng, Z.; Fan, Z.; Liu, J.; Chen, H., Point-of-care testing based on smartphone: The current state-of-the-art (2017–2018). *Biosensors and Bioelectronics* **2019**, *132*, 17-37.
116. Vashist, S. K.; Mudanyali, O.; Schneider, E. M.; Zengerle, R.; Ozcan, A., Cellphone-based devices for bioanalytical sciences. *Analytical and Bioanalytical Chemistry* **2014**, *406* (14), 3263-3277.
117. Contreras-Naranjo, J. C.; Wei, Q.; Ozcan, A., Mobile Phone-Based Microscopy, Sensing, and Diagnostics. *IEEE Journal of Selected Topics in Quantum Electronics* **2016**, *22* (3), 1-14.
118. Dutta, S., Point of care sensing and biosensing using ambient light sensor of smartphone: Critical review. *TrAC Trends in Analytical Chemistry* **2019**, *110*, 393-400.
119. Xu, D.; Huang, X.; Guo, J.; Ma, X., Automatic smartphone-based microfluidic biosensor system at the point of care. *Biosensors and Bioelectronics* **2018**, *110*, 78-88.
120. Vashist, S. K.; Luong, J. H. T., Smartphone-Based Point-of-Care Technologies for Mobile Healthcare. In *Point-of-Care Technologies Enabling Next-Generation Healthcare Monitoring and Management*, Vashist, S. K.; Luong, J. H. T., Eds. Springer International Publishing: Cham, 2019; pp 27-79.
121. Hernández-Neuta, I.; Neumann, F.; Brightmeyer, J.; Ba Tis, T.; Madaboosi, N.; Wei, Q.; Ozcan, A.; Nilsson, M., Smartphone-based clinical diagnostics: towards democratization of evidence-based health care. *Journal of Internal Medicine* **2019**, *285* (1), 19-39.
122. Arumugam, S.; Colburn, D. A. M.; Sia, S. K., Biosensors for Personal Mobile Health: A System Architecture Perspective. *Advanced Materials Technologies* **2019**, *5* (3), 1900720.
123. Kanakasabapathy, M. K.; Pandya, H. J.; Draz, M. S.; Chug, M. K.; Sadasivam, M.; Kumar, S.; Etemad, B.; Yogesh, V.; Safavieh, M.; Asghar, W.; Li, J. Z.; Tsibris, A. M.; Kuritzkes, D. R.; Shafiee, H., Rapid, label-free CD4 testing using a smartphone compatible device. *Lab on a Chip* **2017**, *17* (17), 2910-2919.
124. Kanakasabapathy, M. K.; Sadasivam, M.; Singh, A.; Preston, C.; Thirumalaraju, P.; Venkataraman, M.; Bormann, C. L.; Draz, M. S.; Petrozza, J. C.; Shafiee, H., An automated smartphone-based diagnostic assay for point-of-care semen analysis. *Science Translational Medicine* **2017**, *9* (382), eaai7863.
125. Brangel, P.; Sobarzo, A.; Parolo, C.; Miller, B. S.; Howes, P. D.; Gelkop, S.; Lutwama, J. J.; Dye, J. M.; McKendry, R. A.; Lobel, L.; Stevens, M. M., A Serological Point-of-Care Test for the Detection of IgG Antibodies against Ebola Virus in Human Survivors. *ACS Nano* **2018**, *12* (1), 63-73.

126. Halvorsen, C. P.; Olson, L.; Araújo, A. C.; Karlsson, M.; Nguyễn, T. T.; Khu, D. T. K.; Le, H. T. T.; Nguyễn, H. T. B.; Winblad, B.; Russom, A., A rapid smartphone-based lactate dehydrogenase test for neonatal diagnostics at the point of care. *Scientific Reports* **2019**, *9* (1), 9301.
127. Wang, L.-J.; Chang, Y.-C.; Sun, R.; Li, L., A multichannel smartphone optical biosensor for high-throughput point-of-care diagnostics. *Biosensors and Bioelectronics* **2017**, *87*, 686-692.
128. Kühnemund, M.; Wei, Q.; Darai, E.; Wang, Y.; Hernández-Neuta, I.; Yang, Z.; Tseng, D.; Ahlford, A.; Mathot, L.; Sjöblom, T.; Ozcan, A.; Nilsson, M., Targeted DNA sequencing and in situ mutation analysis using mobile phone microscopy. *Nature Communications* **2017**, *8* (1), 13913.
129. Priye, A.; Bird, S. W.; Light, Y. K.; Ball, C. S.; Negrete, O. A.; Meagher, R. J., A smartphone-based diagnostic platform for rapid detection of Zika, chikungunya, and dengue viruses. *Scientific Reports* **2017**, *7* (1), 44778.
130. Liang, C.; Liu, Y.; Niu, A.; Liu, C.; Li, J.; Ning, D., Smartphone-app based point-of-care testing for myocardial infarction biomarker cTnI using an autonomous capillary microfluidic chip with self-aligned on-chip focusing (SOF) lenses. *Lab on a Chip* **2019**, *19* (10), 1797-1807.
131. Paterson, A. S.; Raja, B.; Mandadi, V.; Townsend, B.; Lee, M.; Buell, A.; Vu, B.; Brgoch, J.; Willson, R. C., A low-cost smartphone-based platform for highly sensitive point-of-care testing with persistent luminescent phosphors. *Lab on a Chip* **2017**, *17* (6), 1051-1059.
132. MarketsandMarkets™ Biosensors Market by Application (POC, Home Diagnostics, Research Labs, Biodefense, Environmental Monitoring, Food & Beverages Industry), Technology, Product (Wearable and Non-Wearable), and Geography - Global Forecast to 2022. <https://www.marketsandmarkets.com/Market-Reports/biosensors-market-798.html#> (accessed October 19th).
133. MarketsandMarkets™ Point-of-Care/Rapid Diagnostics Market by Testing (Glucose, Lipids, HbA1c, HCV, HIV, Influenza, Urinalysis, Hematology, Cancer, Pregnancy, PT/INR), Platform (Lateral Flow, Immunoassay), Mode (Prescription, OTC), End-User - Global Forecast to 2022. <https://www.marketsandmarkets.com/Market-Reports/point-of-care-diagnostic-market-106829185.html> (accessed October 19th).
134. Myers, F. B.; Lee, L. P., Innovations in optical microfluidic technologies for point-of-care diagnostics. *Lab on a Chip* **2008**, *8* (12), 2015-2031.
135. Hinman, S. S.; McKeating, K. S.; Cheng, Q., Surface plasmon resonance: Material and interface design for universal accessibility. *Analytical Chemistry* **2018**, *90* (1), 19-39.
136. Hoa, X. D.; Kirk, A. G.; Tabrizian, M., Towards integrated and sensitive surface plasmon resonance biosensors: A review of recent progress. *Biosens Bioelectron* **2007**, *23* (2), 151-160.
137. Leung, A.; Shankar, P. M.; Mutharasan, R., A review of fiber-optic biosensors. *Sensor Actuat B-Chem* **2007**, *125* (2), 688-703.
138. Pitruzzello, G.; Krauss, T. F., Photonic crystal resonances for sensing and imaging. *J Optics-Uk* **2018**, *20* (7), 073004.
139. Luan, E.; Shoman, H.; Ratner, D. M.; Cheung, K. C.; Chrostowski, L., Silicon photonic biosensors using label-free detection. *Sensors* **2018**, *18*, 3519.
140. Kozma, P.; Kehl, F.; Ehrentreich-Forster, E.; Stamm, C.; Bier, F. F., Integrated planar optical waveguide interferometer biosensors: A comparative review. *Biosens Bioelectron* **2014**, *58*, 287-307.
141. Haes, A. J.; Van Duyne, R. P., A unified view of propagating and localized surface plasmon resonance biosensors. *Analytical and Bioanalytical Chemistry* **2004**, *379* (7-8), 920-930.
142. Sepulveda, B.; Angelome, P. C.; Lechuga, L. M.; Liz-Marzan, L. M., LSPR-based nanobiosensors. *Nano Today* **2009**, *4* (3), 244-251.
143. Bisi, O.; Ossicini, S.; Pavesi, L., Porous silicon: a quantum sponge structure for silicon based optoelectronics. *Surface Science Reports* **2000**, *38* (1), 1-126.
144. Jane, A.; Dronov, R.; Hodges, A.; Voelcker, N. H., Porous silicon biosensors on the advance. *Trends Biotechnol* **2009**, *27* (4), 230-9.
145. Harraz, F. A., Porous silicon chemical sensors and biosensors: A review. *Sensors and Actuators B: Chemical* **2014**, *202*, 897-912.
146. Kumeria, T.; McInnes, S. J. P.; Maher, S.; Santos, A., Porous silicon for drug delivery applications and theranostics: recent advances, critical review and perspectives. *Expert Opinion on Drug Delivery* **2017**, *14* (12), 1407-1422.
147. Gupta, B.; Zhu, Y.; Guan, B.; Reece, P. J.; Gooding, J. J., Functionalised porous silicon as a biosensor: emphasis on monitoring cells in vivo and in vitro. *Analyst* **2013**, *138* (13), 3593-3615.
148. Hernandez-Montelongo, J.; Muñoz-Noval, A.; García-Ruiz, J.; Torres-Costa, V.; Martin-Palma, R.; Manso-Silvan, M., Nanostructured porous silicon: The winding road from photonics to cell scaffolds. A review. *Frontiers in Bioengineering and Biotechnology* **2015**, *3* (60).
149. Martín-Palma, R. J.; Manso-Silván, M.; Torres-Costa, V. In *Biomedical applications of nanostructured porous silicon: a review*, SPIE: 2010; p 21.

150. Uhlir, A., Electrolytic Shaping of Germanium and Silicon. *Bell System Technical Journal* **1956**, 35 (2), 333-347.
151. Canham, L. T., Silicon quantum wire array fabrication by electrochemical and chemical dissolution of wafers. *Applied Physics Letters* **1990**, 57 (10), 1046-1048.
152. Paquin, R. A., Properties of Metals. In *Handbook of Optic*, 2nd ed. ed.; Bass, M.; Van Stryland, E. W.; Williams, D. R.; Wolfe, W. L., Eds. Optical Society of America: Washington, DC, 1994; Vol. II.
153. Ilyas, S.; Böcking, T.; Kilian, K.; Reece, P. J.; Gooding, J.; Gaus, K.; Gal, M., Porous silicon based narrow line-width rugate filters. *Optical Materials* **2007**, 29 (6), 619-622.
154. Lorenzo, E.; Oton, C. J.; Capuj, N. E.; Ghulinyan, M.; Navarro-Urrios, D.; Gaburro, Z.; Pavesi, L., Porous silicon-based rugate filters. *Appl. Opt.* **2005**, 44 (26), 5415-5421.
155. Caroselli, R.; García Castelló, J.; Escorihuela, J.; Bañuls, M.; Maquieira, Á.; García-Rupérez, J., Experimental Study of the Oriented Immobilization of Antibodies on Photonic Sensing Structures by Using Protein A as an Intermediate Layer. *Sensors* **2018**, 18 (4), 1012.
156. Girault, P.; Lorrain, N.; Lemaitre, J.; Poffo, L.; Guendouz, M.; Hardy, I.; Gadonna, M.; Gutierrez, A.; Bodiou, L.; Charrier, J., Racetrack micro-resonators based on ridge waveguides made of porous silica. *Optical Materials* **2015**, 50, 167-174.
157. Rodriguez, G. A.; Hu, S.; Weiss, S. M., Porous silicon ring resonator for compact, high sensitivity biosensing applications. *Opt. Express* **2015**, 23 (6), 7111-7119.
158. Kim, K.; Murphy, T. E., Porous silicon integrated Mach-Zehnder interferometer waveguide for biological and chemical sensing. *Opt. Express* **2013**, 21 (17), 19488-19497.
159. Kilian, K. A.; Böcking, T.; Gooding, J. J., The importance of surface chemistry in mesoporous materials: lessons from porous silicon biosensors. *Chem. Commun.* **2009**, (6), 630-640.
160. Janshoff, A.; Dancil, K.-P. S.; Steinem, C.; Greiner, D. P.; Lin, V. S. Y.; Gurtner, C.; Motesharei, K.; Sailor, M. J.; Ghadiri, M. R., Macroporous p-Type Silicon Fabry-Perot Layers. Fabrication, Characterization, and Applications in Biosensing. *Journal of the American Chemical Society* **1998**, 120 (46), 12108-12116.
161. Salem, M. S.; Sailor, M. J.; Harraz, F. A.; Sakka, T.; Ogata, Y. H., Electrochemical stabilization of porous silicon multilayers for sensing various chemical compounds. *Journal of Applied Physics* **2006**, 100 (8), 083520.
162. Sailor, M. J., *Porous Silicon in Practice*. Wiley-VCH: Weinheim: Germany, 2011.
163. Shtenberg, G.; Massad-Ivanir, N.; Fruk, L.; Segal, E., Nanostructured Porous Si Optical Biosensors: Effect of Thermal Oxidation on Their Performance and Properties. *ACS Applied Materials & Interfaces* **2014**, 6 (18), 16049-16055.
164. Bonanno, L. M.; DeLouise, L. A., Steric Crowding Effects on Target Detection in an Affinity Biosensor. *Langmuir* **2007**, 23 (10), 5817-5823.
165. Schwartz, M. P.; Alvarez, S. D.; Sailor, M. J., Porous SiO₂ Interferometric Biosensor for Quantitative Determination of Protein Interactions: Binding of Protein A to Immunoglobulins Derived from Different Species. *Analytical Chemistry* **2007**, 79 (1), 327-334.
166. Kilian, K. A.; Böcking, T.; Gaus, K.; King-Lacroix, J.; Gal, M.; Gooding, J. J., Hybrid lipid bilayers in nanostructured silicon: a biomimetic mesoporous scaffold for optical detection of cholera toxin. *Chem. Commun.* **2007**, (19), 1936-1938.
167. Kilian, K. A.; Böcking, T.; Gaus, K.; Gal, M.; Gooding, J. J., Peptide-Modified Optical Filters for Detecting Protease Activity. *ACS Nano* **2007**, 1 (4), 355-361.
168. Kim, D.; Zuidema, J. M.; Kang, J.; Pan, Y.; Wu, L.; Warther, D.; Arkles, B.; Sailor, M. J., Facile Surface Modification of Hydroxylated Silicon Nanostructures Using Heterocyclic Silanes. *Journal of the American Chemical Society* **2016**, 138 (46), 15106-15109.
169. Salonen, J.; Mäkilä, E., Thermally Carbonized Porous Silicon and Its Recent Applications. *Advanced Materials* **2018**, 30 (24), 1703819.
170. Kim, D.; Joo, J.; Pan, Y.; Boarino, A.; Jun, Y. W.; Ahn, K. H.; Arkles, B.; Sailor, M. J., Thermally Induced Silane Dehydrocoupling on Silicon Nanostructures. *Angewandte Chemie International Edition* **2016**, 55 (22), 6423-6427.
171. Massad-Ivanir, N.; Shtenberg, G.; Segal, E., Optical Detection of E. coli Bacteria by Mesoporous Silicon Biosensors. *J. Vis. Exp.* **2013**, (81).
172. Massad-Ivanir, N.; Shtenberg, G.; Tzur, A.; Krepker, M. A.; Segal, E., Engineering Nanostructured Porous SiO₂ Surfaces for Bacteria Detection via "Direct Cell Capture". *Analytical Chemistry* **2011**, 83 (9), 3282-3289.
173. Krepker, M. A.; Segal, E., Dual-Functionalized Porous Si/Hydrogel Hybrid for Label-Free Biosensing of Organophosphorus Compounds. *Analytical Chemistry* **2013**, 85 (15), 7353-7360.
174. Shtenberg, G.; Massad-Ivanir, N.; Moscovitz, O.; Engin, S.; Sharon, M.; Fruk, L.; Segal, E., Picking up the Pieces: A Generic Porous Si Biosensor for Probing the Proteolytic Products of Enzymes. *Analytical Chemistry* **2013**, 85 (3), 1951-1956.

175. Rong, G.; Ryckman, J. D.; Mernaugh, R. L.; Weiss, S. M., Label-free porous silicon membrane waveguide for DNA sensing. *Applied Physics Letters* **2008**, *93* (16), 161109.
176. Wei, X.; Weiss, S. M., Guided mode biosensor based on grating coupled porous silicon waveguide. *Opt. Express* **2011**, *19* (12), 11330-11339.
177. Massad-Ivanir, N.; Shtenberg, G.; Raz, N.; Gazenbeek, C.; Budding, D.; Bos, M. P.; Segal, E., Porous Silicon-Based Biosensors: Towards Real-Time Optical Detection of Target Bacteria in the Food Industry. *Scientific Reports* **2016**, *6*, 38099.
178. Bonanno, L. M.; DeLouise, L. A., Whole Blood Optical Biosensor. *Biosens Bioelectron* **2007**, *23* (3), 444-448.
179. Ramakrishnan, S. K.; Jebors, S.; Martin, M.; Cloitre, T.; Agarwal, V.; Mehdi, A.; Martinez, J.; Subra, G.; Gergely, C., Engineered Adhesion Peptides for Improved Silicon Adsorption. *Langmuir* **2015**, *31* (43), 11868-11874.
180. Kilian, K. A.; Böcking, T.; Gaus, K.; Gooding, J. J., Introducing Distinctly Different Chemical Functionalities onto the Internal and External Surfaces of Mesoporous Materials. *Angewandte Chemie* **2008**, *120* (14), 2737-2739.
181. Wu, C.-C.; Sailor, M. J., Selective Functionalization of the Internal and the External Surfaces of Mesoporous Silicon by Liquid Masking. *ACS Nano* **2013**, *7* (4), 3158-3167.
182. Xu, W.; Rytönen, J.; Rönkkö, S.; Nissinen, T.; Kinnunen, T.; Suvanto, M.; Näränen, A.; Lehto, V.-P., A Nanostopper Approach To Selectively Engineer the Surfaces of Mesoporous Silicon. *Chemistry of Materials* **2014**, *26* (23), 6734-6742.
183. Lion, A.; Laidani, N.; Bettotti, P.; Piotta, C.; Pepponi, G.; Barozzi, M.; Scarpa, M., Angle resolved XPS for selective characterization of internal and external surface of porous silicon. *Applied Surface Science* **2017**, *406*, 144-149.
184. Steinem, C.; Janshoff, A.; Lin, V. S. Y.; Völcker, N. H.; Reza Ghadiri, M., DNA hybridization-enhanced porous silicon corrosion: mechanistic investigations and prospect for optical interferometric biosensing. *Tetrahedron* **2004**, *60* (49), 11259-11267.
185. Zhao, Y.; Lawrie, J. L.; Beavers, K. R.; Laibinis, P. E.; Weiss, S. M., Effect of DNA-Induced Corrosion on Passivated Porous Silicon Biosensors. *ACS Applied Materials & Interfaces* **2014**, *6* (16), 13510-13519.
186. Ouyang, H.; DeLouise, L. A.; Miller, B. L.; Fauchet, P. M., Label-Free Quantitative Detection of Protein Using Macroporous Silicon Photonic Bandgap Biosensors. *Analytical Chemistry* **2007**, *79* (4), 1502-1506.
187. De Stefano, L.; Arcari, P.; Lamberti, A.; Sanges, C.; Rotiroli, L.; Rea, I.; Rendina, I., DNA Optical Detection Based on Porous Silicon Technology: from Biosensors to Biochips. *Sensors* **2007**, *7* (2), 214.
188. Rong, G.; Najmaie, A.; Sipe, J. E.; Weiss, S. M., Nanoscale porous silicon waveguide for label-free DNA sensing. *Biosensors and Bioelectronics* **2008**, *23* (10), 1572-1576.
189. Rong, G.; Weiss, S. M., Biomolecule size-dependent sensitivity of porous silicon sensors. *physica status solidi (a)* **2009**, *206* (6), 1365-1368.
190. Anderson, M. A.; Tinsley-Bown, A.; Allcock, P.; Perkins, E. A.; Snow, P.; Hollings, M.; Smith, R. G.; Reeves, C.; Squirrell, D. J.; Nicklin, S.; Cox, T. I., Sensitivity of the optical properties of porous silicon layers to the refractive index of liquid in the pores. *physica status solidi (a)* **2003**, *197* (2), 528-533.
191. Caroselli, R.; Martín Sánchez, D.; Ponce Alcántara, S.; Prats Quilez, F.; Torrijos Morán, L.; García-Rupérez, J., Real-Time and In-Flow Sensing Using a High Sensitivity Porous Silicon Microcavity-Based Sensor. *Sensors* **2017**, *17* (12), 2813.
192. Politi, J.; Dardano, P.; Caliò, A.; Iodice, M.; Rea, I.; De Stefano, L., Reversible sensing of heavy metal ions using lysine modified oligopeptides on porous silicon and gold. *Sensors and Actuators B: Chemical* **2017**, *244*, 142-150.
193. Tsai, W.-T.; Nguyen, M.-H.; Lai, J.-R.; Nguyen, H.-B.; Lee, M.-C.; Tseng, F.-G., ppb-level heavy metal ion detection by electrochemistry-assisted nanoPorous silicon (ECA-NPS) photonic sensors. *Sensors and Actuators B: Chemical* **2018**, *265*, 75-83.
194. Lasmi, K.; Derder, H.; Kermad, A.; Sam, S.; Boukhalfa-Abib, H.; Belhousse, S.; Tighilt, F. Z.; Hamdani, K.; Gabouze, N., Tyrosinase immobilization on functionalized porous silicon surface for optical monitoring of pyrocatechol. *Applied Surface Science* **2018**, *446*, 3-9.
195. Ghosh, R.; Das, R.; Giri, P. K., Label-free glucose detection over a wide dynamic range by mesoporous Si nanowires based on anomalous photoluminescence enhancement. *Sensors and Actuators B: Chemical* **2018**, *260*, 693-704.
196. Myndrul, V.; Viter, R.; Savchuk, M.; Shpyrka, N.; Erts, D.; Jevdokimovs, D.; Silamiķelis, V.; Smyntyna, V.; Ramanavicius, A.; Iatsunskyi, I., Porous silicon based photoluminescence immunosensor for rapid and highly-sensitive detection of Ochratoxin A. *Biosensors and Bioelectronics* **2018**, *102*, 661-667.
197. Myndrul, V.; Viter, R.; Savchuk, M.; Koval, M.; Starodub, N.; Silamiķelis, V.; Smyntyna, V.; Ramanavicius, A.; Iatsunskyi, I., Gold coated porous silicon nanocomposite as a substrate for photoluminescence-based immunosensor suitable for the determination of Aflatoxin B1. *Talanta* **2017**, *175*, 297-304.

198. Liu, R.; Li, W.; Cai, T.; Deng, Y.; Ding, Z.; Liu, Y.; Zhu, X.; Wang, X.; Liu, J.; Liang, B.; Zheng, T.; Li, J., TiO₂ Nanolayer-Enhanced Fluorescence for Simultaneous Multiplex Mycotoxin Detection by Aptamer Microarrays on a Porous Silicon Surface. *ACS Applied Materials & Interfaces* **2018**, *10* (17), 14447-14453.
199. Lv, C.; Jia, Z.; Lv, J.; Zhang, H.; Li, Y., High Sensitivity Detection of CdSe/ZnS Quantum Dot-Labeled DNA Based on N-type Porous Silicon Microcavities. *Sensors* **2017**, *17* (1), 80.
200. Wang, J.; Jia, Z., Metal Nanoparticles/Porous Silicon Microcavity Enhanced Surface Plasmon Resonance Fluorescence for the Detection of DNA. *Sensors* **2018**, *18* (2), 661.
201. Zhang, H.; Lv, J.; Jia, Z., Detection of Ammonia-Oxidizing Bacteria (AOB) Using a Porous Silicon Optical Biosensor Based on a Multilayered Double Bragg Mirror Structure. *Sensors* **2018**, *18* (1), 105.
202. Lv, C.; Jia, Z.; Liu, Y.; Mo, J.; Li, P.; Lv, X., Angle-resolved diffraction grating biosensor based on porous silicon. *Journal of Applied Physics* **2016**, *119* (9), 094502.
203. Novara, C.; Chiadò, A.; Paccotti, N.; Catuogno, S.; Esposito, C. L.; Condorelli, G.; De Franciscis, V.; Geobaldo, F.; Rivolo, P.; Giorgis, F., SERS-active metal-dielectric nanostructures integrated in microfluidic devices for label-free quantitative detection of miRNA. *Faraday Discussions* **2017**, *205* (0), 271-289.
204. Bu, Y.; Zhu, G.; Li, S.; Qi, R.; Bhawe, G.; Zhang, D.; Han, R.; Sun, D.; Liu, X.; Hu, Z.; Liu, X., Silver-Nanoparticle-Embedded Porous Silicon Disks Enabled SERS Signal Amplification for Selective Glutathione Detection. *ACS Applied Nano Materials* **2018**, *1* (1), 410-417.
205. Massad-Ivanir, N.; Bhunia, S. K.; Raz, N.; Segal, E.; Jelinek, R., Synthesis and characterization of a nanostructured porous silicon/carbon dot-hybrid for orthogonal molecular detection. *Npg Asia Materials* **2018**, *10*, e463.
206. Lv, X.; Xin, L.; Lv, G.; Mo, J.; Gao, Z.; Jia, Z.; Wen, H., Preparation of a Photoluminescent Film on a Silicon-On-Insulator Device for the Simple, Rapid, and Quantitative Detection of a Hydatid Disease Diagnostic Protein Marker. *IEEE Photonics Journal* **2017**, *9* (4), 1-7.
207. Li, P.; Jia, Z.; Lü, G., Hydatid detection using the near-infrared transmission angular spectra of porous silicon microcavity biosensors. *Scientific Reports* **2017**, *7*, 44798.
208. Irrera, A.; Leonardi, A. A.; Di Franco, C.; Lo Faro, M. J.; Palazzo, G.; D'Andrea, C.; Manoli, K.; Franzò, G.; Musumeci, P.; Fazio, B.; Torsi, L.; Priolo, F., New Generation of Ultrasensitive Label-Free Optical Si Nanowire-Based Biosensors. *ACS Photonics* **2018**, *5* (2), 471-479.
209. Lee, S.; Hosokawa, K.; Kim, S.; Jeong, O. C.; Lilja, H.; Laurell, T.; Maeda, M., Porous silicon microarray for simultaneous fluorometric immunoassay of the biomarkers prostate-specific antigen and human glandular kallikrein 2. *Microchimica Acta* **2016**, *183* (12), 3321-3327.
210. Ramakrishnan, S. K.; Martin Fernandez, M.; Cloitre, T.; Agarwal, V.; Cuisinier, F. J. G.; Gergely, C., Porous silicon microcavities redefine colorimetric ELISA sensitivity for ultrasensitive detection of autoimmune antibodies. *Sensors and Actuators B: Chemical* **2018**, *272*, 211-218.
211. Krismastuti, F. S. H.; Cavallaro, A.; Prieto-Simon, B.; Voelcker, N. H., Toward Multiplexing Detection of Wound Healing Biomarkers on Porous Silicon Resonant Microcavities. *Advanced Science* **2016**, *3* (6), 1500383.
212. Tang, Y.; Li, Z.; Luo, Q.; Liu, J.; Wu, J., Bacteria detection based on its blockage effect on silicon nanopore array. *Biosensors and Bioelectronics* **2016**, *79*, 715-720.
213. Martin, M.; Taleb Bendiab, C.; Massif, L.; Palestino, G.; Agarwal, V.; Cuisinier, F.; Gergely, C., Matrix metalloproteinase sensing via porous silicon microcavity devices functionalized with human antibodies. *physica status solidi c* **2011**, *8* (6), 1888-1892.
214. Morales, M. A.; Halpern, J. M., Guide to Selecting a Biorecognition Element for Biosensors. *Bioconjugate Chemistry* **2018**, *29* (10), 3231-3239.
215. Zhou, W.; Jimmy Huang, P.-J.; Ding, J.; Liu, J., Aptamer-based biosensors for biomedical diagnostics. *Analyst* **2014**, *139* (11), 2627-2640.
216. Iliuk, A. B.; Hu, L.; Tao, W. A., Aptamer in Bioanalytical Applications. *Analytical Chemistry* **2011**, *83* (12), 4440-4452.
217. Urmann, K.; Tenenbaum, E.; Walter, J.-G.; Segal, E., Porous Silicon Biosensors Employing Emerging Capture Probes. In *Electrochemically Engineered Nanoporous Materials: Methods, Properties and Applications*, Lolic, D.; Santos, A., Eds. Springer International Publishing: Cham, 2015; pp 93-116.
218. Terracciano, M.; Rea, I.; Stefano, L. D.; Rendina, I.; Oliviero, G.; Nici, F.; D'Errico, S.; Piccialli, G.; Borbone, N., Synthesis of mixed-sequence oligonucleotides on mesoporous silicon: chemical strategies and material stability. *Nanoscale Research Letters* **2014**, *9* (1), 317.
219. Tenenbaum, E.; Segal, E., Optical biosensors for bacteria detection by a peptidomimetic antimicrobial compound. *Analyst* **2015**, *140* (22), 7726-7733.
220. Paul, A.; Pauline, G.; Nathalie, L.; Yannick, D.; Loïc, B.; Luiz, P.; Mohammed, G.; Monique, T.; Joël, C., Optimization of porous silicon waveguide design for micro-ring resonator sensing applications. *J Optics-Uk* **2018**, *20* (8), 085301.

221. Wan, Y.; Krueger, N. A.; Ocier, C. R.; Su, P.; Braun, P. V.; Cunningham, B. T., Resonant Mode Engineering of Photonic Crystal Sensors Clad with Ultralow Refractive Index Porous Silicon Dioxide. *Advanced Optical Materials* **2017**, *5* (21), 1700605.
222. Caroselli, R.; Ponce-Alcántara, S.; Quilez, F. P.; Sánchez, D. M.; Morán, L. T.; Barres, A. G.; Bellieres, L.; Bandarenka, H.; Girel, K.; Bondarenko, V.; García-Rupérez, J., Experimental study of the sensitivity of a porous silicon ring resonator sensor using continuous in-flow measurements. *Opt. Express* **2017**, *25* (25), 31651-31659.
223. Rodriguez, G. A.; Ryckman, J. D.; Jiao, Y.; Weiss, S. M., A size selective porous silicon grating-coupled Bloch surface and sub-surface wave biosensor. *Biosensors and Bioelectronics* **2014**, *53*, 486-493.
224. Jamois, C.; Li, C.; Orobtcouk, R.; Benyattou, T., Slow Bloch surface wave devices on porous silicon for sensing applications. *Photonics and Nanostructures - Fundamentals and Applications* **2010**, *8* (2), 72-77.
225. Ryckman, J. D.; Liscidini, M.; Sipe, J. E.; Weiss, S. M., Porous silicon structures for low-cost diffraction-based biosensing. *Applied Physics Letters* **2010**, *96* (17), 171103.
226. Azuelos, P.; Girault, P.; Lorrain, N.; Poffo, L.; Hardy, I.; Guendouz, M.; Thual, M., Theoretical investigation of Vernier effect based sensors with hybrid porous silicon-polymer optical waveguides. *Journal of Applied Physics* **2017**, *121* (14), 144501.
227. Lv, X.; Mo, J.; Jiang, T.; Zhong, F.; Jia, Z.; Li, J.; Zhang, F., Novel multilayered porous silicon-based immunosensor for determining Hydroxysafflor yellow A. *Applied Surface Science* **2011**, *257* (6), 1906-1910.
228. Lv, X.; Zhong, F.; Jia, Z.; Chen, L.; Ma, J.; Zhang, H.; Cao, Z.; Zhou, J. In *Development of silicon-on-insulator-based nanoporous silicon photonic crystals for label-free DNA detection*, SPIE: 2013; p 6.
229. Orosco, M. M.; Pacholski, C.; Miskelly, G. M.; Sailor, M. J., Protein-Coated Porous-Silicon Photonic Crystals for Amplified Optical Detection of Protease Activity. *Advanced Materials* **2006**, *18* (11), 1393-1396.
230. Kilian, K. A.; Lai, L. M. H.; Magenau, A.; Cartland, S.; Böcking, T.; Di Girolamo, N.; Gal, M.; Gaus, K.; Gooding, J. J., Smart Tissue Culture: in Situ Monitoring of the Activity of Protease Enzymes Secreted from Live Cells Using Nanostructured Photonic Crystals. *Nano Letters* **2009**, *9* (5), 2021-2025.
231. Gupta, B.; Mai, K.; Lowe, S. B.; Wakefield, D.; Di Girolamo, N.; Gaus, K.; Reece, P. J.; Gooding, J. J., Ultrasensitive and Specific Measurement of Protease Activity Using Functionalized Photonic Crystals. *Analytical Chemistry* **2015**, *87* (19), 9946-9953.
232. Lee, M.; Fauchet, P. M., Two-dimensional silicon photonic crystal based biosensing platform for protein detection. *Opt. Express* **2007**, *15* (8), 4530-4535.
233. Wang, J.; Lee, G. Y.; Kennard, R.; Barillaro, G.; Bisiewicz, R. H.; Cortez Lemus, N. A.; Cao, X. C.; Anglin, E. J.; Park, J. S.; Potocny, A.; Bernhard, D.; Li, J.; Sailor, M. J., Engineering the Properties of Polymer Photonic Crystals with Mesoporous Silicon Templates. *Chemistry of Materials* **2017**, *29* (3), 1263-1272.
234. WU, B.; RONG, G.; ZHAO, J.; ZHANG, S.; ZHU, Y.; HE, B., A NANOSCALE POROUS SILICON MICROCAVITY BIOSENSOR FOR NOVEL LABEL-FREE TUBERCULOSIS ANTIGEN-ANTIBODY DETECTION. *Nano* **2012**, *07* (06), 1250049.
235. Li, P.; Jia, Z.; Lü, X.; Liu, Y.; Ning, X.; Mo, J.; Wang, J., Spectrometer-free biological detection method using porous silicon microcavity devices. *Opt. Express* **2015**, *23* (19), 24626-24633.
236. Qiao, H.; Guan, B.; Gooding, J. J.; Reece, P. J., Protease detection using a porous silicon based Bloch surface wave optical biosensor. *Opt. Express* **2010**, *18* (14), 15174-15182.
237. Zhao, Y.; Lawrie, J. L.; Laibinis, P. E.; Weiss, S. M. In *Understanding and mitigating DNA induced corrosion in porous silicon based biosensors*, SPIE BiOS, SPIE: 2014; p 9.
238. Lv, X.; Chen, L.; Zhang, H.; Mo, J.; Zhong, F.; Lv, C.; Ma, J.; Jia, Z., Hybridization assay of insect antifreezing protein gene by novel multilayered porous silicon nucleic acid biosensor. *Biosensors and Bioelectronics* **2013**, *39* (1), 329-333.
239. Zhang, H.; Jia, Z.; Lv, X.; Zhou, J.; Chen, L.; Liu, R.; Ma, J., Porous silicon optical microcavity biosensor on silicon-on-insulator wafer for sensitive DNA detection. *Biosensors and Bioelectronics* **2013**, *44*, 89-94.
240. Zhang, H.; Jia, Z.; Lv, X., Surface layer reflective index changes of Au nanoparticle functionalized porous silicon microcavity for DNA detection. *Current Applied Physics* **2015**, *15* (8), 870-876.
241. Zhao, Y.; Gaur, G.; Mernaugh, R. L.; Laibinis, P. E.; Weiss, S. M., Comparative Kinetic Analysis of Closed-Ended and Open-Ended Porous Sensors. *Nanoscale Research Letters* **2016**, *11* (1), 395.
242. Gaur, G.; Koktysh, D. S.; Weiss, S. M., Immobilization of Quantum Dots in Nanostructured Porous Silicon Films: Characterizations and Signal Amplification for Dual-Mode Optical Biosensing. *Advanced Functional Materials* **2013**, *23* (29), 3604-3614.
243. Holthausen, D.; Vasani, R. B.; McInnes, S. J. P.; Ellis, A. V.; Voelcker, N. H., Polymerization-Amplified Optical DNA Detection on Porous Silicon Templates. *ACS Macro Letters* **2012**, *1* (7), 919-921.
244. Szili, E. J.; Jane, A.; Low, S. P.; Sweetman, M.; Macardle, P.; Kumar, S.; Smart, R. S. C.; Voelcker, N. H., Interferometric porous silicon transducers using an enzymatically amplified optical signal. *Sensors and Actuators B: Chemical* **2011**, *160* (1), 341-348.

245. Paratore, F.; Zeidman Kalman, T.; Rosenfeld, T.; Kaigala, G. V.; Bercovici, M., Isotachophoresis-Based Surface Immunoassay. *Analytical Chemistry* **2017**, *89* (14), 7373-7381.
246. Zhang, H.; Jia, Z.; Lv, X.; Hou, J.; Liu, X.; Ma, J.; Zhou, J., Antifreeze protein detection using Rhodamine B as photoluminescence label in porous silicon. *Current Applied Physics* **2013**, *13* (4), 736-742.
247. Jenie, S. N. A.; Prieto-Simon, B.; Voelcker, N. H., Development of l-lactate dehydrogenase biosensor based on porous silicon resonant microcavities as fluorescence enhancers. *Biosensors and Bioelectronics* **2015**, *74*, 637-643.
248. Jenie, S. N. A.; Plush, S. E.; Voelcker, N. H., Recent Advances on Luminescent Enhancement-Based Porous Silicon Biosensors. *Pharmaceutical Research* **2016**, *33* (10), 2314-2336.
249. Krismastuti, F. S. H.; Pace, S.; Voelcker, N. H., Porous Silicon Resonant Microcavity Biosensor for Matrix Metalloproteinase Detection. *Advanced Functional Materials* **2014**, *24* (23), 3639-3650.
250. Chiadò, A.; Novara, C.; Lamberti, A.; Geobaldo, F.; Giorgis, F.; Rivolo, P., Immobilization of Oligonucleotides on Metal-Dielectric Nanostructures for miRNA Detection. *Analytical Chemistry* **2016**, *88* (19), 9554-9563.
251. Jiao, Y.; Koktysh, D. S.; Phambu, N.; Weiss, S. M., Dual-mode sensing platform based on colloidal gold functionalized porous silicon. *Applied Physics Letters* **2010**, *97* (15), 153125.
252. Bonanno, L. M.; Kwong, T. C.; DeLouise, L. A., Label-Free Porous Silicon Immunosensor for Broad Detection of Opiates in a Blind Clinical Study and Results Comparison to Commercial Analytical Chemistry Techniques. *Analytical Chemistry* **2010**, *82* (23), 9711-9718.
253. Bonanno, L. M.; DeLouise, L. A., Tunable Detection Sensitivity of Opiates in Urine via a Label-Free Porous Silicon Competitive Inhibition Immunosensor. *Analytical Chemistry* **2010**, *82* (2), 714-722.
254. Hwang, J.; Hwang, M. P.; Choi, M.; Seo, Y.; Jo, Y.; Son, J.; Hong, J.; Choi, J., Sensitive detection of copper ions via ion-responsive fluorescence quenching of engineered porous silicon nanoparticles. *Scientific Reports* **2016**, *6*, 35565.
255. Krismastuti, F. S. H.; Brooks, W. L. A.; Sweetman, M. J.; Sumerlin, B. S.; Voelcker, N. H., A photonic glucose biosensor for chronic wound prognostics. *Journal of Materials Chemistry B* **2014**, *2* (25), 3972-3983.
256. Tong, W. Y.; Sweetman, M. J.; Marzouk, E. R.; Fraser, C.; Kuchel, T.; Voelcker, N. H., Towards a subcutaneous optical biosensor based on thermally hydrocarbonised porous silicon. *Biomaterials* **2016**, *74*, 217-230.
257. Mairal, T.; Cengiz Özalp, V.; Lozano Sánchez, P.; Mir, M.; Katakis, I.; O'Sullivan, C. K., Aptamers: molecular tools for analytical applications. *Analytical and Bioanalytical Chemistry* **2008**, *390* (4), 989-1007.
258. Sharma, S.; Johnson, R. W.; Desai, T. A., XPS and AFM analysis of antifouling PEG interfaces for microfabricated silicon biosensors. *Biosensors and Bioelectronics* **2004**, *20* (2), 227-239.
259. Yu, Q.; Zhang, Y.; Wang, H.; Brash, J.; Chen, H., Anti-fouling bioactive surfaces. *Acta Biomaterialia* **2011**, *7* (4), 1550-1557.
260. Sweetman, M. J.; Shearer, C. J.; Shapter, J. G.; Voelcker, N. H., Dual Silane Surface Functionalization for the Selective Attachment of Human Neuronal Cells to Porous Silicon. *Langmuir* **2011**, *27* (15), 9497-9503.
261. Lafleur, J. P.; Jönsson, A.; Senkbeil, S.; Kutter, J. P., Recent advances in lab-on-a-chip for biosensing applications. *Biosensors and Bioelectronics* **2016**, *76*, 213-233.
262. Li, Z.; Luo, Q.; Wu, J., Label-free discrimination of membrane-translocating peptides on porous silicon microfluidic biosensors. *Biomicrofluidics* **2016**, *10* (6), 064113.
263. Orabona, E.; Rea, I.; Rendina, I.; Stefano, L. D., Numerical Optimization of a Microfluidic Assisted Microarray for the Detection of Biochemical Interactions. *Sensors* **2011**, *11* (10), 9658.
264. Roda, A.; Michelini, E.; Zangheri, M.; Di Fusco, M.; Calabria, D.; Simoni, P., Smartphone-based biosensors: A critical review and perspectives. *TrAC Trends in Analytical Chemistry* **2016**, *79*, 317-325.
265. Zhang, D.; Liu, Q., Biosensors and bioelectronics on smartphone for portable biochemical detection. *Biosensors and Bioelectronics* **2016**, *75*, 273-284.
266. Gallegos, D.; Long, K. D.; Yu, H.; Clark, P. P.; Lin, Y.; George, S.; Nath, P.; Cunningham, B. T., Label-free biodetection using a smartphone. *Lab on a Chip* **2013**, *13* (11), 2124-2132.
267. Li, C.; Jia, Z.; Li, P.; Wen, H.; Lv, G.; Huang, X., Parallel Detection of Refractive Index Changes in a Porous Silicon Microarray Based on Digital Images. *Sensors* **2017**, *17* (4), 750.
268. Guo, Z.; Jia, Z.; Yang, J.; Kasabov, N.; Li, C., Image Processing of Porous Silicon Microarray in Refractive Index Change Detection. *Sensors* **2017**, *17* (6), 1335.
269. Chen, W.; Jia, Z.; Li, P.; Lv, G.; Lv, X., Refractive index change detection based on porous silicon microarray. *Applied Physics B* **2016**, *122* (5), 120.
270. Cao, T.; Zhao, Y.; Weiss, S. M. In *A smartphone compatible colorimetric biosensing system based on porous silicon*, SPIE BiOS, SPIE: 2017; p 7.
271. Wang, H.; Welker, B.; Gao, Y.; Federici, J. F.; Levy, R. A., Photolithographic patterning of porous silicon using silicon nitride and silicon carbide masks. *Materials Letters* **1995**, *23* (4), 209-214.

272. Ohmukai, M.; Okada, K.; Tsutsumi, Y., Patterned porous silicon formed with photolithography. *Journal of Materials Science: Materials in Electronics* **2005**, *16* (2), 119-121.
273. Nassiopoulos, A. G.; Grigoropoulos, S.; Canham, L.; Halimaoui, A.; Berbezier, I.; Gogolides, E.; Papadimitriou, D., Sub-micrometre luminescent porous silicon structures using lithographically patterned substrates. *Thin Solid Films* **1995**, *255* (1), 329-333.
274. Flavel, B. S.; Sweetman, M. J.; Shearer, C. J.; Shapter, J. G.; Voelcker, N. H., Micropatterned Arrays of Porous Silicon: Toward Sensory Biointerfaces. *ACS Applied Materials & Interfaces* **2011**, *3* (7), 2463-2471.
275. Yamaguchi, R.-t.; Miyamoto, K.-i.; Ishibashi, K.-i.; Hirano, A.; Said, S. M.; Kimura, Y.; Niwano, M., DNA hybridization detection by porous silicon-based DNA microarray in conjugation with infrared microspectroscopy. *Journal of Applied Physics* **2007**, *102* (1), 014303.
276. Chen, L.; Chen, Z.-T.; Wang, J.; Xiao, S.-J.; Lu, Z.-H.; Gu, Z.-Z.; Kang, L.; Chen, J.; Wu, P.-H.; Tang, Y.-C.; Liu, J.-N., Gel-pad microarrays templated by patterned porous silicon for dual-mode detection of proteins. *Lab on a Chip* **2009**, *9* (6), 756-760.
277. Li, H.-F.; Han, H.-M.; Wu, Y.-G.; Xiao, S.-J., Biological functionalization and patterning of porous silicon prepared by Pt-assisted chemical etching. *Applied Surface Science* **2010**, *256* (12), 4048-4051.
278. Rea, I.; Lamberti, A.; Rendina, I.; Coppola, G.; Gioffrè, M.; Iodice, M.; Casalino, M.; Tommasi, E. D.; Stefano, L. D., Fabrication and characterization of a porous silicon based microarray for label-free optical monitoring of biomolecular interactions. *Journal of Applied Physics* **2010**, *107* (1), 014513.
279. Novara, C.; Lamberti, A.; Chiadò, A.; Virga, A.; Rivolo, P.; Geobaldo, F.; Giorgis, F., Surface-enhanced Raman spectroscopy on porous silicon membranes decorated with Ag nanoparticles integrated in elastomeric microfluidic chips. *RSC Advances* **2016**, *6* (26), 21865-21870.
280. Chattopadhyay, S.; Bohn, P. W., Direct-write patterning of microstructured porous silicon arrays by focused-ion-beam Pt deposition and metal-assisted electroless etching. *Journal of Applied Physics* **2004**, *96* (11), 6888-6894.
281. Sirbulu, D. J.; Lowman, G. M.; Scott, B.; Stucky, G. D.; Buratto, S. K., Patterned Microstructures of Porous Silicon by Dry-Removal Soft Lithography. *Advanced Materials* **2003**, *15* (2), 149-152.
282. Khung, Y.-L.; Graney, S. D.; Voelcker, N. H., Micropatterning of Porous Silicon Films by Direct Laser Writing. *Biotechnology Progress* **2006**, *22* (5), 1388-1393.
283. Zhu, Y.; Soeriyadi, A. H.; Parker, S. G.; Reece, P. J.; Gooding, J. J., Chemical patterning on preformed porous silicon photonic crystals: towards multiplex detection of protease activity at precise positions. *Journal of Materials Chemistry B* **2014**, *2* (23), 3582-3588.
284. Zhu, Y.; Gupta, B.; Guan, B.; Ciampi, S.; Reece, P. J.; Gooding, J. J., Photolithographic Strategy for Patterning Preformed, Chemically Modified, Porous Silicon Photonic Crystal Using Click Chemistry. *ACS Applied Materials & Interfaces* **2013**, *5* (14), 6514-6521.
285. Coombs, S. G.; Khodjaniyazova, S.; Bright, F. V., Exploiting the 3-Aminopropyltriethoxysilane (APTES) autocatalytic nature to create bioconjugated microarrays on hydrogen-passivated porous silicon. *Talanta* **2018**, *177*, 26-33.
286. Coombs, S. G.; Bright, F. V., Spatial Characteristics of Contact Pin-Printed Silanes and Bioconjugates on Oxidized Porous Silicon. *The Journal of Physical Chemistry C* **2016**, *120* (11), 6011-6019.
287. McCall, D. T.; Zhang, Y.; Hook, D. J.; Bright, F. V., Optimizing Pin-Printed and Hydrosilylated Microarray Spot Density on Porous Silicon Platforms. *Langmuir* **2015**, *31* (41), 11370-11377.
288. Kraut, N. D.; Brattlie, J. D.; Deuro, R. E.; McGoorty, M. M.; Bright, F. V., High-Throughput Screening System for Creating and Assessing Surface-Modified Porous Silicon. *Applied Spectroscopy* **2012**, *66* (10), 1171-1178.
289. Ressine, A.; Ekström, S.; Marko-Varga, G.; Laurell, T., Macro-/Nanoporous Silicon as a Support for High-Performance Protein Microarrays. *Analytical Chemistry* **2003**, *75* (24), 6968-6974.
290. Ressine, A.; Finnskog, D.; Malm, J.; Becker, C.; Lilja, H.; Marko Varga, G.; Laurell, T., Macro/nano-structured silicon as solid support for antibody arrays. *NanoBiotechnology* **2005**, *1* (1), 93-103.
291. Wang, C.; Jia, X.-M.; Jiang, C.; Zhuang, G.-N.; Yan, Q.; Xiao, S.-J., DNA microarray fabricated on poly(acrylic acid) brushes-coated porous silicon by in situ rolling circle amplification. *Analyst* **2012**, *137* (19), 4539-4545.
292. Meade, S. O.; Chen, M. Y.; Sailor, M. J.; Miskelly, G. M., Multiplexed DNA Detection Using Spectrally Encoded Porous SiO₂ Photonic Crystal Particles. *Analytical Chemistry* **2009**, *81* (7), 2618-2625.
293. Krismastuti, F. S. H.; Dewi, M. R.; Prieto-Simon, B.; Nann, T.; Voelcker, N. H., Disperse-and-Collect Approach for the Type-Selective Detection of Matrix Metalloproteinases in Porous Silicon Resonant Microcavities. *ACS Sensors* **2017**, *2* (2), 203-209.
294. Leonard, H.; Colodner, R.; Halachmi, S.; Segal, E., Recent Advances in the Race to Design a Rapid Diagnostic Test for Antimicrobial Resistance. *ACS Sensors* **2018**.

295. Leonard, H.; Halachmi, S.; Ben-Dov, N.; Nativ, O.; Segal, E., Unraveling Antimicrobial Susceptibility of Bacterial Networks on Micropillar Architectures Using Intrinsic Phase-Shift Spectroscopy. *ACS Nano* **2017**, *11* (6), 6167-6177.
296. Mirsky, Y.; Nahor, A.; Edrei, E.; Massad-Ivanir, N.; Bonanno, L. M.; Segal, E.; Sa'ar, A., Optical biosensing of bacteria and cells using porous silicon based, photonic lamellar gratings. *Applied Physics Letters* **2013**, *103* (3), 033702.
297. Shtenberg, G.; Massad-Ivanir, N.; Segal, E., Detection of trace heavy metal ions in water by nanostructured porous Si biosensors. *Analyst* **2015**, *140* (13), 4507-4514.
298. Yamazaki, H.; Kimura, S.; Tsukahara, M.; Esashika, K.; Saiki, T., Optical detection of DNA translocation through silicon nanopore by ultraviolet light. *Applied Physics A* **2014**, *115* (1), 53-56.
299. Hirohito, Y.; Keiko, E.; Toshiharu, S., A 150 nm ultraviolet excitation volume on a porous silicon membrane for direct optical observation of DNA coil relaxation during capture into nanopores. *Nano Futures* **2017**, *1* (1), 011001.
300. Hirohito, Y.; Shintaro, I.; Keiko, E.; Toshiharu, S., Optical observation of DNA motion during and immediately after nanopore translocation. *Applied Physics Express* **2016**, *9* (1), 017001.
301. Yamazaki, H.; Ito, S.; Esashika, K.; Taguchi, Y.; Saiki, T., Optical observation of DNA translocation through Al₂O₃ sputtered silicon nanopores in porous membrane. *Applied Physics A* **2016**, *122* (3), 216.
302. Tenenbaum, E.; Ben-Dov, N.; Segal, E., Tethered Lipid Bilayers within Porous Si Nanostructures: A Platform for (Optical) Real-Time Monitoring of Membrane-Associated Processes. *Langmuir* **2015**, *31* (18), 5244-5251.
303. Doyle, S. A.; Murphy, M. B. *Aptamers and methods for their in vitro selection and uses thereof*; Lawrence Berkeley National Laboratory (LBNL), Berkeley, CA (United States): 2008.
304. Wu, J.; Wang, C.; Li, X.; Song, Y.; Wang, W.; Li, C.; Hu, J.; Zhu, Z.; Li, J.; Zhang, W.; Lu, Z.; Yang, C. J., Identification, Characterization and Application of a G-Quadruplex Structured DNA Aptamer against Cancer Biomarker Protein Anterior Gradient Homolog 2. *PLOS ONE* **2012**, *7* (9), e46393.
305. Stoltenburg, R.; Schubert, T.; Strehlitz, B., In vitro Selection and Interaction Studies of a DNA Aptamer Targeting Protein A. *PloS one* **2015**, *10* (7), e0134403-e0134403.
306. Kökpınar, Ö.; Walter, J.-G.; Shoham, Y.; Stahl, F.; Scheper, T., Aptamer-based downstream processing of his-tagged proteins utilizing magnetic beads. *Biotechnology and Bioengineering* **2011**, *108* (10), 2371-2379.
307. Nieba, L.; Krebber, A.; Plückthun, A., Competition BIAcore for Measuring True Affinities: Large Differences from Values Determined from Binding Kinetics. *Analytical Biochemistry* **1996**, *234* (2), 155-165.
308. Kim, D.; Herr, A. E., Protein immobilization techniques for microfluidic assays. *Biomicrofluidics* **2013**, *7* (4), 041501.
309. Siller, I. G.; Enders, A.; Steinwedel, T.; Epping, N.-M.; Kirsch, M.; Lavrentieva, A.; Scheper, T.; Bahnemann, J., Real-Time Live-Cell Imaging Technology Enables High-Throughput Screening to Verify in Vitro Biocompatibility of 3D Printed Materials. *Materials* **2019**, *12* (13), 2125.
310. Gerber, D.; Maerkl, S. J.; Quake, S. R., An in vitro microfluidic approach to generating protein-interaction networks. *Nat Meth* **2009**, *6* (1), 71-74.
311. Minekus, M.; Alving, M.; Alvito, P.; Ballance, S.; Bohn, T.; Bourlieu, C.; Carriere, F.; Boutrou, R.; Corredig, M.; Dupont, D.; Dufour, C.; Egger, L.; Golding, M.; Karakaya, S.; Kirkhus, B.; Le Feunteun, S.; Lesmes, U.; Macierzanka, A.; Mackie, A.; Marze, S.; McClements, D. J.; Menard, O.; Recio, I.; Santos, C. N.; Singh, R. P.; Vegarud, G. E.; Wickham, M. S. J.; Weitschies, W.; Brodkorb, A., A standardised static in vitro digestion method suitable for food - an international consensus. *Food & Function* **2014**, *5* (6), 1113-1124.
312. Bergmeyer, H., *Methods of Enzymatic Analysis*, Ed. 2, Vol. 1. *Academic, New York, NY* **1974**, 515-516.
313. Laemmli, U. K., Cleavage of Structural Proteins during the Assembly of the Head of Bacteriophage T4. *Nature* **1970**, *227* (5259), 680-685.
314. Kurganov, B. I.; Lobanov, A. V.; Borisov, I. A.; Reshetilov, A. N., Criterion for Hill equation validity for description of biosensor calibration curves. *Analytica Chimica Acta* **2001**, *427* (1), 11-19.
315. Hill, A. V., PROCEEDINGS OF THE PHYSIOLOGICAL SOCIETY: January 22, 1910. *The Journal of Physiology* **1910**, *40* (suppl), i-vii.
316. Crivianu-Gaita, V.; Thompson, M., Aptamers, antibody scFv, and antibody Fab' fragments: An overview and comparison of three of the most versatile biosensor biorecognition elements. *Biosens Bioelectron* **2016**, *85*, 32-45.
317. Srivastava, M.; Nirala, N. R.; Srivastava, S. K.; Prakash, R., A comparative Study of Aptasensor Vs Immunosensor for Label-Free PSA Cancer Detection on GQDs-AuNRs Modified Screen-Printed Electrodes. *Scientific Reports* **2018**, *8* (1), 1923.
318. Song, S.; Wang, L.; Li, J.; Fan, C.; Zhao, J., Aptamer-based biosensors. *Trends in Analytical Chemistry* **2008**, *27* (2), 108-117.
319. Bunka, D. H. J.; Stockley, P. G., Aptamers come of age - at last. *Nat. Rev. Microbiol.* **2006**, *4* (8), 588-596.

320. Liss, M.; Petersen, B.; Wolf, H.; Prohaska, E., An Aptamer-Based Quartz Crystal Protein Biosensor. *Analytical Chemistry* **2002**, *74* (17), 4488-4495.
321. Hianik, T.; Wang, J., Electrochemical Aptasensors – Recent Achievements and Perspectives. *Electroanalysis* **2009**, *21* (11), 1223-1235.
322. Duan, N.; Wu, S. J.; Dai, S. L.; Gu, H. J.; Hao, L. L.; Ye, H.; Wang, Z. P., Advances in aptasensors for the detection of food contaminants. *Analyst* **2016**, *141* (13), 3942-3961.
323. Ding, S.; Mosher, C.; Lee, X. Y.; Das, S. R.; Cargill, A. A.; Tang, X.; Chen, B.; McLamore, E. S.; Gomes, C.; Hostetter, J. M.; Claussen, J. C., Rapid and Label-Free Detection of Interferon Gamma via an Electrochemical Aptasensor Comprising a Ternary Surface Monolayer on a Gold Interdigitated Electrode Array. *ACS Sensors* **2017**, *2* (2), 210-217.
324. Labib, M.; Sargent, E. H.; Kelley, S. O., Electrochemical Methods for the Analysis of Clinically Relevant Biomolecules. *Chemical Reviews* **2016**, *116* (16), 9001-9090.
325. Conroy, P. J.; Hearty, S.; Leonard, P.; O'Kennedy, R. J., Antibody production, design and use for biosensor-based applications. *Seminars in cell & developmental biology* **2009**, *20* (1), 10-26.
326. Zhang, X.; Sun, M.; Kang, Y.; Xie, H.; Wang, X.; Song, H.; Li, X.; Fang, W., Identification of a high-affinity monoclonal antibody against ochratoxin A and its application in enzyme-linked immunosorbent assay. *Toxicon* **2015**, *106*, 89-96.
327. Modh, H.; Scheper, T.; Walter, J. G., Detection of ochratoxin A by aptamer-assisted real-time PCR-based assay (Apta-qPCR). *Eng Life Sci* **2017**, *17* (8), 923-930.
328. Hianik, T., Affinity Biosensors for Detection Immunoglobulin E and Cellular Prions. Antibodies vs. DNA Aptamers. *Electroanalysis* **2016**, *28* (8), 1764-1776.
329. Schlecht, U.; Malavé, A.; Gronewold, T.; Tewes, M.; Löhndorf, M., Comparison of antibody and aptamer receptors for the specific detection of thrombin with a nanometer gap-sized impedance biosensor. *Analytica Chimica Acta* **2006**, *573-574*, 65-68.
330. Massad-Ivanir, N.; Shtenberg, G.; Zeidman, T.; Segal, E., Construction and Characterization of Porous SiO₂/Hydrogel Hybrids as Optical Biosensors for Rapid Detection of Bacteria. *Advanced Functional Materials* **2010**, *20* (14), 2269-2277.
331. Dancil, K. P. S.; Greiner, D. P.; Sailor, M. J., A porous silicon optical biosensor: Detection of reversible binding of IgG to a protein A-modified surface. *Journal of the American Chemical Society* **1999**, *121* (34), 7925-7930.
332. Tieu, T.; Alba, M.; Elnathan, R.; Cifuentes-Rius, A.; Voelcker, N. H., Advances in Porous Silicon-Based Nanomaterials for Diagnostic and Therapeutic Applications. *Advanced Therapeutics* **2019**, *2* (1), 1800095.
333. Zhu, G.; Lübbecke, M.; Walter, J. G.; Stahl, F.; Scheper, T., Characterization of Optimal Aptamer-Microarray Binding Chemistry and Spacer Design. *Chemical Engineering & Technology* **2011**, *34* (12), 2022-2028.
334. Walter, J.-G.; Kökpinar, Ö.; Friehs, K.; Stahl, F.; Scheper, T., Systematic Investigation of Optimal Aptamer Immobilization for Protein-Microarray Applications. *Analytical Chemistry* **2008**, *80* (19), 7372-7378.
335. Sasakura, Y.; Kanda, K.; Yoshimura-Suzuki, T.; Matsui, T.; Fukuzono, S.; Han, M. H.; Shimizu, T., Protein Microarray System for Detecting Protein-Protein Interactions Using an Anti-His-Tag Antibody and Fluorescence Scanning: Effects of the Heme Redox State on Protein-Protein Interactions of Heme-Regulated Phosphodiesterase from *Escherichia coli*. *Analytical Chemistry* **2004**, *76* (22), 6521-6527.
336. Meier, M.; Patel, T. R.; Booy, E. P.; Marushchak, O.; Okun, N.; Deo, S.; Howard, R.; McEleney, K.; Harding, S. E.; Stetefeld, J.; McKenna, S. A., Binding of G-quadruplexes to the N-terminal Recognition Domain of the RNA Helicase Associated with AU-rich Element (RHAU). *Journal of Biological Chemistry* **2013**, *288* (49), 35014-35027.
337. Zentgraf, H.; Frey, M.; Schwinn, S.; Tessmer, C.; Willemann, B.; Samstag, Y.; Velhagen, I., Detection of histidine-tagged fusion proteins by using a high-specific mouse monoclonal anti-histidine tag antibody. *Nucleic acids research* **1995**, *23* (16), 3347-3348.
338. Cortez-Retamozo, V.; Lauwereys, M.; Hassanzadeh Gh., G.; Gobert, M.; Conrath, K.; Muyldermans, S.; De Baetselier, P.; Revets, H., Efficient tumor targeting by single-domain antibody fragments of camels. *International Journal of Cancer* **2002**, *98* (3), 456-462.
339. Alvarez, M. M.; López-Pacheco, F.; Aguilar-Yañez, J. M.; Portillo-Lara, R.; Mendoza-Ochoa, G. I.; García-Echauri, S.; Freiden, P.; Schultz-Cherry, S.; Zertuche-Guerra, M. I.; Bulnes-Abundis, D.; Salgado-Gallegos, J.; Elizondo-Montemayor, L.; Hernández-Torre, M., Specific Recognition of Influenza A/H1N1/2009 Antibodies in Human Serum: A Simple Virus-Free ELISA Method. *PLOS ONE* **2010**, *5* (4), e10176.
340. Els Conrath, K.; Lauwereys, M.; Wyns, L.; Muyldermans, S., Camel Single-domain Antibodies as Modular Building Units in Bispecific and Bivalent Antibody Constructs. *Journal of Biological Chemistry* **2001**, *276* (10), 7346-7350.

341. Massad-Ivanir, N.; Friedman, T.; Nahor, A.; Eichler, S.; Bonanno, L. M.; Sa'ar, A.; Segal, E., Hydrogels synthesized in electrochemically machined porous Si hosts: effect of nano-scale confinement on polymer properties. *Soft Matter* **2012**, *8* (35), 9166-9176.
342. Drake, A. W.; Klakamp, S. L., A strategic and systematic approach for the determination of biosensor regeneration conditions. *Journal of Immunological Methods* **2011**, *371* (1), 165-169.
343. Goode, J. A.; Rushworth, J. V. H.; Millner, P. A., Biosensor Regeneration: A Review of Common Techniques and Outcomes. *Langmuir* **2015**, *31* (23), 6267-6276.
344. Limbut, W.; Kanatharana, P.; Mattiasson, B.; Asawatreratanakul, P.; Thavarungkul, P., A reusable capacitive immunosensor for carcinoembryonic antigen (CEA) detection using thiourea modified gold electrode. *Analytica Chimica Acta* **2006**, *561* (1), 55-61.
345. March, C.; Manclús, J. J.; Jiménez, Y.; Arnau, A.; Montoya, A., A piezoelectric immunosensor for the determination of pesticide residues and metabolites in fruit juices. *Talanta* **2009**, *78* (3), 827-833.
346. Kandimalla, V. B.; Neeta, N. S.; Karanth, N. G.; Thakur, M. S.; Roshini, K. R.; Rani, B. E. A.; Pasha, A.; Karanth, N. G. K., Regeneration of ethyl parathion antibodies for repeated use in immunosensor: a study on dissociation of antigens from antibodies. *Biosensors and Bioelectronics* **2004**, *20* (4), 903-906.
347. Mattos, A. B.; Freitas, T. A.; Silva, V. L.; Dutra, R. F., A dual quartz crystal microbalance for human cardiac troponin T in real time detection. *Sensors and Actuators B: Chemical* **2012**, *161* (1), 439-446.
348. Kim, J.; Cho, J.; Seidler, P. M.; Kurland, N. E.; Yadavalli, V. K., Investigations of Chemical Modifications of Amino-Terminated Organic Films on Silicon Substrates and Controlled Protein Immobilization. *Langmuir* **2010**, *26* (4), 2599-2608.
349. Socrates, G., *Infrared and Raman characteristic group frequencies: tables and charts*. John Wiley & Sons: 2004.
350. Movilli, J.; Rozzi, A.; Ricciardi, R.; Corradini, R.; Huskens, J., Control of Probe Density at DNA Biosensor Surfaces Using Poly(l-lysine) with Appended Reactive Groups. *Bioconjugate Chemistry* **2018**, *29* (12), 4110-4118.
351. Urmann, K.; Modrejewski, J.; Scheper, T.; Walter, J. G., Aptamer-modified nanomaterials: principles and applications. *BioNanoMaterials* **2016**, *18* (1-2), 20160012.
352. Peterson, A. W.; Heaton, R. J.; Georgiadis, R. M., The effect of surface probe density on DNA hybridization. *Nucleic Acids Research* **2001**, *29* (24), 5163-5168.
353. Rousseaux, J.; Rousseaux-Prévost, R.; Bazin, H., Optimal conditions for the preparation of Fab and F(ab')₂ fragments from monoclonal IgG of different rat IgG subclasses. *Journal of Immunological Methods* **1983**, *64* (1), 141-146.
354. Strehlitz, B.; Nikolaus, N.; Stoltenburg, R., Protein Detection with Aptamer Biosensors. *Sensors (Basel)* **2008**, *8* (7), 4296-4307.
355. Chen, A.; Yang, S., Replacing antibodies with aptamers in lateral flow immunoassay. *Biosensors and Bioelectronics* **2015**, *71*, 230-242.
356. Hopkins, N. A. E., Antibody engineering for Biosensor Applications. In *Recognition Receptors in Biosensors*, Zourob, M., Ed. Springer: New York Dordrecht Heidelberg London, 2010; pp 451-529.
357. Hermanson, G. T., *Bioconjugate Techniques* 1st edition ed.; Academic Press: 1996.
358. Wild, D., *The Immunoassay Handbook: Theory and Applications of Ligand Binding, ELISA and Related Techniques*. Elsevier Science: 2013.
359. Haake, H.-M.; Schütz, A.; Gauglitz, G., Label-free detection of biomolecular interaction by optical sensors. *Fresenius' Journal of Analytical Chemistry* **2000**, *366* (6), 576-585.
360. Jung, Y.; Jeong, J. Y.; Chung, B. H., Recent advances in immobilization methods of antibodies on solid supports. *Analyst* **2008**, *133* (6), 697-701.
361. Trilling, A. K.; Beekwilder, J.; Zuilhof, H., Antibody orientation on biosensor surfaces: a minireview. *Analyst* **2013**, *138* (6), 1619-1627.
362. Song, H. Y.; Zhou, X.; Hogley, J.; Su, X., Comparative Study of Random and Oriented Antibody Immobilization as Measured by Dual Polarization Interferometry and Surface Plasmon Resonance Spectroscopy. *Langmuir* **2012**, *28* (1), 997-1004.
363. Gauglitz, G., Point-of-Care Platforms. *Annual Review of Analytical Chemistry* **2014**, *7* (1), 297-315.
364. Kausaite-Minkstimiene, A.; Ramanaviciene, A.; Kirlyte, J.; Ramanavicius, A., Comparative Study of Random and Oriented Antibody Immobilization Techniques on the Binding Capacity of Immunosensor. *Analytical Chemistry* **2010**, *82* (15), 6401-6408.
365. Neumann, O.; Zhang, D.; Tam, F.; Lal, S.; Wittung-Stafshede, P.; Halas, N. J., Direct Optical Detection of Aptamer Conformational Changes Induced by Target Molecules. *Analytical Chemistry* **2009**, *81* (24), 10002-10006.
366. Radi, A.-E.; O'Sullivan, C. K., Aptamer conformational switch as sensitive electrochemical biosensor for potassium ion recognition. *Chem. Commun.* **2006**, (32), 3432-3434.

367. Lee, J.-O.; So, H.-M.; Jeon, E.-K.; Chang, H.; Won, K.; Kim, Y. H., Aptamers as molecular recognition elements for electrical nanobiosensors. *Analytical and Bioanalytical Chemistry* **2008**, *390* (4), 1023-1032.
368. Cheung, R. C. F.; Wong, J. H.; Ng, T. B., Immobilized metal ion affinity chromatography: a review on its applications. *Applied Microbiology and Biotechnology* **2012**, *96* (6), 1411-1420.
369. Walter, J.-G.; Stahl, F.; Scheper, T., Aptamers as affinity ligands for downstream processing. *Eng Life Sci* **2012**, *12* (5), 496-506.
370. Anderson, G. P.; Jacoby, M. A.; Ligler, F. S.; King, K. D., Effectiveness of protein A for antibody immobilization for a fiber optic biosensor. *Biosensors and Bioelectronics* **1997**, *12* (4), 329-336.
371. Schuck, P.; Minton, A. P., Analysis of Mass Transport-Limited Binding Kinetics in Evanescent Wave Biosensors. *Analytical Biochemistry* **1996**, *240* (2), 262-272.
372. Nair, P. R.; Alam, M. A., Performance limits of nanobiosensors. *Applied Physics Letters* **2006**, *88* (23), 233120.
373. Sheehan, P. E.; Whitman, L. J., Detection Limits for Nanoscale Biosensors. *Nano Letters* **2005**, *5* (4), 803-807.
374. Schuck, P., Kinetics of ligand binding to receptor immobilized in a polymer matrix, as detected with an evanescent wave biosensor. I. A computer simulation of the influence of mass transport. *Biophysical Journal* **1996**, *70* (3), 1230-1249.
375. O'Shannessy, D. J.; Winzor, D. J., Interpretation of Deviations from Pseudo-First-Order Kinetic Behavior in the Characterization of Ligand Binding by Biosensor Technology. *Analytical Biochemistry* **1996**, *236* (2), 275-283.
376. Hu, G.; Gao, Y.; Li, D., Modeling micropatterned antigen-antibody binding kinetics in a microfluidic chip. *Biosensors and Bioelectronics* **2007**, *22* (7), 1403-1409.
377. Zhu, W.; Wang, C.; Wang, H.; Li, G., Theory and simulation of diffusion-adsorption into a molecularly imprinted mesoporous film and its nanostructured counterparts. Experimental application for trace explosive detection. *RSC Advances* **2014**, *4* (77), 40676-40685.
378. Kant, K.; Yu, J.; Priest, C.; Shapter, J. G.; Losic, D., Impedance nanopore biosensor: influence of pore dimensions on biosensing performance. *Analyst* **2014**, *139* (5), 1134-1140.
379. Lu, S.; Song, Z.; He, J., Diffusion-Controlled Protein Adsorption in Mesoporous Silica. *The Journal of Physical Chemistry B* **2011**, *115* (24), 7744-7750.
380. DeLouise, L. A.; Miller, B. L., Quantitative Assessment of Enzyme Immobilization Capacity in Porous Silicon. *Analytical Chemistry* **2004**, *76* (23), 6915-6920.
381. Macias, G.; Ferré-Borrull, J.; Pallarès, J.; Marsal, L. F., Effect of pore diameter in nanoporous anodic alumina optical biosensors. *Analyst* **2015**, *140* (14), 4848-4854.
382. Kumeria, T.; Losic, D., Controlling interferometric properties of nanoporous anodic aluminium oxide. *Nanoscale Research Letters* **2012**, *7* (1), 88.
383. Tinsley-Bown, A. M.; Canham, L. T.; Hollings, M.; Anderson, M. H.; Reeves, C. L.; Cox, T. I.; Nicklin, S.; Squirrell, D. J.; Perkins, E.; Hutchinson, A.; Sailor, M. J.; Wun, A., Tuning the Pore Size and Surface Chemistry of Porous Silicon for Immunoassays. *physica status solidi (a)* **2000**, *182* (1), 547-553.
384. Martin, F.; Walczak, R.; Boiarski, A.; Cohen, M.; West, T.; Cosentino, C.; Ferrari, M., Tailoring width of microfabricated nanochannels to solute size can be used to control diffusion kinetics. *Journal of Controlled Release* **2005**, *102* (1), 123-133.
385. Bouchaud, J.-P.; Georges, A., Anomalous diffusion in disordered media: Statistical mechanisms, models and physical applications. *Physics Reports* **1990**, *195* (4), 127-293.
386. Renkin, E. M., FILTRATION, DIFFUSION, AND MOLECULAR SIEVING THROUGH POROUS CELLULOSE MEMBRANES. *The Journal of General Physiology* **1954**, *38* (2), 225-243.
387. Krishna, R., Describing the Diffusion of Guest Molecules Inside Porous Structures. *The Journal of Physical Chemistry C* **2009**, *113* (46), 19756-19781.
388. Satterfield, C. N.; Colton, C. K.; Pitcher Jr., W. H., Restricted diffusion in liquids within fine pores. *AIChE Journal* **1973**, *19* (3), 628-635.
389. Saltzman, W. M.; Langer, R., Transport rates of proteins in porous materials with known microgeometry. *Biophysical Journal* **1989**, *55* (1), 163-171.
390. Deen, W. M., Hindered transport of large molecules in liquid-filled pores. *AIChE Journal* **1987**, *33* (9), 1409-1425.
391. Mares, J. W.; Weiss, S. M., Diffusion dynamics of small molecules from mesoporous silicon films by real-time optical interferometry. *Appl. Opt.* **2011**, *50* (27), 5329-5337.
392. Zürner, A.; Kirstein, J.; Döblinger, M.; Bräuchle, C.; Bein, T., Visualizing single-molecule diffusion in mesoporous materials. *Nature* **2007**, *450* (7170), 705-708.
393. Rühle, B.; Davies, M.; Lebold, T.; Bräuchle, C.; Bein, T., Highly Oriented Mesoporous Silica Channels Synthesized in Microgrooves and Visualized with Single-Molecule Diffusion. *ACS Nano* **2012**, *6* (3), 1948-1960.

394. Dechadilok, P.; Deen, W. M., Hindrance Factors for Diffusion and Convection in Pores. *Industrial & Engineering Chemistry Research* **2006**, *45* (21), 6953-6959.
395. Marbán, G.; Ramírez-Montoya, L. A.; García, H.; Menéndez, J. Á.; Arenillas, A.; Montes-Morán, M. A., Load-dependent surface diffusion model for analyzing the kinetics of protein adsorption onto mesoporous materials. *Journal of Colloid and Interface Science* **2018**, *511*, 27-38.
396. Lazzara, T. D.; Mey, I.; Steinem, C.; Janshoff, A., Benefits and Limitations of Porous Substrates as Biosensors for Protein Adsorption. *Analytical Chemistry* **2011**, *83* (14), 5624-5630.
397. Wu, C.; Rong, G.; Xu, J.; Pan, S.; Zhu, Y., Physical analysis of the response properties of porous silicon microcavity biosensor. *Physica E: Low-dimensional Systems and Nanostructures* **2012**, *44* (7), 1787-1791.
398. Tyn, M. T.; Gusek, T. W., Prediction of diffusion coefficients of proteins. *Biotechnology and Bioengineering* **1990**, *35* (4), 327-338.
399. Sikavitsas, V.; Nitsche, J. M.; Mountziaris, T. J., Transport and Kinetic Processes Underlying Biomolecular Interactions in the BIACORE Optical Biosensor. *Biotechnology Progress* **2002**, *18* (4), 885-897.
400. Morton, T. A.; Myszka, D. G., Kinetic analysis of macromolecular interactions using surface plasmon resonance biosensors. In *Methods in Enzymology*, Academic Press: 1998; Vol. 295, pp 268-294.
401. Karlsson, R.; Michaelsson, A.; Mattsson, L., Kinetic analysis of monoclonal antibody-antigen interactions with a new biosensor based analytical system. *Journal of Immunological Methods* **1991**, *145* (1), 229-240.
402. Shtenberg, G.; Segal, E., Porous Silicon Optical Biosensors. In *Handbook of Porous Silicon*, Canham, L., Ed. Springer International Publishing: Cham, 2014; pp 857-868.
403. Weiss, S. M.; Rong, G.; Lawrie, J. L., Current status and outlook for silicon-based optical biosensors. *Physica E: Low-dimensional Systems and Nanostructures* **2009**, *41* (6), 1071-1075.
404. Snow, P. A.; Squire, E. K.; Russell, P. S. J.; Canham, L. T., Vapor sensing using the optical properties of porous silicon Bragg mirrors. *Journal of Applied Physics* **1999**, *86* (4), 1781-1784.
405. Cunin, F.; Schmedake, T. A.; Link, J. R.; Li, Y. Y.; Koh, J.; Bhatia, S. N.; Sailor, M. J., Biomolecular screening with encoded porous-silicon photonic crystals. *Nat Mater* **2002**, *1* (1), 39-41.
406. Ouyang, H.; Christophersen, M.; Viard, R.; Miller, B. L.; Fauchet, P. M., Macroporous Silicon Microcavities for Macromolecule Detection. *Advanced Functional Materials* **2005**, *15* (11), 1851-1859.
407. Chan, S.; Fauchet, P.; Li, Y.; Rothberg, L.; Miller, B., Porous silicon microcavities for biosensing applications. *physica status solidi (a)* **2000**, *182* (1), 541-546.
408. Massad-Ivanir, N.; Mirsky, Y.; Nahor, A.; Edrei, E.; Bonanno-Young, L. M.; Ben Dov, N.; Sa'ar, A.; Segal, E., Trap and track: designing self-reporting porous Si photonic crystals for rapid bacteria detection. *Analyst* **2014**, *139* (16), 3885-3894.
409. Karsenty, M.; Rubin, S.; Bercovici, M., Acceleration of Surface-Based Hybridization Reactions Using Isotachophoretic Focusing. *Analytical Chemistry* **2014**, *86* (6), 3028-3036.
410. Han, C. M.; Katilius, E.; Santiago, J. G., Increasing hybridization rate and sensitivity of DNA microarrays using isotachopheresis. *Lab on a Chip* **2014**, *14* (16), 2958-2967.
411. Moghadam, B. Y.; Connelly, K. T.; Posner, J. D., Two Orders of Magnitude Improvement in Detection Limit of Lateral Flow Assays Using Isotachopheresis. *Analytical Chemistry* **2015**, *87* (2), 1009-1017.
412. Malá, Z.; Gebauer, P.; Boček, P., Recent progress in analytical capillary isotachopheresis. *Electrophoresis* **2015**, *36* (1), 2-14.
413. Malá, Z.; Gebauer, P.; Boček, P., Analytical capillary isotachopheresis after 50 years of development: Recent progress 2014–2016. *Electrophoresis* **2017**, *38* (1), 9-19.
414. Jung, B.; Bharadwaj, R.; Santiago, J. G., On-chip millionfold sample stacking using transient isotachopheresis. *Anal Chem* **2006**, *78* (7), 2319-27.
415. Everaerts, F.; Beckers, J.; Verheggen, T., *Isotachopheresis: Theory, Instrumentation and Practice*. Elsevier: New York: 2011.
416. GanOr, N.; Rubin, S.; Bercovici, M., Diffusion dependent focusing regimes in peak mode counterflow isotachopheresis. *Physics of Fluids* **2015**, *27* (7), 072003.
417. Chen, S.; Shamsi, M. H., Biosensors-on-chip: a topical review. *Journal of Micromechanics and Microengineering* **2017**, *27* (8), 083001.
418. Zhong, Q.; Ding, H.; Gao, B.; He, Z.; Gu, Z., Advances of Microfluidics in Biomedical Engineering. *Advanced Materials Technologies* **2019**, *4* (6), 1800663.
419. Walsh, D. I.; Kong, D. S.; Murthy, S. K.; Carr, P. A., Enabling Microfluidics: from Clean Rooms to Makerspaces. *Trends in Biotechnology* **2017**, *35* (5), 383-392.
420. Nielsen, A. V.; Beauchamp, M. J.; Nordin, G. P.; Woolley, A. T., 3D Printed Microfluidics. *Annual Review of Analytical Chemistry* **2020**, *13* (1), 45-65.
421. Macdonald, N. P.; Cabot, J. M.; Smejkal, P.; Guijt, R. M.; Paull, B.; Breadmore, M. C., Comparing Microfluidic Performance of Three-Dimensional (3D) Printing Platforms. *Analytical Chemistry* **2017**, *89* (7), 3858-3866.

422. Arayanarakool, R.; Le Gac, S.; van den Berg, A., Low-temperature, simple and fast integration technique of microfluidic chips by using a UV-curable adhesive. *Lab on a Chip* **2010**, *10* (16), 2115-2121.
423. Temiz, Y.; Lovchik, R. D.; Kaigala, G. V.; Delamar, E., Lab-on-a-chip devices: How to close and plug the lab? *Microelectronic Engineering* **2015**, *132*, 156-175.
424. Langelier, S. M.; Yeo, L. Y.; Friend, J., UV epoxy bonding for enhanced SAW transmission and microscale acoustofluidic integration. *Lab on a Chip* **2012**, *12* (16), 2970-2976.
425. Lu, C.; Lee, L. J.; Juang, Y.-J., Packaging of microfluidic chips via interstitial bonding technique. *ELECTROPHORESIS* **2008**, *29* (7), 1407-1414.
426. Chen, P.-C.; Liu, Y.-M.; Chou, H.-C., An adhesive bonding method with microfabricating micro pillars to prevent clogging in a microchannel. *Journal of Micromechanics and Microengineering* **2016**, *26* (4), 045003.
427. Satyanarayana, S.; Karnik, R. N.; Majumdar, A., Stamp-and-stick room-temperature bonding technique for microdevices. *Journal of Microelectromechanical Systems* **2005**, *14* (2), 392-399.
428. Schlautmann, S.; Besselink, G. A. J.; Prabhu, G. R.; Schasfoort, R. B. M., Fabrication of a microfluidic chip by UV bonding at room temperature for integration of temperature-sensitive layers. *Journal of Micromechanics and Microengineering* **2003**, *13* (4), S81-S84.
429. Chen, P.-C.; Chen, C.-C., Addition of structural features and two-step adhesive bond method to improve bonding quality of thermoplastic microfiltration chip. *Sensors and Actuators A: Physical* **2017**, *258*, 105-114.
430. Carroll, S.; Crain, M. M.; Naber, J. F.; Keynton, R. S.; Walsh, K. M.; Baldwin, R. P., Room temperature UV adhesive bonding of CE devices. *Lab on a Chip* **2008**, *8* (9), 1564-1569.
431. Fraser, L. A.; Kinghorn, A. B.; Dirkzwager, R. M.; Liang, S.; Cheung, Y.-W.; Lim, B.; Shiu, S. C.-C.; Tang, M. S. L.; Andrew, D.; Manitta, J.; Richards, J. S.; Tanner, J. A., A portable microfluidic Aptamer-Tethered Enzyme Capture (APTEC) biosensor for malaria diagnosis. *Biosensors and Bioelectronics* **2018**, *100*, 591-596.
432. Chiadò, A.; Palmara, G.; Chiappone, A.; Tanzanu, C.; Pirri, C. F.; Roppolo, I.; Frascella, F., A modular 3D printed lab-on-a-chip for early cancer detection. *Lab on a Chip* **2020**, *20* (3), 665-674.
433. Siller, I. G.; Preuss, J.-A.; Urmann, K.; Hoffmann, M. R.; Scheper, T.; Bahnemann, J., 3D-Printed Flow Cells for Aptamer-Based Impedimetric Detection of E. coli Crooks Strain. *Sensors* **2020**, *20* (16), 4421.
434. Yu, N.; Wu, J., Rapid and reagentless detection of thrombin in clinic samples via microfluidic aptasensors with multiple target-binding sites. *Biosensors and Bioelectronics* **2019**, *146*, 111726.
435. Arshavsky-Graham, S.; Urmann, K.; Salama, R.; Massad-Ivanir, N.; Walter, J.-G.; Scheper, T.; Segal, E., Aptamers vs. antibodies as capture probes in optical porous silicon biosensors. *Analyst* **2020**, *145* (14), 4991-5003.
436. Preuss, J.-A.; Nguyen, G. N.; Berk, V.; Bahnemann, J., Miniaturized free-flow electrophoresis – production, optimization and application using 3D printing technology. *ELECTROPHORESIS n/a* (n/a).
437. Massad-Ivanir, N.; Shtenberg, G.; Tzur, A.; Krepker, M. A.; Segal, E., Engineering Nanostructured Porous SiO₂ Surfaces for Bacteria Detection via “Direct Cell Capture”. *Analytical Chemistry* **2011**, *83* (9), 3282-3289.
438. Setlow, R. B.; Swenson, P. A.; Carrier, W. L., Thymine Dimers and Inhibition of DNA Synthesis by Ultraviolet Irradiation of Cells. *Science* **1963**, *142* (3598), 1464-1466.
439. Pasquardini, L.; Potrich, C.; Quaglio, M.; Lamberti, A.; Guastella, S.; Lunelli, L.; Cocuzza, M.; Vanzetti, L.; Pirri, C. F.; Pederzoli, C., Solid phase DNA extraction on PDMS and direct amplification. *Lab on a Chip* **2011**, *11* (23), 4029-4035.
440. Weisgrab, G.; Ovsianikov, A.; Costa, P. F., Functional 3D Printing for Microfluidic Chips. *Advanced Materials Technologies* **2019**, *4* (10), 1900275.
441. Urmann, K.; Reich, P.; Walter, J.-G.; Beckmann, D.; Segal, E.; Scheper, T., Rapid and label-free detection of protein a by aptamer-tethered porous silicon nanostructures. *Journal of Biotechnology* **2017**, *257*, 171-177.
442. Urmann, K.; Arshavsky-Graham, S.; Walter, J. G.; Scheper, T.; Segal, E., Whole-cell detection of live lactobacillus acidophilus on aptamer-decorated porous silicon biosensors. *Analyst* **2016**, *141* (18), 5432-5440.
443. Downs, A. M.; Gerson, J.; Hossain, M. N.; Ploense, K.; Pham, M.; Kraatz, H.-B.; Kippin, T.; Plaxco, K. W., Nanoporous Gold for the Miniaturization of In Vivo Electrochemical Aptamer-Based Sensors. *ACS Sensors* **2021**.
444. Borrebaeck, C. A. K., Precision diagnostics: moving towards protein biomarker signatures of clinical utility in cancer. *Nature Reviews Cancer* **2017**, *17* (3), 199-204.
445. Henry, N. L.; Hayes, D. F., Cancer biomarkers. *Molecular Oncology* **2012**, *6* (2), 140-146.
446. Edgell, Tracey A.; Barraclough, Dong L.; Rajic, A.; Dhulia, J.; Lewis, Kate J.; Armes, Jane E.; Barraclough, R.; Rudland, Philip S.; Rice, Gregory E.; Autelitano, Dominic J., Increased plasma concentrations of anterior gradient 2 protein are positively associated with ovarian cancer. *Clinical Science* **2010**, *118* (12), 717-725.

447. Tian, S.-b.; Tao, K.-x.; Hu, J.; Liu, Z.-b.; Ding, X.-l.; Chu, Y.-n.; Cui, J.-y.; Shuai, X.-m.; Gao, J.-b.; Cai, K.-l.; Wang, J.-l.; Wang, G.-b.; Wang, L.; Wang, Z., The prognostic value of AGR2 expression in solid tumours: a systematic review and meta-analysis. *Scientific Reports* **2017**, *7* (1), 15500.
448. LUU, T.-T.-T.; BACH, D.-H.; KIM, D.; HU, R.; PARK, H. J.; LEE, S. K., Overexpression of AGR2 Is Associated With Drug Resistance in Mutant Non-small Cell Lung Cancers. *Anticancer Research* **2020**, *40* (4), 1855-1866.
449. Ondrouskova, E.; Sommerova, L.; Nenutil, R.; Coufal, O.; Bouchal, P.; Vojtesek, B.; Hrstka, R., AGR2 associates with HER2 expression predicting poor outcome in subset of estrogen receptor negative breast cancer patients. *Experimental and Molecular Pathology* **2017**, *102* (2), 280-283.
450. Rodríguez-Blanco, G.; Zeneyedpour, L.; Duijvesz, D.; Hoogland, A. M.; Verhoef, E. I.; Kweldam, C. F.; Burgers, P. C.; Smitt, P. S.; Bangma, C. H.; Jenster, G.; van Leenders, G. J. L. H.; Dekker, L. J. M.; Luiders, T. M., Tissue proteomics outlines AGR2 AND LOX5 as markers for biochemical recurrence of prostate cancer. *Oncotarget* **2018**, *9* (92), 36444-36456.
451. Tian, S.; Hu, J.; Tao, K.; Wang, J.; Chu, Y.; Li, J.; Liu, Z.; Ding, X.; Xu, L.; Li, Q.; Cai, M.; Gao, J.; Shuai, X.; Wang, G.; Wang, L.; Wang, Z., Secreted AGR2 promotes invasion of colorectal cancer cells via Wnt11-mediated non-canonical Wnt signaling. *Experimental Cell Research* **2018**, *364* (2), 198-207.
452. Dumartin, L.; Alrawashdeh, W.; Trabulo, S. M.; Radon, T. P.; Steiger, K.; Feakins, R. M.; di Magliano, M. P.; Heeschen, C.; Esposito, I.; Lemoine, N. R.; Crnogorac-Jurcevic, T., ER stress protein AGR2 precedes and is involved in the regulation of pancreatic cancer initiation. *Oncogene* **2016**, *36*, 3094.
453. Chen, R.; Pan, S.; Duan, X.; Nelson, B. H.; Sahota, R. A.; de Rham, S.; Kozarek, R. A.; McIntosh, M.; Brentnall, T. A., Elevated level of anterior gradient-2 in pancreatic juice from patients with pre-malignant pancreatic neoplasia. *Molecular Cancer* **2010**, *9* (1), 149.
454. Lennon, A. M.; Wolfgang, C. L.; Canto, M. I.; Klein, A. P.; Herman, J. M.; Goggins, M.; Fishman, E. K.; Kamel, I.; Weiss, M. J.; Diaz, L. A.; Papadopoulos, N.; Kinzler, K. W.; Vogelstein, B.; Hruban, R. H., The Early Detection of Pancreatic Cancer: What Will It Take to Diagnose and Treat Curable Pancreatic Neoplasia? *Cancer Research* **2014**, *74* (13), 3381-3389.
455. Wayner, E. A.; Quek, S.-I.; Ahmad, R.; Ho, M. E.; Loprieno, M. A.; Zhou, Y.; Ellis, W. J.; True, L. D.; Liu, A. Y., Development of an ELISA to detect the secreted prostate cancer biomarker AGR2 in voided urine. *The Prostate* **2012**, *72* (9), 1023-1034.
456. Shi, T.; Gao, Y.; Quek, S. I.; Fillmore, T. L.; Nicora, C. D.; Su, D.; Zhao, R.; Kagan, J.; Srivastava, S.; Rodland, K. D.; Liu, T.; Smith, R. D.; Chan, D. W.; Camp, D. G.; Liu, A. Y.; Qian, W.-J., A Highly Sensitive Targeted Mass Spectrometric Assay for Quantification of AGR2 Protein in Human Urine and Serum. *Journal of Proteome Research* **2014**, *13* (2), 875-882.
457. Hu, Y.; Li, L.; Guo, L., The sandwich-type aptasensor based on gold nanoparticles/DNA/magnetic beads for detection of cancer biomarker protein AGR2. *Sensors and Actuators B: Chemical* **2015**, *209*, 846-852.
458. Li, Z.; Miao, X.; Cheng, Z.; Wang, P., Hybridization chain reaction coupled with the fluorescence quenching of gold nanoparticles for sensitive cancer protein detection. *Sensors and Actuators B: Chemical* **2017**, *243*, 731-737.
459. Moretta, R.; De Stefano, L.; Terracciano, M.; Rea, I., Porous Silicon Optical Devices: Recent Advances in Biosensing Applications. *Sensors* **2021**, *21* (4), 1336.
460. Baranowska, M.; Slota, A. J.; Eravuchira, P. J.; Alba, M.; Formentin, P.; Pallarès, J.; Ferré-Borrull, J.; Marsal, L. F., Protein attachment to silane-functionalized porous silicon: A comparison of electrostatic and covalent attachment. *Journal of Colloid and Interface Science* **2015**, *452*, 180-189.
461. Mariani, S.; Paggi, A.; La Mattina, A. A.; Debrassi, A.; Dähne, L.; Barillaro, G., Decoration of Porous Silicon with Gold Nanoparticles via Layer-by-Layer Nanoassembly for Interferometric and Hybrid Photonic/Plasmonic (Bio)sensing. *ACS Applied Materials & Interfaces* **2019**, *11* (46), 43731-43740.
462. Balderas-Valadez, R. F.; Schürmann, R.; Pacholski, C., One Spot—Two Sensors: Porous Silicon Interferometers in Combination With Gold Nanostructures Showing Localized Surface Plasmon Resonance. *Frontiers in Chemistry* **2019**, *7* (593).
463. Layouni, R.; Dubrovsky, M.; Bao, M.; Chung, H.; Du, K.; Boriskina, S. V.; Weiss, S. M.; Vermeulen, D., High contrast cleavage detection for enhancing porous silicon sensor sensitivity. *Opt. Express* **2021**, *29* (1), 1-11.
464. Arshavsky-Graham Sofia, M.-I. N., Paratore Federico, Scheper Thomas, Bercovici Moran, and Segal Ester On Chip Protein Pre-Concentration for Enhancing the Sensitivity of Porous Silicon Biosensors *ACS Sensors* **2017**, *2* (12), 1767-1773.
465. Ward, S. J.; Layouni, R.; Arshavsky-Graham, S.; Segal, E.; Weiss, S. M., Signal Processing Techniques to Reduce the Limit of Detection for Thin Film Biosensors. *arXiv preprint arXiv:2103.07524* **2021**.
466. Patel, P.; Clarke, C.; Barraclough, D. L.; Jowitt, T. A.; Rudland, P. S.; Barraclough, R.; Lian, L.-Y., Metastasis-Promoting Anterior Gradient 2 Protein Has a Dimeric Thioredoxin Fold Structure and a Role in Cell Adhesion. *Journal of Molecular Biology* **2013**, *425* (5), 929-943.

467. Urmann, K.; Modrejewski, J.; Scheper, T.; Walter Johanna, G., Aptamer-modified nanomaterials: principles and applications. In *BioNanoMaterials*, 2017; Vol. 18.
468. Voicu, R.; Boukherroub, R.; Bartzoka, V.; Ward, T.; Wojtyk, J. T. C.; Wayner, D. D. M., Formation, Characterization, and Chemistry of Undecanoic Acid-Terminated Silicon Surfaces: Patterning and Immobilization of DNA. *Langmuir* **2004**, *20* (26), 11713-11720.
469. Pol, L.; Acosta, L. K.; Ferré-Borrull, J.; Marsal, L. F., Aptamer-Based Nanoporous Anodic Alumina Interferometric Biosensor for Real-Time Thrombin Detection. *Sensors* **2019**, *19* (20), 4543.
470. Arshavsky Graham, S.; Boyko, E.; Salama, R.; Segal, E., Mass Transfer Limitations of Porous Silicon-Based Biosensors for Protein Detection. *ACS Sensors* **2020**, *5* (10), 3058-3069.
471. Makawita, S.; Smith, C.; Batruch, I.; Zheng, Y.; Rückert, F.; Grützmann, R.; Pilarsky, C.; Gallinger, S.; Diamandis, E. P., Integrated Proteomic Profiling of Cell Line Conditioned Media and Pancreatic Juice for the Identification of Pancreatic Cancer Biomarkers. *Molecular & Cellular Proteomics* **2011**, *10* (10).
472. Chen, R.; Pan, S.; Brentnall, T. A.; Aebersold, R., Proteomic Profiling of Pancreatic Cancer for Biomarker Discovery. *Molecular & Cellular Proteomics* **2005**, *4* (4), 523-533.
473. Chen, R.; Pan, S.; Yi, E. C.; Donohoe, S.; Bronner, M. P.; Potter, J. D.; Goodlett, D. R.; Aebersold, R.; Brentnall, T. A., Quantitative proteomic profiling of pancreatic cancer juice. *PROTEOMICS* **2006**, *6* (13), 3871-3879.
474. Cullis, A. G.; Canham, L. T., Visible light emission due to quantum size effects in highly porous crystalline silicon. *Nature* **1991**, *353* (6342), 335-338.
475. Guo, S.; Jacroux, T.; Ivory, C. F.; Li, L.; Dong, W.-J., Immunobinding-induced alteration in the electrophoretic mobility of proteins: An approach to studying the preconcentration of an acidic protein under cationic isotachopheresis. *ELECTROPHORESIS* **2019**, *40* (9), 1314-1321.
476. Jacroux, T.; Bottenus, D.; Rieck, B.; Ivory, C. F.; Dong, W.-j., Cationic isotachopheresis separation of the biomarker cardiac troponin I from a high-abundance contaminant, serum albumin. *ELECTROPHORESIS* **2014**, *35* (14), 2029-2038.
477. Stutz, H.; Bordin, G.; Rodriguez, A. R., Capillary zone electrophoresis of metal-binding proteins in formic acid with UV- and mass spectrometric detection using cationic transient capillary isotachopheresis for preconcentration. *ELECTROPHORESIS* **2004**, *25* (7-8), 1071-1089.
478. Kubačák, P.; Mikui, P.; Valáiková, I.; Havránek, E., Simultaneous Determination of Essential Basic Amino Acids in Pharmaceuticals by Capillary Isotachopheresis. *Archiv der Pharmazie* **2006**, *339* (2), 96-99.
479. Sázelová, P.; Kašička, V.; Šolínová, V.; Koval, D., Determination of purity degree and counter-ion content in leirelin by capillary zone electrophoresis and capillary isotachopheresis. *Journal of Chromatography B* **2006**, *841* (1), 145-151.
480. Bottenus, D.; Hossan, M. R.; Ouyang, Y.; Dong, W.-J.; Dutta, P.; Ivory, C. F., Preconcentration and detection of the phosphorylated forms of cardiac troponin I in a cascade microchip by cationic isotachopheresis. *Lab on a Chip* **2011**, *11* (22), 3793-3801.
481. Qu, Y.; Marshall, L. A.; Santiago, J. G., Simultaneous Purification and Fractionation of Nucleic Acids and Proteins from Complex Samples Using Bidirectional Isotachopheresis. *Analytical Chemistry* **2014**, *86* (15), 7264-7268.
482. Eid, C.; Santiago, J. G., Isotachopheresis applied to biomolecular reactions. *Lab on a Chip* **2018**, *18* (1), 11-26.
483. Lynn, N. S.; Sipova, H.; Adam, P.; Homola, J., Enhancement of affinity-based biosensors: effect of sensing chamber geometry on sensitivity. *Lab on a Chip* **2013**, *13* (7), 1413-1421.

9. List of Publications

1. Urmann K., **Arshavsky-Graham S.**, Walter J.G., Scheper T., and Segal E., "Whole-cell Detection of Live *Lactobacillus acidophilus* on Aptamer-Decorated Porous Silicon Biosensors", *Analyst* 141.18 (2016): 5432-5440.
2. **Arshavsky-Graham S.**, Vilneski R., Paratore F., Bercovici M., and Segal E., "1,000-fold Sensitivity Enhancement of Porous Si-based Optical Biosensors for Nucleic Acid and Proteins Detection", *Optics in the Life Sciences Congress*, Optical Society of America (2017): OmM4D.6.
3. **Arshavsky-Graham S.**, Massad-Ivanir N., Paratore F., Scheper T., Bercovici M., and Segal E., "On Chip Protein Pre-Concentration for Enhancing the Sensitivity of Porous Silicon Biosensors", *ACS sensors* 2.12 (2017): 1767-1773.
4. **Arshavsky-Graham S.**, Massad-Ivanir N., Segal E., and Weiss S. M., "Porous Silicon-Based Photonic Biosensors: Current Status and Emerging Applications", *Analytical Chemistry* 91.1 (2019): 441-467.
5. **Arshavsky-Graham S.**, and Segal E., "Lab-on-a-Chip Devices for Point-of-Care Medical Diagnostics". In: *Advances in Biochemical Engineering/Biotechnology*, Springer, Berlin, Heidelberg (2020).
6. **Arshavsky-Graham S.***, Urmann K.*, Salama R., Massad-Ivanir N., Walter J.G., Scheper T., and Segal E., "Aptamers vs. antibodies as capture probes in optical porous silicon biosensors", *Analyst* 145 (2020): 4991-5003 (*equal contribution)
7. **Arshavsky-Graham S.**, Boyko E., Salama R., and Segal E., "Mass transfer limitations of porous silicon-based biosensors for protein detection", *ACS Sensors* 5.10 (2020): 3058-3069.
8. **Arshavsky-Graham S.**, Enders A., Ackerman S., Bahnemann J., and Segal E., "Porous Silicon-Based Aptasensors for Protein Detection in 3D-Printed Microfluidics", *Microchimica Acta* 188 (2021): 67.
9. Ward S.J., Layouni R., **Arshavsky-Graham S.**, Segal E., and Weiss S.M., "Signal Processing Techniques to Reduce the Limit of Detection for Thin Film Biosensors", arXiv:2103.07524 (2021).
10. **Arshavsky-Graham S.**, Massad-Ivanir N., Scheper T., and Segal E. "Porous Silicon-Based Aptasensors: Towards Cancer Protein Biomarker Detection." *Submitted to ACS Measurement Science Au.*

List of Conferences

Oral Presentations:

2. **Arshavsky-Graham S.**, Vilneski R., Paratore F., Bercovici M., and Segal E., "1,000-fold Sensitivity Enhancement of Porous Si-based Optical Biosensors for Nucleic Acid and Proteins Detection", oral presentation at the Optics in Life Sciences OSA Congress, San Diego, CA, USA, 2017.
3. **Arshavsky-Graham S.** and Segal E., "Porous Silicon-Based Biosensors", oral presentation at the Spring Meeting of the Scientific Cooperation between Israel and Lower Saxony, Hannover, Germany, 2017.
4. **Arshavsky-Graham S.**, Massad-Ivanir N., Horev R., Paratore F., Bercovici M., Scheper T. and Segal E., "Microfluidics Integrated Porous Silicon Aptasensors for Label-free and Sensitive Protein Detection", invited oral presentation at the 28th Anniversary World Congress on Biosensors, Miami, United States, 2018.
5. **Arshavsky-Graham S.**, Ackerman S., Sabach O., Epping N.M., Scheper T., Bahnemann J., and Segal E., "Multiplexed Biomarker Detection with Porous Silicon-Based Aptasensors in 3D Printed Microfluidic Devices", oral presentation at the 5th Conference of the Israel Society for Biotechnology and Engineering, Tel Aviv, Israel, 2019.
6. **Arshavsky-Graham S.**, Boyko E., Salama R., Ackerman S., Scheper T., Bercovici M., and Segal E., "Unraveling Mass Transfer Limitations of Porous Silicon-Based Aptasensors for Protein Detection", accepted for an oral presentation at the Porous Semiconductors Science and Technology (PSST), Lido di Camaiore, Tuscany, Italy, 2021.
7. **Arshavsky-Graham S.**, Boyko E., and Segal E., "Nanostructured Porous Silicon Biosensors: Understanding and Overcoming Mass Transfer Limitations", live presentation at the ACS Spring Meeting, 2021.

Posters Presentations:

1. **Arshavsky S.** and Segal E., "Label-Free Optical Biosensor for Early Diagnosis of Pancreatic Cancer", poster presentation at the 3rd Conference of the Israel Society for Biotechnology Engineering (ISBE), Tel-Aviv, Israel, 2015.
2. **Arshavsky S.** and Segal E., "Label-Free Optical Biosensor for Early Diagnosis of Pancreatic Cancer", poster presentation at the 10th International Conference on Porous Semiconductors Science and Technology (PSST), Tarragona, Spain, 2016.
3. **Arshavsky-Graham S.** and Segal E., "Label-Free Optical Biosensor for Early Diagnosis of Pancreatic Cancer", best poster presentation award at the 2nd Israel-Greece Joint Meeting on Nanotechnology and BioNanoscience, Heraklion, Greece, 2016.

References

4. **Arshavsky-Graham S.**, Massad-Ivanir N., Paratore F., Bercovici M., and Segal E., "Label-Free Optical Biosensor for Early Diagnosis of Pancreatic Cancer", best poster presentation award at the Batsheva de Rothschild Seminar on New Concepts in Biosensing, Dead Sea, Israel, 2017.
5. **Arshavsky-Graham S.**, Massad-Ivanir N., Horev R., Paratore F., Bercovici M., Scheper T. and Segal E., "Microfluidics Integrated Porous Silicon Biosensors for Protein Detection", poster presentation at the 4th Conference of the Israel Society for Biotechnology Engineering (ISBE), Tel-Aviv, Israel, 2017.
6. **Arshavsky-Graham S.**, Massad-Ivanir N., Horev R., Paratore F., Bercovici M., Scheper T. and Segal E., "Microfluidics Integrated Porous Silicon Biosensors for Protein Detection", best poster presentation award at the Research day, Faculty of Biotechnology and Food Engineering, Technion, Haifa, Israel, 2018.
7. **Arshavsky-Graham S.**, Massad-Ivanir N., Paratore F., Bercovici M., Scheper T. and Segal E., "Microfluidics Integrated Porous Silicon Biosensors for Protein Detection", poster presentation at the Jacobs Graduate Research Day, Technion, Haifa, Israel, 2019.
8. **Arshavsky-Graham S.**, Enders A., Epping N.M., Scheper T., Bahnemann J. and Segal E., "Integration of Porous Silicon-Based Optical Aptasensors in a 3D-Printed Microfluidic Platform for Protein Detection", poster presentation at the 23rd International Conference on Miniaturized Systems for Chemistry and Life Sciences (μ TAS 2019), Basel, Switzerland, 2019.
9. **Arshavsky-Graham S.**, Boyko E., Salama R., Ackerman S., Scheper T., Bercovici M. and Segal E., "Deciphering Mass Transfer Limitations of Porous Silicon Based Aptasensors for Protein Detection", poster presentation at the 5th Conference of the Israel Society for Biotechnology and Engineering, Tel Aviv, Israel, 2019.
10. **Arshavsky-Graham S.**, Boyko E., Salama R., and Segal E., "Can We Make Porous Silicon Biosensors More Sensitive? Modelling and Limitations", poster presentation at the 24th International Conference on Miniaturized Systems for Chemistry and Life Sciences (μ TAS 2020), virtual conference, 2020.
11. **Arshavsky-Graham S.**, Sabach O., Ackerman S., Epping N.M., Scheper T., Bahnemann J., and Segal E., "Multiplexed Biomarker Detection with Porous Silicon-Based Aptasensors in 3D Printed Microfluidic Devices", accepted for a poster presentation at the Porous Semiconductors Science and Technology (PSST), Lido di Camaiore, Tuscany, Italy, 2020 (postponed due to COVID-19).

Curriculum Vitae – Sofia Arshavsky-Graham

E-mail: sofi.arshavsky7@gmail.com | Phone No. +972-524721728

Academic Degrees:

- 2015 - 2021** **Dual Doctorate Program (PhD and Dr. rer. nat)**
- Department of Biotechnology and Food Engineering, Technion-Israel Institute of Technology, Haifa, Israel - Direct PhD track.
- Institute of Technical Chemistry, Leibniz University, Hannover, Germany.
- Advisors: Prof. Ester Segal and Prof. Thomas Scheper.
- Dissertation title: “*Porous Silicon Biosensors for Protein Targets: Modelling and Sensitivity Enhancement*”.
- 2011 - 2015** **B.Sc. in Biotechnology and Food Engineering - Summa Cum Laude** (GPA 97.9). Technion – Israel Institute of Technology, Haifa, Israel.
-

Experience:

- 2018 – 2020** **Advisor of Undergraduate Students** - laboratory of Multifunctional Nanomaterials, Department of Biotechnology and Food Engineering, Technion, Haifa, Israel. *Instruction of senior B.Sc. students during their research projects.*
- 2014** **Summer Intern** - Institute of Technical Chemistry of the Leibniz University, Hannover, Germany. *Research topic: “Development of a biosensor for bacteria detection”.*
- 2013 - 2014** **Research Assistant** - Laboratory of Multifunctional Nanomaterials, Department of Biotechnology and Food Engineering, Technion, Haifa, Israel. *Research topic: “Development of porous silicon-based nanostructures for drug delivery applications”.*
-

Educational Work:

- 2019 - 2020** **Teaching Assistant, English** - “Packaging of Food, Drugs and Biological Products”, International School, Technion, Haifa, Israel.
- 2017 - 2020** **Senior Teaching Assistant** - “Biochemistry Techniques”, Department of Biotechnology and Food Engineering, Technion, Haifa, Israel.
- 2015 - 2017** **Teaching Assistant** - "Bioprocess Engineering", "Nutrition" and "Food Analysis", Department of Biotechnology and Food Engineering, Technion, Haifa, Israel.
-